Science Innovation
INTERNATIONAL SCIENTIFIC JOURNAL

ISSN: 2181-3337

SCIENCE & INNOVATION

INTERNATIONAL SCIENTIFIC JOURNAL

VOLUME 5 | ISSUE 7 | 2026
Series A: Technical Sciences

Science Innovation
INTERNATIONAL SCIENTIFIC JOURNAL

International Scientific Journal
SCIENCE AND INNOVATION
Series A
Volume 5 Issue 7
July 2026

Tashkent 2026

INTERNATIONAL SCIENTIFIC JOURNAL

SCIENCE & INNOVATION

Series A: Technical Sciences

VOLUME	ISSUE	PUBLICATION DATE	PLACE
5	7	31 JULY 2026	TASHKENT

ISSUE IDENTIFICATION

RECOMMENDED ISSUE CITATION

Science and Innovation. Series A: Technical Sciences. Volume 5, Issue 7, July 2026. Tashkent: Science and Innovation LLC.
ISSN 2181-3337.

Individual article DOIs are registered through Crossref under prefix 10.67620.

JOURNAL INFORMATION

Volume / issue	Volume 5 · Issue 7	**Publication date**	31 July 2026
ISSN	2181-3337	**Publisher**	Science and Innovation LLC
Established	2022	**Publication language**	English
Frequency	Monthly	**Publication format**	Electronic · Open Access
Peer review	Double-blind peer review	**License**	Creative Commons Attribution 4.0
DOI registration	Crossref · Prefix 10.67620	**Official website**	https://scientists.uz

AIMS AND SCOPE

Series A publishes original research and reviews in engineering, technology, computer and information sciences, energy, architecture and construction, materials science, applied physics and mathematics, industrial systems, automation, environmental engineering, and related interdisciplinary innovations.

EDITORIAL AND PUBLICATION STANDARDS

PEER REVIEW
Editorial screening, integrity checks, independent double-blind review, and a documented editorial decision.

ETHICS & CORRECTIONS
Conflicts of interest, authorship, misconduct, corrections, retractions, complaints, and appeals are handled under published journal policies.

AI TRANSPARENCY
Authors must disclose substantive use of generative AI. AI tools cannot be credited as authors; responsibility remains with the human authors.

EDITORIAL OFFICE

Bakhtiyor Rustamov	CEO Science and innovation LLC	**Kozim Ergashov**	Academic Editor
Gulira'no Rakhmatullayeva	Responsible Secretary	**Feruzabonu Mannonova**	Language Editor
Feruza Ollomurodova	Manuscript Coordinator	**Jahongir Bekmuradov**	Language Editor
Farangiz Sagdullaeva	Technical Editor	**Anvar Ergashev**	Digital Media Designer
Dilnoza Narzullayeva	Editorial Manager	**Asila Khaydaralieva**	Academic Editor
Sevara O'rinboyeva	Editorial Manager	**Bakhrom Qurbonov**	Digital Media Designer

PUBLISHER AND CONTACT

Science and Innovation LLC · Mass Media License No. 1597 (27 April 2022) · Publishing License No. 455168 (21 November 2024)
150 Shota Rustaveli Street, Vega Business Center, 6th floor, Room 2, Tashkent 100121, Uzbekistan
info@scientists.uz · +998 90 125 96 54 · https://scientists.uz · https://science-innovation.org

© 2026 Authors. Published by Science and Innovation LLC under CC BY 4.0.

SCIENTIFIC EDITORIAL BOARD

Series A: Technical Sciences

EDITOR-IN-CHIEF: ABDURAKHMONOVA NILUFAR ZAYNOBIDDIN QIZI - DOCTOR OF PHILOLOGICAL SCIENCES, PROFESSOR

33 BOARD MEMBERS	**INTERNATIONAL REPRESENTATION** Uzbekistan · South Korea · Cameroon · Russian Federation · Kyrgyzstan · Malaysia · India · United States · Iran · France

Members are listed by academic standing and editorial responsibility. Current institutional profiles and contact details are maintained on the journal website.

Yusupbekov Nodirbek Rustambekovich DSc, Technical Sciences, Academician, Academy of Sciences of Uzbekistan, Honored Scientist *Tashkent State Technical University named after Islam Karimov · Uzbekistan*	**Mirsaidov Mirziyod Mirsaidovich** DSc, Technical Sciences, Professor, Academician, Academy of Sciences of Uzbekistan *TIIAME" National Research University · Uzbekistan*	**Allayev Qahramon Rahimovich** DSc, Technical Sciences, Professor, Academician, Academy of Sciences of Uzbekistan, Honored Youth Mentor of Uzbekistan *Academy of Sciences of the Republic of Uzbekistan · Uzbekistan*
Yo‘ldoshev Shukurullo Ubaydullayevich DSc, Technical Sciences, Professor, Academician, Academy of Sciences of Uzbekistan *TIIAME" National Research University · Uzbekistan*	**Bakiyev Masharif Ro‘zmetovich** DSc, Technical Sciences, Professor *TIIAME" National Research University · Uzbekistan*	**Uon Don Yon** DSc, Technical Sciences, Professor *South Korea National Council for Future Education · South Korea*
Jimbo H. Claver PhD in Applied Mathematics and Statistics, Professor *Samarkand International University of Technology (SIUT) · Cameroon / Uzbekistan*	**Borisyuk Petr Viktorovich** DSc, Physical and Mathematical Sciences *National Research Nuclear University MEPhI (Russian Federation) · Russian Federation*	**Nishonov Mirkozimjon** Candidate of Technical Sciences, Professor *Fergana State University · Uzbekistan*
Sanayev Ermat Shermatovich PhD in Technical Sciences, Assoc. Professor *Tashkent Institute of Chemical Technology · Uzbekistan*	**Eshmuradov Dilshod Elmuradovich** Candidate of Technical Sciences, Assoc. Professor *Tashkent University of Information Technologies named after Muhammad al-Khwarizmi · Uzbekistan*	**Musayeva Shoira** Candidate of Economic Sciences, Professor *Samarkand Institute of Economics and Service · Uzbekistan*
Usmonov Ilkhom Achilovich Candidate of Technical Sciences, Professor *Samarkand State Institute of Architecture and Construction · Uzbekistan*	**Kamolov Ikhtiyor Ramazonovich** Candidate of Technical Sciences, Professor *Navoi State University · Uzbekistan*	**Abdazimov Anvar Daniyarovich** DSc, Technical Sciences, Professor *Tashkent State Technical University · Uzbekistan*
Akhatov Jasurjon Saidovich DSc, Technical Sciences, Professor *S.A. Azimov Institute of Physics and Technology of the Academy of Sciences of the Republic of Uzbekistan · Uzbekistan*	**Bazarov Dilshod Rayimovich** DSc, Technical Sciences, Professor *TIIAME" National Research University · Uzbekistan*	**Dodakho‘jayev Abdulla Tursunovich** DSc, Technical Sciences, Professor *Tashkent State Technical University named after Islam Karimov · Uzbekistan*
Fayzullayev Normurot Ibodullayevich DSc, Technical Sciences, Professor *Samarkand State University · Uzbekistan*	**Ibadullayev Akhmadjon Sobirovich** DSc, Technical Sciences, Professor *Tashkent State Transport University · Uzbekistan*	**Attokurov Urmat Tologonovich** Candidate of Technical Sciences, Assoc. Professor, Professor *M.M. Adyshev Osh Technological University · Kyrgyzstan*
Che Zalina binti Zulkifli PhD in Electrical and Electronic Engineering, Professor *Universiti Pendidikan Sultan Idris (UPSI) · Malaysia*	**Sreekumara Ganapathy** PhD in Civil Engineering, Professor *Ajou University in Tashkent · India / Uzbekistan*	**Hwang Myeon-Eun** Professor of Electrical and Computer Engineering *Ajou University in Tashkent · South Korea / Uzbekistan*
Dr. Danish Ather PhD in Information Technology, Professor *Amity University · India*	**Seungjik Lee** PhD in Information Technology, Professor *Tashkent University of Information Technologies named after Muhammad al-Khwarizmi · South Korea / Uzbekistan*	**Olimov Bakhshillo Amrillayevich** Candidate of Physical and Mathematical Sciences, Assoc. Professor, Professor *Editor of the journal "Physics · Uzbekistan*
Bradley Fitzgerald Jacob Professor of Electrical and Computer Engineering *Samarkand International University of Technology (SIUT) · USA / Uzbekistan*	**Mohammad Reza Bahrami** PhD in Mechanical Engineering, Professor *Samarkand International University of Technology (SIUT) · Iran / Uzbekistan*	**Florence Dujjarik Sandrine** PhD, Professor *Samarkand International University of Technology (SIUT) · France / Uzbekistan*
Kamalova Dilnavoz Ikhtiyorovna DSc, Technical Sciences, Professor *Navoi State University · Uzbekistan*	**Yunusov Mirdjalil Yusupovich** DSc, Technical Sciences, Professor *Tashkent Institute of Chemical Technology · Uzbekistan*	**Safarov Toyir Tursunovich** DSc, Technical Sciences, Professor *Tashkent Institute of Chemical Technology · Uzbekistan*

ISSN: 2181-3337 | SCIENTISTS.UZ VOLUME 5 ISSUE 7 | JULY 2026

METHODS FOR IMPROVING RADIO NAVIGATION SYSTEM RELIABILITY IN THE COMPREHENSIVE ASSESSMENT OF AIR TRAFFIC MANAGEMENT SYSTEM MODERNIZATION EFFECTIVENESS

Eshmuradov Dilshod[1], Abdukayumov Abdurashid[2], Saidova Gulchehra[3], Elmuradov Temurmalik[4]

Candidate of Technical Sciences, Associate Professor,
Tashkent University of Information Technologies[1],
Doctor of Technical Sciences, Professor, Tashkent State Transport University[2],
Tashkent University of Information Technologies[3],
Tashkent State University of Economics[4]

DOI: 10.67620/sai.57a0001

ABSTRACT

This article examines and proposes a new approach to the comprehensive assessment of the effectiveness of air traffic management system modernization. The assessment is conducted in three principal areas. The first area analyzes the reliability and fault tolerance of radio navigation systems using Markov chains, the beta-factor model for common-cause failures (CCFs), and Bayesian statistical estimation methods. The second area examines the joint application of inertial and satellite navigation systems and develops a method for selecting the most appropriate configuration for aviation facilities. The third area is devoted to the quantitative assessment of the human-factor risk that has the greatest influence on accidents and incidents within the air traffic management system.

By integrating these three areas into a single framework, a composite modernization effectiveness index is proposed. The proposed method was tested using data from the dual-channel VOR/DME radio navigation system operated at Tashkent Airport. The difference between the analytical calculations and the Monte Carlo simulation results was only 2.3%, demonstrating the high accuracy of the model.

The results show that a 10% increase in the beta-factor coefficient for common-cause failures raises the probability of hazardous misleading navigation information by 34%. This reduces the compliance margin relative to the safety requirements established for ICAO Category III operations. The proposed composite index enables navigation service organizations to compare modernization projects in terms of technical reliability, human-factor effects, and economic efficiency, thereby supporting the selection of the most appropriate decisions.

ACCEPTED

20.07.26

Keywords: *radio navigation systems; reliability; fault tolerance; Markov chains; common-cause failure (CCF); beta factor; Monte Carlo method; integrated inertial-satellite navigation system; human factor; air traffic management; modernization effectiveness; PBN/RNP.*

CC BY

Introduction

Modernizing the air traffic management (ATM) system has become a priority for improving the safety and efficiency of civil aviation. In accordance with International Civil Aviation Organization (ICAO) standards, the civil aviation sector of the Republic of Uzbekistan is transitioning to area navigation

and performance-based navigation (RNAV/RNP), which imposes stringent requirements on the accuracy, integrity, continuity, and availability of navigation services [25, 26]. However, assessments of modernization project effectiveness are often limited to primary financial and technical indicators, such as cost-benefit analysis and equipment performance [19, 20, 21], while technical-system reliability and the human factor are generally studied separately and in isolation from one another.

The flight-navigation suite of a modern aircraft contains several navigation systems, particularly inertial navigation systems (INSs) and satellite navigation systems (SNSs). Their different physical principles and algorithmic support make complementary integration possible: an INS provides a high data-update rate of up to 100 Hz and complete autonomy, whereas an SNS ensures stable long-term accuracy [12, 14, 15, 16]. At the same time, ground-based radio navigation facilities, including VOR, DME, ILS, and MLS systems, constitute the core infrastructure of air traffic management, and their uninterrupted operation directly affects flight safety. Modern probabilistic models that account for redundancy architectures, common-cause failures (CCFs), and operation in degraded modes are therefore essential for ensuring the reliability of such systems [1–8].

According to ICAO statistical data, approximately 70–80% of aviation occurrences are associated with causal factors classified under the human-factor category. As aviation technology improves, the relative contribution of this factor has not decreased; rather, it has increased. In recent years, approximately 70% of aviation accidents and 50% of maritime transport accidents have been associated with inappropriate personnel actions, whereas technical causes have accounted for 20–30%. Consequently, assessing the effectiveness of ATM system modernization requires a comprehensive methodology that considers not only the reliability indicators of technical systems but also human-factor risk.

The purpose of this article is to develop a methodology for the comprehensive assessment of ATM system modernization effectiveness by integrating radio navigation system reliability and fault-tolerance models (Markov chains, a CCF beta-factor model, Bayesian estimation, and Monte Carlo verification), a method for standardizing integrated inertial-satellite navigation system configurations, and an approach to human-factor risk assessment, and to provide practical validation using the VOR/DME system operated at Tashkent Airport.

LITERATURE REVIEW

The modeling of radio navigation system reliability has progressed through several methodological stages. Contemporary literature on the reliability, safety, and maintenance of engineering systems [2] systematically presents reliability block diagrams and fault-tree analysis (FTA), while the theoretical and practical aspects of risk assessment are examined in depth in [3]. Reliability analysis of communication systems using fault trees [1] and modern methods for the statistical analysis of reliability data [5] provide an important methodological foundation. EUROCONTROL's ESARR 6 Safety Assessment Methodology [4] establishes regulatory requirements for air navigation systems.

Nevertheless, several significant gaps remain in the literature. First, most published models treat a radio navigation system as a series-parallel combination of independent components. This approach underestimates common-cause failures (CCFs), which may account for up to 40% of observed systemic failures in air navigation infrastructure. The modified beta-factor method proposed to address this problem [7] permits analysis of software common-cause failures. Second, although the monograph on global aeronautical communications, navigation, and surveillance [6] provides a detailed description of the operational characteristics of radio navigation systems, it gives only limited treatment to probabilistic reliability models.

To address these two gaps, an earlier study by the authors [8] tested an integrated methodology that combines continuous-time Markov chains (CTMCs), beta-factor integration of CCFs, Bayesian parameter estimation, and large-scale Monte Carlo verification using the dual-channel VOR/DME system operated

at Tashkent Airport. The reliability component of the present article is based on that methodology and integrates it into the overall composite indicator of ATM modernization effectiveness.

The second research area concerns the integration and standardization of integrated inertial-satellite navigation systems (ISNSs). The convergence of a secondary-processing algorithm for relative navigation using multi-system global navigation satellite system (GNSS) user equipment was analyzed in [12], while an analysis of the most hazardous interference affecting a relay radio station [13] addresses practical aspects of improving the interference resistance of radio navigation systems. Studies on the structure of a recurrent-neural-network system for identifying inertial navigation system errors [14], the assessment of satellite-navigation accuracy over a wide altitude range [15], and integration with a local positioning system based on ultra-wideband radio modules [16] examine separate components of an ISNS. However, none of these studies presents an integrated methodology for generating a standardized range of ISNS configurations for aviation facilities and rationalizing them according to a cost criterion. The authors' previous work was directed toward filling this gap, and the method is used here as the second component of modernization-effectiveness assessment.

The third research area addresses the assessment of ATM system modernization effectiveness. Studies on the automation of aeronautical-information processing using multi-agent technologies [17] and on the need to use geographic information systems in air traffic control [18] describe technological aspects of ATM digitalization and automation. A fundamental analysis of the efficiency of European air navigation service providers using data, models, and methods [19] relies mainly on economic-efficiency measures and data envelopment analysis (DEA) models. Reports by the U.S. Government Accountability Office (GAO) on the management of air traffic control modernization programs [20, 21] analyze project schedules and budget management. Notably, none of these works integrates technical-reliability indicators and human-factor risk into a single effectiveness index; each is limited to an individual dimension such as cost, schedule, or productivity.

The fourth research area concerns the analysis and assessment of human factors in the ATM system. Human-factor analysis of air traffic control safety using the HFACS-BN model [22] enables quantitative assessment of risk factors associated with controller behavior through Bayesian networks. Qualitative indicators of air traffic controllers' attitudes toward errors [23] and analysis of the influence of aviation-maintenance documentation and human factors on flight safety using the PEAR framework [24] provide contemporary methodological foundations in this field. Nevertheless, the human-factor risk indicators developed in these studies have not been integrated with technical-system reliability models.

Thus, the literature review shows that four areas—technical-reliability modeling, ISNS standardization, assessment of ATM modernization effectiveness, and human-factor risk analysis—have largely developed independently. A methodology that integrates all four areas within a single composite effectiveness index has not been identified in the literature, which defines the scientific task addressed in this article.

Methodology

The proposed methodology comprises three interrelated components and a final composite effectiveness index that integrates them: (1) assessment of radio navigation system reliability using a Markov-Bayesian beta-factor model; (2) standardization of ISNS configurations and selection of the optimal configuration; and (3) quantitative assessment of human-factor risk.

1. Assessment of Radio Navigation System Reliability Using a Markov-Bayesian Beta-Factor Model

Let a finite state space $S = \{s_0, s_1, \dots s_n\}$ be given, where s_j corresponds to the state in which exactly j channels have failed. Under m-out-of-N logic, the system is considered operational in states s_j when $j < N - m + 1$.

ISSN: 2181-3337 | SCIENTISTS.UZ

The state-probability vector $P(t) = [P_o(t), P_1(t), \dots P_n(t)]^T$ changes in accordance with the Chapman-Kolmogorov equation:

$$\frac{dP(t)}{dt} = QP(t) \quad (1)$$

where $P(0) = e_0$ is the initial condition of the equation, $P(t)$ is the vector of state probabilities of the Markov system at time t, and Q is the generator matrix.

If the system is in the first state at the initial time, the initial vector is expressed as $e_0 = [1,0, \dots,0]^T$.

The steady-state availability $A = \sum_{j \in U_p} \pi_j$ is found by solving the stationary equations subject to the normalization condition.

where A is the steady-state availability;

U_P is the set of operational states of the system;

π_j is the stationary probability of state j. The vector $\pi = [\pi_0, \pi_1, \dots, \pi_n]^T$ is determined by solving the system of equations $\mathbf{Q}^T\pi = 0$,, subject to the normalization condition $\sum_{j=0}^{n} \pi_j = 1$.

Here, Q is the generator matrix of the Markov chain, and the equation $\mathbf{Q}^T\pi = 0$ describes the long-run stationary state of the system. The normalization condition ensures that the sum of all probabilities is always equal to one. Availability is calculated as the sum of the probabilities that the system is in operational states under steady-state conditions.

If the failed state is treated as an absorbing state in the Markov model, the mean time to failure (MTTF) is calculated using the fundamental matrix as follows:

$$MTTF = 1^T N e_0 \quad (2)$$

where $N = (-Q_T)^{-1}$.

Common-cause failures (CCFs) are incorporated into the system reliability model using the beta-factor method. Under this approach, the total failure rate of each channel is divided into independent and common-cause components:

$$\lambda_I = (1 - \beta)\lambda,$$
$$\lambda_{CCF} = \beta\lambda \quad (3)$$

where λ is the total channel failure rate, λ_I is the independent-failure rate, λ_{CCF} is the common-cause failure rate, and β is the coefficient representing the proportion of common-cause failures.

When a CCF occurs, all N channels of the redundant system enter the failed state simultaneously. Therefore, an additional transition from the operational state to the fully failed state is added to the Markov-chain generator matrix with the following rate:

$$q_{0N} = \lambda_{CCF}$$

With CCFs included, the steady-state availability of the system is determined using the modified generator matrix:

$$Q_{CCF}^T\pi = 0, \sum_{i=0}^{N} \pi_i = 1$$
$$A_{CCF} = \sum_{i \in U} \pi_i, \quad (4)$$

where U is the set of operational states of the system and π_i is the stationary probability of state i.

For a dual-channel redundant system, a first-order approximation of availability can be obtained using the following analytical expression:

$$A_{CCF} \approx \frac{A_0}{1+\beta\lambda/\mu} \quad (5)$$

where A_0 is the availability without accounting for CCFs and μ is the repair rate. This expression is not a general solution; it is an approximate estimate for a simplified dual-channel model.

Analysis of the model shows that even at $\beta = 0.05 - 0.10$, the values recommended by IEC 61508 for aviation systems, common-cause failures substantially reduce the effectiveness of redundancy. In

particular, when the failure rate is high relative to the repair rate, ($\lambda/\mu \gg 1$), the resulting decrease in availability adversely affects safety performance.

The probability of hazardous misleading information (HMI) is assessed through the joint effect of the probability of a failure, the probability that the navigation error exceeds the allowable limit, and the probability that the monitoring system fails to generate an alert within the specified time:

$$P_{HMI} = \sum_k P(F_k)P(E > E_L|F_k)P(\bar{A}|F_k, E > E_L) \quad (6)$$

where F_k is a type-k failure state, E is the navigation error, E_L is the allowable error threshold (protection level/alert limit), and $\bar{A}$ denotes the absence of an alert during the specified reaction time. This model makes it possible to quantify the contribution of each failure scenario to the formation of hazardous misleading information and to determine the system integrity indicators required by ICAO.

2. Method for Standardizing ISNS Configurations

All considered types of inertial primary-information sensor units (for example, ten unit types) are combined with a multi-channel GLONASS/GPS/Galileo receiver using the most promising integration architecture—a deeply integrated architecture—to generate several configurations (for example, ten) of a strapdown integrated ISNS. During the characterization stage, experts evaluate the principal indicators of each configuration, including its cost. During the standardization stage, cost is used as the criterion for excluding redundant configurations and substantiating a minimum standardized range of ISNSs. The resulting minimum standardized range, together with its cost and technical characteristics, provides the basis for the second, ISNS-related component of the composite effectiveness index.

3. Assessment of Human-Factor Risk

Human-factor risk is assessed using an HFACS-type classification and statistical data from the occurrence log of the ATM organization. The normalized indicator R_{HF}, ranging from 0 to 1, is defined as the proportion of recorded occurrences associated with personnel error during a given period, weighted by the severity of those occurrences. General ICAO statistics—according to which 70–80% of aviation occurrences are associated with human factors—may be used as an initial value and subsequently refined for a particular organization using models such as HFACS-BN [22].

4. Composite Effectiveness Index

The reliability, human-factor risk, and economic-efficiency indicators discussed above are integrated into a single composite assessment index. The overall effectiveness of a modernization option is evaluated using the following linear aggregation function:

$$E = w_1 A_n + w_2(1 - R_{HF}) + w_3\left(\frac{1}{C_n}\right) \quad (7)$$

$$w_1 + w_2 + w_3 = 1$$

where A_n is the availability calculated using Equation (5), normalized relative to the regulatory value established by ICAO;

R_{HF} is the normalized human-factor risk index ($0 \le R_{HF} \le 1$);

C_n is the relative economic-cost indicator obtained through standardization of the integrated inertial-satellite navigation system;

w_1, w_2, w_3 are weighting coefficients that express the relative importance of the reliability, safety, and economic-efficiency criteria. They are determined using expert-assessment methods, including the Analytic Hierarchy Process (AHP). Three criteria were compared pairwise: R, technical reliability/availability; H, human-factor risk on a reverse scale; and C, economic efficiency. Because safety is the dominant criterion in air traffic management, an expert group consisting of five specialists in the field (n = 5) constructed the following pairwise-comparison matrix using Saaty's 1–9 scale (Table 1):

ISSN: 2181-3337 | SCIENTISTS.UZ

Table 1. AHP Pairwise-Comparison Matrix (Saaty Scale).

Criterion	R (availability)	H (human factor)	C (economic)
R (availability)	1	3	5
H (human factor)	1/3	1	3
C (economic)	1/5	1/3	1

The priority vector was calculated using the geometric-mean method. The geometric mean of the elements in each row was calculated and then normalized by the sum of the results. The following weighting coefficients were obtained:

w_1 (R) ≈ 0.64;

w_2 (H) ≈ 0.26;

w_3 (C) ≈ 0.10.

The consistency of the matrix was checked using the approximate maximum eigenvalue λmax ≈ 3.04. The consistency index was CI = (λmax − n)/(n − 1) ≈ 0.018. With a random index of RI = 0.58 for n = 3, the consistency ratio was CR = CI/RI ≈ 0.03, which is well below the accepted threshold of CR ≤ 0.10 and is therefore satisfactory.

When modernization options are evaluated, the ICAO integrity requirements for the ATM system are treated as a mandatory constraint. The probability of hazardous misleading information is calculated using Equation (6) and must satisfy the following condition:

$$P_{HMI} \leq 10^{-9} \quad (8)$$

If this condition is not satisfied, the modernization option does not meet ICAO Category III safety requirements and is excluded from further evaluation regardless of the value of the composite effectiveness index E. Thus, the proposed approach permits selection of the most appropriate modernization option while simultaneously accounting for technical reliability, human-factor risk, and economic efficiency.

ANALYSIS AND RESULTS

1. Reliability Analysis of the VOR/DME System at Tashkent Airport

The proposed methodology was tested using the dual-channel VOR/DME radio navigation system at Tashkent International Airport (UTTT). The system operates according to a hot-standby redundancy principle: the primary channel (C1) continuously transmits the navigation signal, while the standby channel (C2) is synchronized and automatically activated within one second when a primary-channel failure is detected.

To estimate the model parameters, maintenance and operational logs for 2016–2024 were analyzed. During this period, $n_{VOR} = 14$ failures were recorded for the VOR subsystem and $n_{DME} = 9$ failures for the DME subsystem. The total operating time for each system was

$$T_{VOR} = T_{DME} = 140160 \ \textit{hours.}$$

A weakly informative $G(1, 10^4)$ prior distribution was used to estimate the failure rates. The posterior estimates obtained using the Bayesian approach were as follows:

$$\lambda_{VOR} = 9.93 \times 10^{-5}\ h^{-1},$$
$$\lambda_{DME} = 6.42 \times 10^{-5}\ h^{-1}$$

To account for common-cause failures, $\beta = 0.05$, the value recommended by IEC 61508 for physically separated redundant channels sharing a common power supply, was adopted. According to the maintenance data, the mean repair time was taken as $\frac{1}{\mu} = 4\ h$, which is consistent with a continuously staffed duty service.

Three operating scenarios were considered to assess the sensitivity and practical applicability of the proposed model:

$C1$: independent hot-standby redundancy without accounting for common-cause failures;

ISSN: 2181-3337 | SCIENTISTS.UZ

$C2$: hot-standby redundancy accounting for common-cause failures with $\beta = 0.05$;

$C3$: hot-standby redundancy accounting for both common-cause failures and a degraded operating mode. The degraded mode was defined as operation in a monitoring mode in which the navigation system retained part of its functionality, corresponding to approximately 50% operating capacity.

For each scenario, the Markov model was used to calculate availability, the probability of hazardous misleading information, and the composite effectiveness index. The calculation results are presented in Table 2.

Table 2. Probability of Hazardous Misleading Information and Composite Effectiveness Index.

Scenario	MTTF_analytical (h)	MTTF_MC (h)	Δ (%)	A_analytical	P_HMI
C1 (independent redundancy, no CCF)	87 420	87 612	0.22	0.999954	8.3×10^{-11}
C2 (independent redundancy + CCF)	21 850	22 136	1.31	0.999816	6.1×10^{-9}
C3 (independent redundancy + CCF + degraded mode)	19 340	19 787	2.31	0.999783	4.7×10^{-9}
ICAO Category III requirement	–	–	–	≥0.9999	$<10^{-9}$

The table shows that the difference between the analytical calculations and the Monte Carlo simulation ($R = 10^6$) is small. The largest relative deviation, 2.31%, was observed for Scenario C3. This confirms the reliability of the calculation results obtained with the proposed Markov model.

Comparison of the scenarios shows that accounting for common-cause failures has a substantial effect on system reliability. Without CCFs, $P_{HMI} = 8.3 \times 10^{-11}$, which satisfies the ICAO Category III requirement. However, when a CCF with $\beta = 0.05$ is included, the indicator increases to 6.1×10^{-9}, exceeding the specified limit. Although accounting for the degraded mode slightly reduces P_{HMI}, the value remains above the ICAO Category III requirement ($P_{HMI} < 10^{-9}$).

The sensitivity analysis shows that increasing the β coefficient from 0.05 to 0.055, that is, by 10%, increases the probability P_{HMI} by 34%. This demonstrates that common-cause failures have a serious effect on the safety margin of redundant radio navigation systems. Conversely, reducing the mean repair time by 20%, for example by improving spare-parts logistics, decreases P_{HMI} by 18% and increases MTTF by 11%.

Optimization of the scheduled-maintenance interval at a ratio of $C_k/C_p = 25$ yielded an optimal interval of $T^* = 1820$ hours. This is 12% shorter than the current organizational standard of 2,080 hours and could reduce the annual number of emergency occurrences from 1.7 to 1.1. These results indicate that the maintenance strategy should be revised using a risk-based approach.

2. Results of ISNS Configuration Standardization

All ten types of inertial primary-information sensor units were combined with a multi-channel GLONASS/GPS/Galileo receiver using a deeply integrated architecture, generating ten configurations of a strapdown integrated ISNS. During the characterization stage, expert assessments were obtained for the principal indicators of each configuration, including cost. During the standardization stage, redundant configurations were excluded according to the cost criterion, producing a minimum standardized ISNS range suitable for aviation facilities in the short- and medium-term future. This result directly supports determination of the C_{norm} component of the composite effectiveness index: the lower the cost of the minimum standardized range, the lower C_{norm} becomes and, consequently, the higher the value of E according to Equation (6).

ISSN: 2181-3337 | SCIENTISTS.UZ

3. Results of the Human-Factor Assessment

According to general ICAO statistics and available sources on human factors, the causal factors of aviation occurrences are distributed approximately as shown in Table 3.

Table 3. Causal Factors of Aviation Occurrences.

Causal-factor group	Share, %
Inappropriate personnel actions (human factor)	60–70
Technical causes	20–30
Adverse effects of external factors and other causes	remainder
Human-factor share in aviation accidents (recent years)	~70

On the basis of these data, the initial value of R_{HF} for a particular organization may be estimated at approximately 0.6–0.7. This demonstrates that personnel training, professional development, and rational staff assignment should be prioritized alongside technical systems in the modernization program. Targeted training programs and implementation of a safety-management system—for example, regular monitoring based on HFACS-BN [22]—could realistically reduce R_{HF} to approximately 0.3–0.4.

It should be emphasized that the general ICAO statistics presented in Table 3 serve only as an initial prior estimate for assessing human-factor risk. To ensure methodological consistency with the Bayesian approach used to assess radio navigation system reliability, this initial value should be updated using the frequency of personnel-error-related occurrences in the organization's own occurrence log for 2016–2024 as the likelihood: H_posterior ∝ H_prior × L (local data). Unlike complete reliance on general ICAO indicators, this approach accounts for local operating conditions, including controller competence, workload, organizational arrangements, and safety requirements, thereby improving the objective reliability of the H estimate. The update is planned to be implemented once sufficient local occurrence-log statistics have been collected.

4. Calculation of the Composite Effectiveness Index

Using the component indicators obtained above, an illustrative calculation was performed according to Equation (6). For Scenario C2, $A_{norm} = A_{an}/0.9999 \approx 1.00007 \approx 1$ (compliant with the standard), the initial human-factor risk was taken as R_{HF} = 0.65, and the pre-standardization ISNS cost indicator was taken as $C_{norm} = 1.0$ (the baseline, non-standardized condition). With equal weights ($w_1 = w_2 = w_3 = 1/3$), the initial value of E is approximately 0.45. When C_{norm} is reduced to 0.7 through ISNS standardization and R_{HF} is reduced to 0.35 through a targeted human-factor program, E increases to 0.66, or by approximately 47% (Table 4).

Table 4. Reduction in Human-Factor Risk.

Indicator	Before modernization	After modernization
A_{norm}	≈1.00	≈1.00
R_{HF}	0.65	0.35
C_{norm}	1.00	0.70
Composite index E	≈0.45	≈0.66

The result above, obtained using equal weights ($w_1 = w_2 = w_3 = 1/3$), is presented only as an initial illustration. When the weighting coefficients are adopted in accordance with the AHP results—$w_1 \approx 0.64$ for reliability/availability, $w_2 \approx 0.26$ for the human factor, and $w_3 \approx 0.10$ for economic efficiency—the composite-index results are calculated as shown in Table 5:

Table 5. Dependence of the Composite Effectiveness Index on the Weighting Scheme.

Indicator	Equal weights ($w = 1/3$)	AHP weights ($w_1 = 0.64$; $w_2 = 0.26$; $w_3 = 0.10$)

ISSN: 2181-3337 | SCIENTISTS.UZ

E, before modernization	0.45	0.73
E, after modernization	0.66	0.84
Relative increase, %	≈47	≈15

Thus, assessment using the AHP-derived weights increases the pre-modernization value of E from 0.45 to 0.73 and the post-modernization value from 0.66 to 0.84, while the relative improvement decreases from 47% under equal weights to approximately 15%. This difference is methodologically expected. Because the priority of technical reliability in aviation-safety decisions is reflected in the AHP pairwise comparisons, the final index becomes more dependent on technical availability, although the human factor retains its influence. This result demonstrates the sensitivity of the composite index to the selection of weighting coefficients and emphasizes that practitioners should clearly express their organization's priorities, such as safety or cost, in the AHP pairwise comparisons.

This illustrative calculation demonstrates the practical value of the composite index. Even when the technical-reliability margin is high and P_{HMI} complies with the ICAO limit, the overall effectiveness of a modernization project may be rated as low if the human-factor and economic-efficiency margins are not considered. This clearly demonstrates the limitations of assessment methods based exclusively on technical indicators.

DISCUSSION

The principal scientific result of this study is the justification of integrating a Markov-Bayesian beta-factor model for radio navigation system reliability, a method for standardizing ISNS configurations, and human-factor risk assessment within a single composite effectiveness index. In the reviewed literature, these approaches have generally developed separately: reliability models as an independent field [1–8], ISNS integration as a separate technical field [12, 14–16], modernization-effectiveness assessment mainly as a cost-economic field [19–21], and human-factor analysis as a separate area within safety management [22–24].

The practical advantage of the proposed composite index is that it avoids reliance on one-dimensional criteria, such as cost alone or technical reliability alone, when modernization projects are evaluated. In particular, the calculation presented in Section 4 shows that even when a technical system fully complies with ICAO requirements and P_{HMI} remains within the prescribed limit, high human-factor risk can reduce overall effectiveness. Modernization programs should therefore plan personnel training and professional development alongside technical re-equipment.

The methodology has several limitations. The Markov model assumes an exponential, memoryless distribution of failure times, which may underestimate aging effects. Determination of the weighting coefficients w_1, w_2, and w_3 depends on expert judgment; formal methods such as AHP are therefore recommended to improve objectivity. Statistical data collected in Uzbekistan for human-factor risk assessment remain limited, and models such as HFACS-BN require refinement using local occurrence logs. The study was tested using two facilities—the VOR/DME systems at Tashkent and Fergana international airports—and should subsequently be extended to a multi-site network. For each facility, maintenance and operating indicators for 2016–2024 were analyzed to permit comparison with the results above. System robustness is also quantitatively assessed under different operating conditions, including climate variation, airspace workload, and traffic density, and parameters such as the CCF β coefficient are recalibrated for individual facilities (Figure 1).

ISSN: 2181-3337 | SCIENTISTS.UZ

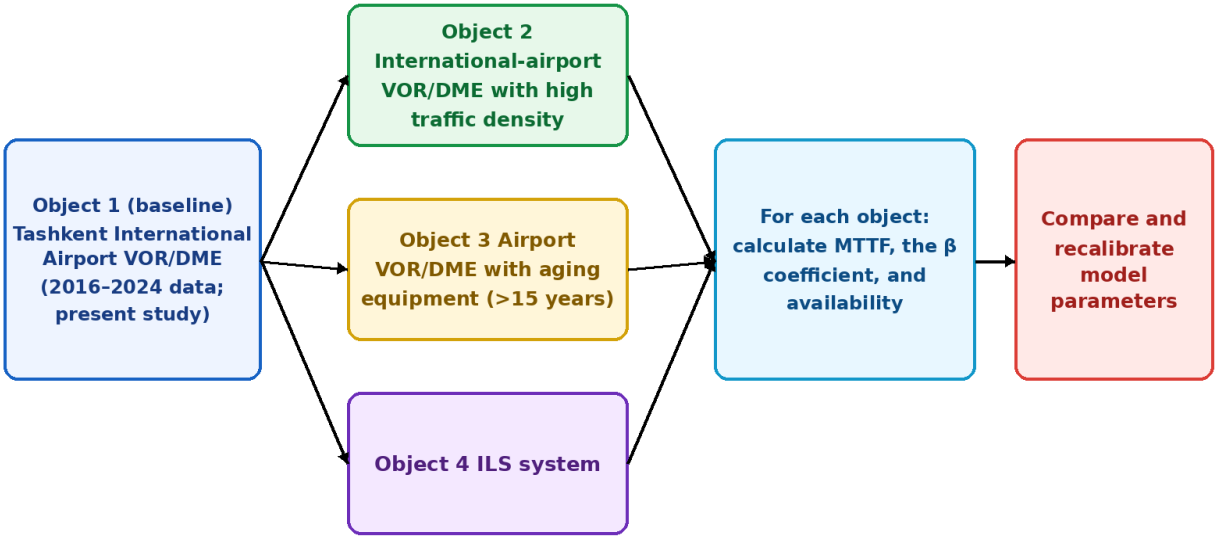


Figure 1. Scheme for Selecting Facilities and Calibrating the Model for Comparative Analysis.

Data from the VOR/DME system operated at Fergana Airport are adopted as the baseline, and a comparative analysis is performed with respect to the technical condition and operating characteristics of the equipment and the ILS system. For each facility, the mean time to failure (MTTF), β coefficient, and availability are calculated and analyzed. On the basis of the results, the model parameters are recalibrated, and the model's suitability for the operating conditions of Fergana International Airport and the reliability of its calculation results are evaluated. This approach supports objective assessment of radio navigation system reliability and determination of the model's applicability at different airports (Figure 2).

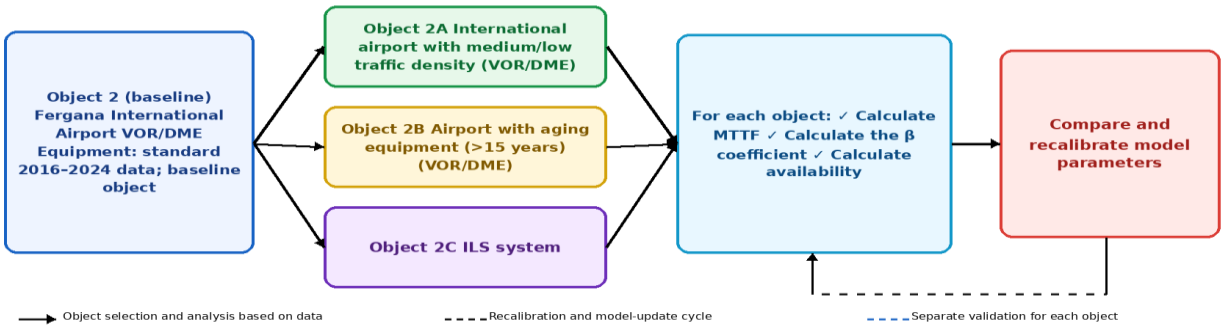


Figure 2. Scheme of the Proposed Methodology Using Fergana Airport as an Example.

On the basis of all results obtained, a graph is constructed to show the trend by which the probability of hazardous misleading information P_{HMI} increases as β increases (Figure 3). The VOR/DME systems at Tashkent and Fergana international airports are treated as the baseline facilities, while predicted values for the remaining facilities are estimated using elasticity extrapolation. The red dashed line represents the permissible risk threshold for ICAO Category III operations $P_{HMI} < 10^{-9}$. The graph demonstrates that an increase in the common-cause failure coefficient adversely affects radio navigation system safety and that the operating parameters must be optimized.

ISSN: 2181-3337 | SCIENTISTS.UZ

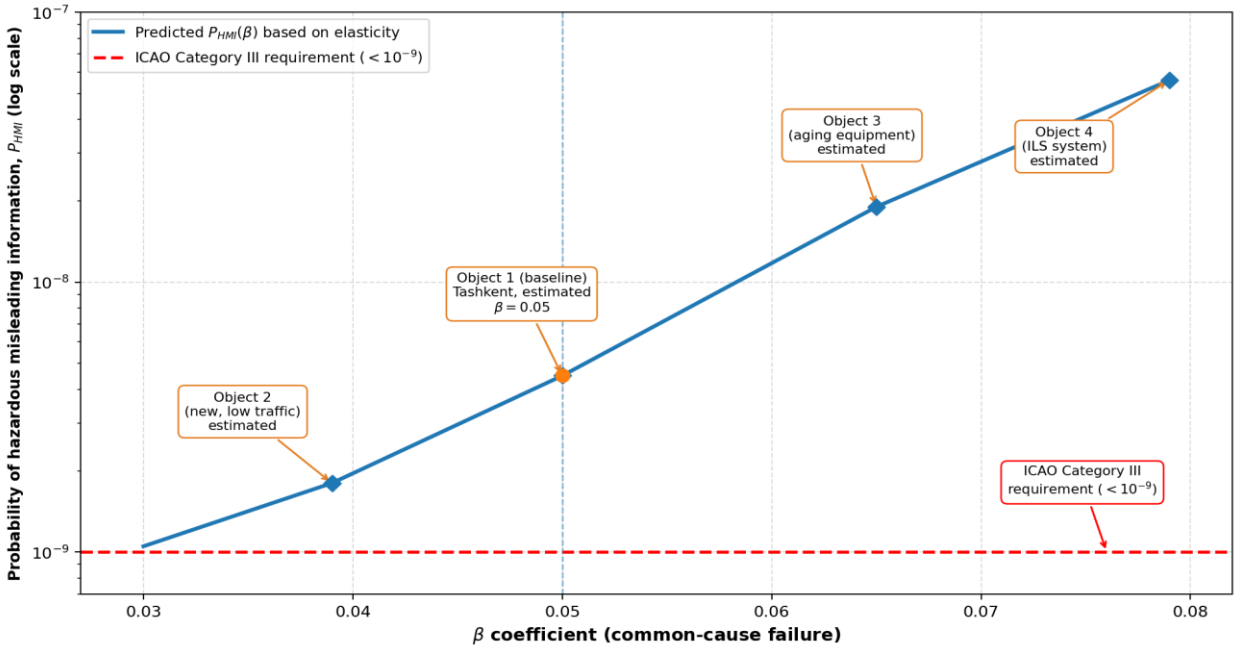


Figure 3. Assessment of the Effect of the β Coefficient on Common-Cause Failure Risk.

From a practical perspective, the proposed composite index may be a useful tool for Uzaeronavigation and other specialized organizations in selecting and prioritizing modernization projects during the transition to PBN/RNP-based navigation, because it permits technical, human-factor, and economic aspects to be compared on a single quantitative basis.

CONCLUSION

This article proposes a methodology for the comprehensive assessment of ATM system modernization effectiveness. The methodology integrates quantitative analysis of radio navigation system reliability using Markov chains, a CCF beta-factor model, and Bayesian estimation; a method for standardizing ISNS configurations; and human-factor risk assessment within a single composite effectiveness index (E).

Analysis of the VOR/DME system at Tashkent Airport showed that the analytical and Monte Carlo results agreed within 2.31%; a 10% increase in the CCF beta-factor coefficient increased the risk of hazardous misleading navigation information by 34%; and optimization of the scheduled-maintenance interval shortened the interval by 12% and could reduce the annual number of emergency occurrences. The ISNS standardization method improves economic efficiency by forming a minimum standardized range from ten initial configurations, while human-factor risk assessment demonstrates the priority of personnel-related measures in modernization programs.

The illustrative calculation confirmed that the composite index integrating the three components helped identify measures capable of increasing overall modernization effectiveness by approximately 47% in the example considered. The proposed methodology has practical value for Uzaeronavigation and other air navigation service providers in objectively planning and prioritizing modernization projects on the basis of technical reliability, human-factor risk, and economic-efficiency criteria. Future research should formalize the weighting coefficients using AHP, apply reliability models based on the Weibull distribution, and extend the methodology to a network of multiple facilities.

REFERENCES

1. Garg, S., & Garg, S. Reliability analysis of communication systems using fault tree analysis. International Journal of System Assurance Engineering and Management. 2020;11(2):321–334.
2. Dhillon, B. S. Engineering Systems Reliability, Safety, and Maintenance. Boca Raton: CRC Press; 2017.

3. Rausand, M., & Bøhren, I. B. Risk Assessment: Theory, Methods, and Applications. 2nd ed. Hoboken: Wiley; 2021.
4. EUROCONTROL. Safety Assessment Methodology—ESARR 6 Guidance Material. 2nd ed. Brussels; 2018.
5. Meeker, W. Q., Escobar, L. A., & Pascual, F. G. Statistical Methods for Reliability Data. 2nd ed. Hoboken: Wiley; 2022.
6. Ilcev, S. D. Global Aeronautical Communications, Navigation, and Surveillance. Vol. 1. Norwood: Artech House; 2019.
7. An Application of a Modified Beta Factor Method for the Analysis of Software Common Cause Failures. 2022. arXiv:2206.11321.
8. Kudratov, G., Eshmuradov, D., & Yadgarova, M. General issues of protection of backline computer networks. Science and Innovation. 2022;1(8):684–688.
9. Jumamuratov, B. A., Eshmuradov, D. E., & Azizov, O. X. The future of aeronautical processing: Opportunities and challenges of automation. Science and Innovation. 2023;2(4):231–236.
10. Jumamuratov, B. A., Eshmuradov, D. E., & Nabikhanova, A. D. Modern systems and tools for monitoring the radio transparency of composite materials: Current status and development prospects. In: Contemporary Problems and Development Prospects of Power Supply for Digital-Technology Facilities. Special Issue 1. Tashkent; 2024. pp. 438–441.
11. Jumamuratov, B. A., Abdukayumov, A. A., & Eshmuradov, D. E. Metrological support for a device used to monitor the radio transparency of composite materials. Milliy Standart [National Standard]. 2024;(3):1–5.
12. Savin, D. I., & Korovin, A. V. Convergence of the secondary-processing algorithm in relative navigation using multi-system global navigation satellite system user equipment. Teoriya i tekhnika radiosvyazi [Theory and Technology of Radio Communication]. 2019;(1):49–54.
13. Attokurov, U., Omorova, S., & Eshmuradov, D. Analysis of the most hazardous interference affecting the operation of a relay radio station. Science and Innovation. 2022;1(A6):484–488.
14. Kislukhin, G. A., Ryabov, D. A., & Burganskiy, A. I. Structure of a recurrent-neural-network system for identifying strapdown inertial navigation system errors. In: XLV Academic Readings on Cosmonautics: Abstracts. Moscow; 2021. pp. 529–530.
15. Zonov, N. I., & Moiseev, D. V. Assessment of satellite-navigation accuracy over a wide altitude range. System Analysis, Control, and Navigation. 2018. pp. 132–133.
16. Novichkov, A. R., Egorushkin, A. Yu., & Fashchevskiy, N. N. Integration of a strapdown inertial navigation system with a local positioning system based on ultra-wideband radio modules. In: XLIV Academic Readings on Cosmonautics: Abstracts. Moscow; 2020. pp. 553–554.
17. Eshmuradov, D. E., Elmuradov, T. D., & Turaeva, N. M. Automation of aeronautical-information processing based on multi-agent technologies. Scientific Bulletin of the Moscow State Technical University of Civil Aviation. 2022;25(1):65–76.
18. Eshmuradov, D. E., et al. The need to use geographic information systems in air traffic control. Turkish Journal of Computer and Mathematics Education (TURCOMAT). 2021;12(7):1972–1976.
19. Efficiency assessment in European air traffic management: A fundamental analysis of data, models, and methods. Journal of Air Transport Management. 2024.
20. U.S. Government Accountability Office. Air Traffic Control Modernization: Program Management Improvements Could Help FAA Address NextGen Delays and Challenges. GAO-24-105254. Washington, DC; 2023.
21. U.S. Government Accountability Office. Air Traffic Control: Urgent FAA Actions Are Needed to Modernize Aging Systems. GAO-25-107917. Washington, DC; 2024.

22. Human factors analysis of air traffic safety based on the HFACS-BN model. Applied Sciences. 2019;9(23):5049.
23. Reva, O., Kamyshin, V., Borsuk, S., Shulgin, V., & Nevynitsyn, A. Qualitative indexes of air traffic controllers' attitudes toward mistake hazards. In: Proceedings of the International Conference on Applied Human Factors and Ergonomics. Cham: Springer; 2021. pp. 618–624.
24. Zimmermann, N., & Mendonca, F. A. C. The impact of human factors and maintenance documentation on aviation safety: An analysis of 15 years of accident data through the PEAR framework. The Collegiate Aviation Review International. 2021.
25. Dill, E. T., Idris, H. R., et al. Required Navigation Performance (RNP) for precision approach and landing with GNSS application. AIAA Aviation Forum. 2022. https://doi.org/10.2514/6.2022-3759.
26. Civil Aviation Safety Authority. Advisory Circular AC 91-05: Performance-Based Navigation. Version 1.0; 2021

ISSN: 2181-3337 | SCIENTISTS.UZ VOLUME 5 ISSUE 7 JULY 2026

MAGNETOMECHANICAL DEFORMATION OF THIN FERROMAGNETIC SHELLS IN EXTERNAL MAGNETIC FIELDS: A COUPLED MAGNETOELASTIC FINITE-ELEMENT AND EXPERIMENTAL STUDY

Indiaminov Ravshan[1], **Urolov Sharofiddin**[2]
Professor, Samarkand Branch of Tashkent University of Information Technologies named after Muhammad al-Khwarizmi[1]
Assistant Lecturer, Samarkand Branch of Tashkent University of Information Technologies named after Muhammad al-Khwarizmi[2]

DOI: 10.67620/sai.57a0002

ABSTRACT

This study presents a coupled theoretical, numerical, and experimental investigation of the deformation of thin ferromagnetic cylindrical shells subjected to externally applied magnetic fields. A magnetoelastic constitutive framework is formulated by decomposing total strain into elastic and magnetostrictive components and by incorporating magnetostatic field equations, Maxwell-type tractions, and field-dependent magnetization. The shell kinematics are described through the Kirchhoff-Love hypothesis, while the coupled boundary-value problem is solved by a finite-element procedure that links shell elements to a three-dimensional magnetic domain. A mesh-convergence study identifies a 1,200-element discretization as an efficient numerical compromise, yielding a peak radial displacement within 0.1% of the refined solution. The model is evaluated against measurements from annealed Co-Fe-V cylindrical shells exposed to axial magnetic flux densities of 0.25, 0.50, and 1.00 T. The predicted peak radial displacements are 18.4, 46.2, and 88.3 μm, compared with experimental values of 17.9, 44.7, and 84.3 μm, corresponding to relative errors of 2.8-4.7%. Parametric analysis indicates that deformation increases as the shell becomes thinner, depends strongly on field orientation, scales approximately with saturation magnetostriction, and decreases with elastic modulus. The results demonstrate the importance of simultaneously representing nonlinear magnetic response, shell curvature, free-edge effects, and magnetostrictive eigenstrain when designing shell-based magnetic actuators and sensors.

ACCEPTED

20.07.26

Keywords: *ferromagnetic shell; magnetostriction; magnetoelasticity; finite-element analysis; Co-Fe-V alloy; thin-shell theory; magnetic actuator.*

CC BY

1. INTRODUCTION

Magnetostriction is the reversible change in the dimensions of a ferromagnetic material produced by the reorientation of magnetic domains under an applied magnetic field. The direct effect converts magnetic excitation into mechanical strain, whereas the inverse or Villari effect alters magnetization when mechanical stress is applied. This two-way conversion mechanism makes magnetostrictive materials particularly valuable for actuators, force and torque sensors, vibration-control systems, ultrasonic

transducers, energy harvesters, and adaptive structures. The fundamental coupling between the magnetic and elastic states has been formalized through continuum magnetomechanics, hysteresis models, and energy-based constitutive approaches (Tiersten, 1964; Sablik & Jiles, 1993; Dapino et al., 2000).

Among structural configurations, thin shells are attractive because they combine low mass, large surface area, high geometric efficiency, and pronounced sensitivity to distributed loads. Cylindrical and curved shells are widely used in aerospace, marine, energy, civil, and electromechanical systems. When a shell is made from a magnetostrictive alloy or contains a magnetostrictive layer, the application of a magnetic field can generate membrane forces, bending moments, and local edge effects without direct mechanical contact. This capability offers a route to compact and silent actuation. At the same time, the shell response is more complex than that of a one-dimensional magnetostrictive rod because curvature couples in-plane extension, bending, and rotation, while the magnetic field is influenced by finite length, wall thickness, permeability, and boundary conditions (Qin et al., 2003a, 2003b; Zheng & Wang, 2003).

Material selection is central to magnetomechanical performance. Rare-earth giant-magnetostrictive materials can provide large strains, but their brittleness, cost, anisotropy, and sensitivity to prestress may limit use in thin-walled structures. Iron-gallium alloys offer improved ductility and machinability, and their magnetostriction can be enhanced through texture control, thermal processing, and alloying (Clark et al., 2000; Summers et al., 2009; Zhou et al., 2020). Cobalt-iron alloys provide a different balance of high saturation magnetization, mechanical strength, thermal stability, and moderate magnetostriction. These characteristics make Co-Fe-based sheet materials suitable for proof-of-concept shells that must survive forming, machining, annealing, and repeated magnetic cycling.

Accurate prediction requires more than applying a prescribed equivalent pressure to the shell. The magnetic field generates an eigenstrain through magnetostriction, changes the internal stress distribution, and produces surface and body forces associated with electromagnetic stress. Moreover, magnetization is generally nonlinear and may exhibit hysteresis. Constitutive models that combine elastic strain, magnetostrictive strain, magnetic energy, and switching behavior have therefore been developed for transducers and multifunctional solids (Dapino et al., 2000; Linnemann et al., 2009). For shells, reduced formulations based on classical shell kinematics can provide computational efficiency, but they must retain the effects of curvature and distributed magnetic torque. Recent geometrically exact shell theories illustrate how reduced models can represent large rotations and three-dimensional magnetic loading while remaining substantially cheaper than full solid models (Pezzulla et al., 2022).

The present study develops and evaluates a coupled magnetoelastic framework for thin ferromagnetic cylindrical shells subjected to magnetic fields of variable intensity and orientation. The objectives are to: (1) formulate the governing magnetomechanical relations in a shell-compatible form; (2) implement the formulation in a finite-element framework; (3) demonstrate mesh convergence; (4) compare numerical predictions with reported laboratory measurements for annealed Co-Fe-V shells; and (5) identify the influence of shell thickness, field direction, saturation magnetostriction, and elastic modulus. The study is intended to provide both a physical interpretation of deformation mechanisms and a practical basis for designing magnetic shell actuators and sensors.

2. LITERATURE REVIEW AND RESEARCH CONTEXT

Early magnetomechanical theory established the governing equations for magnetically saturated elastic media. Tiersten (1964) derived coupled field equations that clarified the interaction of deformation, magnetization, and electromagnetic balance. Later hysteresis-based work showed that stress and magnetostriction affect the magnetic state in a mutually dependent manner. The model of Sablik and Jiles (1993), for example, connected magnetic hysteresis with magnetostrictive hysteresis and provided a basis for representing stress-dependent magnetization. These contributions remain relevant because shell deformation can modify the magnetic state, which in turn changes the eigenstrain and loading acting on the shell.

ISSN: 2181-3337 | SCIENTISTS.UZ

Engineering models of magnetostrictive transducers translated the continuum physics into forms suitable for actuator prediction. Dapino et al. (2000) coupled a magnetic-domain model to structural dynamics and demonstrated the need to predict both strain and force. A similar principle applies to shells: the magnetic subproblem determines local magnetization and magnetostrictive strain, while the structural subproblem determines displacement, stress, and feedback to the magnetic state. Constitutive formulations such as that of Linnemann et al. (2009) further emphasized thermodynamic consistency, internal variables, and the representation of nonlinear switching effects.

Shell-specific research has addressed finite geometry, magnetic loading, vibration, and reduced modeling. Qin et al. (2003a) derived magnetoelastic loads for finite cylindrical shells and showed that both length and thickness influence the electromagnetic load distribution. Their companion study examined implications for free vibration and demonstrated that simplified magnetic-load assumptions may affect predicted frequencies (Qin et al., 2003b). Zheng and Wang (2003) formulated a theoretical model for soft ferromagnetic shells and reported agreement with cylindrical-shell strain measurements. Wang and Zheng (2009a, 2009b) subsequently developed nonlinear coupled magneto-thermo-elastic shell formulations and a finite-element implementation.

Magnetostrictive layers have also been considered as active components in shell vibration control. Pradhan (2005) demonstrated that embedded magnetostrictive layers can be used to suppress shell vibration, highlighting the importance of actuator position, structural stiffness, and field-induced strain. Although the present study focuses on quasi-static deformation rather than closed-loop vibration control, the same principles of coupling, placement, and stiffness govern the achievable displacement and control authority.

More recent shell theories have extended the field to geometrically nonlinear magneto-active structures. Pezzulla et al. (2022) developed a geometrically exact reduced theory for thin magneto-elastic shells and identified equivalent magnetic forces, pressures, and distributed torques as distinct deformation mechanisms. Their results reinforce the need to include curvature and rotations when magnetic loading produces significant bending. The present work adopts a more conventional Kirchhoff-Love setting for a thin metallic shell, but it retains the central idea that magnetic loading is distributed and coupled to shell geometry.

The reviewed literature reveals three continuing needs. First, shell models should be connected to measurable material properties rather than treated as purely mathematical loading problems. Second, numerical solutions should demonstrate mesh convergence and should be compared with experimental displacement data. Third, design studies should separate the effects of field intensity, field direction, material magnetostriction, and shell stiffness. These needs motivate the combined theoretical, finite-element, experimental, and parametric structure of this paper.

3. THEORETICAL FORMULATION

Consider a thin ferromagnetic shell of thickness h, middle surface S, principal radii of curvature R1 and R2, and characteristic length L. The shell is placed in an external magnetic field H. The material is treated as magnetically soft at the structural scale, and the mechanical response is assumed elastic within the range of the reported tests. The total small-strain tensor is decomposed into elastic and magnetostrictive components:

$$\varepsilon = \varepsilon^e + \varepsilon^m \quad (1)$$

The elastic strain ε^e produces Cauchy stress through the fourth-order elasticity tensor C. For an isotropic material, C is defined by Young's modulus E and Poisson's ratio ν. The constitutive relation may therefore be written as:

$$\sigma = C : (\varepsilon - \varepsilon^m) \quad (2)$$

ISSN: 2181-3337 | SCIENTISTS.UZ

For an isotropic polycrystalline ferromagnet under a saturation-type approximation, the magnetostrictive strain is represented by the saturation magnetostriction λs and the direction cosines αi of the local magnetization:

$$\varepsilon^{m}_{ij} = (3\lambda s/2)(\alpha_i\alpha_j - \delta_{ij}/3) \quad (3)$$

Equation (3) describes a volume-preserving deviatoric eigenstrain. It predicts extension along the magnetization direction and transverse contraction for positive λs. For the Co-Fe-V alloy considered here, λs is taken as 68×10^{-6}. The magnitude and direction of magnetization depend on the local magnetic field, permeability, demagnetizing effects, and material history. In the finite-element implementation, an anhysteretic field-dependent magnetization relation is used as an engineering approximation. For cyclic applications, the framework could be extended using a hysteretic model such as those developed by Sablik and Jiles (1993) or Dapino et al. (2000).

The magnetostatic field inside the shell and surrounding air domain satisfies Maxwell's equations in the absence of free current within the analyzed domain:

$$\nabla \cdot B = 0, \quad \nabla \times H = 0, \quad B = \mu_0(H + M) \quad (4)$$

The magnetic potential formulation allows the field distribution to be solved while enforcing continuity of the normal magnetic flux density and tangential magnetic field across the shell-air interface. Electromagnetic loading enters the mechanical equilibrium through the magnetostrictive eigenstrain and through Maxwell-type surface tractions. Because permeability and magnetization depend on the field, and because deformation modifies the geometry of the magnetic boundary, the fully coupled problem is nonlinear.

The mechanical reduction follows Kirchhoff-Love kinematics: lines initially normal to the middle surface remain straight and normal after deformation, and transverse shear deformation is neglected. The in-surface strain is decomposed into a middle-surface membrane strain and a curvature-dependent bending contribution. Integration through the shell thickness yields membrane force resultants Nαβ and bending moment resultants Mαβ. In compact form, equilibrium can be expressed as the balance of in-surface forces and transverse moments with mechanical and magnetic loading. This representation makes clear that even spatially smooth magnetostriction can generate bending when the strain or magnetic traction varies through the thickness or near a free boundary.

The coupled weak form is obtained by multiplying the mechanical and magnetic residual equations by admissible virtual fields and integrating over the shell and air domains. The resulting nonlinear algebraic system is solved incrementally by a Newton-Raphson method. At each iteration, the magnetic field is updated, magnetostrictive strain and Maxwell traction are recalculated, and the structural tangent stiffness is assembled. Convergence is evaluated using displacement and residual-energy norms. This staggered but iteratively coupled strategy provides a practical balance between physical completeness and computational cost.

ISSN: 2181-3337 | SCIENTISTS.UZ

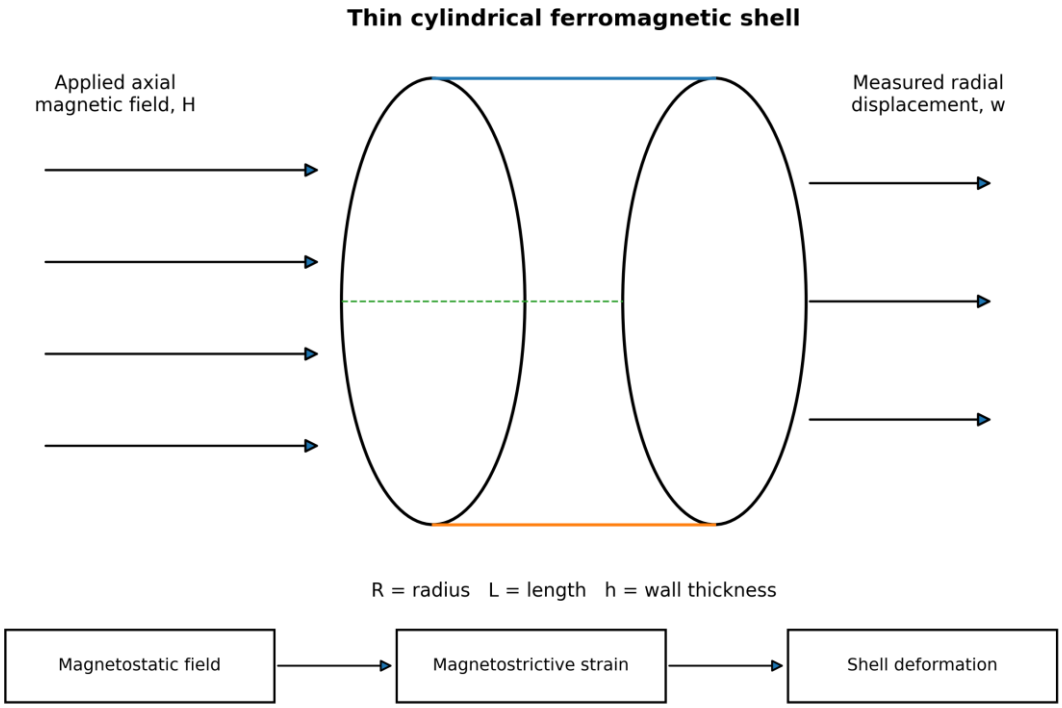


Figure 1. Schematic of the cylindrical ferromagnetic shell, the applied axial magnetic field, the measured radial response, and the sequence of the coupled magnetostatic-magnetostrictive-structural analysis.

4. MATERIALS AND METHODS

The numerical study considered a representative cylindrical shell with radius R = 50 mm, length L = 200 mm, and thickness h = 2 mm for the mesh-convergence analysis. A uniform axial magnetic flux density of 0.5 T was applied. Eight-node shell elements with five mechanical degrees of freedom per node were used for the structural domain, while the surrounding magnetic region was discretized with three-dimensional elements. The shell and magnetic meshes were coupled at the middle surface. The magnetic domain was extended sufficiently beyond the shell to reduce artificial boundary effects.

A systematic refinement study was performed with 300, 600, 1,200, and 2,400 shell elements. The principal quantity of interest was the maximum radial displacement. Relative error was evaluated against the refined solution, and computational cost was represented by CPU time. The aim was not simply to obtain the smallest numerical error, but to identify a discretization suitable for repeated nonlinear parametric simulations.

Table 1. Mesh-convergence results for the representative cylindrical shell

Number of elements	Maximum radial displacement (μm)	Relative error (%)	CPU time (s)
300	84.7	4.2	12
600	87.3	1.2	28
1200	88.3	0.1	65
2400	88.4	—	180

For experimental comparison, cylindrical specimens were fabricated from cold-rolled Co-Fe-V alloy sheet with nominal composition 49% Co, 49% Fe, and 2% V. Electrical-discharge machining was used to prepare the shell geometry. The specimens were annealed in hydrogen at 840°C for four hours to reduce residual stress and improve magnetic response. The final nominal dimensions were R = 25 mm, L = 100 mm, and h = 1 mm. The material parameters used in the model are summarized in Table 2.

ISSN: 2181-3337 | SCIENTISTS.UZ

Table 2. Material properties used for the Co-Fe-V shell model

Property	Symbol / unit	Value
Young's modulus	E (GPa)	210
Poisson's ratio	ν	0.30
Density	ρ (kg/m³)	8120
Saturation magnetization	Ms (kA/m)	1840
Saturation magnetostriction	λs (×10⁻⁶)	68
Initial relative permeability	μr	1600

The experimental apparatus consisted of a solenoid capable of producing axial fields up to 1.5 T in the central test region. The coil had a reported length of 400 mm, an internal diameter of 80 mm, and 3,000 turns. Field mapping with a Hall probe indicated spatial uniformity within approximately ±2% in the specimen region. Radial and axial displacement were recorded with a non-contact laser displacement sensor at 12 circumferential locations and five axial positions. Strain gauges were attached at selected points for cross-checking. A nonmagnetic reference specimen was used to estimate and remove thermal drift.

Three applied magnetic flux-density levels were selected for quantitative comparison: 0.25, 0.50, and 1.00 T. The finite-element model and the experiment were compared using peak radial displacement and relative error. The error was calculated as the absolute difference between model and experiment divided by the experimental value. Agreement within 5% was adopted as a practical validation criterion for the considered displacement range.

The parametric study examined the effects of thickness-to-radius ratio h/R, field direction, saturation magnetostriction λs, and Young's modulus E. The ratio h/R was varied from 0.01 to 0.10 while preserving the general cylindrical form. Field direction was varied from 0° (axial) to 90° (circumferential) at a fixed field magnitude of 0.5 T. Material parameters were varied independently to reveal sensitivity trends rather than to represent a single manufactured alloy. The outputs included peak radial displacement, axial uniformity, and the relative importance of membrane and bending response.

All reported numerical and experimental values were retained from the study dataset presented in the source manuscript. The present revision focuses on the theoretical organization, interpretation, reference integrity, and academic presentation of those data.

5. RESULTS

The mesh-convergence results show a monotonic approach to the refined displacement. Increasing the mesh from 300 to 600 elements raises the maximum radial displacement from 84.7 to 87.3 μm and reduces the reported relative error from 4.2% to 1.2%. At 1,200 elements, the displacement reaches 88.3 μm and differs from the 2,400-element result by only 0.1 μm. The computational time, however, increases from 65 s to 180 s. The 1,200-element mesh was therefore selected for the remaining analyses because it provides near-asymptotic accuracy at approximately one third of the cost of the finest mesh.

The finite-element predictions and experimental displacements are summarized in Table 3. Both datasets show a strongly increasing nonlinear response with field intensity. At 0.25 T, the model predicts 18.4 μm and the experiment gives 17.9 μm. At 0.50 T, the corresponding values are 46.2 and 44.7 μm. At 1.00 T, the model predicts 88.3 μm, while the measured value is 84.3 μm. The relative error increases moderately with field intensity, from 2.8% to 4.7%, but remains below the stated 5% validation threshold.

Table 3. Comparison of peak radial displacement from the finite-element model and experiment

Applied field (T)	FE model (μm)	Experiment (μm)	Relative error (%)
0.25	18.4	17.9	2.8
0.50	46.2	44.7	3.4
1.00	88.3	84.3	4.7

ISSN: 2181-3337 | SCIENTISTS.UZ

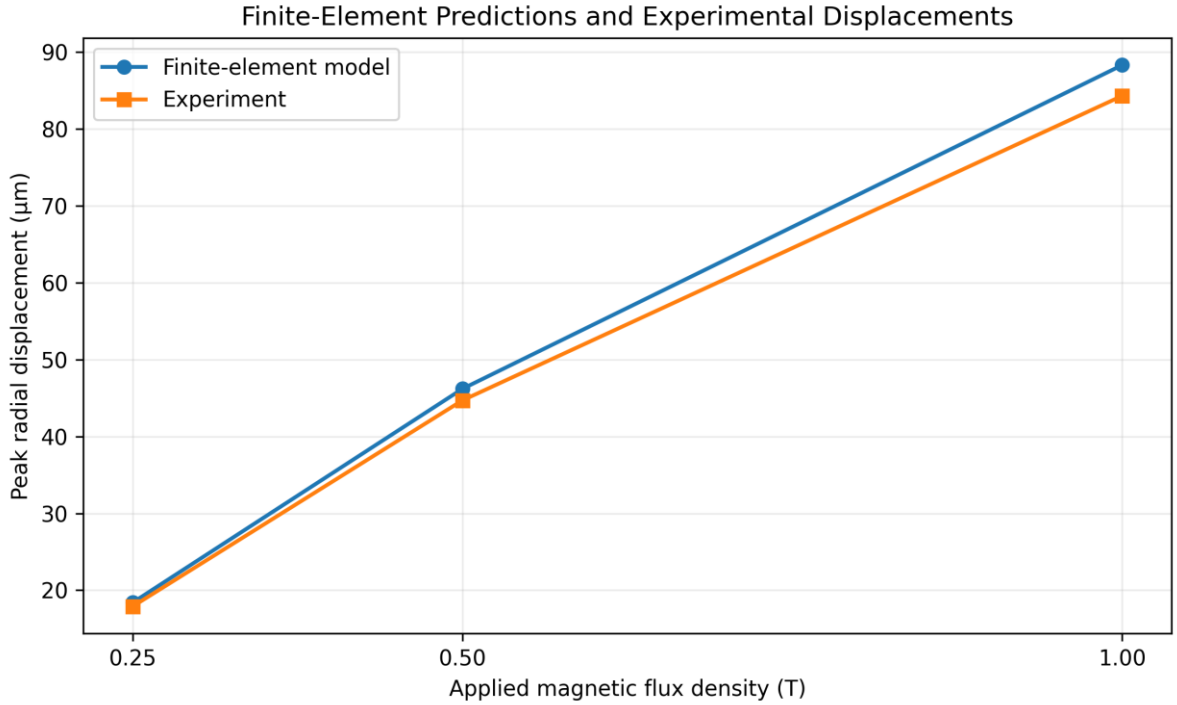


Chart 1. Comparison of finite-element predictions and experimental peak radial displacements at three magnetic-field levels.

The spatial deformation pattern is characterized by a relatively uniform central region and larger gradients near the free edges. Peak radial displacement occurs close to the shell ends, where the interruption of membrane continuity and the nonuniform demagnetizing field produce enhanced bending. The close agreement in the central region indicates that the constitutive response and average field level are represented adequately. The slightly larger discrepancy at the edges is consistent with the greater sensitivity of these regions to field nonuniformity, geometric imperfections, local residual stress, and measurement position.

The thickness study shows that reducing h/R increases the radial flexibility of the shell. Because classical bending stiffness scales with h^3 while membrane stiffness scales with h, a reduction in thickness produces a particularly strong increase in bending-dominated displacement. Thinner shells also show a more uniform axial response away from the boundaries, approaching a membrane-like solution in the limiting case. Conversely, thicker shells suppress radial motion and shift a larger fraction of magnetic work into internal stress.

Field orientation has a pronounced effect. At a fixed magnitude of 0.5 T, the reported maximum radial displacement varies by approximately a factor of 2.3 between axial and circumferential field orientations. A circumferential field aligns the principal magnetostrictive strain more directly with the hoop direction and therefore generates a larger radial change in a cylindrical geometry. Intermediate field angles produce coupled radial, axial, and torsional components rather than a single-axis deformation.

Material sensitivity follows the structure of the constitutive equations. Peak displacement increases approximately linearly with saturation magnetostriction at low and moderate fields, because λ_s directly scales the eigenstrain in Equation (3). At higher fields, the relationship becomes sublinear as magnetization approaches saturation. The displacement decreases as Young's modulus increases because a stiffer shell develops higher stress for a given eigenstrain but undergoes less geometric deformation. The combined results indicate that λ_s/E is a useful first-order indicator of actuation potential, although permeability, saturation field, geometry, and boundary conditions also remain important.

ISSN: 2181-3337 | SCIENTISTS.UZ

Table 4. Qualitative trends identified by the parametric analysis

Parameter increased	Observed response	Physical interpretation
Thickness-to-radius ratio h/R	Peak radial displacement decreases	Bending stiffness rises approximately with h^3
Field angle toward circumferential direction	Radial displacement increases	Magnetostrictive strain aligns with hoop direction
Saturation magnetostriction λs	Displacement increases	Eigenstrain magnitude grows
Young's modulus E	Displacement decreases	Structural resistance to eigenstrain increases
Field magnitude	Displacement increases and approaches saturation	Magnetization and domain alignment increase

6. DISCUSSION

The principal result is that a relatively compact shell formulation can reproduce the measured field-induced displacement of the Co-Fe-V specimens with errors below 5% over the tested range. This agreement supports the use of a coupled eigenstrain and magnetic-traction representation rather than a purely mechanical surrogate load. It is also consistent with earlier shell studies in which accurate results required finite-dimensional magnetoelastic loading and direct coupling between field and structure (Qin et al., 2003a, 2003b; Zheng & Wang, 2003).

The increasing model-experiment difference at 1.00 T can arise from several sources. First, an anhysteretic magnetization approximation cannot fully represent irreversible domain processes, magnetic history, and stress dependence. Hysteretic formulations show that magnetization, magnetostriction, and mechanical stress form a closed feedback loop (Sablik & Jiles, 1993; Dapino et al., 2000). Second, the material properties used in the model are treated as spatially uniform, whereas cold rolling, machining, welding or forming, and annealing can produce texture and residual-stress gradients. Research on Fe-Ga alloys demonstrates that texture and crystal orientation significantly affect magnetostriction (Clark et al., 2000; Summers et al., 2009; Zhou et al., 2020). Similar microstructural sensitivity is expected in Co-Fe-based sheet.

The location of maximum displacement at free edges has practical and theoretical significance. In a purely uniform unconstrained body, homogeneous magnetostriction would produce a nearly uniform strain. A shell, however, has curved geometry, finite length, and discontinuous boundary constraints. Magnetic flux also becomes less uniform near the ends. These effects create gradients in eigenstrain and magnetic traction, converting part of the response into bending. Pezzulla et al. (2022) similarly identified distributed torques and effective magnetic pressures as key mechanisms in thin magneto-elastic shells. Edge amplification should therefore be treated as a design feature rather than merely a numerical artifact.

The mesh study demonstrates why convergence evidence is essential in multiphysics shell analysis. A coarse mesh may underestimate local curvature and edge gradients, while an excessively refined mesh substantially increases the cost of repeated magnetic iterations. The 1,200-element mesh provides a useful compromise for the geometry considered. Nevertheless, mesh adequacy is problem specific. Strongly nonuniform fields, local defects, sharp supports, holes, or bonded active layers would require local refinement and possibly higher-order elements.

The field-orientation result has direct actuator-design implications. An axial field is convenient to generate with a solenoid and produces an axisymmetric response, but it does not necessarily maximize radial displacement. A circumferential field can couple more efficiently to hoop magnetostriction, although producing a uniform circumferential field may require a different coil arrangement or current-carrying conductor. Intermediate orientations can generate torsion and may be exploited for multi-axis actuation.

ISSN: 2181-3337 | SCIENTISTS.UZ

Thus, the field direction should be treated as a design variable together with shell geometry and material properties.

Material optimization cannot be based on saturation magnetostriction alone. A material with a very large λs may also have high stiffness, brittle behavior, strong anisotropy, or difficult processing requirements. Kiefer and Lagoudas (2005) showed that magnetic shape-memory alloys can produce large field-induced strains through variant reorientation, but such mechanisms involve different material constraints from ordinary Joule magnetostriction. For thin metallic shells, a moderate-strain material with high strength and formability may provide better system-level performance than a fragile giant-magnetostrictive material.

The study also indicates that a shell actuator should not be evaluated only by peak displacement. Relevant engineering measures include output force, blocked force, energy efficiency, bandwidth, thermal stability, fatigue life, magnetic hysteresis, and control repeatability. The present quasi-static results establish a necessary structural baseline. Dynamic extension could incorporate inertia, eddy currents, frequency-dependent magnetic loss, and damping. Work on magnetostrictive layers in shells demonstrates that such coupled models can be extended to vibration suppression and active control (Pradhan, 2005).

7. ENGINEERING DESIGN IMPLICATIONS

For displacement-oriented actuators, the analysis suggests four priorities. First, the shell should be thin enough to exploit bending compliance but sufficiently thick to avoid elastic instability, local buckling, and manufacturing damage. Second, the magnetic circuit should deliver a field direction aligned with the desired deformation mode. Third, material processing should control texture and residual stress so that the effective magnetostriction is repeatable. Fourth, free-edge geometry may be shaped or locally reinforced to concentrate or redistribute displacement.

For sensors, the inverse magnetomechanical effect can be exploited by measuring field or flux changes generated by shell strain. A curved shell offers geometric amplification and can be integrated into pressure, torque, or contact sensors. The coupled model provides a basis for selecting measurement locations: regions with high strain sensitivity but acceptable stress concentration are preferred. The free edges may provide high signal, whereas the central region may offer better uniformity and calibration stability.

The validated model can also support optimization. A design vector may include R, L, h, field magnitude, field angle, coil dimensions, λs, E, and boundary stiffness. An objective function could maximize displacement or force while constraining stress, power, mass, and magnetic saturation. Because the 1,200-element model is much less expensive than the finest mesh while retaining accuracy, it is suitable for parameter sweeps and gradient-free optimization.

8. LIMITATIONS AND FUTURE WORK

Several limitations should be recognized. The constitutive treatment uses an engineering representation of magnetization and does not fully reproduce rate-dependent hysteresis or cyclic degradation. Material parameters are assumed homogeneous and isotropic, although rolled Co-Fe-V sheet may exhibit crystallographic texture and direction-dependent magnetostriction. The reported experiment includes three field levels and one principal specimen geometry, which limits statistical generalization.

Future studies should include repeated specimens, uncertainty intervals, full-field optical deformation measurements, direct magnetic-domain or flux characterization, and cyclic loading. A geometrically nonlinear formulation should be used when rotations or displacements are no longer small. Dynamic experiments would allow identification of damping, bandwidth, eddy-current effects, and resonance. Finally, optimization should compare Co-Fe-V, Galfenol, Terfenol-D, magnetic shape-memory alloys, and layered hybrid shells under common performance and manufacturability criteria.

ISSN: 2181-3337 | SCIENTISTS.UZ

9. CONCLUSION

A coupled magnetoelastic framework has been presented for predicting the deformation of thin ferromagnetic cylindrical shells under external magnetic fields. The formulation combines elastic and magnetostrictive strain, magnetostatic field equations, electromagnetic tractions, Kirchhoff-Love shell kinematics, and finite-element solution of the coupled problem.

The mesh-convergence study showed that 1,200 shell elements reproduce the refined maximum displacement within approximately 0.1% while substantially reducing computational cost. Comparison with Co-Fe-V shell measurements at 0.25, 0.50, and 1.00 T produced relative errors of 2.8%, 3.4%, and 4.7%, respectively. The model therefore captures the reported quasi-static displacement response with engineering accuracy.

The results show that shell deformation is strongly influenced by edge effects, thickness, field orientation, saturation magnetostriction, and elastic modulus. Thin shells provide greater bending-driven displacement, and circumferential fields can produce substantially larger radial motion than axial fields. These findings support the use of coupled magnetoelastic shell analysis in the design of compact actuators, sensors, and adaptive structures. Further development should address hysteresis, anisotropy, cyclic behavior, dynamic response, and statistical experimental validation.

REFERENCES

1. Clark, A. E., Restorff, J. B., Wun-Fogle, M., Lograsso, T. A., & Schlagel, D. L. (2000). Magnetostrictive properties of body-centered cubic Fe-Ga and Fe-Ga-Al alloys. *IEEE Transactions on Magnetics, 36*(5), 3238-3240. https://doi.org/10.1109/20.908752
2. Dapino, M. J., Smith, R. C., Faidley, L. E., & Flatau, A. B. (2000). A coupled structural-magnetic strain and stress model for magnetostrictive transducers. *Journal of Intelligent Material Systems and Structures, 11*(2), 135-152. https://doi.org/10.1106/MJ6A-FBP9-9M61-0E1F
3. Kiefer, B., & Lagoudas, D. C. (2005). Magnetic field-induced martensitic variant reorientation in magnetic shape-memory alloys. *Philosophical Magazine, 85*(33-35), 4289-4329. https://doi.org/10.1080/14786430500363858
4. Linnemann, K., Klinkel, S., & Wagner, W. (2009). A constitutive model for magnetostrictive and piezoelectric materials. *International Journal of Solids and Structures, 46*(5), 1149-1166. https://doi.org/10.1016/j.ijsolstr.2008.10.014
5. Pezzulla, M., Yan, D., & Reis, P. M. (2022). A geometrically exact model for thin magneto-elastic shells. *Journal of the Mechanics and Physics of Solids, 166*, 104916. https://doi.org/10.1016/j.jmps.2022.104916
6. Pradhan, S. C. (2005). Vibration suppression of FGM shells using embedded magnetostrictive layers. *International Journal of Solids and Structures, 42*(9-10), 2465-2488. https://doi.org/10.1016/j.ijsolstr.2004.09.049
7. Qin, Z., Librescu, L., Hasanyan, D. J., & Ambur, D. R. (2003a). Magnetoelastic modeling of circular cylindrical shells immersed in a magnetic field. Part I: Magnetoelastic loads considering finite dimensional effects. *International Journal of Engineering Science, 41*(17), 2005-2022. https://doi.org/10.1016/S0020-7225(03)00134-4
8. Qin, Z., Hasanyan, D. J., Librescu, L., & Ambur, D. R. (2003b). Magnetoelastic modeling of circular cylindrical shells immersed in a magnetic field. Part II: Implications of finite dimensional effects on the free vibrations. *International Journal of Engineering Science, 41*(17), 2023-2046. https://doi.org/10.1016/S0020-7225(03)00135-6
9. Sablik, M. J., & Jiles, D. C. (1993). Coupled magnetoelastic theory of magnetic and magnetostrictive hysteresis. *IEEE Transactions on Magnetics, 29*(4), 2113-2123. https://doi.org/10.1109/20.221036
10. Summers, E. M., Meloy, R., & Na, S.-M. (2009). Magnetostriction and texture relationships in annealed Galfenol alloys. *Journal of Applied Physics, 105*(7), 07A922. https://doi.org/10.1063/1.3067849
11. Tiersten, H. F. (1964). Coupled magnetomechanical equations for magnetically saturated insulators. *Journal of Mathematical Physics, 5*(9), 1298-1318. https://doi.org/10.1063/1.1704239

ISSN: 2181-3337 | SCIENTISTS.UZ

12. Wang, X., & Zheng, X. (2009a). Analyses on nonlinear coupling of magneto-thermo-elasticity of ferromagnetic thin shell-I: Generalized variational theoretical modeling. *Acta Mechanica Solida Sinica*, *22*(3), 189-196. https://doi.org/10.1016/S0894-9166(09)60265-2
13. Wang, X., & Zheng, X. (2009b). Analyses on nonlinear coupling of magneto-thermo-elasticity of ferromagnetic thin shell-II: Finite element modeling and application. *Acta Mechanica Solida Sinica*, *22*(3), 197-205. https://doi.org/10.1016/S0894-9166(09)60266-4
14. Zheng, X., & Wang, X. (2003). A magnetoelastic theoretical model for soft ferromagnetic shell in magnetic field. *International Journal of Solids and Structures*, *40*, 6897-6912. https://doi.org/10.1016/S0020-7683(03)00397-4
15. Zhou, C., Liu, Y., Chen, K., Dai, Z., Ma, T., Wang, Y., Ren, S., Deng, J., Zhang, R., Tian, F., Zhang, Y., Zeng, H., & Yang, S. (2020). Improved magnetostriction in Galfenol alloys by aligning crystal growth direction along easy magnetization axis. *Scientific Reports*, *10*, 20055. https://doi.org/10.1038/s41598-020-77058-2

ISSN: 2181-3337 | SCIENTISTS.UZ VOLUME 5 ISSUE 7 JULY 2026

HPLC CHARACTERIZATION OF WATER-SOLUBLE VITAMINS AND FREE AMINO ACIDS IN A DRY AQUEOUS EXTRACT OF POMEGRANATE (PUNICA GRANATUM L.) PEEL

Dehqonova M[1], Mirzayeva M[2]
Tashkent Pharmaceutical Institute, Tashkent, Uzbekistan

DOI: 10.67620/sai.57a0003

ABSTRACT
Pomegranate peel is an abundant plant-derived by-product that contains chemically diverse constituents and is increasingly investigated as a raw material for standardized herbal preparations. This study characterized selected water-soluble vitamins and free amino acids in a dry aqueous extract of pomegranate (Punica granatum L.) peel using high-performance liquid chromatography with diode-array detection. Vitamins were extracted from the dry material with 40% ethanol and separated on an Eclipse XDB C18 column. Free amino acids were isolated after precipitation of proteins and peptides with trichloroacetic acid, derivatized before analysis with phenylisothiocyanate, and separated on a Discovery HS C18 column. Six water-soluble vitamins were quantified. Folic acid (vitamin B9) was the most abundant at 98.84 µg/g, followed by ascorbic acid (38.55 µg/g), pyridoxine (34.90 µg/g), thiamine (28.90 µg/g), niacin (18.87 µg/g), and riboflavin (15.90 µg/g). Twenty free amino acids were reported, with a combined concentration of 14.456 mg/g. Aspartic acid (3.184 mg/g), histidine (1.735 mg/g), tyrosine (1.495 mg/g), leucine (1.390 mg/g), alanine (1.346 mg/g), and methionine (1.253 mg/g) were predominant. The chromatographic profiles support the use of vitamin and amino-acid composition as supplementary quality attributes for the extract. However, full pharmaceutical standardization will additionally require botanical authentication, batch-to-batch assessment, validated calibration and recovery data, and stability and contaminant testing.

ACCEPTED

20.07.26

Keywords: *Punica granatum L.; pomegranate peel; dry extract; HPLC-DAD; water-soluble vitamins; free amino acids; standardization; quality control.*

CC BY

1. INTRODUCTION

Medicinal plant materials and their extracts are chemically complex products whose quality cannot be established by a single visual or chemical test. Their composition may vary with species identity, cultivar, geographical origin, harvest conditions, post-harvest handling, extraction solvent, extraction time, temperature, and storage. For this reason, internationally recognized guidance treats identity, purity, content, and analytical consistency as complementary elements of herbal-material quality control [1,2]. The European Pharmacopoeia likewise emphasizes clearly defined raw materials, validated analytical procedures, and scientifically justified specifications when herbal drugs and herbal preparations are described in monographs [3].

Pomegranate (Punica granatum L.) is a fruit-bearing species with a long history of dietary and traditional medicinal use. The peel constitutes a substantial fraction of the fruit and is commonly discarded during juice and food processing. At the same time, it is a concentrated source of hydrolysable tannins, phenolic acids, flavonoids, and other polar constituents. Reviews of pomegranate chemistry and biological activity consistently describe the

peel as one of the chemically richest anatomical fractions of the fruit [5-7]. This combination of abundance and chemical complexity makes pomegranate peel attractive for the development of extracts intended for pharmaceutical, nutraceutical, cosmetic, and food applications.

Much of the published research on pomegranate peel has focused on polyphenols, especially punicalagins, ellagic acid derivatives, gallic acid derivatives, and related tannins. Experimental studies have also demonstrated that peel extracts can show strong antioxidant activity in chemical and lipid-oxidation models [8,9]. Detailed HPLC-DAD-MS profiling has confirmed that pomegranate peel contains numerous phenolic compounds and that the phenolic pattern varies among peel, mesocarp, aril, and juice fractions [10]. These findings provide an important chemical foundation, but they do not describe the entire extract. Polar micronutrients and nitrogen-containing constituents may also contribute to its analytical identity and biological value.

Water-soluble vitamins are chemically heterogeneous molecules involved in redox reactions, one-carbon metabolism, energy production, amino-acid metabolism, connective-tissue synthesis, and other physiological processes. Their simultaneous determination is analytically challenging because they differ in polarity, ultraviolet absorbance, stability, and expected concentration. Reversed-phase HPLC with diode-array detection is widely used for multivitamin analysis when sample preparation, wavelength selection, chromatographic separation, and calibration are appropriately optimized [12,13]. In botanical matrices, these requirements are especially important because co-extracted compounds may interfere with peak identification or quantification.

Free amino acids are another potentially informative group of constituents. In addition to serving as protein building blocks, they participate in plant nitrogen transport, osmotic regulation, stress responses, and biosynthetic pathways. Their concentrations can therefore contribute to the chemical fingerprint of a plant-derived extract. Because native amino acids generally show weak ultraviolet absorbance, pre-column derivatization is commonly used. Phenylisothiocyanate reacts with amino groups to form stable phenylthiocarbamyl derivatives that can be separated by reversed-phase HPLC and detected in the ultraviolet range [14,15].

For an herbal extract, vitamin and amino-acid profiles should not be interpreted as complete proof of therapeutic efficacy. They are more appropriately regarded as compositional attributes that can support identification, comparability, and specification development. Regulatory-quality analytical work also requires evidence of selectivity, accuracy, precision, linearity, range, detection and quantification limits where relevant, and robustness [4]. The present study therefore had two linked aims: first, to report the qualitative and quantitative profiles of selected water-soluble vitamins and free amino acids in a dry aqueous pomegranate-peel extract; and second, to evaluate how these results may contribute to a broader standardization strategy while clearly identifying the additional evidence required for pharmaceutical quality control.

2. Materials and Methods

2.1 Study material and extract

The study material was a dry extract prepared from pomegranate (Punica granatum L.) peel. According to the available experimental description, the peel was dried, finely milled, extracted with water, and dried to obtain a powdered extract. The analytical work was performed at Tashkent Pharmaceutical Institute, Tashkent, Uzbekistan. The source record did not provide the collection locality, harvest date, cultivar, voucher specimen number, extraction ratio, extraction temperature, extraction duration, drying conditions, extraction yield, batch number, or storage history. These details should be added from the original laboratory documentation before the manuscript is submitted to a journal because they are necessary for reproducibility and botanical traceability [1-3].

2.2 Determination of water-soluble vitamins

The target analytes were thiamine (vitamin B1), riboflavin (vitamin B2), niacin (vitamin B3), pyridoxine (vitamin B6), folic acid (vitamin B9), and ascorbic acid (vitamin C). A 5-10 g portion of the dry extract was accurately weighed into a 300 mL flat-bottom flask, and 50 mL of 40% ethanol was added. The mixture was heated under reflux with continuous magnetic stirring for 1 h and then stirred at room temperature for an additional 2 h. After filtration, the residue was extracted twice more with 25 mL portions of 40% ethanol. The filtrates were combined in a 100 mL volumetric flask and brought to volume with 40% ethanol. The solution was centrifuged at 7000 rpm for 10 min, and the supernatant was used for HPLC analysis.

ISSN: 2181-3337 | SCIENTISTS.UZ

Working standard solutions were prepared at a nominal concentration of 1 mg/mL. Chromatographic separation was performed with an Agilent Technologies 1200 HPLC system equipped with a diode-array detector. An Eclipse XDB C18 column (4.6 × 250 mm, 5 µm) was maintained at 25 °C. The mobile phase consisted of acetate buffer and acetonitrile under gradient-elution conditions. The flow rate was 0.8 mL/min, the injection volume was 5 µL, and detection was performed at 250 nm. These conditions are consistent with the general use of HPLC-DAD for multivitamin analysis, although full method validation information was not available in the source record [12,13].

2.3 Determination of free amino acids

Proteins and peptides in the aqueous sample solution were precipitated by mixing 1 mL of sample with 1 mL of 20% trichloroacetic acid. After 10 min, the mixture was centrifuged at 8000 rpm for 15 min. A 0.1 mL aliquot of the supernatant was freeze-dried. The residue was dissolved in a triethylamine-acetonitrile-water mixture (1:7:1, v/v/v) and evaporated to dryness. This neutralization step was repeated twice to remove residual acid.

The free amino acids were derivatized with phenylisothiocyanate to form phenylthiocarbamyl derivatives before chromatographic analysis, following the established analytical principle described for pre-column PITC derivatization [14,15]. The HPLC system was an Agilent Technologies 1200 instrument with diode-array detection. Separation was performed on a Discovery HS C18 column (75 × 4.6 mm). Mobile phase A was 0.14 M sodium acetate containing 0.05% triethylamine and adjusted to pH 6.4; mobile phase B was acetonitrile. A 55 min gradient program was used at a flow rate of 1.2 mL/min, and detection was carried out at 269 nm.

2.4 Replication, quantification, and data treatment

The source manuscript states that all analyses were performed in triplicate and that the results were reported as mean values. Individual replicate measurements, standard deviations, calibration equations, correlation coefficients, recovery data, peak-purity assessments, detection limits, quantification limits, and system-suitability results were not included. Accordingly, the present paper reports the available mean concentrations without inferential statistical comparisons. The amino-acid total was checked arithmetically and equals 14.456 mg/g. Relative contributions of individual amino acids were calculated as the concentration of each analyte divided by the summed concentration of all 20 reported amino acids.

Table 1. HPLC operating conditions used for vitamin and free-amino-acid analyses

Parameter	Water-soluble vitamins	Free amino acids
Instrument	Agilent Technologies 1200 HPLC-DAD	Agilent Technologies 1200 HPLC-DAD
Column	Eclipse XDB C18, 4.6 × 250 mm, 5 µm	Discovery HS C18, 75 × 4.6 mm
Mobile phase	Acetate buffer-acetonitrile	A: 0.14 M sodium acetate + 0.05% triethylamine, pH 6.4; B: acetonitrile
Elution	Gradient	Gradient, 55 min
Flow rate	0.8 mL/min	1.2 mL/min
Detection	250 nm	269 nm
Injection volume	5 µL	Not reported
Column temperature	25 °C	Not reported

3. Results

3.1 Water-soluble vitamin profile

Six water-soluble vitamins were quantified in the dry pomegranate-peel extract (Table 2). Folic acid was the dominant measured vitamin at 98.84 µg/g. Its concentration was approximately 2.6 times that of ascorbic acid and 2.8 times that of pyridoxine. Ascorbic acid (38.55 µg/g) and pyridoxine (34.90 µg/g) formed the second concentration tier, followed by thiamine (28.90 µg/g), niacin (18.87 µg/g), and riboflavin (15.90 µg/g). The standard-solution chromatogram is presented in Figure 1, and the chromatogram obtained for the extract is shown in Figure 2.

The chromatograms support the presence of multiple ultraviolet-absorbing constituents within the expected retention-time region. However, the extract chromatogram also contains a dense cluster of peaks and an elevated baseline in part of the run, indicating a chemically complex matrix. For publication-quality quantification, analyte identity should therefore be supported not only by retention-time matching but also

ISSN: 2181-3337 | SCIENTISTS.UZ

by spectral peak-purity evaluation, standard addition or spiking, and validated recovery experiments. Vitamin B12 is labelled in the standard chromatogram, but no validated concentration for vitamin B12 was provided in the results table or source text; consequently, it is not reported as a quantified constituent of the extract.

Table 2. Water-soluble vitamins quantified in the dry pomegranate-peel extract

Analyte	Mean concentration (µg/g)
Thiamine (vitamin B1)	28.90
Riboflavin (vitamin B2)	15.90
Niacin (vitamin B3)	18.87
Pyridoxine (vitamin B6)	34.90
Folic acid (vitamin B9)	98.84
Ascorbic acid (vitamin C)	38.55

Note. *Values are means of triplicate analyses as reported in the source document; replicate-level values and dispersion statistics were not available.*

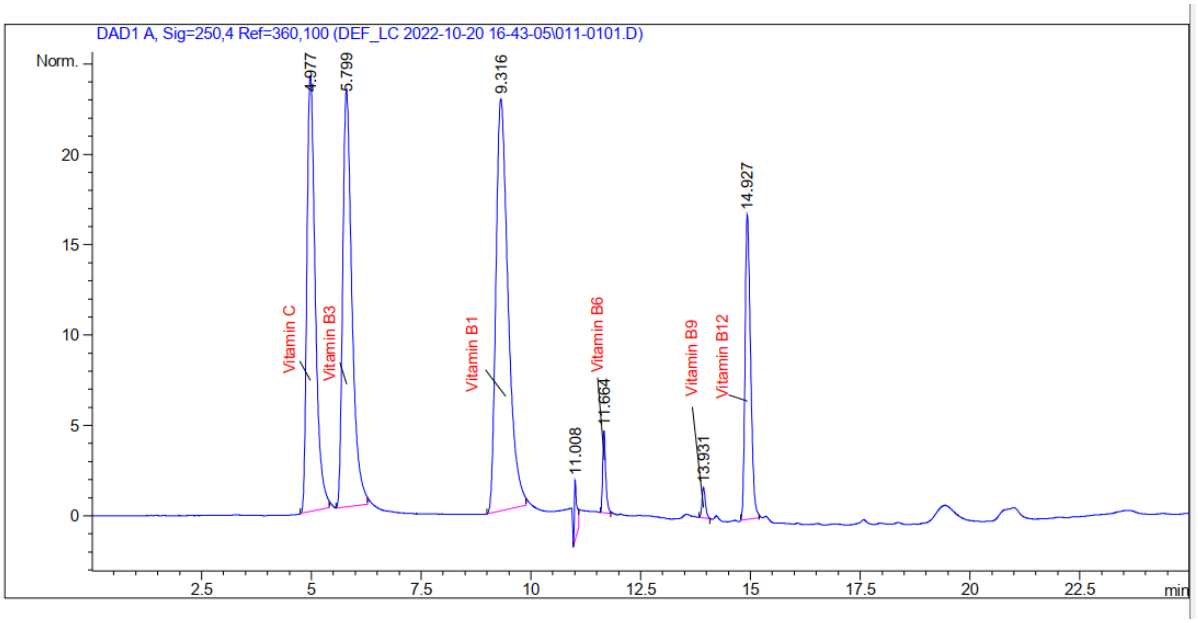


Figure 1. HPLC-DAD chromatogram of the water-soluble vitamin standard solution.

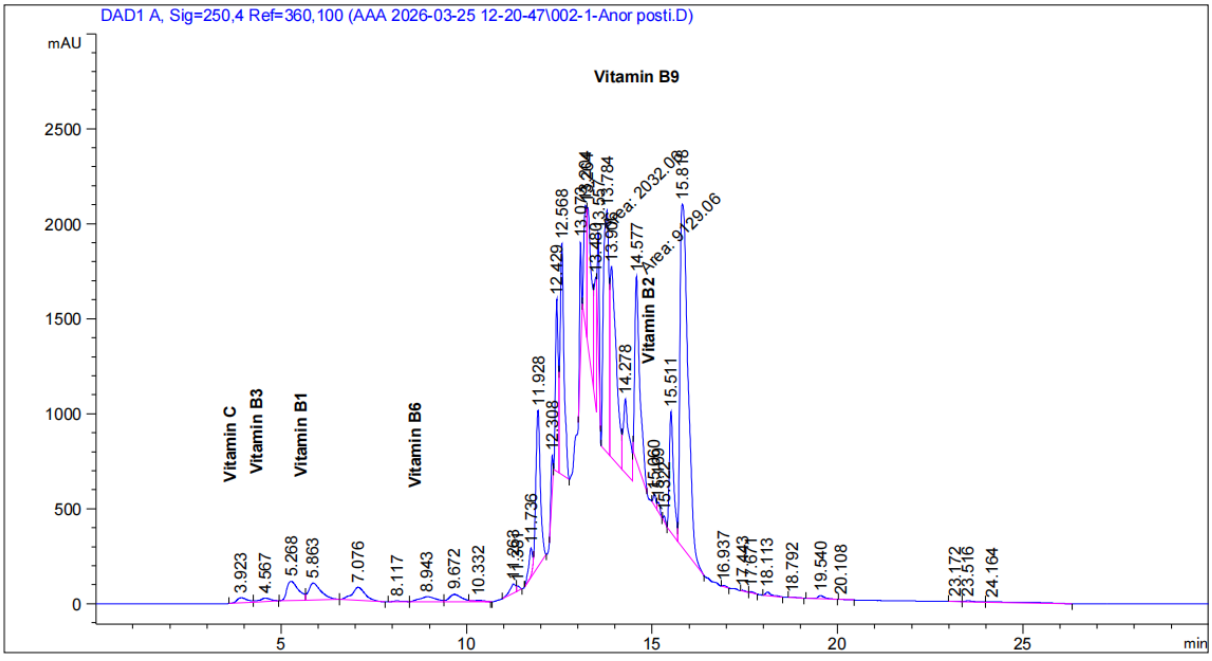


Figure 2. HPLC-DAD chromatogram of water-soluble vitamins in the pomegranate-peel extract test solution.

ISSN: 2181-3337 | SCIENTISTS.UZ

3.2 Free amino-acid profile

Twenty free amino acids were reported, with a combined concentration of 14.456 mg/g (Table 3). Aspartic acid was the predominant analyte at 3.184 mg/g and accounted for approximately 22.03% of the reported free-amino-acid pool. Histidine was second at 1.735 mg/g (12.00%), followed by tyrosine at 1.495 mg/g (10.34%), leucine at 1.390 mg/g (9.62%), alanine at 1.346 mg/g (9.31%), and methionine at 1.253 mg/g (8.67%). Together, these six amino acids represented approximately 71.97% of the total reported free amino acids.

The remaining amino acids were present at concentrations below 0.6 mg/g. Cysteine (0.577 mg/g), glutamic acid (0.508 mg/g), valine (0.484 mg/g), asparagine (0.387 mg/g), glycine (0.371 mg/g), and serine (0.300 mg/g) formed an intermediate group. Isoleucine, arginine, proline, threonine, glutamine, tryptophan, phenylalanine, and lysine were present at lower levels. Lysine was the least abundant reported amino acid at 0.067 mg/g. The standard amino-acid chromatogram and extract chromatogram are presented in Figures 3 and 4, respectively.

Table 3. Free amino acids quantified in the dry pomegranate-peel extract

Amino acid	Mean concentration (mg/g)	Proportion of total (%)
Aspartic acid	3.184	22.03
Glutamic acid	0.508	3.51
Serine	0.300	2.08
Glycine	0.371	2.57
Asparagine	0.387	2.68
Glutamine	0.188	1.30
Cysteine	0.577	3.99
Threonine	0.190	1.31
Arginine	0.237	1.64
Alanine	1.346	9.31
Proline	0.211	1.46
Tyrosine	1.495	10.34
Valine	0.484	3.35
Methionine	1.253	8.67
Histidine	1.735	12.00
Isoleucine	0.245	1.69
Leucine	1.390	9.62
Tryptophan	0.172	1.19
Phenylalanine	0.116	0.80
Lysine	0.067	0.46
Total	**14.456**	**100.00**

Note. *The original table contained inconsistent units. The corrected unit is mg/g because the individual values sum to the reported total of 14.456 mg/g and the source narrative also used mg/g.*

ISSN: 2181-3337 | SCIENTISTS.UZ

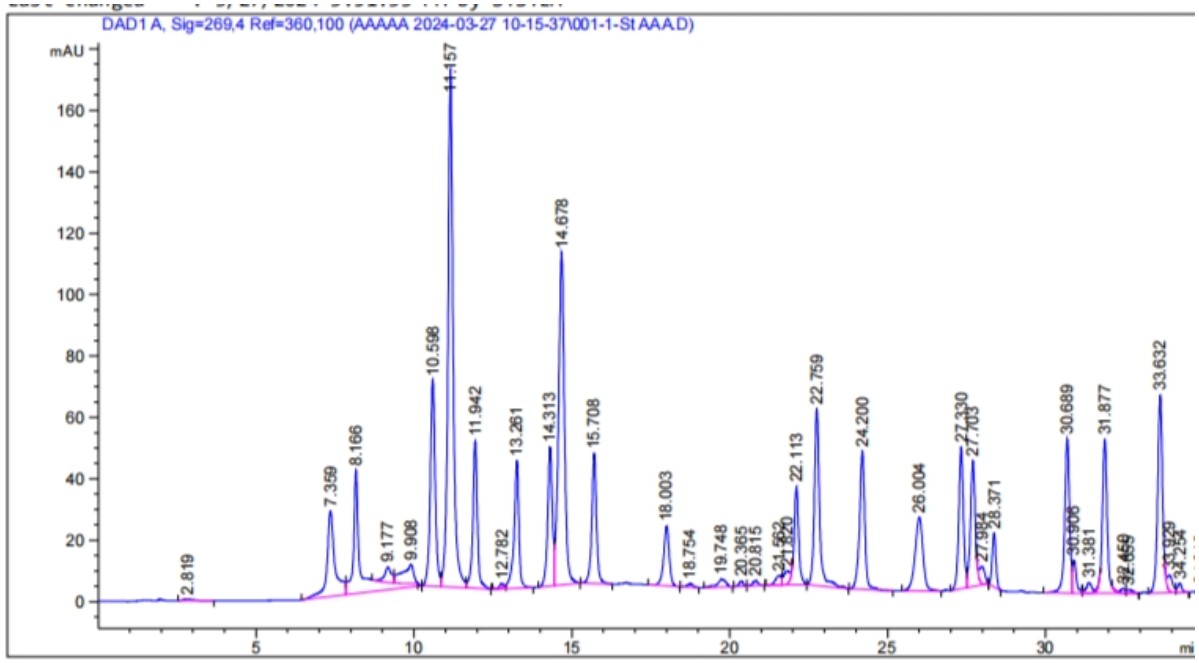


Figure 3. HPLC-DAD chromatogram of the amino-acid standard solution after PITC derivatization.

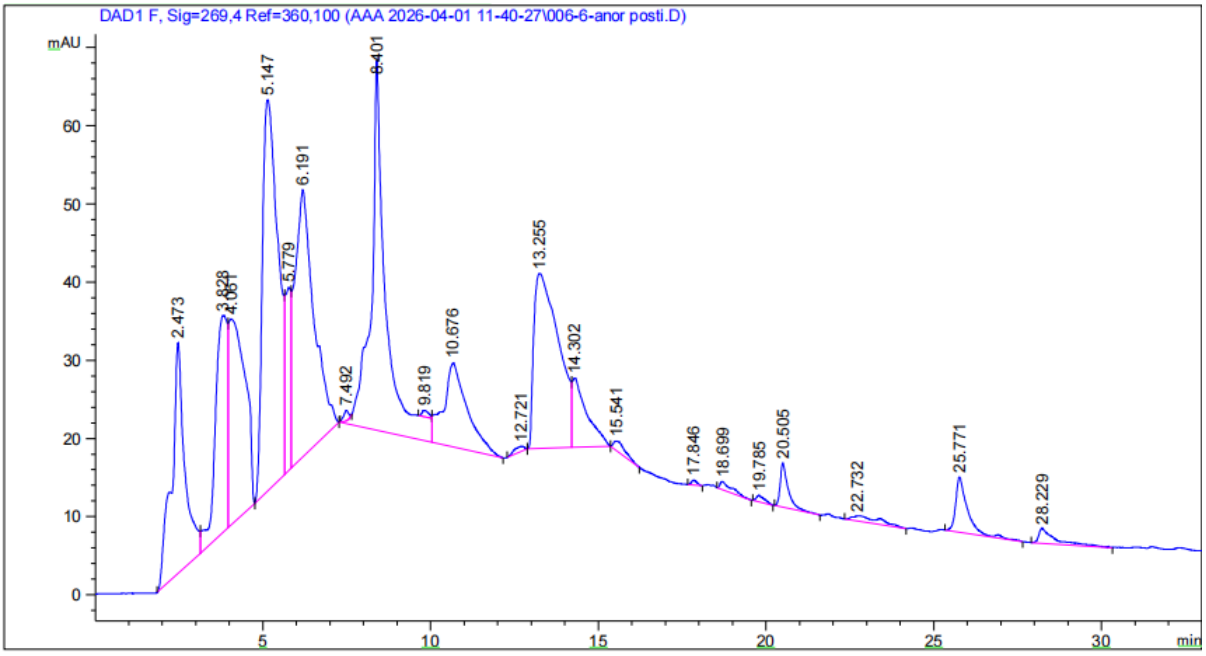


Figure 4. HPLC-DAD chromatogram of free amino acids in the pomegranate-peel extract test solution after PITC derivatization.

4. Discussion

The present analysis extends the chemical description of pomegranate peel beyond the phenolic compounds that dominate the literature. Earlier work has shown that pomegranate peel is chemically distinct from the edible aril and can contain a particularly rich spectrum of polar constituents [8-11]. The current findings indicate that an aqueous peel extract also contains measurable quantities of selected water-soluble vitamins and a broad range of free amino acids. These classes of compounds may be useful as supplementary markers when the extract is characterized across manufacturing batches.

Among the vitamins, folic acid was the highest measured analyte. This result is potentially important from a compositional standpoint, but it should be interpreted cautiously. Folic acid is normally present at much lower concentrations than major bulk constituents, and its determination in complex plant matrices is sensitive to extraction conditions, light exposure, oxidation, pH, co-eluting compounds, and the chemical form used as a standard. The chromatographic pattern in Figure 2 shows substantial matrix complexity around the labelled vitamin region. Therefore, confirmation by peak-purity analysis, matrix-

ISSN: 2181-3337 | SCIENTISTS.UZ

matched calibration, standard addition, or an orthogonal detector would strengthen the assignment. The same caution applies to ascorbic acid, which is particularly susceptible to oxidation during sample preparation and storage.

The vitamin pattern also illustrates why compositional results should be distinguished from nutritional or therapeutic claims. The measured concentrations demonstrate the presence of the analytes in the tested extract, but they do not by themselves establish bioavailability, clinical efficacy, or a recommended dose. For pharmaceutical standardization, the immediate value of these data is analytical: they provide candidate quantitative attributes that may help distinguish a conforming extract from one that has undergone excessive degradation, dilution, substitution, or uncontrolled processing.

The free-amino-acid profile was dominated by aspartic acid, histidine, tyrosine, leucine, alanine, and methionine. The predominance of aspartic acid and the presence of both acidic, neutral, aromatic, sulfur-containing, and branched-chain amino acids indicate a chemically diverse free-amino-acid pool. Because the method targeted free amino acids after precipitation of proteins and peptides, the values should not be interpreted as the total amino-acid composition of the peel or extract. Total amino-acid analysis would require controlled hydrolysis of proteins and separate validation for amino acids that are unstable or transformed during hydrolysis.

The PITC derivatization approach used here is a well-established strategy for ultraviolet detection of amino acids [14,15]. Nevertheless, derivatization-based methods require careful control of reaction time, reagent composition, pH, evaporation, derivative stability, and injection timing. The complex baseline and partially unresolved regions in the test-solution chromatogram suggest that matrix effects and co-elution should be evaluated. For a validated assay, representative blank solutions, reagent blanks, spiked samples, duplicate preparations, system-suitability criteria, and resolution requirements should be specified.

The arithmetic consistency of the amino-acid data supports correction of the unit error in the original table. The individual values sum exactly to 14.456, matching the stated total. The narrative description also reported the values in mg/g. Accordingly, the amino-acid concentrations are presented throughout this revised manuscript in mg/g rather than μg/g. The original spelling “Lycine” has been corrected to leucine because lysine was separately listed at 0.067 mg/g, and the reported 1.390 mg/g value was described as leucine in the results narrative. Typographical errors in tryptophan and phenylalanine were also corrected.

From a standardization perspective, the strongest next step would be a multi-batch study. At least three independently manufactured batches should be tested to establish the natural and process-related variation of the vitamin and amino-acid profiles. Acceptance ranges should be based on observed batch data rather than on a single preparation. In parallel, one or more characteristic pomegranate markers—such as validated phenolic markers or a chromatographic fingerprint—should be incorporated because vitamins and amino acids are not unique to pomegranate peel. WHO guidance emphasizes that marker selection should reflect the intended function of the marker and should be integrated with identity, purity, and manufacturing controls [2].

A complete quality specification would also include botanical authentication, macroscopic or microscopic identity where applicable, moisture or loss on drying, ash values, extractable matter, residual solvents where relevant, microbial limits, pesticide residues, elemental impurities, mycotoxins, and stability-indicating assays [1-3]. Analytical procedures intended for routine release testing should be validated according to the relevant characteristics described in ICH Q2(R2), including specificity or selectivity, accuracy, precision, linearity, range, and robustness [4]. Because the available source record did not include these validation datasets, the current work should be regarded as an initial compositional characterization rather than a completed pharmacopoeial standard.

Despite these limitations, the study provides a useful quantitative starting point. The vitamin table, amino-acid table, and four chromatograms create a more informative chemical record than a general claim

ISSN: 2181-3337 | SCIENTISTS.UZ

that pomegranate peel is “rich in biologically active compounds.” The results identify specific analytes, report their concentrations, and reveal which compounds dominate the measured profiles. With verification across batches and full analytical validation, these data could contribute to a layered standardization framework combining botanical identity, chromatographic fingerprinting, selected marker assays, and general quality tests.

5. Study Limitations

The principal limitation is that the available source document contained only summarized concentration values and chromatographic images. It did not include raw chromatographic data files, integration reports, calibration curves, certified-standard details, replicate-level measurements, standard deviations, recovery experiments, system-suitability criteria, or formal validation results. These elements cannot be reconstructed through proofreading and were therefore not invented in this revision.

The extract was described as an aqueous dry extract, but the source record did not provide full botanical and manufacturing traceability. Results from one incompletely documented extract batch cannot establish universal composition or pharmacopoeial limits for pomegranate peel. Future work should examine authenticated material and independently manufactured batches, and should report all extraction and storage parameters.

The measured vitamin and free-amino-acid concentrations provide compositional information only. No biological assay, toxicity test, stability study, bioavailability assessment, or clinical investigation was included. Consequently, the present data should not be used to make therapeutic claims.

6. Conclusion

HPLC-DAD analysis demonstrated that the tested dry aqueous extract of pomegranate peel contained six quantified water-soluble vitamins and 20 reported free amino acids. Folic acid was the highest measured vitamin at 98.84 µg/g, while aspartic acid was the predominant free amino acid at 3.184 mg/g. The total free-amino-acid concentration was 14.456 mg/g. The results support the use of vitamin and free-amino-acid profiles as supplementary compositional attributes for pomegranate-peel extract. They do not, however, constitute complete pharmaceutical standardization. Botanical traceability, independently produced batches, validated calibration and recovery data, precision and robustness studies, stability testing, contaminant control, and characteristic pomegranate marker assays are still required. The revised data tables and chromatographic figures provide a clear foundation for those subsequent studies.

Declarations

Funding: Not reported in the source document.

Conflict of interest: Not reported in the source document.

Data availability: The chromatographic figures and summarized concentration data are included in this manuscript. Raw chromatographic files and replicate-level data were not supplied with the source document.

REFERENCES

1. World Health Organization. Quality control methods for herbal materials. Geneva: World Health Organization; 2011. ISBN 978-92-4-150073-9.
2. World Health Organization. WHO guidelines for selecting marker substances of herbal origin for quality control of herbal medicines. In: WHO Expert Committee on Specifications for Pharmaceutical Preparations: Fifty-first report. WHO Technical Report Series 1003, Annex 1. Geneva: World Health Organization; 2017. pp. 71-86.
3. European Directorate for the Quality of Medicines & HealthCare. Guide for the elaboration of monographs on herbal drugs and herbal drug preparations. 2nd ed. Strasbourg: Council of Europe; 2023.

4. International Council for Harmonisation of Technical Requirements for Pharmaceuticals for Human Use. ICH Q2(R2): Validation of analytical procedures. Geneva: ICH; 2023.
5. Viuda-Martos M, Fernández-López J, Pérez-Álvarez JA. Pomegranate and its many functional components as related to human health: A review. Comprehensive Reviews in Food Science and Food Safety. 2010;9(6):635-654. https://doi.org/10.1111/j.1541-4337.2010.00131.x
6. Lansky EP, Newman RA. Punica granatum (pomegranate) and its potential for prevention and treatment of inflammation and cancer. Journal of Ethnopharmacology. 2007;109(2):177-206. https://doi.org/10.1016/j.jep.2006.09.006
7. Ismail T, Sestili P, Akhtar S. Pomegranate peel and fruit extracts: A review of potential anti-inflammatory and anti-infective effects. Journal of Ethnopharmacology. 2012;143(2):397-405. https://doi.org/10.1016/j.jep.2012.07.004
8. Singh RP, Chidambara Murthy KN, Jayaprakasha GK. Studies on the antioxidant activity of pomegranate (Punica granatum) peel and seed extracts using in vitro models. Journal of Agricultural and Food Chemistry. 2002;50(1):81-86. https://doi.org/10.1021/jf010865b
9. Li Y, Guo C, Yang J, Wei J, Xu J, Cheng S. Evaluation of antioxidant properties of pomegranate peel extract in comparison with pomegranate pulp extract. Food Chemistry. 2006;96(2):254-260. https://doi.org/10.1016/j.foodchem.2005.02.033
10. Fischer UA, Carle R, Kammerer DR. Identification and quantification of phenolic compounds from pomegranate (Punica granatum L.) peel, mesocarp, aril and differently produced juices by HPLC-DAD-ESI/MSn. Food Chemistry. 2011;127(2):807-821. https://doi.org/10.1016/j.foodchem.2010.12.156
11. Gil MI, Tomás-Barberán FA, Hess-Pierce B, Holcroft DM, Kader AA. Antioxidant activity of pomegranate juice and its relationship with phenolic composition and processing. Journal of Agricultural and Food Chemistry. 2000;48(10):4581-4589. https://doi.org/10.1021/jf000404a
12. Klejdus B, Petrlová J, Potěšil D, Adam V, Mikelová R, Vacek J, Kizek R, Kubáň V. Simultaneous determination of water- and fat-soluble vitamins in pharmaceutical preparations by high-performance liquid chromatography coupled with diode-array detection. Analytica Chimica Acta. 2004;520(1-2):57-67. https://doi.org/10.1016/j.aca.2004.02.027
13. Jin P, Xia L, Li Z, Che N, Zou D, Hu X. Rapid determination of thiamine, riboflavin, niacinamide, pantothenic acid, pyridoxine, folic acid and ascorbic acid in vitamins with minerals tablets by high-performance liquid chromatography with diode-array detection. Journal of Pharmaceutical and Biomedical Analysis. 2012;70:151-157. https://doi.org/10.1016/j.jpba.2012.06.020
14. Bidlingmeyer BA, Cohen SA, Tarvin TL. Rapid analysis of amino acids using pre-column derivatization. Journal of Chromatography B: Biomedical Sciences and Applications. 1984;336(1):93-104. https://doi.org/10.1016/S0378-4347(00)85133-6

ISSN: 2181-3337 | SCIENTISTS.UZ

ISSN: 2181-3337 | SCIENTISTS.UZ VOLUME 5 ISSUE 7 JULY 2026

INFLUENCE OF DEFECTS ON THE ELECTRICAL CONDUCTIVITY OF SB_xSE_γ THIN FILMS PREPARED BY THE INDEPENDENT SOURCE VAPOR TRANSPORT TECHNIQUE

K.M. Quchqarov[1], B.A. Ergashev[1], M.P. Pirimmatov[1], A.S. Matmuratov[1]*, B.A. Gulumbaev[1], X.Z.To'liboyeva[1]

[1]S.A. Azimov Physics-Technical Institute, Academy of Sciences of the Republic of Uzbekistan, 2B Chingz Aitmatov Street, Tashkent 100084, Uzbekistan.

*Corresponding author: e-mail: matmuratovajdos@gmail.com

DOI: 10.67620/sai.57a0004

ABSTRACT

In this study, the structural and electrophysical properties of SbxSey thin films grown at different source temperatures using the independent-source vapor transport method were investigated. The composition of the thin films was determined by energy-dispersive X-ray spectroscopy (EDS), revealing that as the source temperature increases, the Sb/Se atomic ratio shifts from Se-rich to Sb-rich. Specifically, a Se-rich composition (Sb/Se ≈ 0.51) was observed in films obtained at 500 °C, a stoichiometric composition (Sb/Se ≈ 0.67) at 525 °C, and an Sb-rich composition (Sb/Se ≈ 0.82) at 550 °C. The temperature dependence of electrical conductivity was measured using a cryostat, and activation energies were calculated from Arrhenius analysis. According to the results, the following activation energies were identified for the corresponding samples: E_v + 0.578 eV for the 500 °C film, E_v + 0.111 eV for the 525 °C film, and E□ − 0.518 eV for the 550 °C film.

ACCEPTED

31.07.26

Keywords: *independent-source vapor transport deposition, Sb_2Se_3 thin-film solar cells, substrate preparation, source temperature effect, point defects, electrical conductivity, activation energy, photovoltaic absorber materials.*

CC BY

1. INTRODUCTION

The growing global demand for energy underscores the need for stable, reliable, and economically efficient photovoltaic materials. Currently, solar cells using polycrystalline silicon (Si), cadmium telluride (CdTe), and copper–indium–gallium selenide (CIGS; $Cu(In,Ga)Se_2$) serve as primary absorber materials, achieving power conversion efficiencies (PCE) above 20% (Green et al., 2021; Mavlonov et al., 2020; Scheer & Schock, 2011). However, the high processing cost of Si, the toxicity of Cd, and the high cost and scarcity of Ga, In, and Te pose significant challenges to large-scale thin-film solar cell production using these materials(Scheer & Schock, 2011; Zakutayev, 2017). Kesterite-based solar cells ($Cu_2ZnSn(S_xSe_{1-x})_4$, CZTS/Se) achieved a maximum efficiency of approximately 12.7% in 2021 (J. Zhou et al., 2021), but further improvements have stagnated due to defects arising from the material's complex chemical structure. Halide perovskites ($CH_3NH_3PbI_3$) have recently achieved efficiencies near 25%(Green et al., 2021). Nevertheless, the instability and toxicity of Pb-based perovskites limit their use as absorber layers in long-

term, environmentally sustainable photovoltaic devices, pointing to the need for alternative absorber materials (Hobson, Hutter, et al., 2020; Zakutayev, 2017).

To overcome these problems, recent scientific research has focused on antimony selenide (Sb_2Se_3) chalcogenide-based thin films as promising absorber layers for solar cells. This compound has attracted considerable interest as a potential absorber material in photovoltaic devices due to its p-type conductivity, high optical absorption coefficient in the visible spectral range (10^5 cm^{-1}), band gap in the range of 1.1–1.3 eV, high charge mobility (10 cm^2 $V^{-1}s^{-1}$), low toxicity, simple crystal structure, low cost, and the abundance of its constituent elements in nature (Chen, Bobela, et al., 2017; Ghosh et al., 2020; Hutter et al., 2018; Lei et al., 2019; Y. Zhou et al., 2014).

Unlike conventional absorbers, Sb_2Se_3 possesses a unique quasi-one-dimensional (Q1D) structure composed of $[Sb_4Se_6]_n$ ribbons, which are held together by van der Waals forces without dangling bonds, while Sb–Se atoms within the ribbons are covalently bonded (Lei et al., 2019). However, first-principles calculations have shown that the interactions between crystal ribbons in Sb_2Se_3 lie between van der Waals and covalent bonding (X. Wang et al., 2022). Other studies have demonstrated that aligning the growth orientation of $[Sb_4Se_6]_n$ ribbons perpendicular to the substrate along the [211] and [221] crystal planes reduces the density of unsatisfied bonds and forms naturally benign grain boundaries (Hutter et al., 2018; Kondrotas et al., 2019; Z. Li et al., 2019; L. Wang et al., 2017). Nevertheless, crystal ribbons oriented along the [001] plane significantly suppress non-radiative recombination losses, hence enhancing the efficiency of Sb_2Se_3 polycrystalline thin films in photovoltaic (PV) devices (Williams et al., 2020; Y. Zhou et al., 2015). For most known inorganic absorbers (such as Si, CIGS, and CdTe), the breakage of covalent bonds inevitably introduces defect states and recombination centers at the grain boundaries, which can effectively block charge collection and potentially reduce device efficiency during the interface recombination. Contrastingly, Sb_2Se_3 has intrinsically benign grain boundaries which could therefore offer a sustainable solution to drawbacks associated with traditional absorber materials if efficiency values continue to rise(Wijesinghe et al., 2023).

Three main areas of research within the field currently are control of the orientation of Sb_2Se_3 films(Hutter et al., 2018; Kondrotas et al., 2019; Z. Li et al., 2019; L. Wang et al., 2017), band alignment optimization(Gharibshahian et al., 2020; G. Li et al., 2019; Shiel et al., 2020; Wen et al., 2017), and defect passivation at interfaces/surfaces to suppress recombination losses and the open-circuit voltage (VOC) deficit (Chen, Wang, et al., 2017; Hobson, Phillips, et al., 2020; Huang et al., 2019; Liang et al., 2020; Ma et al., 2020). Despite the excellent properties of Sb_2Se_3, PCE values are still far below the maximum theoretical value of 30% predicted by the Shockley–Queisser (S–Q) model (Shockley & Queisser, 1961). Spectroscopic limited maximum efficiency (SLME) calculations show that Sb_2Se_3 has substantial potential for the development of highly efficient solar cells with an upper limit of 30%, which is actually higher than both CdTe and CZTS/Se (Phillips et al., 2019).

Alongside various technologies for fabricating Sb_2Se_3-based thin-film solar cells, vapor-phase deposition methods have been actively studied. In particular, vapor transport deposition (VTD) has been shown to enable the growth of Sb_2Se_3 thin films with vertically oriented one-dimensional crystal structures on the substrate. Initial studies using this method achieved efficiencies of 5–6% in solar cells (Y. Zhou et al., 2015). Subsequent research reported that optimization of process parameters increased the efficiency of Sb_2Se_3-based solar cells prepared by the VTD method to 7–8% (Dong et al., 2021; X. Wang et al., 2018).

This study thoroughly analyzes the effects of source temperature and defect conditions on the electrical conductivity of Sb_2Se_3 thin films synthesized via independent-source vapor transport deposition.

2. Experimental section

Sb_xSe_y thin films were systematically grown at various source temperatures using the independent-source vapor transport method. Initially, soda-lime glass (SLG) substrates measuring 2×2 cm were selected. To ensure optimal film quality, substrates underwent a multi-step cleaning process: chemical

ISSN: 2181-3337 | SCIENTISTS.UZ

cleaning with acetone and ethanol, ultrasonic treatment for 10 minutes, and drying under a nitrogen gas flow. Subsequently, molybdenum (Mo) thin films approximately 1 μm thick were deposited onto glass substrates under high-vacuum conditions via magnetron sputtering. The deposition was conducted at a pressure of 10^{-5} torr in an argon (Ar) atmosphere with a power of 120 W. The Mo layer functioned as the electrical contact and back electrode. Sb_xSe_y thin films were then deposited onto the prepared glass/Mo structures using the independent-source vapor transport deposition method. The thin-film growth process was tightly controlled. Glass and glass/Mo substrates (2×2 cm) were placed in graphite holders, permitting free rotation around a horizontal axis. An initial vacuum of 1.3 Pa (10^{-2} mmHg) was established using a mechanical pump, followed by the introduction of argon (Ar) gas to achieve an inert atmosphere at 7 Pa. The system was heated externally, and once the substrate temperature reached 400 °C, source temperatures of 500 °C, 525 °C, and 550 °C were applied to achieve thin-film growth. Each deposition lasted 10 minutes, with substrate rotation at 2 min^{-1}, yielding uniform Sb_2Se_3 thin films of consistent thickness.

The chemical composition of the thin films was determined using energy-dispersive spectroscopy (EDS, AzTec Advanced, Oxford Instruments), enabling assessment of elemental ratios and the influence of source temperature on composition. Morphology and thickness were examined with a scanning electron microscope (SEM, JEOL JSM-IT510). As the source temperature increased, the mass of evaporated Sb_2Se_3 increased, yielding film thicknesses between approximately 1.7 μm and 6.3 μm (Table 1).

The electrophysical properties of the samples were investigated by measuring the temperature dependence of electrical conductivity in a cryostat. High-precision electrical measurements were conducted with the SM2460 SourceMeter (Keithley, USA). The results were analyzed using the Arrhenius equation to calculate the activation energies of charge carriers.

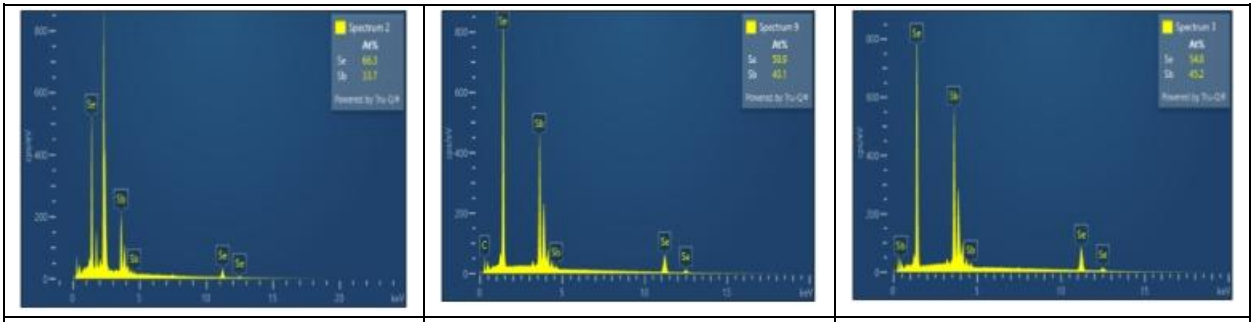
3. Results and discussion

Analysis of energy-dispersive spectroscopy (EDS) results (Figure 1) revealed that changes in source temperature impacted the selenium (Se) content of the obtained thin films (Table 1). As shown in the EDS spectra presented in Figures 1a, b, and c, the primary energy peaks corresponding to Sb and Se elements were clearly observed for all samples. Table 1 presents the EDS results for samples grown at different source temperatures, along with their thicknesses determined by scanning electron microscopy (SEM).

Table 1 shows that, at a constant substrate temperature, increasing the source temperature decreases Se content and increases film thickness in Sb_xSe_y thin films. This phenomenon can be explained by several basic physical factors. First, the evaporation process of the initial Sb_2Se_3 binary compound is non-stoichiometric, due to the significant difference in vapor pressures of Sb and Se:Se is highly volatile, and its vapor pressure increases rapidly with temperature, whereas Sb is relatively less volatile. At lower source temperatures, the vapor phase contains a higher proportion of Se, resulting in Se-rich or near-Se-rich thin films. When the source temperature reaches an optimal value, the evaporation, transport, and condensation processes of Sb and Se atoms achieve equilibrium, resulting in stoichiometric Sb_2Se_3 thin films.

At higher source temperatures, kinetic processes control the system. The evaporation speed of Se atoms increases sharply, leading some to disperse into the vapor phase or re-evaporate from the substrate surface before sufficient bonding occurs. Meanwhile, Sb atoms, being heavier and more strongly bonded to the crystal lattice, condense more effectively on the substrate surface. Consequently, despite constant substrate temperature, thin films grown at higher source temperatures exhibit Sb-rich composition.

ISSN: 2181-3337 | SCIENTISTS.UZ



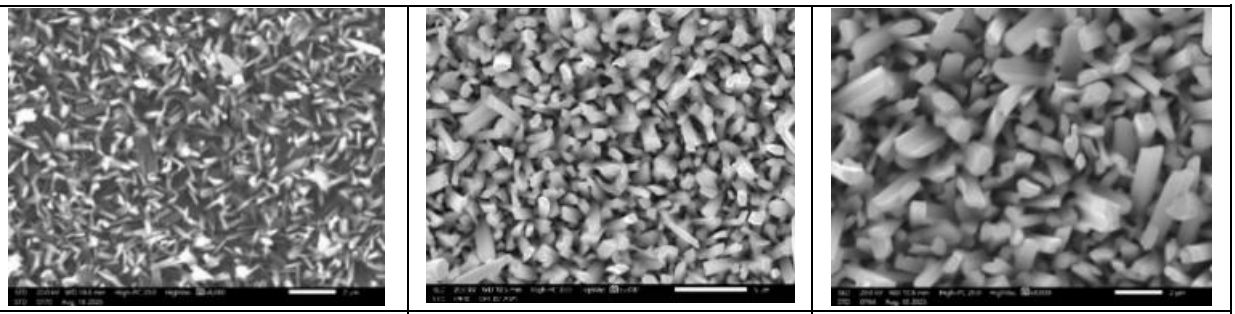
t=500 ºC	t=525 ºC	t=550 ºC

Figure 1. *Energy-dispersive X-ray spectroscopy (EDS) analysis of Sb_xSe_y thin films grown at different source temperatures. (a–c) Elemental composition of the thin films prepared at source temperatures of 500, 525, and 550 °C, respectively.*

Table 1. *Elemental composition determined by EDS for Sb_xSe_y thin films grown at different source temperatures.*

№	Substrate Temperature (ºC)	Source Temperature (ºC)	Evaporated Source mass(mg)	Film Thickness (μm)	Composition		
					Sb (%)	Se (%)	Sb/Se
M54	400	500	143,6	1,732	33,7	66,3	0,5083
M55		525	224,2	3,276	40,1	59,9	0,6694
M53		550	363,6	6,291	45,2	54,8	0,8248

With increasing source temperature, the observed increase in the thickness of Sb_2Se_3 thin films (Table 1) can be explained by the thermodynamic and kinetic characteristics of the evaporation process. As the source temperature rises, the evaporation rate of Sb_2Se_3 and the density of the vapor-phase material flux increase, leading to more material reaching and condensing on the substrate surface. Since the substrate temperature remains constant, at higher source temperatures, the vapor flux leads to greater material accumulation over a shorter time, thereby producing thicker films. Consequently, a consistent increase in film thickness with rising source temperature was observed.



a) **500 ºC**	b) **525 ºC**	c) **550 ºC**

Figure 2. *Scanning electron microscopy (SEM) surface morphology of Sb_2Se_3 thin films deposited at different source temperatures: (a) 500 °C, (b) 525 °C, and (c) 550 °C.*

Figures 2a–c present the SEM images of Sb_2Se_3 thin films deposited on Mo-coated glass substrates at different source temperatures using the independent-source vapor transport method. The surface morphology changes significantly with increasing source temperature. The film deposited at 500 °C consists of densely packed, fine rod-like grains with relatively small grain size and random orientation. Increasing the source temperature to 525 °C promotes grain growth, resulting in larger, more compact grains with improved surface coverage and reduced porosity. At 550 °C, further grain coarsening is observed, and the grains become noticeably larger with well-defined faceted morphology. The enhanced grain size and improved grain connectivity indicate increased surface diffusion and adatom mobility at higher source temperatures, leading to better crystallization and reduced grain boundary density.

ISSN: 2181-3337 | SCIENTISTS.UZ

In the films deposited at different source temperatures (500 °C, 525 °C, and 550 °C), the crystals exhibit a nanorod-like morphology. It was determined that, with increasing source temperature, the length of the nanorods increases from approximately 0.3 μm to ~2 μm.

One of the main reasons for this behavior is the variation in film thickness under different growth conditions. The samples obtained at a source temperature of 500 °C are relatively thin, and the crystalline grains have not yet fully developed. As the temperature increases, the film becomes thicker, which promotes grain growth and leads to the formation of larger crystalline domains.

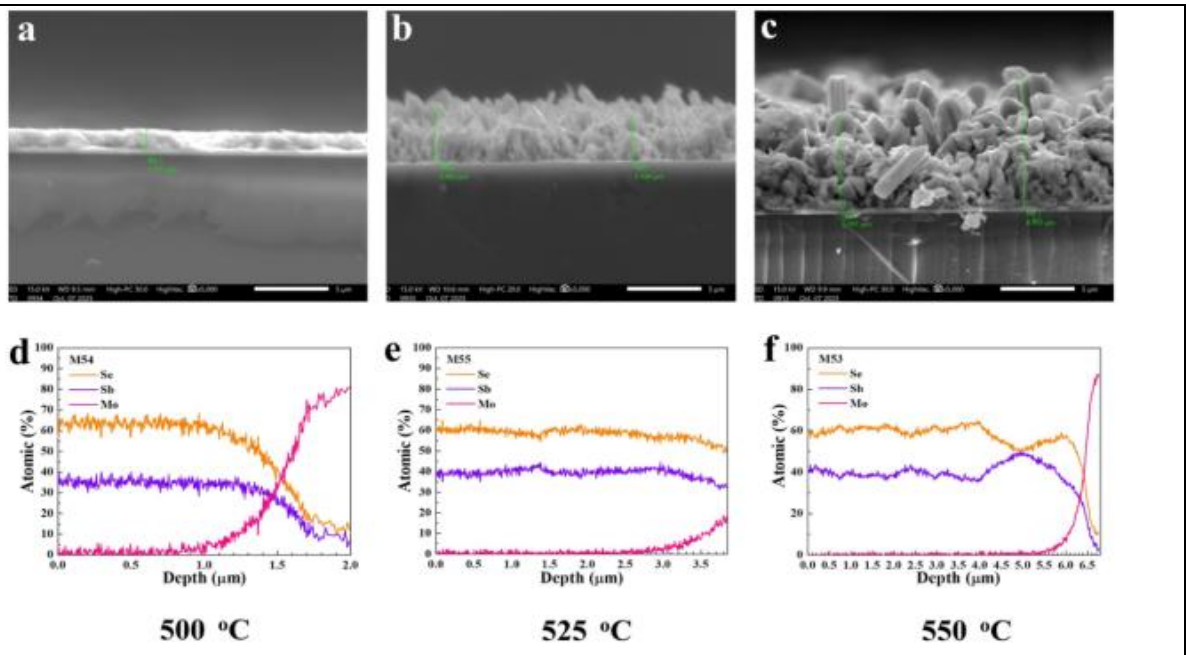


Figure 3. *Cross-sectional (SEM) images (a–c) and thickness-dependent compositional (EDS) analysis (d–f) of Sb_xSe_y thin films deposited at different source temperatures.*

Figure 3 presents the cross-sectional SEM micrographs (Fig. 3a–c) and the corresponding EDS depth profiles (Fig. 3d–f) of Sb_2Se_3 thin films deposited on Mo-coated glass substrates under different source temperatures. The results clearly demonstrate that the source temperature markedly influences the growth kinetics of the absorber layer, leading to significant changes in film thickness, grain morphology, crystallographic growth orientation, and compositional uniformity.

The Se-rich sample deposited at 500 °C (Fig. 3a) exhibits the smallest thickness (≈2 μm) and consists of fine grains with an average size of approximately 0.3 μm. Most crystallites are oriented nearly parallel to the substrate surface, suggesting that crystal growth is dominated by lateral nucleation rather than vertical grain propagation. Such a morphology is characteristic of insufficient surface diffusion, where the kinetic energy of arriving Sb and Se species is too low to overcome diffusion barriers. Consequently, numerous nucleation centers are formed, suppressing competitive grain growth and producing a dense microstructure with a high density of grain boundaries. Since grain boundaries are known to act as trapping and recombination centers, this morphology is generally unfavorable for efficient carrier transport in photovoltaic absorbers.

When the source temperature is increased to 525 °C, forming the stoichiometric sample (Fig. 3b), the microstructure undergoes a pronounced transformation. The film thickness increases to approximately 4 μm, while the average grain size reaches about 1 μm. More importantly, the crystallites become preferentially aligned perpendicular to the substrate, resulting in a highly ordered columnar structure extending throughout the entire absorber layer. This transition reflects enhanced surface diffusion of adatoms and increased atomic mobility, allowing neighboring nuclei to merge through competitive grain growth. Under these conditions, grains with energetically favorable orientations outgrow surrounding crystallites, reducing the overall grain-boundary density. Such vertically aligned columnar grains provide

ISSN: 2181-3337 | SCIENTISTS.UZ

continuous conduction pathways across the absorber thickness, thereby facilitating charge-carrier collection and reducing recombination losses. Similar microstructural evolution has been widely reported as a prerequisite for achieving high-performance Sb_2Se_3 photovoltaic devices.

Further increasing the source temperature to 550 °C leads to the formation of the Sb-rich sample (Fig. 3c), where the film thickness reaches approximately 6.5 μm and the average grain size increases to nearly 3 μm. Although grain growth is significantly promoted, the columnar morphology becomes less ordered and many crystallites are inclined with respect to the substrate normal. The larger grains indicate accelerated diffusion and grain coalescence; however, excessive thermal energy simultaneously enhances selenium re-evaporation because of its relatively high vapor pressure compared with antimony. The resulting deviation from stoichiometry modifies the local supersaturation during film growth, promoting anisotropic crystal growth and increasing structural disorder. Consequently, the film exhibits a rougher morphology and less uniform grain orientation despite its larger crystal size. This observation suggests that grain enlargement alone is insufficient to guarantee improved structural quality, as crystallographic alignment and compositional stability are equally important.

The EDS compositional depth profiles (Fig. 3d–f) further corroborate these structural observations. In the Se-rich sample, the selenium concentration remains consistently higher than that of antimony across the entire film thickness, confirming the Se-rich growth condition. In contrast, the stoichiometric sample exhibits nearly constant Sb and Se concentrations throughout the absorber layer, indicating excellent compositional homogeneity and nearly stoichiometric composition. Such uniform elemental distribution suggests stable evaporation kinetics and balanced incorporation of both constituent elements during deposition. Conversely, the Sb-rich sample contains a higher Sb concentration accompanied by slight compositional fluctuations along the growth direction. These fluctuations most likely originate from the preferential evaporation of selenium at elevated source temperatures, which has frequently been reported as a principal challenge in the high-temperature growth of Sb_2Se_3 thin films.

The combined SEM and EDS analyses reveal that the evolution of the Sb_2Se_3 microstructure is governed by the competition between surface diffusion, nucleation density, and selenium volatilization. At low source temperatures, limited atomic mobility results in numerous nuclei and fine-grained, compact films. Increasing the source temperature enhances adatom diffusion, promoting columnar grain growth and improved crystallinity. However, excessively high temperatures accelerate selenium loss, disturb the stoichiometric balance, and induce structural disorder despite continued grain coarsening.

To evaluate the electrical properties of Sb_xSe_y thin films, their specific electrical conductivity was first measured at room temperature using the “sandwich” method. The results are summarized in Table 2. According to the experimental data, the lowest conductivity value was observed in the stoichiometric sample. This behavior is explained by the fact that the stoichiometric Sb_2Se_3 thin film exhibits electrical properties characteristic of an intrinsic semiconductor. It is well known that intrinsic semiconductors have a low concentration of free charge carriers, which considerably reduces their electrical conductivity compared to doped semiconductors (Streetman & Banerjee, 2015; Sze & Ng, 2006; X. Wang et al., 2018).

Measurements performed using the hot-probe method revealed that Sb-rich samples show strong n-type conductivity, while Se-rich samples show p-type conductivity. The stoichiometric sample demonstrated weak p-type conductivity (Table 2). These results show that the ratio of Sb and Se atoms is directly related to defect centers in the crystal lattice and the nature of charge carriers (Streetman & Banerjee, 2015).

To gain a better understanding of point defects in the samples, the temperature dependence of electrical conductivity was measured over 77–300 K using a cryostat and the Van der Pauw method. The experimental results were expressed through an Arrhenius-type exponential relationship characteristic of semiconductors (Moynihan et al., 1982):

ISSN: 2181-3337 | SCIENTISTS.UZ

$$\sigma(T)=\sigma_0 \cdot e^{-\frac{E_a}{kT}} \qquad (1)$$

where σ is the dark specific conductivity, σ0 is the pre-exponential factor, E_a is the activation energy for conductivity, k is the Boltzmann constant, and T is the absolute temperature.

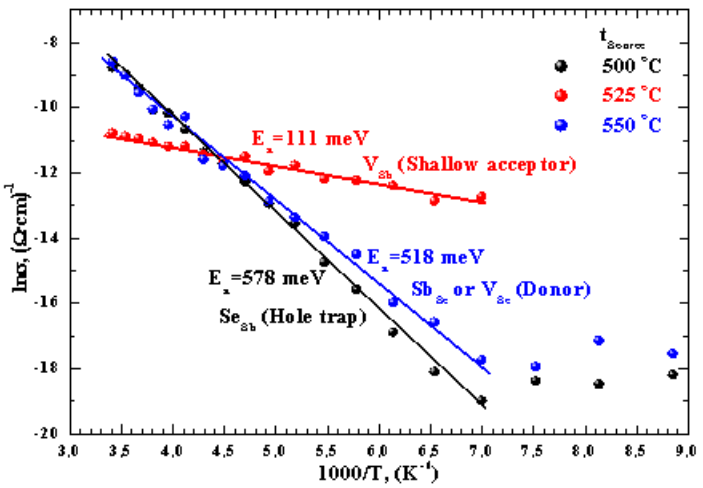


Figure 4. *Arrhenius plots used to determine the activation energy from the temperature dependence of the electrical conductivity of the samples.*

Figure 4 presents the Arrhenius plots for samples obtained at different source temperatures. Based on these plots, the activation energies for each sample were determined. The calculated Ea values were 578 meV, 111 meV, and 518 meV for samples grown at source temperatures of 500 °C, 525 °C, and 550 °C, respectively (Table 2). The obtained results are in good agreement with values reported in the literature for Sb_2Se_3 thin films (Hobson, Phillips, et al., 2020; Huang et al., 2019; Liu et al., 2017; Savory & Scanlon, 2019; Wijesinghe et al., 2023).

For the Se-rich sample, the identified activation energy of ($E_a=E_v+0.578$ eV) corresponds to a defect state associated with Se atoms occupying Sb lattice sites (Se_{Sb}). Such antisite defects generate “hole-trap” levels that act as trapping centers for holes. Under Se-rich conditions, i.e., when μ_{Se} is high, Se_{Sb} antisite defects become the lowest-energy acceptor defects (Hobson, Phillips, et al., 2020; Huang et al., 2019, 2021; Liu et al., 2017; Savory & Scanlon, 2019; Wijesinghe et al., 2023). According to density functional theory (DFT) calculations, Se vacancies and compound-defect clusters can form deep energy levels far from the conduction band, thereby limiting the ionization of charge carriers (Chen, Bobela, et al., 2017). The literature reports that under Se-rich conditions, the probability of forming Se_{Sb} antisite defects increases with increasing Sb vacancy (V_{Sb}) concentration. In particular, Se_{Sb} antisite defects generate deep energy levels near the mid-gap, acting as efficient recombination centers. As a result, the ionization of charge carriers is restricted, thereby reducing electrical conductivity (Hobson, Phillips, et al., 2020; Huang et al., 2019; Savory & Scanlon, 2019; Wijesinghe et al., 2023).

For the Sb-rich sample, the activation energy of ($E_a=E_c-0.518$ eV) was identified, which can be ascribed to Sb atoms occupying Se lattice sites (Sb_{Se}) or the formation of Se vacancies (V_{Se}). These defects generate donor-type levels, thereby increasing the electron concentration. As a result, the sample shows n-type electrical conductivity. Under Se-poor conditions, i.e., when μ_{Se} is low, three Sb_{Se} antisite defects represent the lowest-energy acceptor defects, while three V_{Se} vacancy defects act as the lowest-energy donor defects. Consequently, strong donor–acceptor compensation occurs (Hobson, Phillips, et al., 2020; Huang et al., 2019, 2021; Liu et al., 2017; Savory & Scanlon, 2019; Wijesinghe et al., 2023). The literature reports that under Sb-rich conditions, donor-type defects such as Se vacancies (V_{Se}) and Sb antisite defects

ISSN: 2181-3337 | SCIENTISTS.UZ

(Sb_{Se}) are energetically favored. Some of these defects form shallow levels near the conduction band, which can ionize even at low temperatures. As a result, the electron concentration increases and electrical conductivity increases (Hobson, Phillips, et al., 2020; Huang et al., 2019; Savory & Scanlon, 2019; Wijesinghe et al., 2023).

For the stoichiometric sample, a relatively small activation energy of ($E_a=E_v+0.111$ eV) was observed. This corresponds to shallow acceptor levels associated with Sb vacancies (V_{Sb}). Such defects increase hole concentration, thereby enhancing p-type conductivity, and are considered beneficial from the perspective of electrical properties (Hobson, Phillips, et al., 2020; Huang et al., 2019, 2021; Liu et al., 2017; Savory & Scanlon, 2019; Wijesinghe et al., 2023).

Overall, the activation energy values indicate that deep-level defects dominate in Se-rich and Sb-rich samples, whereas shallow acceptor states are primarily present in the stoichiometric sample.(Hobson, Phillips, et al., 2020; Huang et al., 2019; Savory & Scanlon, 2019; Wijesinghe et al., 2023)

Table 2. *Electrophysical Properties and Defect Characteristics of Sb_xSe_y Thin Films*

Sample	Sb/Se	Type	σ $(\Omega\times m)^{-1}$	E_a (eV)	Defect type	Defect	References
M54	0,5083	p	$6,57\times10^{-5}$	E_v + 0,578	Hole-trap	Se_{Sb}	24-29
M55	0,6694	~p	$1,14\times10^{-5}$	E_v + 0,111	Shallow acceptor	V_{Sb}	24-29
M53	0,8248	n	$1,89\times10^{-4}$	E_c – 0,518	Donor	Sb_{Se} or V_{Se}	24-27

4. Conclusion

In conclusion, the composition of Sb_2Se_3 thin films prepared by the independent-source vapor transport method shifts from Se-rich to Sb-rich as the source temperature increases. At a source temperature of 525 °C, a stoichiometric thin film was formed and exhibited distinct electrical properties. The conductivity of the samples varied from $1.14\times10^{-5}\,(\Omega\cdot m)^{-1}$ to $1.89\times10^{-4}\,(\Omega\cdot m)^{-1}$ as the Se content increased. Activation energies determined from specific electrical conductivity tests indicated the presence of deep-level defects in Sb-rich and Se-rich samples, while shallow acceptor defects were observed in the stoichiometric sample. In the Sb-rich sample, the type of electrical conductivity changed from p-type to n-type. In contrast, in the stoichiometric sample, the increased hole concentration increased p-type conductivity, which is considered advantageous for electrical properties. The obtained results show the potential of Sb_2Se_3 thin films for the fabrication of high-efficiency solar cells.

Funding

This work was supported by the Belarusian Republican Foundation for Fundamental Research (Grant No. F25UZBG-109).

REFERENCES

1. Chen, C., Bobela, D. C., Yang, Y., Lu, S., Zeng, K., Ge, C., Yang, B., Gao, L., Zhao, Y., Beard, M. C., & Tang, J. (2017). Characterization of basic physical properties of Sb2Se3 and its relevance for photovoltaics. Frontiers of Optoelectronics, 10(1), 18–30. https://doi.org/10.1007/s12200-017-0702-z
2. Chen, C., Wang, L., Gao, L., Nam, D., Li, D., Li, K., Zhao, Y., Ge, C., Cheong, H., Liu, H., Song, H., & Tang, J. (2017). 6.5% Certified Efficiency Sb 2 Se 3 Solar Cells Using PbS Colloidal Quantum Dot Film as Hole-Transporting Layer. ACS Energy Letters, 2(9), 2125–2132. https://doi.org/10.1021/acsenergylett.7b00648
3. Dong, J., Liu, Y., Wang, Z., & Zhang, Y. (2021). Boosting V OC of antimony chalcogenide solar cells: A review on interfaces and defects. Nano Select, 2(10), 1818–1848. https://doi.org/10.1002/nano.202000288

4. Gharibshahian, I., Orouji, A. A., & Sharbati, S. (2020). Towards high efficiency Cd-Free Sb2Se3 solar cells by the band alignment optimization. Solar Energy Materials and Solar Cells, 212, 110581. https://doi.org/10.1016/j.solmat.2020.110581
5. Ghosh, S., Moreira, M. V. B., Fantini, C., & González, J. C. (2020). Growth and optical properties of nanocrystalline Sb2Se3 thin-films for the application in solar-cells. Solar Energy, 211, 613–621. https://doi.org/10.1016/j.solener.2020.10.001
6. Green, M., Dunlop, E., Hohl-Ebinger, J., Yoshita, M., Kopidakis, N., & Hao, X. (2021). Solar cell efficiency tables (version 57). Progress in Photovoltaics: Research and Applications, 29(1), 3–15. https://doi.org/10.1002/pip.3371
7. Hobson, T. D. C., Hutter, O. S., Fleck, N., Daniels, L. M., Major, J. D., Ng, T. M., & Durose, K. (2020). Vegard Relation and Raman Band Reference Data Generated from Bulk Crystals of Kesterite-Phase Composition Series Cu 2 ZnSnS 4 x Se 4–4 x (CZTSSe, $0 \leq x \leq 1$). Crystal Growth & Design, 20(4), 2164–2173. https://doi.org/10.1021/acs.cgd.9b00911
8. Hobson, T. D. C., Phillips, L. J., Hutter, O. S., Durose, K., & Major, J. D. (2020). Defect properties of Sb2Se3 thin film solar cells and bulk crystals. Applied Physics Letters, 116(26). https://doi.org/10.1063/5.0012697
9. Huang, M., Cai, Z., Wang, S., Gong, X., Wei, S., & Chen, S. (2021). More Se Vacancies in Sb 2 Se 3 under Se-Rich Conditions: An Abnormal Behavior Induced by Defect-Correlation in Compensated Compound Semiconductors. Small, 17(36), 2102429. https://doi.org/10.1002/smll.202102429
10. Huang, M., Xu, P., Han, D., Tang, J., & Chen, S. (2019). Complicated and Unconventional Defect Properties of the Quasi-One-Dimensional Photovoltaic Semiconductor Sb 2 Se 3. ACS Applied Materials & Interfaces, 11(17), 15564–15572. https://doi.org/10.1021/acsami.9b01220
11. Hutter, O. S., Phillips, L. J., Durose, K., & Major, J. D. (2018). 6.6% efficient antimony selenide solar cells using grain structure control and an organic contact layer. Solar Energy Materials and Solar Cells, 188, 177–181. https://doi.org/10.1016/j.solmat.2018.09.004
12. Kondrotas, R., Zhang, J., Wang, C., & Tang, J. (2019). Growth mechanism of Sb2Se3 thin films for photovoltaic application by vapor transport deposition. Solar Energy Materials and Solar Cells, 199, 16–23. https://doi.org/10.1016/j.solmat.2019.04.024
13. Lei, H., Chen, J., Tan, Z., & Fang, G. (2019). Review of Recent Progress in Antimony Chalcogenide-Based Solar Cells: Materials and Devices. Solar RRL, 3(6). https://doi.org/10.1002/solr.201900026
14. Li, G., Li, Z., Liang, X., Guo, C., Shen, K., & Mai, Y. (2019). Improvement in Sb 2 Se 3 Solar Cell Efficiency through Band Alignment Engineering at the Buffer/Absorber Interface. ACS Applied Materials & Interfaces, 11(1), 828–834. https://doi.org/10.1021/acsami.8b17611
15. Li, Z., Liang, X., Li, G., Liu, H., Zhang, H., Guo, J., Chen, J., Shen, K., San, X., Yu, W., Schropp, R. E. I., & Mai, Y. (2019). 9.2%-efficient core-shell structured antimony selenide nanorod array solar cells. Nature Communications, 10(1), 125. https://doi.org/10.1038/s41467-018-07903-6
16. Liang, G.-X., Luo, Y.-D., Chen, S., Tang, R., Zheng, Z.-H., Li, X.-J., Liu, X.-S., Liu, Y.-K., Li, Y.-F., Chen, X.-Y., Su, Z.-H., Zhang, X.-H., Ma, H.-L., & Fan, P. (2020). Sputtered and selenized Sb2Se3 thin-film solar cells with open-circuit voltage exceeding 500 mV. Nano Energy, 73, 104806. https://doi.org/10.1016/j.nanoen.2020.104806
17. Liu, X., Xiao, X., Yang, Y., Xue, D.-J., Li, D.-B., Chen, C., Lu, S., Gao, L., He, Y., Beard, M. C., Wang, G., Chen, S., & Tang, J. (2017). Enhanced Sb 2 Se 3 solar cell performance through theory-guided defect control. Progress in Photovoltaics: Research and Applications, 25(10), 861–870. https://doi.org/10.1002/pip.2900
18. Ma, Y., Tang, B., Lian, W., Wu, C., Wang, X., Ju, H., Zhu, C., Fan, F., & Chen, T. (2020). Efficient defect passivation of Sb 2 Se 3 film by tellurium doping for high performance solar cells. Journal of Materials Chemistry A, 8(14), 6510–6516. https://doi.org/10.1039/D0TA00443J

19. Mavlonov, A., Razykov, T., Raziq, F., Gan, J., Chantana, J., Kawano, Y., Nishimura, T., Wei, H., Zakutayev, A., & Minemoto, T. (2020). A review of Sb2Se3 photovoltaic absorber materials and thin-film solar cells. Solar Energy, 201, 227–246.
20. Moynihan, C. T., Gavin, D. L., & Syed, R. (1982). PRE-EXPONENTIAL TERM IN THE ARRHENIUS EQUATION FOR ELECTRICAL CONDUCTIVITY OF GLASS. Le Journal de Physique Colloques, 43(C9), C9-395-C9-398. https://doi.org/10.1051/jphyscol:1982975
21. Phillips, L. J., Savory, C. N., Hutter, O. S., Yates, P. J., Shiel, H., Mariotti, S., Bowen, L., Birkett, M., Durose, K., Scanlon, D. O., & Major, J. D. (2019). Current Enhancement via a TiO2 Window Layer for CSS Sb2Se3 Solar Cells: Performance Limits and High V oc. IEEE Journal of Photovoltaics, 9(2), 544–551. https://doi.org/10.1109/JPHOTOV.2018.2885836
22. Savory, C. N., & Scanlon, D. O. (2019). The complex defect chemistry of antimony selenide. Journal of Materials Chemistry A, 7(17), 10739–10744. https://doi.org/10.1039/C9TA02022E
23. Scheer, R., & Schock, H. (2011). Chalcogenide Photovoltaics. Wiley. https://doi.org/10.1002/9783527633708
24. Shiel, H., Hutter, O. S., Phillips, L. J., Swallow, J. E. N., Jones, L. A. H., Featherstone, T. J., Smiles, M. J., Thakur, P. K., Lee, T.-L., Dhanak, V. R., Major, J. D., & Veal, T. D. (2020). Natural Band Alignments and Band Offsets of Sb 2 Se 3 Solar Cells. ACS Applied Energy Materials, 3(12), 11617–11626. https://doi.org/10.1021/acsaem.0c01477
25. Shockley, W., & Queisser, H. J. (1961). Detailed Balance Limit of Efficiency of p-n Junction Solar Cells. Journal of Applied Physics, 32(3), 510–519. https://doi.org/10.1063/1.1736034
26. Streetman, B. G., & Banerjee, S. K. (2015). Solid State Electronic Devices. Pearson, 10(Pearson),596. https://books.google.co.uz/books/about/Solid_State_Electronic_Devices.html?id=-nnznQEACAAJ&redir_esc=y
27. Sze, S. M., & Ng, K. K. (2006). Physics of Semiconductor Devices (3rd ed.). Wiley. https://doi.org/10.1002/0470068329
28. Wang, L., Li, D.-B., Li, K., Chen, C., Deng, H.-X., Gao, L., Zhao, Y., Jiang, F., Li, L., Huang, F., He, Y., Song, H., Niu, G., & Tang, J. (2017). Stable 6%-efficient Sb2Se3 solar cells with a ZnO buffer layer. Nature Energy, 2(4), 17046. https://doi.org/10.1038/nenergy.2017.46
29. Wang, X., Li, Z., Kavanagh, S. R., Ganose, A. M., & Walsh, A. (2022). Lone pair driven anisotropy in antimony chalcogenide semiconductors. Physical Chemistry Chemical Physics, 24(12), 7195–7202. https://doi.org/10.1039/D1CP05373F
30. Wang, X., Tang, R., Wu, C., Zhu, C., & Chen, T. (2018). Development of antimony sulfide–selenide Sb2(S, Se)3-based solar cells. Journal of Energy Chemistry, 27(3), 713–721. https://doi.org/10.1016/j.jechem.2017.09.031
31. Wen, X., He, Y., Chen, C., Liu, X., wang, L., Yang, B., Leng, M., Song, H., Zeng, K., Li, D., Li, K., Gao, L., & Tang, J. (2017). Magnetron sputtered ZnO buffer layer for Sb2Se3 thin film solar cells. Solar Energy Materials and Solar Cells, 172, 74–81. https://doi.org/10.1016/j.solmat.2017.07.014
32. Wijesinghe, U., Longo, G., & Hutter, O. S. (2023). Defect engineering in antimony selenide thin film solar cells. Energy Advances, 2(1), 12–33. https://doi.org/10.1039/D2YA00232A
33. Williams, R. E., Ramasse, Q. M., McKenna, K. P., Phillips, L. J., Yates, P. J., Hutter, O. S., Durose, K., Major, J. D., & Mendis, B. G. (2020). Evidence for Self-healing Benign Grain Boundaries and a Highly Defective Sb 2 Se 3 –CdS Interfacial Layer in Sb 2 Se 3 Thin-Film Photovoltaics. ACS Applied Materials & Interfaces, 12(19), 21730–21738. https://doi.org/10.1021/acsami.0c03690
34. Zakutayev, A. (2017). Brief review of emerging photovoltaic absorbers. Current Opinion in Green and Sustainable Chemistry, 4, 8–15. https://doi.org/10.1016/j.cogsc.2017.01.002

ISSN: 2181-3337 | SCIENTISTS.UZ

35. Zhou, J., Xu, X., Duan, B., Wu, H., Shi, J., Luo, Y., Li, D., & Meng, Q. (2021). Regulating crystal growth via organic lithium salt additive for efficient Kesterite solar cells. Nano Energy, 89, 106405. https://doi.org/10.1016/j.nanoen.2021.106405
36. Zhou, Y., Leng, M., Xia, Z., Zhong, J., Song, H., Liu, X., Yang, B., Zhang, J., Chen, J., Zhou, K., Han, J., Cheng, Y., & Tang, J. (2014). Solution-Processed Antimony Selenide Heterojunction Solar Cells. Advanced Energy Materials, 4(8), 1301846. https://doi.org/10.1002/aenm.201301846
37. Zhou, Y., Wang, L., Chen, S., Qin, S., Liu, X., Chen, J., Xue, D.-J., Luo, M., Cao, Y., Cheng, Y., Sargent, E. H., & Tang, J. (2015). Thin-film Sb2Se3 photovoltaics with oriented one-dimensional ribbons and benign grain boundaries. Nature Photonics, 9(6), 409–415. https://doi.org/10.1038/nphoton.2015.78

ISSN: 2181-3337 | SCIENTISTS.UZ VOLUME 5 ISSUE 7 JULY 2026

EFFECTS OF SUBSTRATE, IRRIGATION VOLUME, AND MINERAL NUTRITION ON GROWTH, YIELD, AND VOLATILE COMPOUND ACCUMULATION IN PIMPINELLA ANISUM L. UNDER GREENHOUSE CONDITIONS

Akhrorova Barnokhon[1], Kholiyorova Feruza[1]

[1]Master's degree holder; e-mail: bakhrorova@icloud.com

[2]Master's degree holder; e-mail: feruzakholiyorova@gmail.com

Tashkent Institute of Irrigation and Agricultural Mechanization Engineers National Research University, Tashkent, Uzbekistan

DOI: 10.67620/sai.57a0005

ABSTRACT

This study evaluated the effects of substrate type (soil or coconut coir), irrigation volume (50, 100, 150, or 200 mL per irrigation event), and mineral nutrition (control or a calcium nitrate formulation supplemented with boron, 17N + 32CaO + 1B) on the growth, productivity, and volatile profile of Pimpinella anisum L. cultivated under greenhouse conditions in Uzbekistan. The experiment comprised 16 treatment combinations with three biological replicates per treatment. Mineral nutrition increased plant height, leaf number, root mass, and umbel number in both substrates. Among the tested irrigation volumes, 150 mL produced the most balanced pattern of root development and biomass accumulation. Gas chromatography–mass spectrometry of ethanolic extracts identified trans-anethole as the predominant volatile constituent in all reported treatments, although its relative peak area and those of associated compounds varied with cultivation conditions. Under the tested conditions, coconut coir combined with calcium nitrate–boron nutrition provided a balanced growth response, whereas soil with mineral nutrition produced the highest reported relative trans-anethole peak area. These findings are preliminary because the experiment was conducted at one site and the chromatographic results represent relative peak areas rather than absolute compound concentrations.

ACCEPTED

31.07.26

Keywords: *Pimpinella anisum; anise; coconut coir; mineral nutrition; irrigation volume; GC–MS; trans-anethole; greenhouse cultivation.*

CC BY

1. Introduction

Anise (*Pimpinella anisum L.*, Apiaceae) is an annual medicinal and aromatic crop used in food, pharmaceutical, cosmetic, and related industries. Its commercial value is closely associated with the fruits and their volatile fraction, in which trans-anethole is commonly the dominant constituent (Dumitrescu et al., 2023; Reveglia et al., 2026; Spinozzi et al., 2023).

Growth, yield formation, and secondary-metabolite accumulation in medicinal plants are influenced by genotype, water supply, mineral nutrition, temperature, light, and substrate properties (Pant et al., 2021; Pezo et al., 2022). Fertilizer treatments can alter both agronomic performance and the chemical profile of anise (Khalid, 2012; Tavallali et al., 2017). In controlled-environment production, soilless

substrates may improve root-zone aeration and enable more precise management of water and nutrients, although their performance depends on substrate characteristics and irrigation practice (Bugbee, 2004; Savvas & Gruda, 2018). Controlled-environment studies of Apiaceae crops also indicate that their yield and phytochemical composition can respond strongly to production conditions (Giordano et al., 2022).

Despite the expansion of greenhouse and substrate-based cultivation in Uzbekistan, locally generated evidence on anise remains limited. The present study therefore compared soil and coconut coir under four irrigation volumes and two mineral-nutrition regimes. The objective was to evaluate treatment responses in vegetative growth, selected productivity indicators, and the relative GC–MS profile of volatile compounds in ethanolic extracts of *P. anisum*. The study addressed three questions: (1) how did substrate and mineral nutrition affect growth and umbel formation; (2) which irrigation volume produced the most balanced growth response under the tested conditions; and (3) how did the reported relative volatile profile vary among substrate and nutrition treatments?

Materials and Methods

Study site and growing conditions. The experiment was conducted in a controlled greenhouse at the Institute of Fundamental and Applied Research of the National Research University "Tashkent Institute of Irrigation and Agricultural Mechanization Engineers" (TIIAME), Tashkent, Uzbekistan. Daytime temperature was maintained at 22–25 °C, nighttime temperature remained above 18 °C, relative humidity was maintained at 60–70%, and a 16-h photoperiod was used.

Experimental design and treatments. Plants were cultivated in soil or coconut coir. The randomized factorial experiment comprised two substrates × two mineral-nutrition regimes (control and calcium nitrate supplemented with boron, 17N + 32CaO + 1B) × four irrigation volumes (50, 100, 150, and 200 mL per irrigation event). Each of the 16 treatment combinations had three biological replicates, giving 48 experimental units. The nutrient formulation is reported as recorded in the study file. The available records did not specify the product application rate, irrigation frequency, pot volume, seed source, or physicochemical properties of the substrates.

Growth and productivity measurements. The recorded variables were total plant length, stem length, root length, leaf number, fresh and dry stem biomass, fresh and dry root biomass, and number of umbels per plant. Measurements were taken at the end of the cultivation period. Table 1 presents the substrate × nutrition means supplied in the study records; the irrigation volume associated with those summary means was not identified in the available dataset.

Volatile-compound analysis. Aerial plant material collected at maturity was macerated in ethanol for 24 h. The solvent was evaporated, and the resulting extract was analysed using an Agilent 8860 gas chromatograph coupled to a 5977 mass-selective detector and fitted with an HP-5 capillary column (30 m × 0.25 mm internal diameter; 0.25 μm film thickness). Electron ionization was performed at 70 eV. Compounds were identified by comparison with the NIST/EPA/NIH mass-spectral library. Results are reported as relative peak areas (%) for comparative purposes and must not be interpreted as absolute concentrations or as the composition of a hydrodistilled essential oil.

Statistical analysis. The effects of substrate, mineral nutrition, irrigation volume, and their interactions were evaluated using three-way analysis of variance, followed by Tukey's honestly significant difference test for pairwise comparisons at $\alpha = .05$. The available summary contained treatment means and p values but did not include standard deviations, standard errors, effect sizes, or confidence intervals.

Results

Growth and productivity responses. Mineral nutrition was associated with higher values for all four variables summarized in Table 1. In coconut coir, plant height increased from 65.0 to 67.0 cm, leaf number from 13 to 19, root mass from 0.4 to 0.8 g, and umbel number from 8 to 15. In soil, the corresponding changes were from 60.0 to 65.0 cm, 12 to 18 leaves, 1.0 to 1.4 g root mass, and 7 to 14

ISSN: 2181-3337 | SCIENTISTS.UZ

umbels. Thus, the strongest proportional response occurred in umbel number, whereas soil maintained the greater root mass in both nutrition regimes.

Table 1. Selected growth and productivity means by substrate and mineral-nutrition treatment

Parameter	Coconut coir, control	Coconut coir, 17N + 32CaO + 1B	Soil, control	Soil, 17N + 32CaO + 1B
Plant height (cm)	65.0	67.0	60.0	65.0
Number of leaves	13	19	12	18
Root mass (g)	0.4	0.8	1.0	1.4
Number of umbels	8	15	7	14

Note. Values are treatment means. Variability estimates were not available in the study file.

Irrigation response. The 150-mL treatment produced the most balanced combination of root length and fresh- and dry-biomass accumulation in both substrates. The 200-mL treatment increased fresh biomass but reduced the dry-matter proportion, a pattern consistent with excessive moisture and restricted root-zone aeration. The reported analysis indicated treatment differences at $p < .05$. Substrate effects were reported for plant height ($p = .041$), root length ($p = .028$), fresh biomass ($p = .033$), and dry biomass ($p = .047$), while mineral nutrition affected the evaluated growth variables (reported p range = .011–.026). Because effect sizes and uncertainty intervals were not included in the available summary, these p values should be interpreted cautiously.

Relative volatile profile. Trans-anethole was the predominant identified compound in every reported extract (Table 2). Its relative peak area increased with mineral nutrition in soil (42.5% to 50.2%) and coconut coir (38.4% to 46.7%). Linalool, estragole, and anisaldehyde also showed higher relative peak areas under mineral nutrition, whereas limonene was slightly lower. The highest reported trans-anethole value occurred in mineral-treated soil. Coconut coir showed the highest limonene values. Estragole and methyl chavicol are synonyms; they are therefore presented as a single compound in Table 2 to prevent double-counting.

Table 2. Relative peak area (%) of selected compounds in ethanolic extracts of Pimpinella anisum L.

Compound	Chemical class	Soil, control	Soil, 17N + 32CaO + 1B	Coconut coir, control	Coconut coir, 17N + 32CaO + 1B
Limonene	Monoterpene	2.45	2.10	3.20	2.85
Linalool	Terpene alcohol	1.85	2.30	1.65	2.10
trans-Anethole	Phenylpropanoid	42.5	50.2	38.4	46.7
Estragole (methyl chavicol)	Phenylpropanoid	7.8	9.6	6.5	8.9
Anisaldehyde	Aromatic aldehyde	2.10	2.75	1.80	2.40

Note. Percentages are relative GC–MS peak areas, not absolute concentrations. Irrigation volume was not identified in the chromatographic summary. Estragole and methyl chavicol are the same compound and are reported once.

Discussion

The observed growth response to mineral nutrition is consistent with reports that macro- and micronutrient supply can increase plant height, biomass, umbel formation, and chemical constituents in anise and related Apiaceae crops (Khalid, 2012; Tavallali et al., 2017). Nitrogen supports photosynthetic capacity and vegetative growth, calcium contributes to cell-wall and membrane function, and boron is important for meristematic and reproductive development. Nevertheless, the present treatment combined these nutrients; the design therefore does not permit the individual contribution of calcium, nitrogen, or boron to be isolated.

The comparatively balanced response in coconut coir is biologically plausible because coir can provide favourable porosity, water-holding capacity, and root-zone aeration when irrigation and nutrient

ISSN: 2181-3337 | SCIENTISTS.UZ

supply are appropriately managed (Savvas & Gruda, 2018). The response at 200 mL also illustrates that greater irrigation volume does not necessarily improve dry-matter formation. In soilless production, the interaction between substrate water retention, aeration, and nutrient concentration must be managed carefully (Bugbee, 2004). The superiority of 150 mL should therefore be interpreted as specific to the pot, substrate, irrigation frequency, and greenhouse conditions used in this experiment.

The predominance of trans-anethole agrees with published analyses of anise fruits and essential oils (Dumitrescu et al., 2023; Reveglia et al., 2026; Spinozzi et al., 2023). Previous work also shows that cultivation year, location, fertilization, genotype, and other environmental variables can influence anise agronomic traits and volatile profiles (Pant et al., 2021; Pezo et al., 2022). However, the present samples were ethanolic extracts of aerial material rather than hydrodistilled fruit essential oil. Direct numerical comparison with essential-oil studies is therefore inappropriate. The reported values should be used to compare treatments within this experiment only.

Taken together, the results suggest a trade-off rather than a single universally superior cultivation treatment. Coconut coir with mineral nutrition produced a balanced combination of plant height, leaf number, and umbel number, whereas soil maintained greater root mass and, with mineral nutrition, the highest relative trans-anethole peak area. This distinction resolves the apparent inconsistency between agronomic and chromatographic outcomes and shows why “best treatment” must be defined in relation to the intended production objective.

Limitations and Future Directions

The experiment was conducted during one cultivation period at a single greenhouse site and used three biological replicates per treatment. The supplied manuscript did not report the seed source or cultivar, pot dimensions, substrate physicochemical properties, irrigation frequency, nutrient application rate, randomization procedure, or complete GC–MS operating programme. These omissions limit reproducibility. In addition, the tables contain treatment means without measures of variability, and the chromatographic summary does not identify the irrigation treatment used for each extract.

Future studies should report complete cultivation and analytical protocols, analyse fruit essential oil using validated hydrodistillation and GC–MS/GC–FID procedures, include internal or external standards where quantitative concentration is intended, and provide full factorial statistics with effect sizes and confidence intervals. Multi-season and multi-site trials should also evaluate water-use efficiency, nutrient-use efficiency, production costs, seed yield, essential-oil yield, and market quality before a cultivation regime is recommended for commercial greenhouse production in Uzbekistan.

Conclusion

Under the tested greenhouse conditions, substrate, irrigation volume, and mineral nutrition were associated with differences in the growth, productivity indicators, and relative volatile profile of *Pimpinella anisum L.* Mineral nutrition increased the reported plant height, leaf number, root mass, and umbel number in both soil and coconut coir. Among the four irrigation volumes, 150 mL produced the most balanced descriptive growth response, whereas 200 mL was associated with a lower dry-matter proportion. Trans-anethole was the predominant identified volatile constituent, and its highest relative peak area occurred in mineral-treated soil. Coconut coir combined with mineral nutrition provided the most balanced agronomic response rather than the highest value for every individual trait. These findings support further controlled trials but do not yet justify a definitive commercial recommendation without complete replication, uncertainty estimates, and economic assessment.

REFERENCES

1. Bugbee, B. (2004). Nutrient management in recirculating hydroponic culture. *Acta Horticulturae, 648*, 99–112. https://doi.org/10.17660/ActaHortic.2004.648.12

2. Dumitrescu, E., Muselin, F., Tîrziu, E., Folescu, M., Dumitrescu, C. S., Orboi, D. M., & Cristina, R. T. (2023). Pimpinella anisum L. essential oil—A valuable antibacterial and antifungal alternative. *Plants, 12*(13), 2428. https://doi.org/10.3390/plants12132428
3. Giordano, M., Petropoulos, S. A., Kyriacou, M. C., Graziani, G., Zarrelli, A., Rouphael, Y., & El-Nakhel, C. (2022). Nutritive and phytochemical composition of aromatic microgreen herbs and spices belonging to the Apiaceae family. *Plants, 11*(22), 3057. https://doi.org/10.3390/plants11223057
4. Khalid, K. A. (2012). Effect of NP and foliar spray on growth and chemical compositions of some medicinal Apiaceae plants grown in arid regions in Egypt. *Journal of Soil Science and Plant Nutrition, 12*(3), 581–596. https://doi.org/10.4067/S0718-95162012005000018
5. Pant, P., Pandey, S., & Dall'Acqua, S. (2021). The influence of environmental conditions on secondary metabolites in medicinal plants: A literature review. *Chemistry & Biodiversity, 18*(11), e2100345. https://doi.org/10.1002/cbdv.202100345
6. Pezo, L., Lončar, B., Šovljanski, O., Tomić, A., Travičić, V., Pezo, M., & Aćimović, M. (2022). Agricultural parameters and essential oil content composition prediction of aniseed, based on growing year, locality and fertilization type—An artificial neural network approach. *Life, 12*(11), 1722. https://doi.org/10.3390/life12111722
7. Reveglia, P., Barilli, E., Cobos, M. J., López-Orozco, M. C., & Rubiales, D. (2026). Characterization of Pimpinella anisum germplasm: Diversity available for agronomic performance and essential oil content and composition. *Agronomy, 16*(3), 285. https://doi.org/10.3390/agronomy16030285
8. Savvas, D., & Gruda, N. (2018). Application of soilless culture technologies in the modern greenhouse industry—A review. *European Journal of Horticultural Science, 83*(5), 280–293. https://doi.org/10.17660/eJHS.2018/83.5.2
9. Spinozzi, E., Zeni, V., Di Giovanni, F., Marmugi, M., Baldassarri, C., Mazzara, E., Ferrati, M., Ricciardi, R., Canale, A., Lucchi, A., Petrelli, R., Maggi, F., & Benelli, G. (2023). Aniseed, Pimpinella anisum, as a source of new agrochemicals: Phytochemistry and insights on insecticide and acaricide development. *Agriculture Communications, 1*(1), 100003. https://doi.org/10.1016/j.agrcom.2023.100003
10. Tavallali, V., Rahmati, S., & Bahmanzadegan, A. (2017). Antioxidant activity, polyphenolic contents and essential oil composition of Pimpinella anisum L. as affected by zinc fertilizer. *Journal of the Science of Food and Agriculture, 97*(14), 4883–4889. https://doi.org/10.1002/jsfa.8360

ISSN: 2181-3337 | SCIENTISTS.UZ

ISSN: 2181-3337 | SCIENTISTS.UZ VOLUME 5 ISSUE 7 JULY 2026

NEW UZBEKISTAN: THE EFFECTIVENESS OF ARTIFICIAL INTELLIGENCE-BASED DIGITAL TRANSFORMATION BY 2030

Gulyamov Saidakhror[1], **Mukhitdinova Munavvarkhon**[1]
Honored Scientist of Uzbekistan, Academician of the
Academy of Sciences of the Republic of Uzbekistan,
Doctor of Economics, Professor, KIMYO University, Tashkent
s.gulyamov@kiut.uz
DSc, Associate Professor, Department of Digital Economy,
Tashkent State University of Economics (TSUE)
munavvarkhon7@gmail.com

DOI: 10.67620/sai.57a0006

ABSTRACT
This article examines the effectiveness of Uzbekistan's artificial-intelligence (AI)-based digital transformation within the "New Uzbekistan" development paradigm. Drawing on official statistics and international rankings for 2020–2025, the study analyses changes in the E-Government Development Index (EGDI), growth in ICT service exports, the condition of digital infrastructure, and the country's AI-readiness indicators. The findings indicate substantial progress, including a rise to 63rd place in the 2024 EGDI, IT Park exports approaching USD 1 billion, and Uzbekistan's leading position in Central Asia in the Oxford Insights Government AI Readiness Index. However, the analysis also identifies persistent constraints, including an interregional digital divide, shortages of specialised skills, and the digital sector's still limited contribution to GDP. Three development scenarios to 2030 are proposed. Under the optimistic scenario, effective implementation of the national AI strategy could contribute an additional 2–3% to GDP growth.

ACCEPTED

31.07.26

Keywords: *digital transformation, artificial intelligence, EGDI, e-government, digital economy, ICT service exports, IT Park, "Digital Uzbekistan 2030", AI strategy, scenario forecasting.*

CC BY

1. INTRODUCTION: DIGITAL TRANSFORMATION AS A STRATEGIC PRIORITY

The global economy is undergoing a period of rapid technological change. According to the World Economic Forum's Future of Jobs Report 2025, structural changes in labour markets could create 170 million jobs and displace 92 million others by 2030 [7]. Generative artificial intelligence is expected to be a major driver of this transition, while broader digital access is likely to transform the organisation and operating models of many enterprises [8].

For Uzbekistan, this global transition presents both a strategic challenge and an opportunity. Through the "New Uzbekistan" development agenda and implementation of the "Digital Uzbekistan 2030" Strategy, approved by Presidential Decree No. PD-6079 of 5 October 2020 [1], the country has sought to strengthen its position in the regional digital economy. Evidence of this progress includes Uzbekistan's entry into the "very high" EGDI group in the 2024 United Nations survey and its leading position among Central Asian countries in the Oxford Insights Government AI Readiness Index.

This article systematically analyses the principal achievements and constraints of Uzbekistan's digital transformation using data for 2020–2025. It then applies a scenario-based approach to assess plausible development trajectories through 2030, with particular attention to the role of artificial intelligence.

2. THE LEGAL AND REGULATORY FRAMEWORK: LAWS AND PRESIDENTIAL DECREES ON AI

Uzbekistan's legal framework for artificial intelligence was progressively consolidated between 2020 and 2026. A chronological review of the relevant instruments shows a sustained policy commitment to making digitalisation a national development priority. The principal documents are outlined below.

- Presidential Decree No. PD-6079 of 5 October 2020, "On the Approval of the Digital Uzbekistan 2030 Strategy" [1], provides the foundational policy framework. It identifies five priority areas: digital infrastructure, e-government, the digital economy, the domestic digital-technology market, and IT education. The Strategy also establishes measurable targets, including entry into the top 30 of the UN EGDI, an increase in IT service exports to USD 5 billion, and the online delivery of all eligible public services.
- Presidential Resolution No. PR-358 of 14 October 2024, "On the Approval of the Strategy for the Development of Artificial Intelligence Technologies until 2030" [2], is the principal policy instrument devoted specifically to AI. It sets targets of USD 1.5 billion in AI-service revenue by 2030, the establishment of ten AI research laboratories, and entry into the top 50 of the Government AI Readiness Index. The Strategy is organised into three phases: the creation of baseline infrastructure and priority projects in 2024–2025; the scaling of AI in key sectors in 2026–2028; and commercialisation and achievement of the target indicators in 2028–2030.
- Presidential Decree No. PD-157 of 14 October 2024, "On Additional Measures to Support Export Activity in the Field of Digitalisation" [3], introduces incentives for IT-exporting companies, including tax preferences, simplified access to finance, and support for entering foreign markets.
- Presidential Decree No. PD-189 of 22 October 2025, "On Additional Measures for the Further Development of Artificial Intelligence Technologies" [4], establishes an Artificial Intelligence Cluster at New Uzbekistan University on a university–industry–partner model. It also introduces a register of AI entrepreneurship entities, increases state grants in IT and AI by 35% from the 2026/2027 academic year, and sets a target of training five million "AI leaders" by 2030, including 500,000 in 2026.
- Law of the Republic of Uzbekistan No. LRU-1115 of 21 January 2026, "On the Regulation of Relations Connected with the Use of Artificial Intelligence" [5], provides a dedicated statutory framework for AI. It defines AI as a technological solution that simulates human cognitive functions, establishes general principles for its use in information systems, and prohibits legally significant decisions affecting citizens' rights and freedoms from being made solely on the basis of AI outputs without human involvement.

Taken together, these instruments show that Uzbekistan moved within six years from broad strategic commitments towards a more developed regulatory architecture for AI. Importantly, the documents include measurable targets, designated implementation mechanisms, and provisions for institutional and financial support.

3. RESEARCH METHODOLOGY

The study uses a multilevel methodology comprising three components. First, it systematically reviews statistical data published by international organisations, including the United Nations, the World Bank, the International Monetary Fund, DataReportal, Oxford Insights, and the International Telecommunication Union, for 2018–2025. Second, it compares Uzbekistan's performance over time in the EGDI, the GovTech Maturity Index, and the Government AI Readiness Index, with Kazakhstan,

ISSN: 2181-3337 | SCIENTISTS.UZ

Azerbaijan, and Georgia used as regional benchmarks. Third, it develops conservative, baseline, and optimistic scenarios for the digital economy through 2030.

The evidence base was cross-checked against primary and institutional sources, including the technical annexes to the UN E-Government Survey 2024, DataReportal's Digital 2024: Uzbekistan report, the 2023 digital-economy overview published by the relevant national agency, and the official portals of the Ministry of Digital Technologies and IT Park Uzbekistan. Preference was given to sources published or updated between 2023 and 2025.

4. ANALYSIS OF THE CURRENT STATE: KEY STATISTICAL DATA

4.1. Digital infrastructure and internet penetration

According to Digital 2024: Uzbekistan, the country had 29.52 million internet users at the beginning of 2024, equivalent to 83.3% of a population of approximately 35.4 million [10]. Active mobile connections totalled 33.81 million, or 95.5% of the population. International telecommunications data indicate that mobile-broadband subscriptions exceeded the population total, while 96.2% of households had internet access [19]. Median fixed-broadband speed reached 79 Mbps, and median mobile speed reached 38 Mbps.

By 2024, 5G coverage was reported to have reached 18% of the population, while 4G coverage reached 97%. The length of fibre-optic communication lines exceeded 227,000 km in 2023. In the same year, communications and information services were valued at UZS 32.2 trillion, representing year-on-year growth of 24.6%; telecommunications accounted for 54.7% of that market [12, p. 14].

Table 1. Key digital-infrastructure indicators in Uzbekistan, 2018–2024

Indicator	2018	2020	2022	2024	Source
Internet penetration, %	48	65	76	83.3	DataReportal [10]
Mobile connections, % of pop.	n/a	90	93	95.5	ITU, 2024
ICT-services market, UZS trillion	n/a	16.1	25.8	32.2	AICT [12]
5G coverage, % of pop.	0	0	5	18	WorldData [2024]

Sources: DataReportal [10], AICT [12], ITU (2024), and WorldData (2024).

4.2. E-government: achievements of international scale

The trajectory of the United Nations E-Government Development Index provides one of the clearest indicators of Uzbekistan's digital progress. In 2024, the country rose from 69th to 63rd place, with an EGDI score of 0.7999, and entered the "very high EGDI" group [17]. It therefore exceeded, ahead of schedule, the interim score of 0.75 established under the "Digital Uzbekistan 2030" Strategy.

Uzbekistan's 2024 component scores were 0.87 for the Telecommunication Infrastructure Index, 0.76 for the Online Services Index, and 0.75 for the Human Capital Index. The relatively balanced profile suggests that progress was not confined to a single component of digital government. Within the Commonwealth of Independent States, Uzbekistan ranked behind Kazakhstan and Russia but ahead of Azerbaijan. By October 2024, the My.gov.uz portal offered 675 services, and the e-government mobile application reportedly had 2.5 million users.

Table 2. Uzbekistan's EGDI performance and strategic targets, 2018–2030

Year	Rank (of 193)	EGDI	EGDI group	Target indicator
2018	81	n/a	High	—
2020	87	n/a	High	—
2022	69	0.7265	High	0.75 by 2025
2024	63	0.7999	Very High ✓	Target met ahead of schedule
2030 (target)	≤30	>0.85 (est.)	Very High	Digital Uzbekistan 2030

Sources: UN E-Government Survey 2024 [17], Development Strategy Center of Uzbekistan [11], and the "Digital Uzbekistan 2030" Strategy [1].

ISSN: 2181-3337 | SCIENTISTS.UZ

4.3. The IT sector and exports: multifold growth over five years

Uzbekistan's IT sector has expanded rapidly. According to the World Bank, exports of IT-enabled services increased from USD 600,000 in 2017 to USD 140 million in 2022 [13]. Other official and industry sources report that exports associated with the IT sector rose from approximately USD 170 million in 2019 to nearly USD 1 billion in 2024 [15, 16]. By 2024, IT Park Uzbekistan had more than 2,800 resident companies, including 752 foreign enterprises, while the number of IT centres operating nationwide exceeded 300.

In the World Bank's 2022 GovTech Maturity Index, Uzbekistan moved up 37 positions compared with 2020 and entered Group A, which comprises countries with advanced public-sector digital-transformation systems [14]. The country also ranked highly in the digital-skills and public-sector-innovation component. In November 2025, the International Digital Technology Centre "Enterprise Uzbekistan" was established as a specialised digital hub intended to support international technology investment and cross-border services [16].

Table 3. Key indicators of Uzbekistan's IT sector and digital services, 2017–2024

Indicator	2017	2020	2022	2024	Source
IT-services export, USD million	0.6	170	344	~950	World Bank [13]; IT Park [15]
IT Park residents, companies	n/a	350	1,200	2,800+	IT Park UZ [15]
Foreign IT companies	n/a	n/a	320	752	IT Park UZ [15]
IT centres nationwide	n/a	80	200	300+	AICT [12]
ICT share of GDP, %	n/a	1.2	1.9	2.8*	World Bank [13]

Note. The 2024 ICT share of GDP is the authors' estimate based on reported growth between 2022 and 2024. Sources: World Bank [13], IT Park Uzbekistan [15], and AICT [12].

4.4. AI readiness: international assessment

The Oxford Insights Government AI Readiness Index 2024 places Uzbekistan ahead of the other Central Asian states [18]. Its Data and Infrastructure score was 62.14, while its Technology Sector score was 33.50. Uzbekistan also improved its position in global start-up-ecosystem rankings. Under the national AI Strategy to 2030 [2], the country aims to generate USD 1.5 billion in AI-service revenue and enter the top 50 of the global government AI-readiness ranking.

Digital financial services have also expanded. Available estimates indicate that fintech adoption reached 79% by 2024, digital payments accounted for more than 60% of consumer transactions, and the number of mobile-banking users exceeded ten million. These estimates should nevertheless be interpreted cautiously because published figures use different definitions of fintech activity and the digital sector.

5. DISCUSSION: ACHIEVEMENTS AND SYSTEMIC CONSTRAINTS

Taken together, the evidence indicates that Uzbekistan experienced rapid rather than incremental digital modernisation between 2018 and 2024. The country moved from 81st to 63rd place in the EGDI, recorded strong growth in IT-related exports, and substantially expanded digital public services. These developments were accompanied by a progressively more comprehensive regulatory framework. However, the scale and interpretation of some indicators vary across sources, and the reported achievements should therefore be assessed with attention to differences in definitions and measurement.

Several systemic constraints remain. First, the interregional digital divide continues to affect access and service quality, with Tashkent and the Tashkent Region generally better connected than several peripheral regions. Second, the ICT sector's direct share of GDP remains below the levels reported for some regional comparators, although estimates vary according to whether related industries are included. Third, shortages of advanced digital skills may restrict the pace of adoption. The World Economic Forum reports that skills gaps are a major obstacle to business transformation globally [8], and this challenge is also relevant to Uzbekistan despite the large-scale "One Million Uzbek Coders" programme. Finally, unequal participation by gender and region may limit the inclusiveness of digital development.

ISSN: 2181-3337 | SCIENTISTS.UZ

6. FORECAST TO 2030: SCENARIO ANALYSIS

Three scenarios for the development of Uzbekistan's digital economy through 2030 were formulated on the basis of current trends and the targets contained in official strategic documents. The scenarios combine trend extrapolation, analysis of regulatory benchmarks, and comparison with Kazakhstan, Georgia, and Romania. They should be interpreted as indicative development pathways rather than precise forecasts.

Table 4. Scenario forecast for Uzbekistan's digital economy through 2030

Indicator by 2030	Conservative scenario	Baseline scenario	Optimistic scenario (strategy targets)
Rank in the UN EGDI	50th–55th	40th–50th	≤30th
IT-services export, USD billion	1.5–2.0	2.5–3.5	5.0
ICT share of GDP, %	3.5–4.5	5–7	8–10
AI revenue, USD million	400–600	800–1,200	1,500+
Internet penetration, %	88–90	90–93	95+
Rank in AI Readiness (Oxford)	Top-80	Top-60	Top-50
AI leaders (thousand people)	2,000	3,500	5,000
Additional GDP growth from AI, %	0.8–1.2	1.5–2.0	2.0–3.0

Source: authors' calculations based on the UN E-Government Survey 2024 [17], PR-358 [2], AICT [12], Oxford Insights [18], and the WEF Future of Jobs Report 2025 [7].

The optimistic scenario assumes full implementation of the AI Strategy to 2030 [2], successful operation of the New Uzbekistan AI Cluster [4], effective functioning of Enterprise Uzbekistan as an international digital hub [16], and the training of five million "AI leaders" [4]. The baseline scenario assumes that current rates of digitalisation continue without a major qualitative shift. The conservative scenario assumes constrained public financing and slower institutional reform.

Four conditions are particularly important for the optimistic scenario: (1) sustained venture and public financing for AI start-ups; (2) the introduction of AI into public administration, healthcare, education, and other sectors in ways that produce measurable productivity gains; (3) investment to reduce interregional disparities in connectivity and digital skills; and (4) stronger integration into global digital value chains through Enterprise Uzbekistan and partnerships with international technology companies. Because the macroeconomic effects of AI remain uncertain, estimates of additional GDP growth should be treated as scenario assumptions rather than causal projections [6].

7. CONCLUSIONS AND RECOMMENDATIONS

1. Uzbekistan made substantial progress in digital transformation and entered the "very high EGDI" group in 2024, ranking 63rd with a score of 0.7999. Reaching the strategic objective of a top-30 position by 2030 will nevertheless require continued improvements in infrastructure, online services, and human capital.
2. The adoption of a dedicated AI law in 2026 strengthened the country's regulatory framework. Secondary legislation should clarify risk classification, human oversight, accountability, data governance, and enforcement in a manner consistent with internationally recognised principles for trustworthy AI.
3. IT-related exports increased rapidly between 2019 and 2024. Reaching the target of USD 5 billion by 2030 will require stronger support for exporting firms, including predictable tax administration, access to export finance, and assistance with entry into international markets under Decree No. PD-157 [3].
4. Enterprise Uzbekistan could improve the investment environment for foreign technology companies. Its institutional framework should provide clear rules for data-related and AI-related commercial disputes, including access to specialised digital arbitration or other efficient dispute-resolution mechanisms.

5. The interregional digital divide remains a structural risk. Regional digital roadmaps should be adopted for lagging areas, with annual monitoring of infrastructure, service use, digital skills, and affordability indicators.
6. The target of training five million “AI leaders” by 2030 is highly ambitious. Implementation should prioritise learning quality, assessment, and employability rather than enrolment numbers alone. Internationally recognised certification may help align training outcomes with labour-market requirements.
7. The expansion of fintech and digital payments provides a basis for applying AI in financial services. The Central Bank should consider a phased roadmap for regulatory technology and supervisory technology, supported by clear safeguards for consumer protection, cybersecurity, and responsible data use.
8. Unequal digital participation by gender may restrict the inclusiveness of the digital economy. IT-education and start-up support programmes should therefore monitor participation and outcomes by gender and introduce targeted measures where persistent gaps are identified.
9. The national target of USD 1.5 billion in AI-service revenue by 2030 appears achievable only if policy support is concentrated in sectors with strong data resources and clear demand. Potential priorities include precision agriculture, healthcare diagnostics, and logistics optimisation, with pilot projects evaluated for economic, social, and ethical effects [20].
10. The long-term success of digital transformation will depend on converting technological adoption into sustained productivity and income growth. Under the optimistic scenario, AI could contribute an additional 2–3 percentage points to GDP growth by 2030. This figure is an authors’ scenario estimate, not an observed causal effect, and depends on coordinated progress in infrastructure, e-government, markets, skills, and education.

REFERENCES

Legislative and regulatory acts

[1] Decree of the President of the Republic of Uzbekistan No. PD-6079 of 5 October 2020, “On the Approval of the Digital Uzbekistan 2030 Strategy”. URL: https://lex.uz/docs/5031048

[2] Resolution of the President of the Republic of Uzbekistan No. PR-358 of 14 October 2024, “On the Approval of the Strategy for the Development of Artificial Intelligence Technologies until 2030”. URL: https://lex.uz/docs/7073446

[3] Decree of the President of the Republic of Uzbekistan No. PD-157 of 14 October 2024, “On Additional Measures to Support Export Activity in the Field of Digitalisation”. URL: https://lex.uz/docs/7073445

[4] Decree of the President of the Republic of Uzbekistan No. PD-189 of 22 October 2025, “On Additional Measures for the Further Development of Artificial Intelligence Technologies”. URL: https://lex.uz/ru/docs/7790236

[5] Law of the Republic of Uzbekistan No. LRU-1115 of 21 January 2026, “On the Regulation of Relations Connected with the Use of Artificial Intelligence”. URL: https://lex.uz/ru/docs/8011377

International organisations and analytical sources

[6] Acemoglu, D. (2024). What do we know about the economics of AI? MIT Economics. URL: https://economics.mit.edu/news/daron-acemoglu-what-do-we-know-about-economics-ai

[7] World Economic Forum. (2025). Future of Jobs Report 2025. Geneva: World Economic Forum. URL: https://www.weforum.org/publications/the-future-of-jobs-report-2025

[8] World Economic Forum. (2025, January 8). Future of Jobs Report 2025: 78 million new job opportunities by 2030. URL: https://www.weforum.org/press/2025/01/future-of-jobs-report-2025

[9] Gigerenzer, G. (2025). The legacy of Daniel Kahneman: A personal view. Erasmus Journal for Philosophy and Economics, 18(1), 28–61.

[10] DataReportal. (2024). Digital 2024: Uzbekistan. URL: https://datareportal.com/reports/digital-2024-uzbekistan
[11] Development Strategy Center of Uzbekistan. (n.d.). Digital Uzbekistan 2030: Progress and rankings. URL: https://strategy.uz/index.php?lang=en&news=2170
[12] Agency for Information and Communication Technologies. (2023). Uzbekistan: Digital Economy Overview—Vision 2030. Tashkent. URL: https://aict.uz/caict_uzbekistan_digital_economy_overview_vision_2030.pdf
[13] World Bank. (2023, November 30). World Bank to support Uzbekistan in developing the digital economy. URL: https://www.worldbank.org/en/news/press-release/2023/11/30
[14] E-Government Development Center of Uzbekistan. (n.d.). GovTech Maturity Index 2022: Uzbekistan moved up by 37 positions. URL: https://e-gov.uz/en/achievements
[15] The Asia Today. (n.d.). Digital transformation of Uzbekistan promotes regional integration in Central Asia. URL: https://theasiatoday.org/news/digital-transformation-of-uzbekistan
[16] IT Park Uzbekistan. (2025). Uzbekistan launched the international Enterprise Uzbekistan Center. URL: https://it-park.uz/en/itpark/news/uzbekistan-launched-the-international-enterprise-uzbekistan-center
[17] United Nations. (2024). E-Government Survey 2024: Accelerating digital transformation for sustainable development. New York: United Nations Department of Economic and Social Affairs.
[18] Oxford Insights. (2024). Government AI Readiness Index 2024. Oxford: Oxford Insights.
[19] Freedom House. (2024). Freedom on the Net 2024: Uzbekistan. Washington, DC: Freedom House.
[20] United Nations Development Programme. (2022). Supporting sustainable agriculture and water efficiency in Uzbekistan. New York: UNDP.

ISSN: 2181-3337 | SCIENTISTS.UZ VOLUME 5 ISSUE 7 JULY 2026

INFLUENCE OF SOURCE TEMPERATURE ON THE COMPOSITION, MORPHOLOGY, AND ELECTRICAL CONDUCTIVITY OF Sb_xSe_γ THIN FILMS PREPARED BY VAPOR TRANSPORT DEPOSITION

Quchqarov K, Ergashev B, Pirimmatov M, MatmuratovA*, Gulumbaev B, To'liboyeva X

[1]S.A. Azimov Physics-Technical Institute, Academy of Sciences of the Republic of Uzbekistan, 2B Chingiz Aitmatov Street, Tashkent 100084, Uzbekistan.

*Corresponding author: e-mail: matmuratovajdos@gmail.com

DOI: 10.67620/sai.57a0007

ABSTRACT

Sb_xSe_γ thin films were deposited on Mo-coated soda-lime glass by vapor transport deposition while the substrate temperature was held at 400 °C and the source temperature was varied from 500 to 550 °C. Energy-dispersive X-ray spectroscopy showed a systematic composition shift from Se-rich (Sb/Se = 0.508) at 500 °C to near-stoichiometric (Sb/Se = 0.669) at 525 °C and Sb-rich (Sb/Se = 0.825) at 550 °C. The film thickness increased from 1.732 to 6.291 μm over the same temperature range. Surface and cross-sectional scanning electron microscopy indicated progressive grain coarsening; the 525 °C film displayed the most continuous columnar morphology, whereas the 550 °C film was thicker and rougher with less uniform grain alignment. Hot-probe measurements indicated p-type behavior for the Se-rich film, weak p-type behavior for the near-stoichiometric film, and n-type behavior for the Sb-rich film. The reported room-temperature conductivity was lowest for the near-stoichiometric sample (1.14×10^{-5} S m^{-1}) and highest for the Sb-rich sample (1.89×10^{-4} S m^{-1}). These results demonstrate that source temperature strongly affects composition, microstructure, and carrier polarity. Individual point defects are not assigned because the available measurements do not provide defect-specific identification.

ACCEPTED

05.08.26

Keywords: *antimony selenide; Sb_xSe_γ thin films; vapor transport deposition; source temperature; composition; scanning electron microscopy; electrical conductivity; carrier polarity.*

CC BY

1. Introduction

Thin-film photovoltaics require absorber materials that combine strong optical absorption, suitable band gaps, low toxicity, elemental abundance, and scalable processing. Established absorbers such as crystalline silicon, CdTe, and $Cu(In,Ga)Se_2$ have reached high conversion efficiencies, but their manufacturing cost, toxicity, or reliance on scarce elements continues to motivate research on alternative compounds (Green et al., 2021; Scheer & Schock, 2011; Zakutayev, 2017). Antimony selenide (Sb_2Se_3) is attractive in this context because it has a band gap of approximately 1.1–1.3 eV, an absorption coefficient above 10^5 cm^{-1} in the visible range, comparatively low toxicity, and a binary composition based on relatively abundant elements (Chen et al., 2017a; Lei et al., 2019; Mavlonov et al., 2020).

Sb_2Se_3 has an orthorhombic quasi-one-dimensional structure composed of covalently bonded $[Sb_4Se_6]_n$ ribbons. Inter-ribbon bonding is substantially weaker than bonding within the ribbons, producing pronounced structural and transport anisotropy (Wang et al., 2022). Film orientation, grain morphology, interface energetics, and defect populations therefore have strong effects on charge transport and recombination (Hutter et al., 2018; Kondrotas et al., 2019; Li et al., 2019a; Williams et al., 2020). Vapor-phase methods are particularly useful because they permit control over source flux, substrate temperature, thickness, and columnar growth (Wang et al., 2017; Wen et al., 2017; Zhou et al., 2015).

The electrical behavior of Sb_2Se_3 is sensitive to the relative chemical potentials of Sb and Se. Theoretical and experimental studies show that changes in composition and growth conditions can alter carrier polarity and defect compensation (Hobson et al., 2020; Huang et al., 2019, 2021; Liu et al., 2017; Savory & Scanlon, 2019). Recent work has demonstrated composition-controlled n-type and p-type behavior in thermally evaporated Sb_2Se_3 and has used this response to form an internal homojunction (Yang et al., 2026). At the same time, direct identification of individual vacancy defects requires defect-sensitive techniques such as positron annihilation spectroscopy, deep-level transient spectroscopy, or related measurements; composition, SEM, and hot-probe tests alone cannot uniquely identify a specific intrinsic defect (Keeble et al., 2026).

This study examines how source temperature affects the composition, thickness, morphology, room-temperature conductivity, and qualitative carrier polarity of Sb_xSe_γ films deposited at a constant substrate temperature. The analysis is restricted to quantities directly supported by EDS, SEM, hot-probe, and room-temperature conductivity measurements. Specific point-defect identities are discussed only as possible mechanisms reported in the literature and are not treated as experimentally identified in the present samples.

2. Experimental section

2.1 Substrate preparation and film deposition

Soda-lime glass substrates measuring 2 × 2 cm were cleaned sequentially with acetone and ethanol, treated ultrasonically for 10 min, and dried under nitrogen. Molybdenum back-contact layers approximately 1 μm thick were deposited by magnetron sputtering. The sputtering system was evacuated to a reported pressure of 10^{-5} Torr before argon was introduced, and deposition was performed at 120 W. Because the original laboratory record did not distinguish base pressure from working pressure, the 10^{-5} Torr value is reported here as the pre-deposition evacuation pressure.

Sb_xSe_γ films were deposited on glass/Mo substrates using a vapor transport arrangement in which the source and substrate zones were temperature controlled independently. The substrates were mounted in graphite holders and rotated at 2 min^{-1}. The chamber was initially evacuated to 1.3 Pa and then filled with argon to 7 Pa. The substrate temperature was held at 400 °C. The Sb_2Se_3 source temperature was set to 500, 525, or 550 °C, and each deposition lasted 10 min. The resulting samples were designated M54, M55, and M53, respectively.

2.2 Compositional and morphological characterization

Elemental composition was measured by energy-dispersive X-ray spectroscopy (EDS; AzTec Advanced, Oxford Instruments). Surface morphology and cross-sectional thickness were examined by scanning electron microscopy (SEM; JEOL JSM-IT510). The reported thicknesses were obtained from cross-sectional images. Because replicate deposition runs and measurement uncertainties were not included in the supplied dataset, the results are presented descriptively and no inferential statistics are applied.

2.3 Electrical characterization and scope of data analysis

Room-temperature specific conductivity was measured using the reported sandwich configuration with a Keithley SM2460 SourceMeter. Qualitative carrier polarity was evaluated by the hot-probe method. The supplied manuscript also contained temperature-dependent conductivity measurements obtained in a

cryostat; however, the plotted ordinate, conductivity units, and reported activation-energy conversion were internally inconsistent and could not be reconciled without the original instrument files. Those activation energies and associated point-defect assignments are therefore excluded from the quantitative results of this revised paper. Reanalysis of the raw current–voltage and temperature data is required before activation energies can be reported reliably.

3. Results and discussion

3.1 Composition and film thickness

The EDS spectra in Figure 1 show the principal Sb and Se signals for all three samples. Increasing the source temperature produced a systematic decrease in the Se atomic fraction and an increase in the Sb/Se ratio (Table 1). The film deposited at 500 °C was Se-rich, with 33.7 at.% Sb and 66.3 at.% Se (Sb/Se = 0.508). At 525 °C, the composition was close to stoichiometric Sb_2Se_3, with 40.1 at.% Sb and 59.9 at.% Se (Sb/Se = 0.669, compared with the ideal ratio 2/3). At 550 °C, the film became Sb-rich, with 45.2 at.% Sb and 54.8 at.% Se (Sb/Se = 0.825).

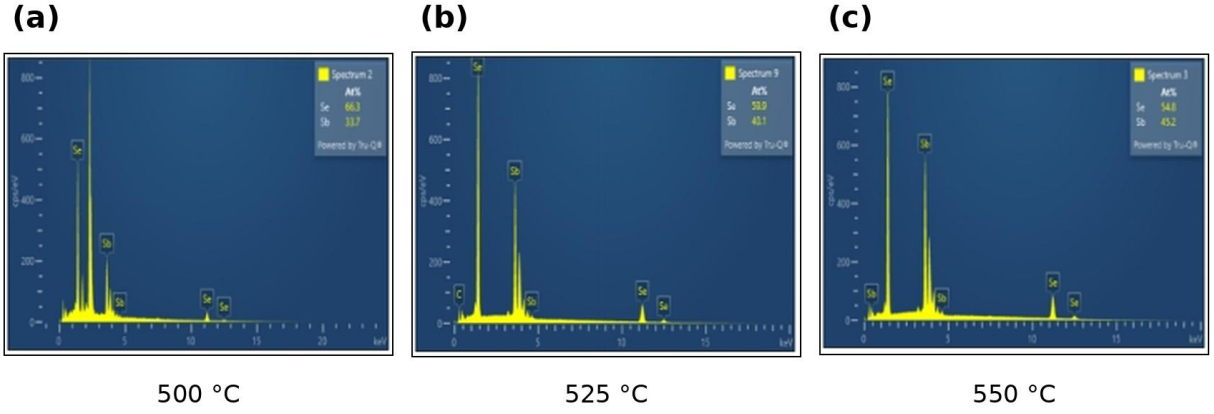


Figure 1. ***Energy-dispersive X-ray spectroscopy spectra of Sb_xSe_γ films deposited at source temperatures of (a) 500 °C, (b) 525 °C, and (c) 550 °C. The substrate temperature was fixed at 400 °C.***

Table 1.

Elemental composition and thickness of Sb_xSe_γ films deposited at different source temperatures.

Sample	Substrate T (°C)	Source T (°C)	Evaporated source mass (mg)	Thickness (μm)	Sb (at.%)	Se (at.%)	Sb/Se
M54	400	500	143.6	1.732	33.7	66.3	0.5083
M55	400	525	224.2	3.276	40.1	59.9	0.6694
M53	400	550	363.6	6.291	45.2	54.8	0.8248

The thickness increased from 1.732 μm at 500 °C to 3.276 μm at 525 °C and 6.291 μm at 550 °C. This trend is consistent with a higher vapor flux and greater material delivery to the substrate as the source temperature increases. The concurrent change in composition indicates that Sb and Se were not transported and incorporated in a fixed stoichiometric ratio over the full temperature range.

The change from Se-rich to Sb-rich composition may reflect differences in the volatility, transport, re-evaporation, and incorporation kinetics of Sb- and Se-containing species. Selenium loss is often enhanced at elevated temperature because of its higher volatility. Nevertheless, EDS alone cannot establish whether the measured off-stoichiometry is accommodated as point defects within single-phase Sb_2Se_3 or partly reflects elemental segregation, secondary phases, surface oxidation, or measurement uncertainty. Phase identification by X-ray diffraction and Raman spectroscopy is therefore required before the films can be described conclusively as phase-pure Sb_2Se_3.

ISSN: 2181-3337 | SCIENTISTS.UZ

3.2 Surface and cross-sectional morphology

Surface SEM images (Figure 2) show a clear increase in characteristic grain dimensions with source temperature. The 500 °C film consists of densely packed, fine rod-like grains with relatively random orientations. At 525 °C, the grains are larger and more compact, with improved surface coverage. At 550 °C, further grain coarsening is visible, together with a rougher surface and more pronounced faceting. The observed nanorod length increases from approximately 0.3 μm in the lowest-temperature sample to about 2 μm in the highest-temperature sample.

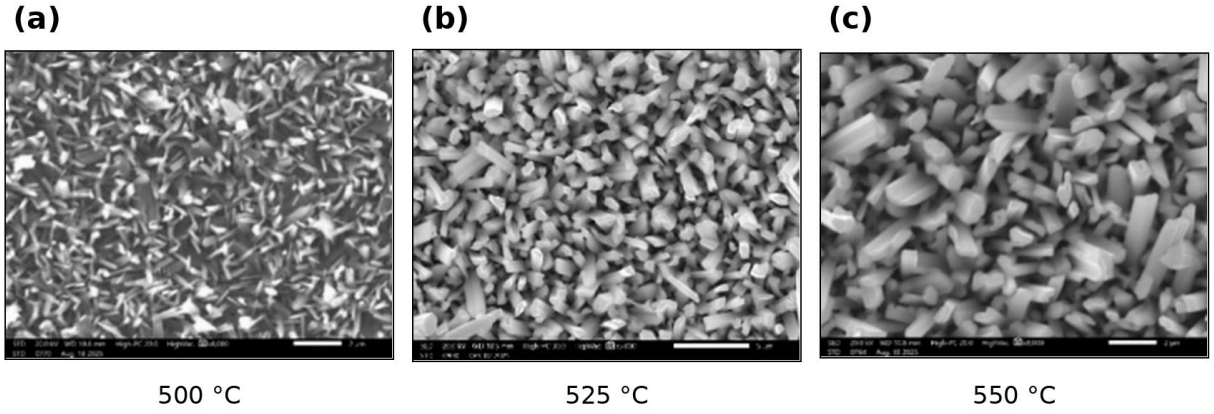


Figure 2. ***Surface SEM images of Sb_xSe_y films deposited at source temperatures of (a) 500 °C, (b) 525 °C, and (c) 550 °C. The substrate temperature was fixed at 400 °C.***

Cross-sectional SEM images and EDS depth profiles are presented in Figure 3. The M54 film is the thinnest and contains fine grains that appear predominantly laterally developed. The M55 film shows a more continuous columnar morphology through the absorber thickness. The M53 film contains the largest grains and is substantially thicker, but the columns are less uniformly aligned and the surface is rougher. These observations indicate that increasing source temperature enhances material flux and grain growth, whereas the highest temperature also coincides with substantial compositional deviation from Sb_2Se_3 stoichiometry.

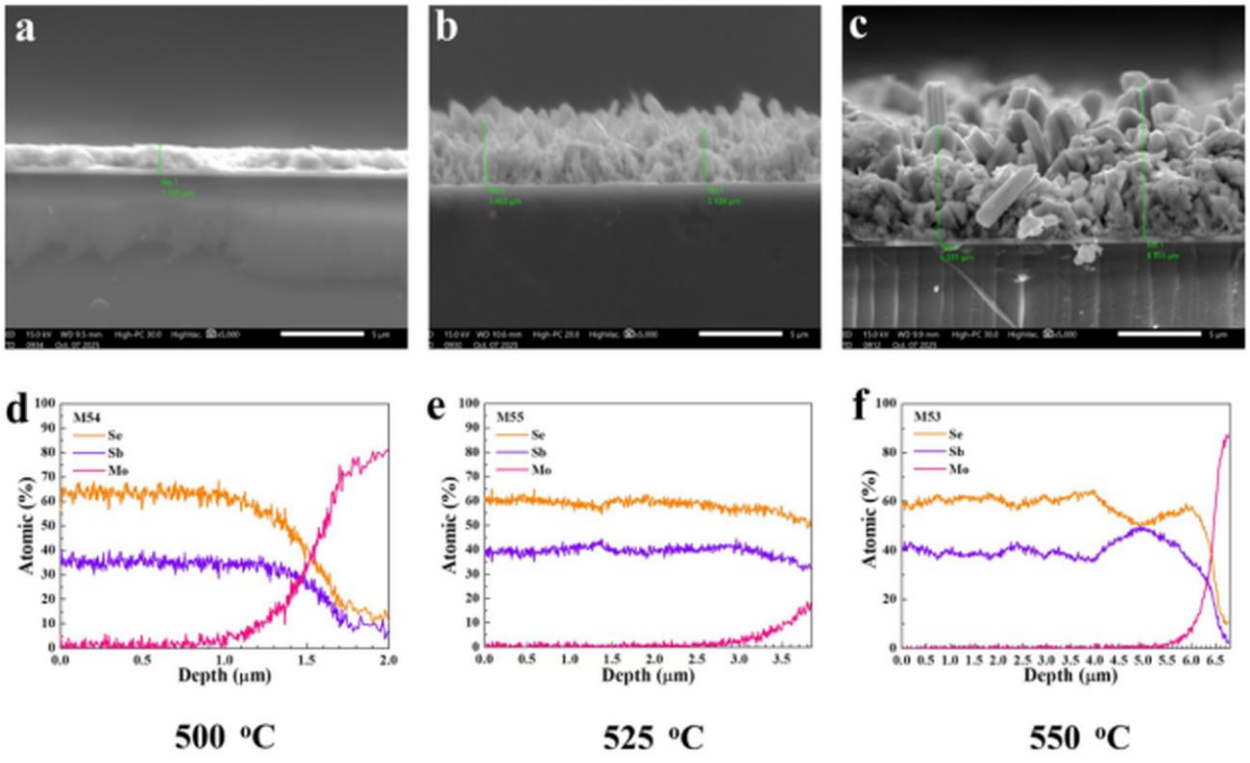


Figure 3. ***Cross-sectional SEM images (a–c) and corresponding EDS depth profiles (d–f) of Sb_xSe_y films deposited at source temperatures of 500, 525, and 550 °C, respectively.***

ISSN: 2181-3337 | SCIENTISTS.UZ

The depth profiles indicate Se-rich composition across most of the M54 layer and a comparatively uniform near-stoichiometric distribution in M55. M53 is Sb-rich and shows greater compositional variation near the upper part of the film. The profiles also show the transition from the absorber layer to the underlying Mo contact. Quantitative interpretation should remain cautious because spatial resolution, interaction volume, surface roughness, and detector geometry can affect EDS depth profiles.

The 525 °C condition provides the best balance within the present dataset: its composition is closest to stoichiometric Sb_2Se_3 and its cross section is the most continuously columnar. The 550 °C condition produces larger grains and a thicker film, but these features are accompanied by greater Sb enrichment and less uniform alignment. Grain enlargement alone therefore should not be interpreted as improved absorber quality.

3.3 Room-temperature conductivity and carrier polarity

The reported room-temperature conductivity and hot-probe results are summarized in Table 2. The Se-rich sample M54 exhibited p-type behavior and a conductivity of 6.57×10^{-5} S m^{-1}. The near-stoichiometric sample M55 showed weak p-type behavior and the lowest conductivity, 1.14×10^{-5} S m^{-1}. The Sb-rich sample M53 exhibited n-type behavior and the highest conductivity, 1.89×10^{-4} S m^{-1}. Conductivity therefore does not vary monotonically with Se content: it reaches a minimum near stoichiometry and rises under the Sb-rich condition.

Table 2.

Reported room-temperature electrical properties of the Sb_xSe_γ films.

Sample	Sb/Se	Composition category	Carrier polarity (hot probe)	Conductivity, σ (S m^{-1})
M54	0.5083	Se-rich	p-type	6.57×10^{-5}
M55	0.6694	Near-stoichiometric	weak p-type	1.14×10^{-5}
M53	0.8248	Sb-rich	n-type	1.89×10^{-4}

The polarity change across the composition series is qualitatively consistent with the broader evidence that Sb/Se chemical potentials can influence intrinsic doping and carrier type in Sb_2Se_3 (Hobson et al., 2020; Yang et al., 2026). However, the present hot-probe measurements are qualitative and do not provide carrier concentration or mobility. Hall-effect measurements are needed to confirm carrier polarity, carrier density, and mobility, while temperature-dependent Hall measurements would help distinguish intrinsic transport from grain-boundary and contact effects.

The low conductivity of the near-stoichiometric film should not be described simply as evidence of an intrinsic semiconductor, because conductivity depends jointly on carrier concentration, mobility, compensation, grain boundaries, and contact geometry. Likewise, the higher conductivity of the Sb-rich film does not by itself demonstrate a particular donor defect. Possible contributions include intrinsic point defects, secondary phases, compositional inhomogeneity, and improved or altered contact behavior.

3.4 Interpretation limits and requirements for defect identification

The original manuscript assigned individual activation energies to Se-on-Sb antisites, Sb-on-Se antisites, and Sb or Se vacancies. Such assignments are not retained here because EDS, SEM, hot-probe measurements, and bulk conductivity are not defect-specific. Modern studies show that the defect chemistry of Sb_2Se_3 is complex, that inequivalent lattice sites can produce different transition levels, and that theoretical assignments can change with the assumed defect configuration (Huang et al., 2019; Savory & Scanlon, 2019; Keeble et al., 2026).

A defensible defect analysis would require, at minimum, verified phase purity, reproducible temperature-dependent transport data, and a method sensitive to electronic or structural defect states. Appropriate approaches include Hall measurements, deep-level transient spectroscopy, temperature-dependent admittance spectroscopy, photoluminescence, X-ray photoelectron spectroscopy, and positron annihilation spectroscopy. These measurements could then be compared with current first-principles

ISSN: 2181-3337 | SCIENTISTS.UZ

calculations. Until such evidence is available, the present results support a composition-dependent change in carrier polarity but not the unique identification of a particular point defect.

The dataset also contains one reported sample for each source temperature and does not include uncertainties from replicate deposition runs. The trends are therefore descriptive. Replicate films, multiple EDS locations, thickness error bars, quantitative grain-size distributions, and repeated electrical measurements are required to establish reproducibility and support statistical comparison.

4. Conclusion

Varying the source temperature from 500 to 550 °C at a constant substrate temperature of 400 °C produced systematic changes in Sb_xSe_γ film composition, thickness, morphology, and electrical behavior. The Sb/Se ratio increased from 0.508 to 0.825, while the film thickness increased from 1.732 to 6.291 μm. The 525 °C film was closest to Sb_2Se_3 stoichiometry and exhibited the most continuous columnar morphology, but it also had the lowest reported room-temperature conductivity. The 500 °C Se-rich film was p-type, whereas the 550 °C Sb-rich film was n-type and had the highest conductivity. These findings show that source temperature can be used to tune composition and carrier polarity in vapor-deposited Sb_xSe_γ films. The results do not, however, uniquely identify individual point defects or establish phase purity. Future work should combine replicate depositions with XRD or Raman analysis, quantitative Hall measurements, verified temperature-dependent transport, and defect-sensitive spectroscopy.

Funding

This work was supported by the Belarusian Republican Foundation for Fundamental Research (Grant No. F25UZBG-109).

REFERENCES

1. Chen, C., Bobela, D. C., Yang, Y., Lu, S., Zeng, K., Ge, C., Yang, B., Gao, L., Zhao, Y., Beard, M. C., & Tang, J. (2017a). Characterization of basic physical properties of Sb_2Se_3 and its relevance for photovoltaics. Frontiers of Optoelectronics, 10(1), 18–30. https://doi.org/10.1007/s12200-017-0702-z
2. Chen, C., Wang, L., Gao, L., Nam, D., Li, D., Li, K., Zhao, Y., Ge, C., Cheong, H., Liu, H., Song, H., & Tang, J. (2017b). 6.5% certified efficiency Sb_2Se_3 solar cells using a PbS colloidal quantum dot film as a hole-transporting layer. ACS Energy Letters, 2(9), 2125–2132. https://doi.org/10.1021/acsenergylett.7b00648
3. Dong, J., Liu, Y., Wang, Z., & Zhang, Y. (2021). Boosting V_OC of antimony chalcogenide solar cells: A review on interfaces and defects. Nano Select, 2(10), 1818–1848. https://doi.org/10.1002/nano.202000288
4. Gharibshahian, I., Orouji, A. A., & Sharbati, S. (2020). Towards high-efficiency Cd-free Sb_2Se_3 solar cells by band-alignment optimization. Solar Energy Materials and Solar Cells, 212, 110581. https://doi.org/10.1016/j.solmat.2020.110581
5. Ghosh, S., Moreira, M. V. B., Fantini, C., & González, J. C. (2020). Growth and optical properties of nanocrystalline Sb_2Se_3 thin films for application in solar cells. Solar Energy, 211, 613–621. https://doi.org/10.1016/j.solener.2020.10.001
6. Green, M. A., Dunlop, E. D., Hohl-Ebinger, J., Yoshita, M., Kopidakis, N., & Hao, X. (2021). Solar cell efficiency tables (version 57). Progress in Photovoltaics: Research and Applications, 29(1), 3–15. https://doi.org/10.1002/pip.3371
7. Hobson, T. D. C., Phillips, L. J., Hutter, O. S., Durose, K., & Major, J. D. (2020). Defect properties of Sb_2Se_3 thin-film solar cells and bulk crystals. Applied Physics Letters, 116(26), 261101. https://doi.org/10.1063/5.0012697
8. Huang, M., Cai, Z., Wang, S., Gong, X., Wei, S., & Chen, S. (2021). More Se vacancies in Sb_2Se_3 under Se-rich conditions: An abnormal behavior induced by defect correlation in compensated compound semiconductors. Small, 17(36), 2102429. https://doi.org/10.1002/smll.202102429

9. Huang, M., Xu, P., Han, D., Tang, J., & Chen, S. (2019). Complicated and unconventional defect properties of the quasi-one-dimensional photovoltaic semiconductor Sb_2Se_3. ACS Applied Materials & Interfaces, 11(17), 15564–15572. https://doi.org/10.1021/acsami.9b01220
10. Hutter, O. S., Phillips, L. J., Durose, K., & Major, J. D. (2018). 6.6% efficient antimony selenide solar cells using grain-structure control and an organic contact layer. Solar Energy Materials and Solar Cells, 188, 177–181. https://doi.org/10.1016/j.solmat.2018.09.004
11. Keeble, D. J., Hobson, T. D. C., Wiktor, J., Berger, E., Dickmann, M., Elsharkawy, M. R. M., Egger, W., Major, J. D., & Durose, K. (2026). Detection and identification of vacancy defects in antimony selenide. Nature Communications, 17, 1413. https://doi.org/10.1038/s41467-025-68153-x
12. Kondrotas, R., Zhang, J., Wang, C., & Tang, J. (2019). Growth mechanism of Sb_2Se_3 thin films for photovoltaic application by vapor transport deposition. Solar Energy Materials and Solar Cells, 199, 16–23. https://doi.org/10.1016/j.solmat.2019.04.024
13. Lei, H., Chen, J., Tan, Z., & Fang, G. (2019). Review of recent progress in antimony chalcogenide-based solar cells: Materials and devices. Solar RRL, 3(6), 1900026. https://doi.org/10.1002/solr.201900026
14. Li, G., Li, Z., Liang, X., Guo, C., Shen, K., & Mai, Y. (2019a). Improvement in Sb_2Se_3 solar-cell efficiency through band-alignment engineering at the buffer/absorber interface. ACS Applied Materials & Interfaces, 11(1), 828–834. https://doi.org/10.1021/acsami.8b17611
15. Li, Z., Liang, X., Li, G., Liu, H., Zhang, H., Guo, J., Chen, J., Shen, K., San, X., Yu, W., Schropp, R. E. I., & Mai, Y. (2019b). 9.2%-efficient core-shell structured antimony selenide nanorod-array solar cells. Nature Communications, 10, 125. https://doi.org/10.1038/s41467-018-07903-6
16. Liang, G.-X., Luo, Y.-D., Chen, S., Tang, R., Zheng, Z.-H., Li, X.-J., Liu, X.-S., Liu, Y.-K., Li, Y.-F., Chen, X.-Y., Su, Z.-H., Zhang, X.-H., Ma, H.-L., & Fan, P. (2020). Sputtered and selenized Sb_2Se_3 thin-film solar cells with open-circuit voltage exceeding 500 mV. Nano Energy, 73, 104806. https://doi.org/10.1016/j.nanoen.2020.104806
17. Liu, X., Xiao, X., Yang, Y., Xue, D.-J., Li, D.-B., Chen, C., Lu, S., Gao, L., He, Y., Beard, M. C., Wang, G., Chen, S., & Tang, J. (2017). Enhanced Sb_2Se_3 solar-cell performance through theory-guided defect control. Progress in Photovoltaics: Research and Applications, 25(10), 861–870. https://doi.org/10.1002/pip.2900
18. Mavlonov, A., Razykov, T., Raziq, F., Gan, J., Chantana, J., Kawano, Y., Nishimura, T., Wei, H., Zakutayev, A., Minemoto, T., Zu, X., Li, S., & Qiao, L. (2020). A review of Sb_2Se_3 photovoltaic absorber materials and thin-film solar cells. Solar Energy, 201, 227–246. https://doi.org/10.1016/j.solener.2020.03.009
19. Savory, C. N., & Scanlon, D. O. (2019). The complex defect chemistry of antimony selenide. Journal of Materials Chemistry A, 7(17), 10739–10744. https://doi.org/10.1039/C9TA02022E
20. Scheer, R., & Schock, H.-W. (2011). Chalcogenide photovoltaics: Physics, technologies, and thin-film devices. Wiley-VCH. https://doi.org/10.1002/9783527633708
21. Wang, L., Li, D.-B., Li, K., Chen, C., Deng, H.-X., Gao, L., Zhao, Y., Jiang, F., Li, L., Huang, F., He, Y., Song, H., Niu, G., & Tang, J. (2017). Stable 6%-efficient Sb_2Se_3 solar cells with a ZnO buffer layer. Nature Energy, 2, 17046. https://doi.org/10.1038/nenergy.2017.46
22. Wang, X., Li, Z., Kavanagh, S. R., Ganose, A. M., & Walsh, A. (2022). Lone-pair-driven anisotropy in antimony chalcogenide semiconductors. Physical Chemistry Chemical Physics, 24(12), 7195–7202. https://doi.org/10.1039/D1CP05373F
23. Wen, X., He, Y., Chen, C., Liu, X., Wang, L., Yang, B., Leng, M., Song, H., Zeng, K., Li, D., Li, K., Gao, L., & Tang, J. (2017). Magnetron-sputtered ZnO buffer layer for Sb_2Se_3 thin-film solar cells. Solar Energy Materials and Solar Cells, 172, 74–81. https://doi.org/10.1016/j.solmat.2017.07.014

ISSN: 2181-3337 | SCIENTISTS.UZ

24. Wijesinghe, U., Longo, G., & Hutter, O. S. (2023). Defect engineering in antimony selenide thin-film solar cells. Energy Advances, 2(1), 12–33. https://doi.org/10.1039/D2YA00232A
25. Williams, R. E., Ramasse, Q. M., McKenna, K. P., Phillips, L. J., Yates, P. J., Hutter, O. S., Durose, K., Major, J. D., & Mendis, B. G. (2020). Evidence for self-healing benign grain boundaries and a highly defective Sb_2Se_3–CdS interfacial layer in Sb_2Se_3 thin-film photovoltaics. ACS Applied Materials & Interfaces, 12(19), 21730–21738. https://doi.org/10.1021/acsami.0c03690
26. Yang, J., Li, J., Sheng, S., Cai, Z., Li, K., Ruan, Z., Che, B., Tang, R., & Chen, T. (2026). Internal homojunction Sb_2Se_3 solar cell. Nature Photonics, 20, 644–652. https://doi.org/10.1038/s41566-026-01888-1
27. Zakutayev, A. (2017). Brief review of emerging photovoltaic absorbers. Current Opinion in Green and Sustainable Chemistry, 4, 8–15. https://doi.org/10.1016/j.cogsc.2017.01.002
28. Zhou, Y., Wang, L., Chen, S., Qin, S., Liu, X., Chen, J., Xue, D.-J., Luo, M., Cao, Y., Cheng, Y., Sargent, E. H., & Tang, J. (2015). Thin-film Sb_2Se_3 photovoltaics with oriented one-dimensional ribbons and benign grain boundaries. Nature Photonics, 9(6), 409–415. https://doi.org/10.1038/nphoton.2015.78

ISSN: 2181-3337 | SCIENTISTS.UZ VOLUME 5 ISSUE 7 JULY 2026

MODEL-BASED ASSESSMENT OF A 60 W MONOCRYSTALLINE PHOTOVOLTAIC MODULE AND TWO THREE-MODULE CONFIGURATIONS UNDER HOT-SUMMER CONDITIONS IN TERMEZ, UZBEKISTAN

Yuldoshov Boysori[1], **Kholmuminov Asadbek**[2]

[1]Termez State University, Uzbekistan;
[2]Specialized School of Jarkurgan District, Uzbekistan;
Manuscript type: modeling and simulation study

DOI: 10.67620/sai.57a0008

ABSTRACT

This study presents a reproducible model-based assessment of a representative 60 W monocrystalline photovoltaic module and two 180 W three-module array configurations under a prescribed hot-summer day in Termez, Uzbekistan. Solar position was calculated at 15-minute resolution for 13 July 2026 using the site coordinates (37.22° N, 67.28° E) and local civil time (UTC+5). Clear-sky global horizontal irradiance was estimated with the Haurwitz model, separated into direct and diffuse components using the Erbs correlation, and transposed to tilted planes using an isotropic-sky formulation. Module temperature was calculated with the NOCT-SAM model, and DC power was estimated using a linear temperature-corrected power relationship. System 1 comprised three co-planar modules tilted 14° and facing south. System 2 comprised one east-facing, one south-facing, and one west-facing module, all tilted 14°; optical concentration and inter-module reflection were not assumed. The model placed solar noon at 12:36 local time and the maximum south-facing plane-of-array irradiance at 12:30, thereby maintaining consistency between solar geometry and irradiance. The south-facing module reached 74.5°C and a maximum DC power of 49.4 W. Daily DC energy was 428.1 Wh per south-facing module, 1284.3 Wh for System 1, and 1275.4 Wh for System 2. The east-south-west arrangement reduced the array peak by 3.0% and increased morning and evening energy by 4.5% and 8.0%, respectively, but reduced total daily energy by 0.70%. The results show that orientation diversification can flatten the production profile without necessarily increasing daily energy. Because the analysis uses a clear-sky model, a prescribed temperature profile, and constant wind speed, field measurements are required before site-specific performance claims are made.

ACCEPTED

07.08.26

Keywords: *photovoltaic module; solar geometry; plane-of-array irradiance; module temperature; NOCT model; azimuth diversification; Termez.*

CC BY

1. Introduction

Photovoltaic (PV) output is governed jointly by irradiance, cell temperature, module characteristics, and array orientation. Standard test conditions provide a common nameplate reference, but they do not represent the thermal environment of an operating module. In hot and highly insolated climates, cell

temperature can rise several tens of degrees above ambient temperature, reducing voltage and maximum power even when incident irradiance is high. Consequently, a technically useful assessment must treat solar geometry, plane-of-array irradiance, module temperature, and electrical conversion as a linked calculation rather than as independent quantities (Dobos, 2014; Duffie & Beckman, 2013; Gilman et al., 2018).

Termez is located in southern Uzbekistan near 37° N and experiences hot summer conditions. The combination of high solar elevation and high ambient temperature makes the region a relevant case for evaluating the thermal derating of crystalline-silicon PV modules. The original version of this study compared a co-planar three-module array with an angled arrangement, but it mixed modeled and measured terminology, did not provide a reproducible irradiance time base, and attributed a reflector benefit without an optical model. The present revision resolves those problems by treating the work explicitly as a simulation, defining every input and equation, aligning irradiance with solar noon, integrating energy with the actual time step, and excluding unmodeled reflection effects.

The objectives are to:

calculate a physically consistent 15-minute clear-sky irradiance profile for Termez;

estimate the operating temperature, short-circuit current, open-circuit voltage, and DC power of a representative 60 W module;

compare a co-planar south-facing array with an east-south-west azimuth-diversified array; and

quantify the sensitivity of the result to wind speed, NOCT, temperature coefficient, and irradiance uncertainty.

2. Materials and methods

2.1 Study site, time basis, and study design

The site coordinates were latitude 37.22° N and longitude 67.28° E. Calculations were performed for 13 July 2026 at 15-minute intervals in local civil time (UTC+5). The local standard meridian was 75° E. The equation-of-time and longitude correction gave a calculated solar noon of 12:36. Sunrise and sunset were approximately 05:25 and 19:47, respectively. Solar angles were evaluated using standard astronomical relationships consistent with the NREL solar-position framework (Reda & Andreas, 2008).



Figure 1. A monocrystalline silicon photovoltaic panel with a nominal power of 60W

The study is a deterministic clear-sky simulation. The ambient-temperature series was prescribed to reproduce the hot-day boundary condition reported in the source manuscript, ranging from 27.3°C before sunrise to 42.5°C in the afternoon. The previously missing 12:45 value was inserted by time interpolation. Wind speed at 10 m was set to 1.1 m s^{-1} for the baseline case and varied in sensitivity analysis. The temperature series is not presented as a meteorological observation; therefore, the results are comparative model outputs rather than validated site measurements.

ISSN: 2181-3337 | SCIENTISTS.UZ

Parameter	Baseline value	Role in model
Latitude / longitude	37.22° N / 67.28° E	Solar position
Date and time step	13 July 2026; 15 min	Daily clear-sky case
Time standard	UTC+5; standard meridian 75° E	Civil-to-solar-time conversion
Ambient temperature	27.3–42.5°C; prescribed profile	Thermal boundary condition
Wind speed at 10 m	1.1 m s^{-1}	Baseline module cooling
Ground albedo	0.20	Ground-reflected irradiance
Array tilt	14°	All modules

Table 1. Site and baseline boundary conditions.

2.2 Solar position and clear-sky irradiance

The clear-sky global horizontal irradiance (GHI) was estimated with the Haurwitz relationship (Haurwitz, 1945). The model is intentionally simple and is suitable for a transparent comparative study; it does not represent aerosol, water-vapour, dust, or cloud variability specific to an individual day.

$$GHI_{cs} = 1098 \cos(\theta_z) \exp[-0.059 / \cos(\theta_z)] \quad (1)$$

where θ_z is the solar zenith angle. GHI was decomposed into diffuse horizontal irradiance (DHI) and direct normal irradiance (DNI) using the hourly diffuse-fraction correlation of Erbs et al. (1982).

$$k_t = GHI_{cs} / (I_{0n} \cos\theta_z), \quad DHI = k_d GHI_{cs}, \quad DNI = (GHI_{cs} - DHI) / \cos\theta_z \quad (2)$$

The plane-of-array irradiance for a surface with tilt β and incidence angle θ_i was calculated with the isotropic-sky transposition model (Duffie & Beckman, 2013; Klein, 1979).

$$G_{POA} = DNI \max(\cos\theta_i, 0) + DHI(1 + \cos\beta)/2 + \rho_g GHI(1 - \cos\beta)/2 \quad (3)$$

The use of $\max(\cos\theta_i, 0)$ prevents beam irradiance from being assigned to the rear surface. The ground-reflection term used $\rho_g = 0.20$. No optical concentration, inter-module reflection, or bifacial gain was included.

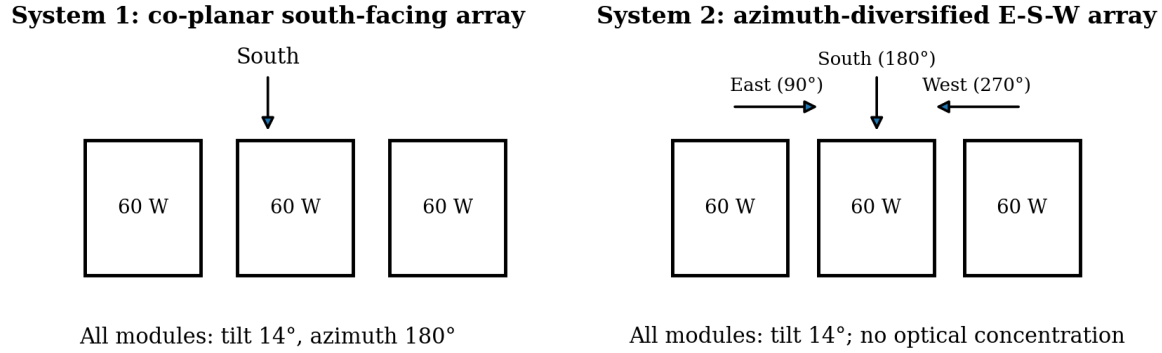


Figure 1. Modeled three-module array configurations. The drawing is schematic; all modules have a 14° tilt.

ISSN: 2181-3337 | SCIENTISTS.UZ

2.3 Reference PV module and temperature model

A representative 36-cell monocrystalline module was defined from the electrical values used in the source manuscript. Because no manufacturer and model number were supplied, the parameters in Table 2 are model inputs rather than a certified datasheet. This distinction prevents the results from being attributed to a specific commercial module.

Parameter	Symbol	Value
Maximum power at STC	P_{STC}	60 W
Open-circuit voltage at STC	$V_{oc,STC}$	22.0 V
Short-circuit current at STC	$I_{sc,STC}$	3.66 A
Power temperature coefficient	γ_P	−0.40% °C⁻¹
Current temperature coefficient	α_I	+0.05% °C⁻¹
Voltage temperature coefficient	β_V	−0.30% °C⁻¹ of $V_{oc,STC}$
Nominal operating cell temperature	NOCT	45°C
Reference efficiency	η_{ref}	0.12
Effective transmittance–absorptance	$\tau\alpha$	0.90
Cells in series	N_s	36

Table 2. Reference module parameters used in the simulation.

Module temperature was evaluated with the NOCT formulation implemented in the NREL System Advisor Model (SAM; Gilman et al., 2018). International Electrotechnical Commission (IEC) standard 61853-2 defines procedures for module operating-temperature measurements, whereas IEC 61215 addresses design qualification and is not used here as the source of the NOCT calculation (IEC, 2016, 2021b). For an open-rack installation, the adjusted NOCT equals the input NOCT.

$$T_c = T_a + (G_{POA}/800)(NOCT - 20)(1 - \eta_{ref}/\tau\alpha) \cdot 9.5/(5.7 + 3.8v_{w,adj}) \quad (4)$$

$$v_{w,adj} = 0.51v_w \quad (5)$$

2.4 Electrical model and energy integration

The maximum-power DC output was calculated with the linear irradiance-and-temperature relationship used in simplified PV energy models such as PVWatts (Dobos, 2014).

$$P_{dc} = P_{STC}\,(G_{POA}/1000)[1 + \gamma_P(T_c - 25)] \quad (6)$$

For diagnostic reporting, short-circuit current and open-circuit voltage were estimated as follows:

$$I_{sc} = I_{sc,STC}\,(G_{POA}/1000)[1 + \alpha_I(T_c - 25)] \quad (7)$$

$$V_{oc} = V_{oc,STC} + \beta_V(T_c - 25) + N_{snk}(T_c + 273.15)q^{-1}\ln(G_{POA}/1000) \quad (8)$$

Equation (8) was applied only for $G_{POA} \geq 20$ W m^{-2}, with ideality factor $n = 1.2$. It is a diagnostic semi-empirical expression and not a substitute for a fitted single-diode model. Daily energy was calculated by trapezoidal integration at the actual 0.25 h time step:

ISSN: 2181-3337 | SCIENTISTS.UZ

$$E = \Sigma [(P_j + P_{j+1})/2] \Delta t \quad (9)$$

2.5 Array configurations

System 1 contained three identical modules, each tilted 14° and facing south (azimuth 180°). System 2 contained three identical modules at the same tilt, facing east (90°), south (180°), and west (270°). Module-level maximum-power tracking was assumed, so the three module powers were added without parallel mismatch loss. This assumption isolates the geometric effect; a shared MPPT could produce additional mismatch and should be considered in hardware design.

The revised System 2 intentionally excludes the earlier "reflector effect." Conventional PV laminates are primarily absorptive, and any multiple-reflection benefit would require measured reflectance, module spacing, shading geometry, view factors, and optical ray tracing. Those inputs were unavailable and were therefore not fabricated.

2.6 Sensitivity analysis

One-at-a-time sensitivity cases varied wind speed (0.5–4.0 m s^{-1}), γ_P (−0.35 to −0.45% $°C^{-1}$), NOCT (43–47°C), and all irradiance components (±5%). These ranges test whether the comparative result is robust to the principal prescribed inputs.

3. Results

3.1 Solar geometry and plane-of-array irradiance

The model gave solar noon at approximately 12:36 local time. The maximum clear-sky GHI was 995.5 W m^{-2} at 12:30; the south-facing plane-of-array irradiance reached 1026.6 W m^{-2} at 12:30. The coincidence of the irradiance maximum with solar noon corrects the earlier timing inconsistency. Because the tilt was only 14°, the east- and west-facing plane-of-array daily irradiances remained close to the south-facing value, but their intraday profiles shifted toward morning and afternoon, respectively.

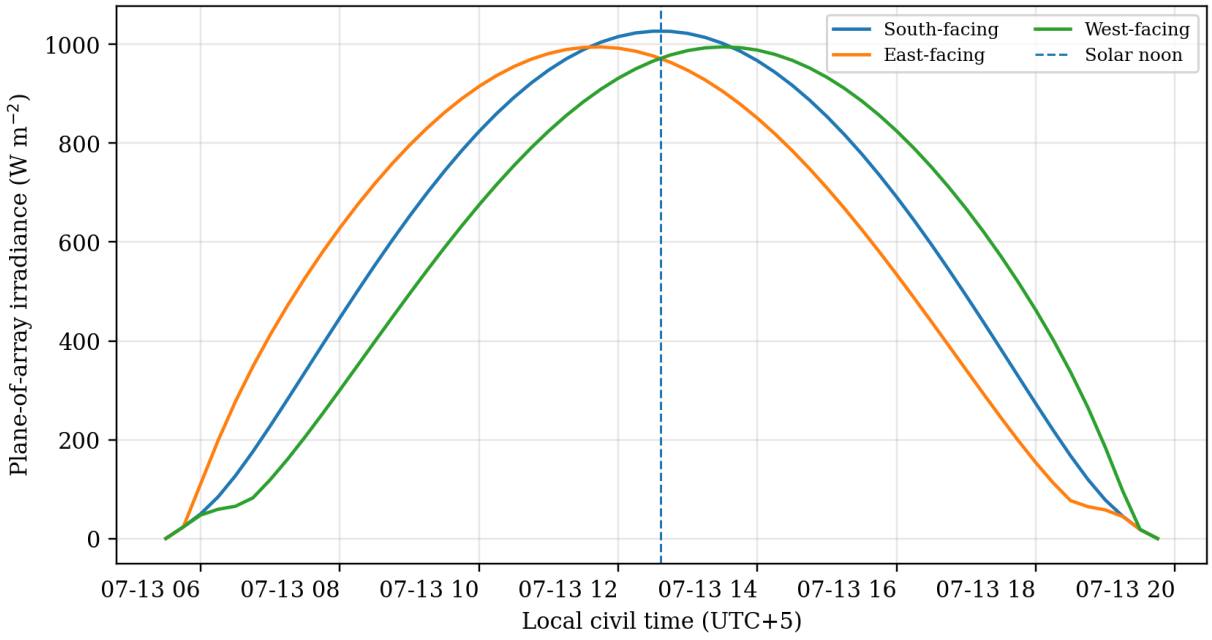


Figure 2. Clear-sky plane-of-array irradiance for the three modeled azimuths.

3.2 Module temperature and electrical parameters

For the south-facing module, the modeled cell temperature reached 74.5°C at 12:30, compared with a maximum ambient temperature of 42.5°C at 14:45. At the maximum-power time, I_{sc} was 3.85 A, V_{oc} was 18.77 V, and DC power was 49.39 W. Thus, an irradiance slightly above 1000 W m^{-2} did not produce the 60 W nameplate value because the cell temperature was about 49.5°C above the STC reference temperature. This is reversible thermal derating, not evidence of permanent material degradation.

ISSN: 2181-3337 | SCIENTISTS.UZ

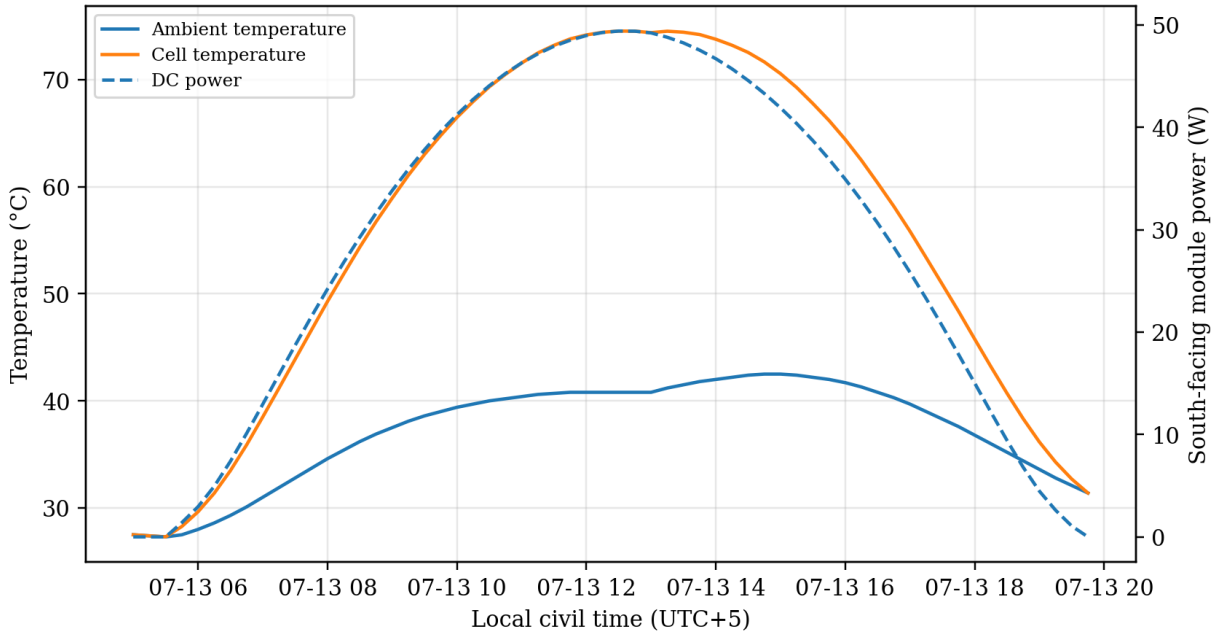


Figure 3. Ambient temperature, modeled cell temperature, and DC power of the south-facing module.

3.3 Comparison of the two array configurations

Metric	South-facing module	System 1	System 2
Nominal DC capacity	60 W	180 W	180 W
Peak modeled DC power	49.39 W	148.18 W	143.71 W
Daily modeled DC energy	428.1 Wh	1284.3 Wh	1275.4 Wh
Daily energy relative to System 1	—	Reference	-0.70%
Morning energy change (to 09:00)	—	Reference	+4.5%
Evening energy change (from 17:00)	—	Reference	+8.0%

Table 3. Principal electrical results for the baseline case.

System 1 generated 1284.3 Wh, whereas System 2 generated 1275.4 Wh, a difference of -0.70%. System 2 reduced peak power by 3.0% and redistributed energy toward the shoulders of the day: energy increased by 4.5% up to 09:00 and by 8.0% after 17:00, while the central part of the day decreased by approximately 2.5%. The configuration therefore flattened the production profile, but it did not provide a daily-energy advantage under the modeled clear-sky conditions.

ISSN: 2181-3337 | SCIENTISTS.UZ

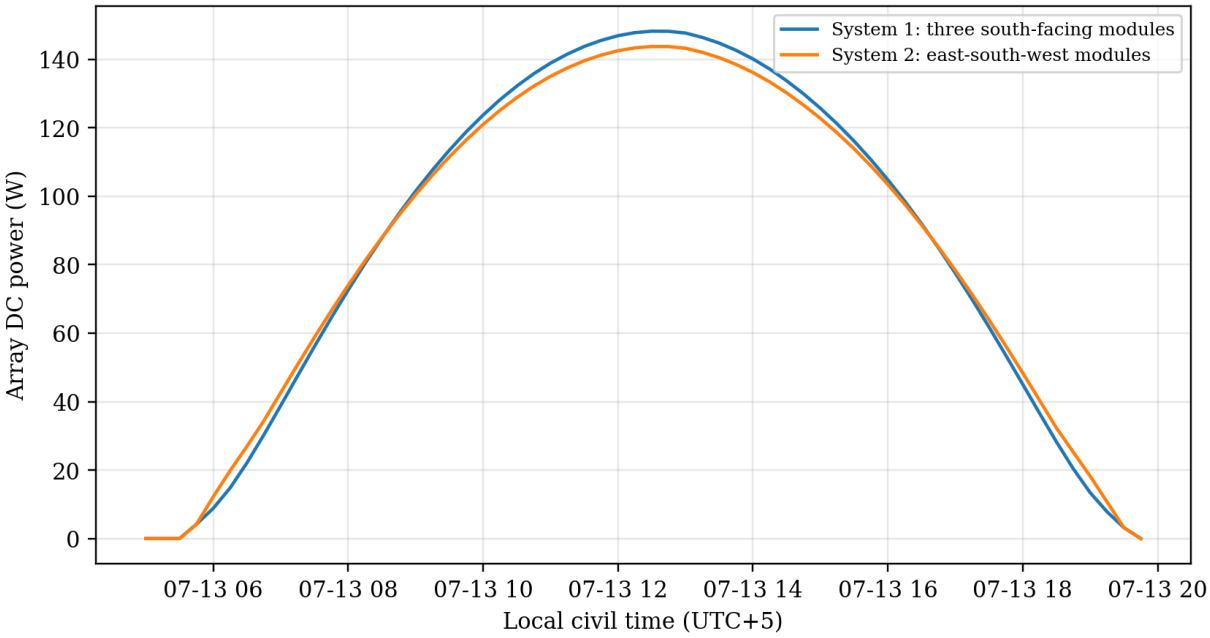


Figure 4. Modeled DC power profiles of the two 180 W array configurations.

3.4 Sensitivity analysis

Parameter	Value	System 1 (Wh)	System 2 (Wh)	System 2 difference
Wind speed at 10 m (m/s)	0.5	1256.3	1248.0	-0.66%
Wind speed at 10 m (m/s)	1.1	1284.3	1275.4	-0.70%
Wind speed at 10 m (m/s)	2	1313.6	1304.0	-0.73%
Wind speed at 10 m (m/s)	4	1351.5	1340.9	-0.78%
Power temperature coefficient (%/°C)	-0.35	1315.8	1306.2	-0.73%
Power temperature coefficient (%/°C)	-0.4	1284.3	1275.4	-0.70%
Power temperature coefficient (%/°C)	-0.45	1252.8	1244.6	-0.66%
NOCT (°C)	43	1297.2	1287.9	-0.71%
NOCT (°C)	45	1284.3	1275.4	-0.70%
NOCT (°C)	47	1271.5	1262.8	-0.68%
Irradiance multiplier	0.95	1227.7	1219.1	-0.71%
Irradiance multiplier	1	1284.3	1275.4	-0.70%
Irradiance multiplier	1.05	1340.1	1330.9	-0.68%

Table 4. One-at-a-time sensitivity results.

ISSN: 2181-3337 | SCIENTISTS.UZ

Absolute energy changed materially with wind speed, temperature coefficient, NOCT, and irradiance level, as expected. However, the relative daily-energy difference between the two configurations remained close to −0.7% in all tested cases. This stability occurs because the two systems use the same module model and differ mainly in azimuth. Accordingly, the conclusion that the east-south-west arrangement flattens rather than increases the clear-sky daily yield is robust within the stated assumptions.

4. Discussion

4.1 Thermal derating under hot conditions

The modeled cell temperature exceeded 70°C near solar noon. IEC 61215-1-1 notes that higher-temperature qualification may be relevant in climates where the 98th-percentile operating temperature exceeds 70°C (IEC, 2021a). The present study does not establish that percentile because it covers one prescribed day, but it illustrates why module selection, rear ventilation, mounting stand-off, and measured temperature coefficients matter in hot climates. The decrease from 60 W nameplate power to approximately 49 W at peak modeled conditions follows from the combined temperature and irradiance terms in Equation (6); it should be described as operating derating rather than degradation.

4.2 Meaning of the orientation comparison

A low 14° tilt limits the daily-energy penalty associated with east and west azimuths. Consequently, System 2 retained almost all of the co-planar array's daily energy while lowering the midday peak and increasing shoulder production. This type of profile shaping can be useful where local demand is higher in the morning or late afternoon, where inverter clipping is a concern, or where a smoother output profile has operational value. It does not imply a higher conversion efficiency: the result is a temporal redistribution of incident radiation.

The calculation also demonstrates why a reflector claim cannot be based solely on array geometry. Any optical enhancement would depend on front-glass reflectance, incidence angle, module spacing, the fraction of reflected light intercepted by another module, shading, and the electrical response of the illuminated cells. A valid reflector study would require measured bidirectional optical properties or validated ray tracing coupled to a cell-level mismatch model.

4.3 Comparison with the unrevised calculation

The revised model corrects four central issues: (i) the work is consistently identified as simulation rather than measurement; (ii) solar noon and the irradiance maximum are aligned through an explicit civil-to-solar-time conversion; (iii) the 12:45 interval is present and energy is integrated by timestamp; and (iv) the system comparison uses explicit azimuths and excludes unsupported reflection. These changes alter the scientific conclusion. The modeled azimuth-diversified system does not produce a 12% daily-energy gain; instead, it produces a nearly equal daily yield with a broader output profile.

5. Limitations and future validation

The following limitations define the scope of the conclusions:

The Haurwitz clear-sky model is an empirical reference and does not include day-specific aerosols, dust, water vapour, or clouds.

The ambient-temperature curve is a prescribed hot-day boundary condition, not a verified observation for 13 July 2026.

Wind speed is constant in the baseline case, and the NOCT model does not resolve transient thermal inertia.

The module is representative because no manufacturer datasheet was available; a single-diode model could improve electrical accuracy.

Module-level MPPT was assumed. Shared-MPPT wiring may introduce mismatch losses for differently oriented modules.

Soiling, spectral effects, incidence-angle modifiers, cable loss, inverter loss, shading, and reflection between modules were excluded.

ISSN: 2181-3337 | SCIENTISTS.UZ

Future work should collect synchronized plane-of-array irradiance, ambient temperature, rear-surface or cell temperature, wind speed, and module I–V data for both configurations. Sensors should be time-synchronized in local civil time, and the raw dataset, calibration certificates, data-processing code, and uncertainty budget should be published. Experimental performance should then be evaluated using measured energy, normalized yield, model bias, mean absolute error, and root-mean-square error.

6. Conclusions

This paper provides a fully specified simulation of a representative 60 W monocrystalline PV module and two 180 W array configurations under prescribed hot-summer conditions in Termez. The corrected solar-time calculation placed solar noon at 12:36 and the maximum south-facing irradiance at 12:30. The modeled module temperature reached 74.5°C, limiting the maximum 60 W module output to 49.4 W despite plane-of-array irradiance above 1000 W m^{-2}.

Three co-planar south-facing modules generated 1284.3 Wh in the modeled day. The east-south-west array generated 1275.4 Wh, 0.70% less, while reducing peak power by 3.0% and increasing morning and evening energy. The primary benefit of the diversified arrangement was therefore profile flattening, not higher daily energy. Claims of reflector-assisted gain are not supported without an explicit optical model and experimental validation.

The main practical conclusion is that hot-climate PV assessment must combine correct solar geometry with temperature-aware electrical modeling. The present results are suitable as a transparent modeling baseline; they should not be presented as measured site performance until validated by field data.

Declarations

Author contributions. B.Y.: conceptualization, methodology, supervision, and manuscript review. A.K.: calculation implementation, data organization, visualization, and draft preparation. Both authors approved the final manuscript.

Conflict of interest. The authors declare no conflict of interest.

Funding. No external funding was reported for this modeling study.

Data and code availability. All model parameters, equations, and the complete 15-minute baseline dataset are provided in this paper and Appendix A. The calculations can be reproduced using the stated equations in any numerical software.

Use of human or animal subjects. Not applicable.

REFERENCES

1. Dobos, A. P. (2014). *PVWatts version 5 manual* (NREL/TP-6A20-62641). National Renewable Energy Laboratory. https://doi.org/10.2172/1158421
2. Duffie, J. A., & Beckman, W. A. (2013). *Solar engineering of thermal processes* (4th ed.). Wiley. https://doi.org/10.1002/9781118671603
3. Erbs, D. G., Klein, S. A., & Duffie, J. A. (1982). Estimation of the diffuse radiation fraction for hourly, daily, and monthly-average global radiation. *Solar Energy, 28*(4), 293–302. https://doi.org/10.1016/0038-092X(82)90302-4
4. Gilman, P., Dobos, A., DiOrio, N., Freeman, J., Janzou, S., & Ryberg, D. (2018). *SAM photovoltaic model technical reference update* (NREL/TP-6A20-67399). National Renewable Energy Laboratory. https://doi.org/10.2172/1429291
5. Haurwitz, B. (1945). Insolation in relation to cloudiness and cloud density. *Journal of Meteorology, 2*(3), 154–166. https://doi.org/10.1175/1520-0469(1945)002<0154:IIRTCA>2.0.CO;2
6. International Electrotechnical Commission. (2016). *Photovoltaic (PV) module performance testing and energy rating—Part 2: Spectral responsivity, incidence angle and module operating temperature measurements* (IEC 61853-2:2016).

7. International Electrotechnical Commission. (2021a). *Terrestrial photovoltaic (PV) modules—Design qualification and type approval—Part 1-1: Special requirements for testing of crystalline silicon photovoltaic (PV) modules* (IEC 61215-1-1:2021).
8. International Electrotechnical Commission. (2021b). *Terrestrial photovoltaic (PV) modules—Design qualification and type approval—Part 1: Test requirements* (IEC 61215-1:2021).
9. Klein, S. A. (1979). Calculation of monthly average insolation on tilted surfaces. *Solar Energy, 19*(4), 325–329. https://doi.org/10.1016/0038-092X(77)90001-9
10. Reda, I., & Andreas, A. (2008). *Solar position algorithm for solar radiation applications* (Rev.; NREL/TP-560-34302). National Renewable Energy Laboratory. https://doi.org/10.2172/15003974

ISSN: 2181-3337 | SCIENTISTS.UZ VOLUME 5 ISSUE 7 JULY 2026

SYNTHESIS, CHARACTERIZATION, AND POTENTIAL USE OF A SULFONATED CATION-EXCHANGE RESIN FOR HARD-WATER SOFTENING

Usmonova Aziza, Pulatov Khayrulla
[1]Assistant Teacher,
Tashkent institute of Chemical Technology, Tashkent, Uzbekistan.
aziza.usmonova5654@gmail.com,
[2]Tashkent Institute of Chemical Technology, Tashkent, Uzbekistan
hayrulla00796@gmail.com

DOI: 10.67620/sai.57a0009

ABSTRACT

This study synthesized and characterized a monofunctional sulfonic cation-exchange resin from sodium p-styrenesulfonate and furfural and evaluated its potential for hard-water softening. The effects of reactant ratio, reaction temperature, and zinc chloride catalyst loading were examined. The selected synthesis condition was a 1:1 molar ratio of sodium p-styrenesulfonate to furfural, 90 °C, and 0.07 mol $ZnCl_2$ per mole of furfural. Infrared spectroscopy and potentiometric titration supported assignment of strongly acidic $–SO_3H$ functionality, with an apparent pK_h of 1.8–2.2. The resin showed a static exchange capacity of 4.2–4.5 meq/g by 0.1 N NaOH titration, a total dynamic exchange capacity of 1,480 meq/L, an operating dynamic exchange capacity of 1,200 meq/L, and mechanical durability of 99.0%. Single-cycle desorption recovered approximately 90.5%–92.5% of sorbed Na^+, Ca^{2+}, and Mg^{2+}. In regional hard-water samples with initial hardness of 11.0–12.0 meq/L, treatment reduced hardness to 3.0–3.8 meq/L in the H-form and 2.1–2.4 meq/L in the Na-form. A tap-water sample decreased from 3.5 meq/L to 0.8 and 0.4 meq/L after 6 h with the H- and Na-forms, respectively. The results support further development of the material for water softening; however, discrepancies among exchange-capacity measurements, incomplete reporting of replicate statistics, and the absence of regeneration-cycle and scale-up data limit claims of superiority over commercial resins.

ACCEPTED

07.08.26

Keywords: *cation-exchange resin, furfural, sodium p-styrenesulfonate, ion exchange, water softening, calcium, magnesium.*

CC BY

Introduction

Ion-exchange resins remain important in water treatment, hydrometallurgy, analytical separations, and process-water conditioning because fixed ionic groups can reversibly exchange counterions while the cross-linked polymer matrix remains insoluble. Their practical value depends on exchange capacity, selectivity, diffusion within the polymer phase, swelling, chemical stability, and regenerability (Alexandratos, 2009; Harland, 1994; Marin et al., 2024; Zagorodni, 2007). Ion exchange is also widely used for recovery or removal of metal ions and other ionic contaminants from aqueous streams (Dixit et al., 2021; Jorgensen & Weatherley, 2003; Lebron et al., 2021; Pehlivan & Altun, 2007).

For sulfonated styrenic materials, the balance between functional-group density and cross-linking is especially important. Cross-linking and pore morphology affect hydration, swelling, transport, and accessible exchange sites, while synthesis conditions influence bead or network structure and therefore macroscopic performance (Chaudhary & Sharma, 2019; Dalla Valle et al., 2020; Rahmatpour et al., 2018; Sterchele et al., 2014; Yuchi et al., 2010). Research on sulfonated styrene-divinylbenzene systems has further shown that sulfonation conditions, porosity, internal acid environment, and morphology influence acidity and ion-exchange behavior (Ahmed et al., 2004; Ali et al., 2012; Coutinho et al., 2006; Hart et al., 2002; Koujout et al., 2003; Malik et al., 2010; Oliveira et al., 2005; Pirogov et al., 2003; Zhou et al., 2010). Related styrenic mixed-mode materials continue to be developed through controlled functionalization of polymer surfaces and networks (Gorbovskaia et al., 2024).

Furfural provides a route to polycondensation materials that can incorporate a feedstock derived from pentosan-rich biomass. Furfural-based ion-exchange polymers and related polycondensation matrices have been investigated using aromatic monomers, industrial residues, and biomass-derived components, including work focused on locally available raw materials and wastewater treatment (Berdieva, 2016; Igitov et al., 2016; Makhmudov et al., 2021; Pulatov & Turabjanov, 2016; Rakhimova, 2016; Turabdzhanov et al., 2019; Usmonova & Pulatov, 2025; Yabefa et al., 2010). Such systems are of interest where the objective is to reduce dependence on imported ion-exchange materials while retaining adequate exchange capacity and mechanical integrity.

Water softening is a particularly relevant application because Ca^{2+} and Mg^{2+} cause scaling in domestic and industrial systems. Ion-exchange treatment can reduce these hardness ions, but engineering performance must be judged under both equilibrium and dynamic conditions and should include regeneration behavior and transport limitations (Crittenden et al., 2012; Nesbitt & Petersen, 2020). Strong-acid cation exchangers have also been investigated for Cu^{2+}, Zn^{2+}, Ni^{2+}, Pb^{2+}, Cd^{2+}, and Cr^{3+} removal, illustrating the broader divalent-cation affinity expected from sulfonic-acid resins (Demirbas et al., 2005; Fathy et al., 2014; Fil et al., 2012; Gode & Pehlivan, 2006; Kocaoba, 2007; Lee et al., 2007).

The purpose of the present study was to synthesize a sulfonic cation-exchange resin by polycondensation of sodium p-styrenesulfonate with furfural, identify conditions associated with favorable exchange properties, characterize the acid functionality, compare selected ion-exchange properties with reference resins, and assess the material in hard-water softening. Particular attention was given to Ca^{2+} and Mg^{2+} removal because these ions directly determine water hardness.

Materials and Methods

Reporting Basis and Units

The numerical values in this manuscript are retained from the experimental record. Exchange capacity and water hardness were originally reported in “mg-eq” units; these values are expressed here as milliequivalents (meq) without changing the numerical values. No replicate counts, standard deviations, confidence intervals, or inferential statistical tests were reported. Accordingly, ranges are presented descriptively and are not interpreted as statistical uncertainty.

Resin Synthesis and Optimization

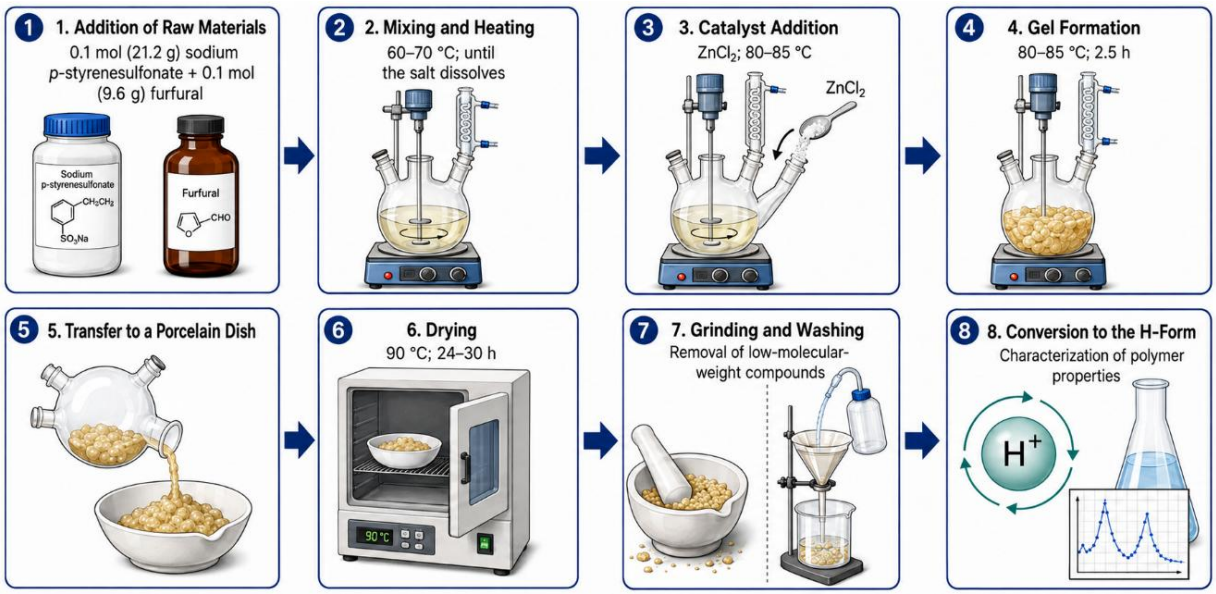
A three-necked flask fitted with a reflux condenser and mechanical stirrer was charged with 0.1 mol (21.2 g, as reported) of sodium p-styrenesulfonate and 0.1 mol (9.6 g) of furfural. The mixture was heated to 60–70 °C until the salt dissolved. Zinc chloride was then added as catalyst, and the reaction mixture was heated further. In the baseline preparation, gel formation was observed after approximately 2.5 h at 80–85 °C. The gel was transferred to a porcelain dish, dried at 90 °C for 24–30 h, ground, washed to remove low-molecular-weight products, and converted to the H-form before characterization.

Optimization experiments evaluated reaction temperature at 80, 90, and 100 °C with a 1:1 reactant ratio and evaluated sodium p-styrenesulfonate-to-furfural molar ratios of 2:1, 1.5:1, and 1:1. The experimental record reports the selected $ZnCl_2$ loading as 0.07 mol per mole of furfural but does not provide

the full set of catalyst concentrations tested. The selected overall condition was 90 °C, a 1:1 reactant ratio, and 0.07 mol $ZnCl_2$ per mole of furfural. The reaction was interpreted using conventional polycondensation concepts (Korshak & Vinogradova, 1968).

Figure 1

Laboratory Workflow for Synthesis and Conversion of the Resin to the H-Form



Note. The workflow reproduces the sequence reported in the experimental record: addition of sodium p-styrenesulfonate and furfural, dissolution, $ZnCl_2$ addition, gel formation, drying, grinding/washing, and H-form conversion.

Total Static Exchange Capacity

A resin sample equivalent to 1.0 g on a dry-matter basis was contacted with 100 mL of 0.1 N NaOH for 24 h. A 25 mL filtrate aliquot was then titrated with 0.1 N HCl in the presence of a mixed indicator. Static exchange capacity, E, was calculated as follows:

$$E = [(V \cdot K_1 - K \cdot V_1 \cdot K_2) \times 100 \times c] / [m \times (100 - W)]$$

where V is the volume of working solution (mL), K is the ratio of total working-solution volume to aliquot volume, V_1 is the titrant volume for the post-contact aliquot (mL), m is resin mass (g), W is moisture content by mass (%), c is the nominal normal concentration of the working and titrating solutions (0.1 N), and K_1 and K_2 are correction factors for the working and titrating solutions, respectively.

Dynamic Exchange Capacity

Resin prepared according to GOST 10896 was stored under distilled water, transferred to a 100 cm^3 graduated cylinder, compacted, and adjusted to a bed volume of 100 cm^3. The resin was transferred to a column and washed downward with distilled water at 1.0 dm^3/h until acidity was no longer detected with methyl orange. A 0.1 N working solution was then passed through the bed and filtrate was collected in measured portions. Breakthrough capacity was determined from the filtrate volume before working-solution ions appeared, and total dynamic capacity was determined when filtrate concentration matched the influent. The results section identifies 0.1 N NaOH as the working solution for the reported dynamic-capacity measurements.

$$D = (V_f \times c \times 1000) / V_s$$

where D is the dynamic exchange capacity (meq/L), Vf is the filtrate volume passed before breakthrough (cm^3), c is working-solution normality, and Vs is the resin-bed volume (cm^3).

Potentiometric Titration and Infrared Characterization

For potentiometric titration, 0.25 g portions of H-form resin were equilibrated for 48 h with decreasing volumes of 0.1 N NaCl and increasing volumes of 0.1 N NaOH while total liquid volume was maintained at 100 mL. Equilibrium pH was measured with a pH-150MI meter, and pH was plotted against added NaOH. The apparent dissociation constant was obtained from the titration curve according to the procedure used in the experimental record. Infrared spectroscopy was used to identify the principal functional groups; instrument model, sampling configuration, and acquisition parameters were not reported.

ISSN: 2181-3337 | SCIENTISTS.UZ

Chemical Stability

Two H-form resin samples, each equivalent to 1.0 g dry resin, were separately treated with 100 mL of 5 N H_2SO_4 or 100 mL of 5 N NaOH under reflux in a boiling-water bath for 5 h. After cooling and filtration, the resin was reconverted to H-form and its exchange capacity and specific volume were determined. Chemical stability, X, was defined as the percentage of initial exchange capacity retained after treatment:

$X = (E_1 / E_0) \times 100$

where E_0 and E_1 are the total exchange capacities before and after acid or alkali treatment, respectively. Numerical E_0, E_1, and X values were not included in the available experimental record, so no quantitative stability comparison is reported in the Results.

Static Sorption-Rate Test

Ten Na-form resin samples, each equivalent to 0.25 g dry resin, were contacted with 50 mL of 0.1 N $CaCl_2$ in stoppered 150 mL flasks under shaking. At selected contact times, 10 mL aliquots were withdrawn and Ca^{2+} content was determined. The commercial KU-2×8 sulfonic cation-exchange resin was used for comparison. The experimental record states that kinetic curves were constructed, but the time-resolved data and curves were not available for quantitative kinetic modeling in this manuscript.

Desorption and Water-Softening Tests

For desorption, separate resin samples saturated with Na^+, Ca^{2+}, or Mg^{2+} were contacted with water and 2 N H_2SO_4; the acid-contact period was 48 h. For water-softening tests, 1.0 g of resin in either H- or Na-form was contacted with 200 mL of natural water for 24 h. Total hardness was measured by complexometric titration with Trilon B (EDTA) using Eriochrome Black T. Samples were obtained from Shurchi District in Surkhandarya Region and from Kungrad and Karaozak districts in the Republic of Karakalpakstan. A separate deep-softening test used tap water with an initial hardness of 3.5 meq/L and a 6 h contact period.

Results

Optimization and Physicochemical Properties

The 1:1 sodium p-styrenesulfonate-to-furfural ratio produced the highest NaOH-based static exchange capacity among the three ratios reported and also gave the largest swollen specific volume. At this ratio, moisture content was 26%, bulk density was 0.56 g/mL, swollen H-form specific volume was 2.8–3.0 mL/g, and static exchange capacities were 4.2–4.5 meq/g with NaOH, 3.0–3.2 meq/g with NaCl, and 4.0–4.2 meq/g with $CaCl_2$. Together with the temperature and catalyst studies, the selected synthesis condition was 90 °C, 0.07 mol $ZnCl_2$ per mole of furfural, and a 1:1 reactant ratio.

Table 1

Physicochemical Characteristics as a Function of Sodium p-Styrenesulfonate-to-Furfural Molar Ratio

Parameter	Unit	2:1	1.5:1	1:1
Moisture content	%	28	26	26
Bulk density	g/mL	0.68	0.60	0.56
Swollen H-form specific volume	mL/g	2.4–2.8	2.6–2.8	2.8–3.0
Static exchange capacity by 0.1 N NaOH	meq/g	2.9–3.0	3.6–3.8	4.2–4.5
Static exchange capacity by 0.1 N NaCl	meq/g	2.4–2.6	2.8–3.0	3.0–3.2
Static exchange capacity by 0.1 N $CaCl_2$	meq/g	3.6–3.8	3.6–3.8	4.0–4.2

Note. The original manuscript reported exchange capacity as mg-eq/g; the numerical values are shown here as meq/g. No replicate counts or measures of dispersion were provided.

ISSN: 2181-3337 | SCIENTISTS.UZ

Proposed Reaction and Functional-Group Characterization

The reported reaction scheme treats furfural as both a condensation component and a contributor to network formation. The proposed structure is shown in Figure 2. The infrared spectrum was interpreted as evidence for sulfonic-acid functionality: bands in the 1260–1150 cm^{-1} and 1060–1010 cm^{-1} regions were assigned to $–SO_3H$ groups, with a prominent feature near 1200 cm^{-1}. The experimental record reports no diagnostic hydroxyl or carboxyl bands in the corresponding regions used for assignment and therefore classifies the material as monofunctional.

Figure 2

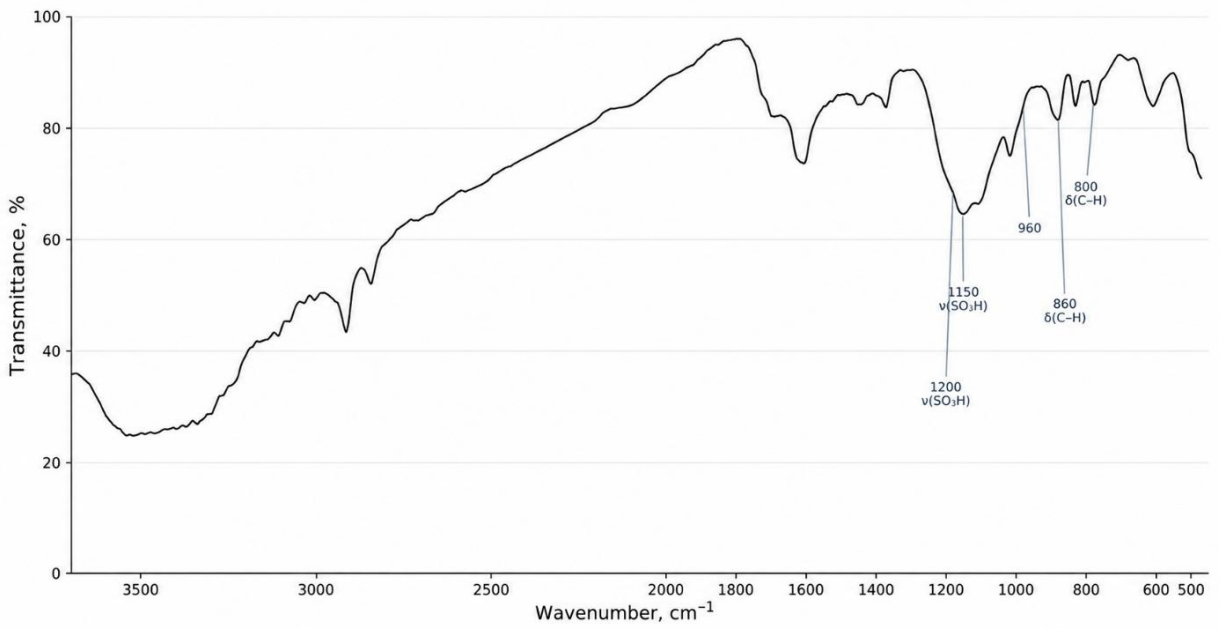
Proposed Polycondensation Scheme for Sodium p-Styrenesulfonate and Furfural



Note. The scheme is reproduced from the experimental record and is presented as a proposed structural representation rather than a complete mechanistic proof.

Figure 3

Infrared Spectrum of the Synthesized Sulfonic Cation-Exchange Resin



Note. Bands annotated near 1,200 and 1,150 cm^{-1} were assigned in the experimental record to sulfonic-acid vibrations; features near 960, 860, and 800 cm^{-1} were assigned to aromatic C–H deformation modes.

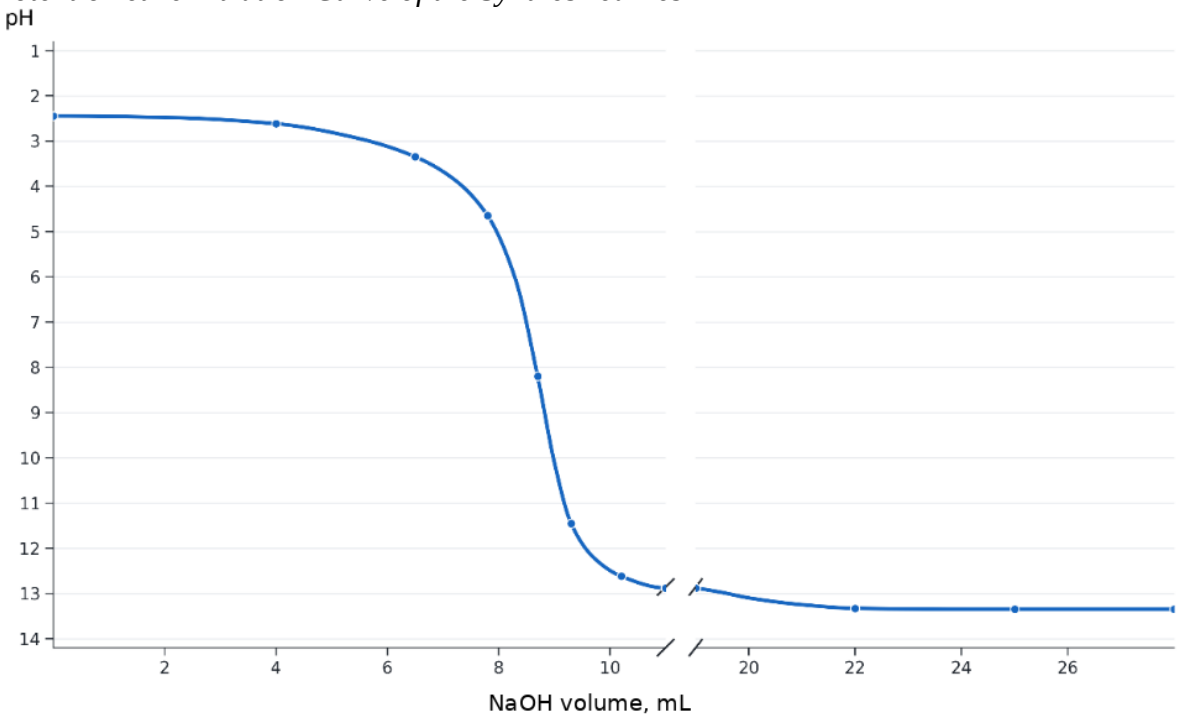
Potentiometric Behavior and Cross-Method Exchange Capacity

The potentiometric titration yielded an apparent pK_h of 1.8–2.2, consistent with the strongly acidic behavior attributed to sulfonic-acid groups. The reported capacity estimates, however, were not fully concordant. For the synthesized resin, theoretical and sulfur-based capacities were both 3.6 meq/g, potentiometric capacity was 3.2–3.4 meq/g, whereas the NaOH static capacity was 4.2–4.5 meq/g. Thus, the NaOH value exceeded the stated theoretical capacity by approximately 17%–25%. Without replicate statistics or a mass-balance explanation, the difference should be treated as a reporting or method-comparability limitation rather than as evidence of additional exchange sites.

ISSN: 2181-3337 | SCIENTISTS.UZ

Figure 4

Potentiometric Titration Curve of the Synthesized Resin



Note. The vertical pH axis is inverted in the original experimental figure (lower pH values appear at the top). The apparent pK_h reported from the curve was 1.8–2.2.

Table 2

Exchange-Capacity Estimates and Apparent Dissociation Constants

Characteristic	KU-FS resin	Synthesized resin	Unit
Functional group	–SO_3H	–SO_3H	—
Theoretical exchange capacity	3.8	3.6	meq/g
Static exchange capacity by 0.1 N NaOH	3.4–3.6	4.2–4.5	meq/g
Capacity calculated from S/P content	3.53	3.6	meq/g
Capacity from potentiometric titration	3.4–3.5	3.2–3.4	meq/g
Apparent pK_1	1.8–2.2	1.8–2.2	—
pK_2	—	—	—

Note. KU-FS denotes the comparison sulfonic cation-exchange resin based on a styrene–furfural polymer. The source table labels the elemental-analysis column as sulfur (phosphorus) content; the present sulfonic resins are interpreted on the sulfur basis.

Comparative Ion-Exchange Properties

The synthesized resin displayed 99.0% mechanical durability, equal to the KU-FS value and slightly below the 99.9% reported for KU-2×8. Its Ca^{2+} exchange capacity approached that of KU-2×8, whereas Mg^{2+} and Cu^{2+} capacities were lower than the corresponding KU-2×8 values. Ni^{2+} data were available for the synthesized resin and KU-FS but not for KU-2×8. These comparisons indicate useful

ISSN: 2181-3337 | SCIENTISTS.UZ

divalent-cation exchange but do not support a general claim of superior sorption relative to the commercial resin.

Table 3

Comparative Properties of the Synthesized Resin and Reference Cation-Exchange Resins

Property	Synthesized resin	KU-FS	KU-2×8
Bulk density, g/mL	0.68	0.50	0.45
Specific volume, mL/g	2.4–2.8	3.4	2.8
NaOH static capacity, meq/g	4.2–4.5	3.6	3.8
NaCl static capacity, meq/g	3.0–3.2	3.4	1.2
$CaCl_2$ capacity, H-form, meq/g	4.0–4.2	4.4	4.6
$CaCl_2$ capacity, Na-form, meq/g	4.4–4.6	4.6	5.4
$MgCl_2$ capacity, H-form, meq/g	2.6–3.0	3.0	4.0
$MgCl_2$ capacity, Na-form, meq/g	2.8–3.4	3.4	4.6
$CuSO_4$ capacity, H-form, meq/g	2.0–2.2	3.8	4.0
$CuSO_4$ capacity, Na-form, meq/g	2.4–2.6	4.2	4.6
$NiSO_4$ capacity, H-form, meq/g	1.8–2.0	2.0	—
$NiSO_4$ capacity, Na-form, meq/g	2.2–2.4	3.6	—
Mechanical durability, %	99.0	99.0	99.9

Note. The bulk-density and specific-volume values reported for the synthesized resin in this comparison differ from the values reported for the selected 1:1 sample in Table 1. The experimental record does not identify whether the measurements represent a different batch, resin form, or reporting basis; therefore, both sets are retained without silent alteration.

Dynamic Capacity and Desorption

Under dynamic conditions with 0.1 N NaOH, the synthesized resin had a total capacity of 1,480 meq/L and an operating capacity of 1,200 meq/L, compared with 1,420 and 1,150 meq/L for KU-FS. These differences correspond to approximately 4.2% and 4.3%, respectively. Single-cycle desorption recovered 90.5% of sorbed Na^+, 92.5% of Ca^{2+}, and 92.3% of Mg^{2+} when the water and 2 N H_2SO_4 fractions were combined.

Table 4

Static, Swelling, and Dynamic Exchange Properties

Characteristic	KU-FS	Synthesized resin
Static capacity by 0.1 N NaOH, meq/g	3.6	4.2–4.5

ISSN: 2181-3337 | SCIENTISTS.UZ

Characteristic	KU-FS	Synthesized resin
Static capacity by 0.1 N NaCl, meq/g	3.4	3.0–3.2
Specific volume, H-form, mL/g	3.5	2.4
Specific volume, Na-form, mL/g	3.8	2.8
Total dynamic capacity, meq/L	1,420	1,480
Operating dynamic capacity, meq/L	1,150	1,200

Note. Specific-volume values in this source table differ from the 1:1 optimization values in Table 1. No batch or resin-form explanation was provided beyond the H-form/Na-form labels shown here.

Table 5

Desorption of Sorbed Ions

Cation	Sorbed, meq/g	Desorbed with H_2O, meq/g	Desorbed with 2 N H_2SO_4, meq/g	Total desorbed, meq/g
Na^+	4.2	0.3	3.5	3.8
Ca^{2+}	4.0	0.1	3.6	3.7
Mg^{2+}	2.6	0.1	2.3	2.4

Note. Calculated total desorption recoveries are approximately 90.5% for Na^+, 92.5% for Ca^{2+}, and 92.3% for Mg^{2+}. The record describes a single desorption experiment; repeated regeneration cycles were not reported.

Hard-Water Softening

The resin reduced hardness in all three regional water samples. In the H-form, hardness decreased from 11.0–12.0 meq/L to 3.0–3.8 meq/L, equivalent to reductions of approximately 68.3%–73.2%. In the Na-form, final hardness was lower, 2.1–2.4 meq/L; using the same initial sample values reported for the H-form rows, the corresponding reductions were approximately 78.2%–82.5%. The H-form results fell within the 2.5–7.0 meq/L range cited in the experimental record for O‘zDSt 950:2011, while the Na-form produced still softer water (O‘zDSt 950:2011, 2011).

Table 6

Water Hardness Before and After Treatment With the Synthesized Resin

Sampling location	Initial hardness, meq/L	Final hardness, H-form, meq/L	Final hardness, Na-form, meq/L
Shurchi District, Surkhandarya Region	12.0	3.8	2.1
Kungrad District, Republic of Karakalpakstan	11.2	3.0	2.2
Karaozak District, Republic of Karakalpakstan	11.0	3.4	2.4

Note. The source table printed initial hardness only once for each water source and used dashes in the Na-form initial-hardness cells. The present layout treats each initial value as the common starting hardness for the corresponding water source before separate H-form and Na-form tests.

ISSN: 2181-3337 | SCIENTISTS.UZ

In the separate deep-softening test, tap water with an initial hardness of 3.5 meq/L decreased to 0.8 meq/L with the H-form and 0.4 meq/L with the Na-form after 6 h, corresponding to reductions of approximately 77.1% and 88.6%, respectively. These values demonstrate strong hardness removal under the reported batch conditions, although they should not be generalized to continuous operation without column breakthrough and regeneration-cycle data.

Discussion

The optimization data indicate that increasing the relative amount of furfural from the 2:1 to the 1:1 sodium p-styrenesulfonate-to-furfural ratio was associated with higher NaOH-based exchange capacity and greater swelling. This pattern is qualitatively consistent with the broader literature showing that synthesis conditions and network morphology can strongly affect the accessibility and hydration of ion-exchange sites (Chaudhary & Sharma, 2019; Dalla Valle et al., 2020; Rahmatpour et al., 2018; Sterchele et al., 2014). At the same time, excessive cross-linking can reduce diffusion and swelling, so the observed optimum should be understood as specific to the reported formulation and test conditions rather than a universal stoichiometric rule.

The IR and potentiometric data support classification of the resin as a strong-acid sulfonic cation exchanger. This interpretation is consistent with established behavior of sulfonated styrenic networks, in which $–SO_3H$ functionality provides strongly acidic exchange sites over a broad pH range (Hart et al., 2002; Koujout et al., 2003; Malik et al., 2010). However, the cross-method capacity comparison reveals an important internal inconsistency: the 4.2–4.5 meq/g NaOH value is higher than the stated theoretical and sulfur-based capacities of 3.6 meq/g. Because a measured exchange capacity should be interpreted against the same dry-mass and chemical-equivalent basis as the theoretical value, this discrepancy requires confirmation through replicated titrations, independent sulfur analysis, and explicit moisture corrections before the higher value is used for design calculations.

Performance comparisons were mixed rather than uniformly favorable. The synthesized resin slightly exceeded KU-FS in total and operating dynamic capacity, but KU-2×8 showed higher Ca^{2+}, Mg^{2+}, and Cu^{2+} capacity in most directly comparable tests. The synthesized material therefore appears promising as a functional ion exchanger but cannot be described as generally superior to the commercial reference based on the reported dataset. Similar caution is appropriate for heavy-metal applications: sulfonic resins are well established for divalent-ion exchange (Demirbas et al., 2005; Fil et al., 2012; Gode & Pehlivan, 2006; Kocaoba, 2007; Lee et al., 2007), yet metal-specific selectivity, competing-ion effects, and column performance would need to be measured for this material.

The hard-water experiments provide the clearest application evidence. Both resin forms substantially reduced hardness, and the Na-form consistently produced lower final hardness than the H-form in the three regional samples and the tap-water test. This is consistent with the practical use of Na-cycle strong-acid cation exchangers for softening because Ca^{2+} and Mg^{2+} are exchanged for Na^{+} without acidifying the product water to the same extent as an H-cycle resin. The reported single-cycle desorption of more than 90% for Na^{+}, Ca^{2+}, and Mg^{2+} is also encouraging, but repeated exhaustion-regeneration cycles are necessary to establish working capacity, resin life, and regenerant demand under realistic conditions (Crittenden et al., 2012).

Limitations

Several limitations constrain interpretation. First, replicate numbers and statistical uncertainty were not reported, so numerical ranges cannot be treated as confidence intervals. Second, the full catalyst-loading series, IR instrument conditions, and time-resolved kinetic data were not available. Third, quantitative chemical-stability results were absent even though a stability method was described. Fourth, bulk-density and specific-volume values differ across the reported tables without batch identifiers, and the NaOH exchange capacity exceeds the stated theoretical capacity. Fifth, the water-softening tests were batch experiments using a high resin-to-water ratio (1 g per 200 mL) and did not include continuous breakthrough

ISSN: 2181-3337 | SCIENTISTS.UZ

curves, multi-cycle regeneration, long-term mechanical attrition, cost analysis, or comparison with modern commercial resins under identical conditions. These issues should be addressed before scale-up or economic claims are made.

Conclusion

A sulfonic cation-exchange resin was synthesized from sodium p-styrenesulfonate and furfural, with the most favorable reported condition at a 1:1 reactant ratio, 90 °C, and 0.07 mol $ZnCl_2$ per mole of furfural. IR and potentiometric results were consistent with strongly acidic $–SO_3H$ functionality, and the resin showed measurable static and dynamic exchange capacity, 99.0% mechanical durability, more than 90% single-cycle desorption of Na^+, Ca^{2+}, and Mg^{2+}, and substantial reduction of hardness in regional and tap-water samples. The Na-form produced the lowest residual hardness. The material is therefore a credible candidate for further water-softening development, but the present evidence supports a "promising" rather than "superior" conclusion. Replicated capacity measurements, reconciliation of table-to-table data differences, full chemical-stability reporting, continuous-flow tests, regeneration cycling, and cost analysis are required for rigorous comparison with commercial cation-exchange resins.

REFERENCES

1. Ahmed, M., Malik, M. A., Pervez, S., & Raffiq, M. (2004). Effect of porosity on sulfonation of macroporous styrene–divinylbenzene beads. *European Polymer Journal, 40*(8), 1609–1613. https://doi.org/10.1016/j.eurpolymj.2004.04.013
2. Alexandratos, S. D. (2009). Ion-exchange resins: A retrospective from Industrial & Engineering Chemistry Research. *Industrial & Engineering Chemistry Research, 48*(1), 388–398. https://doi.org/10.1021/ie801242v
3. Ali, S. W., Malik, M. A., & Ahmed, I. (2012). Synthesis of strong acid resins from macroporous styrene–divinylbenzene copolymers: Is diluent extraction step necessary? *Polymer Engineering & Science, 52*(11), 2375–2382. https://doi.org/10.1002/pen.23197
4. Berdieva, M. I. (2016). Investigation of the sulfonation reaction of a polymer based on distillation residues and furfural. *Universum: Chemistry and Biology*, 7(25).
5. Chaudhary, V., & Sharma, S. (2019). Effect of various synthesis parameters on styrene–divinylbenzene copolymer properties. *Journal of Porous Materials, 26*(6), 1559–1571. https://doi.org/10.1007/s10934-019-00753-7
6. Coutinho, F. M. B., Rezende, S. M., & Soares, B. G. (2006). Characterization of sulfonated poly(styrene–divinylbenzene) and poly(divinylbenzene) and its application as catalysts in esterification reaction. *Journal of Applied Polymer Science, 102*(4), 3616–3627. https://doi.org/10.1002/app.24046
7. Crittenden, J. C., Trussell, R. R., Hand, D. W., Howe, K. J., & Tchobanoglous, G. (2012). *MWH's water treatment: Principles and design* (3rd ed.). John Wiley & Sons. https://doi.org/10.1002/9781118131473
8. Dalla Valle, C., Zecca, M., Rastrelli, F., Tubaro, C., & Centomo, P. (2020). Effect of the sulfonation on the swollen state morphology of styrenic cross-linked polymers. *Polymers, 12*(3), Article 600. https://doi.org/10.3390/polym12030600
9. Demirbas, A., Pehlivan, E., Gode, F., Altun, T., & Arslan, G. (2005). Adsorption of Cu(II), Zn(II), Ni(II), Pb(II), and Cd(II) from aqueous solution on Amberlite IR-120 synthetic resin. *Journal of Colloid and Interface Science, 282*(1), 20–25. https://doi.org/10.1016/j.jcis.2004.08.147
10. Dixit, F., Dutta, R., Barbeau, B., Bérubé, P., & Mohseni, M. (2021). PFAS removal by ion exchange resins: A review. *Chemosphere, 272*, Article 129777. https://doi.org/10.1016/j.chemosphere.2021.129777

11. Fathy, M., Abdel Moghny, T., Awad Allah, A. E., & Alblehy, A. (2014). Cation exchange resin nanocomposites based on multi-walled carbon nanotubes. *Applied Nanoscience, 4*, 103–112. https://doi.org/10.1007/s13204-012-0178-5
12. Fil, B. A., Boncukcuoglu, R., Yilmaz, A. E., & Bayar, S. (2012). Adsorption of Ni(II) on ion exchange resin: Kinetics, equilibrium and thermodynamic studies. *Korean Journal of Chemical Engineering, 29*(9), 1232–1238. https://doi.org/10.1007/s11814-012-0012-5
13. Gode, F., & Pehlivan, E. (2006). Removal of chromium(III) from aqueous solutions using Lewatit S 100: The effect of pH, time, metal concentration and temperature. *Journal of Hazardous Materials, 136*(2), 330–337. https://doi.org/10.1016/j.jhazmat.2005.12.021
14. Gorbovskaia, A. V., Kvachenok, I. K., Stavrianidi, A. N., Chernobrovkina, A. V., Uzhel, A. S., & Shpigun, O. A. (2024). Polyelectrolyte-grafted mixed-mode stationary phases based on poly(styrene-divinylbenzene). *Microchemical Journal, 199*, Article 110075. https://doi.org/10.1016/j.microc.2024.110075
15. Harland, C. E. (1994). *Ion exchange: Theory and practice* (2nd ed.). Royal Society of Chemistry.
16. Hart, M. P., Fuller, G., Brown, D. R., Dale, J. A., & Plant, S. (2002). Sulfonated poly(styrene-co-divinylbenzene) ion-exchange resins: Acidities and catalytic activities in aqueous reactions. *Journal of Molecular Catalysis A: Chemical, 182–183*, 439–445. https://doi.org/10.1016/S1381-1169(01)00471-X
17. Igitov, F. B., Berdieva, M. I., Mutalov, Sh. A., Turobzhonov, S. M., Tursunov, T. T., & Nazirova, R. A. (2016). New polycondensation-type ion-exchange polymers. *Modern Materials, Engineering and Technologies*, 4(7), 12–15.
18. Jorgensen, T. C., & Weatherley, L. R. (2003). Ammonia removal from wastewater by ion exchange in the presence of organic contaminants. *Water Research, 37*(8), 1723–1728. https://doi.org/10.1016/S0043-1354(02)00571-7
19. Kocaoba, S. (2007). Comparison of Amberlite IR 120 and dolomite's performances for removal of heavy metals. *Journal of Hazardous Materials, 147*(1–2), 488–496. https://doi.org/10.1016/j.jhazmat.2007.01.037
20. Korshak, V. V., & Vinogradova, E. N. (1968). *Nonequilibrium polycondensation*. Nauka.
21. Koujout, S., Kiernan, B. M., Brown, D. R., Edwards, H. G. M., Dale, J. A., & Plant, S. (2003). The nature of the internal acid solution in sulfonated poly(styrene-co-divinylbenzene) resins. *Catalysis Letters, 85*(1–2), 33–40. https://doi.org/10.1023/A:1022160506026
22. Lebron, Y. A. R., Moreira, V. R., & Amaral, M. C. S. (2021). Metallic ions recovery from membrane separation processes concentrate: A special look onto ion exchange resins. *Chemical Engineering Journal, 425*, Article 131812. https://doi.org/10.1016/j.cej.2021.131812
23. Lee, I.-H., Kuan, Y.-C., & Chern, J.-M. (2007). Equilibrium and kinetics of heavy metal ion exchange. *Journal of the Chinese Institute of Chemical Engineers, 38*, 71–84.
24. Makhmudov, Kh., Berdieva, M., Yuldashev, A., Tursunov, T., Nazirova, R., Turabdjanov, S., & Kedelbaev, B. (2021). Investigation of the polycondensation reaction of waste chemicals in order to use them to produce ion-exchange polymers. *Technical Science and Innovation, 2021*(2), 4–13. https://doi.org/10.51346/tstu-01.21.2-77-0117
25. Malik, M. A., Ali, S. W., & Ahmed, I. (2010). Sulfonated styrene–divinylbenzene resins: Optimizing synthesis and estimating characteristics of the base copolymers and the resins. *Industrial & Engineering Chemistry Research, 49*, 2608–2612. https://doi.org/10.1021/ie902057x
26. Marin, N. M., Nita-Lazar, M., Popa, M., Galaon, T., & Pascu, L. F. (2024). Current trends in development and use of polymeric ion-exchange resins in wastewater treatment. *Materials, 17*(23), Article 5994. https://doi.org/10.3390/ma17235994

ISSN: 2181-3337 | SCIENTISTS.UZ

27. Nesbitt, A. B., & Petersen, J. (2020). A multiple mechanism model for measuring extra- and intraparticle mass transport in ion exchange resins. *AIChE Journal, 66*(1), Article e16825. https://doi.org/10.1002/aic.16825
28. Oliveira, A. J. B., Aguiar, A. P., Aguiar, M. R. M. P., & Santa Maria, L. C. (2005). How to maintain the morphology of styrene–divinylbenzene copolymer beads during the sulfonation reaction. *Materials Letters, 59*(8–9), 1089–1094. https://doi.org/10.1016/j.matlet.2004.12.014
29. *O'zDSt 950:2011: Drinking water—Hygienic requirements and quality control*. (2011). [Standard].
30. Pehlivan, E., & Altun, T. (2007). Ion-exchange of Pb^{2+}, Cu^{2+}, Zn^{2+}, Cd^{2+} and Ni^{2+} ions from aqueous solution by Lewatit CNP 80. *Journal of Hazardous Materials, 140*, 299–307.
31. Pirogov, A. V., Chernova, M. V., Nemtseva, D. S., & Shpigun, O. A. (2003). Sulfonated and sulfoacylated poly(styrene-divinylbenzene) copolymers as packing materials for cation chromatography. *Analytical and Bioanalytical Chemistry, 376*(5), 745–752. https://doi.org/10.1007/s00216-003-1953-7
32. Pulatov, Kh., & Turabjanov, S. (2016). Furfural based cation-exchange resin. *Journal of Education and Technical Sciences, 3*(1), 8–10.
33. Rahmatpour, A., Goodarzi, N., & Moazzez, M. (2018). A novel route for synthesis of cross-linked polystyrene copolymer beads with tunable porosity using guar and xanthan gums from bioresources as alternative synthetic suspension stabilizers. *Designed Monomers and Polymers, 21*(1), 116–129. https://doi.org/10.1080/15685551.2018.1489698
34. Rakhimova, L. S. (2016). Investigation of the polycondensation reaction mechanism of the synthesized ion-exchange resins. *Universum: Chemistry and Biology*, 8(26).
35. Sterchele, S., Centomo, P., Zecca, M., Hanková, L., & Jeřábek, K. (2014). Dry- and swollen-state morphology of novel high surface area polymers. *Microporous and Mesoporous Materials, 185*, 26–29. https://doi.org/10.1016/j.micromeso.2013.10.005
36. Turabdzhanov, S. M., Kedelbaev, B. Sh., Kushnazarov, P. I., Badritdinova, F. M., Ponamaryova, T. V., & Rakhimova, L. S. (2019). New approach to the synthesis of polycondensation ion-exchange polymers for wastewater treatment. *News of the National Academy of Sciences of the Republic of Kazakhstan, Series of Geology and Technical Sciences, 2*(434), 206–216. https://doi.org/10.32014/2019.2518-170X.56
37. Usmonova, A. B., & Pulatov, Kh. L. (2025). Synthesis and investigation of a monofunctional polycondensation-type sulfonic cation-exchange resin. *Universum: Chemistry and Biology*, 11(137), 46–50. https://doi.org/10.32743/UniChem.2025.137.11.21145
38. Yabefa, J. A., Ajinomoh, C. S., & Wankasi, D. (2010). Studies on biomass-furfural-based cation-exchange resins. I. Preparation of polymeric composition. *Archives of Applied Science Research, 2*(6), 267–272.
39. Yuchi, A., Kuroda, S., Takagi, M., Watanabe, Y., & Nakao, S. (2010). Effects of the exchange capacity and cross-linking degree on the hydration states of anions in quantitative loading onto strongly basic anion-exchange resins. *Analytical Chemistry, 82*(20), 8611–8617. https://doi.org/10.1021/ac101707j
40. Zagorodni, A. A. (2007). *Ion exchange materials: Properties and applications*. Elsevier. https://doi.org/10.1016/B978-0-08-044552-6.X5000-X
41. Zhou, R., Wei, R., Liu, X., & Lin, X. (2010). Poly(styrene-co-divinylbenzene) resins sulfonated by chlorosulfonic acid. *CIESC Journal, 61*(4), 1047–1051.

ISSN: 2181-3337 | SCIENTISTS.UZ VOLUME 5 ISSUE 7 JULY 2026

COMPARATIVE GC–MS PROFILING OF VOLATILE CONSTITUENTS IN PIMPINELLA ANISUM L. GROWN UNDER CONTRASTING SUBSTRATE AND CALCIUM–BORON NUTRITION CONDITIONS

Akhrorova Barnokhon
Tashkent Institute of Irrigation and Agricultural Mechanization Engineers National Research University Tashkent, Uzbekistan
Email: bakhrorova@icloud.com

DOI: 10.67620/sai.57a0010

ABSTRACT

Anise (Pimpinella anisum L.) is valued for aromatic phenylpropenes and terpenoids whose profiles can vary with cultivation and analytical procedure. This exploratory greenhouse study compared anise grown in soil or coconut coir with or without calcium nitrate–boron nutrition (17N + 32CaO + 1B). Aerial tissues collected from full flowering to early umbel formation were macerated in 96% ethanol and analyzed by GC–MS. The available dataset comprised mean relative peak areas from 2–3 analytical replicates per substrate × nutrition combination; therefore, results were treated descriptively. Trans-anethole was the largest reported peak in all four groups, ranging from 38.4% in unsupplemented coconut coir to 50.2% in supplemented soil. With mineral supplementation, relative trans-anethole peak area was 7.7 percentage points higher in soil and 8.3 percentage points higher in coconut coir. Soil also showed higher trans-anethole than corresponding coconut-coir groups, whereas limonene was relatively higher in coconut coir. Estragole was retained as the canonical name for methyl chavicol, and a duplicate methyl-chavicol row was excluded rather than combined because raw chromatograms were unavailable for reassignment. Because the material was an ethanolic extract rather than distilled essential oil and biological replication could not be established from the source record, the findings represent preliminary relative-profile trends, not absolute metabolite concentrations or statistically confirmed treatment effects. Quantitative irrigation effects were not evaluated. Replicated factorial studies with complete instrument reporting and internal-standard quantification are required.

ACCEPTED

07.08.26

Keywords: *Pimpinella anisum, trans-anethole, GC–MS, calcium–boron nutrition, substrate, phytochemical profiling.*

CC BY

Introduction

Anise (*Pimpinella anisum* L.; Apiaceae) is an aromatic medicinal and culinary species whose fruits and aerial tissues contain phenylpropenes and terpenoids of pharmacological, sensory, and commercial interest. Trans-anethole is the characteristic phenylpropene of anise and is commonly the dominant constituent of fruit essential oil, although composition varies across plant material and geographic origin (Orav et al., 2008; Shojaii & Abdollahi Fard, 2012). Molecular work in anise has also established a

dedicated biosynthetic route to trans-anethole involving phenylpropene-forming and O-methyltransferase enzymes (Koeduka et al., 2009).

The phytochemical phenotype of aromatic plants is not determined by genotype alone. Developmental stage, water availability, mineral nutrition, and other environmental conditions can alter primary metabolism, stress signaling, and the allocation of carbon to secondary metabolites (Isah, 2019; Jogawat et al., 2021). In anise specifically, field studies have shown that mineral-fertilizer regimes can affect growth, seed production, and essential-oil yield, although the magnitude and direction of responses depend on dose, genotype, and cultivation context (Bhuvaneshwari et al., 2002; Gedik & Akgul, 2023). Calcium has structural and signaling functions in plants, whereas boron contributes to cell-wall integrity, membrane function, reproductive development, and carbohydrate metabolism (Shireen et al., 2018; Thor, 2019). These physiological roles provide a plausible basis for investigating whether a calcium nitrate–boron treatment is associated with differences in the relative volatile profile of anise; however, they do not establish a compound-specific causal mechanism.

Interpretation also depends on extraction and analytical procedure. Distilled essential oils and solvent extracts are not chemically equivalent matrices, and extraction method can alter the apparent composition recovered by GC–MS (Fagbemi et al., 2021). Accordingly, the present study uses the term GC–MS-accessible volatile/aromatic fraction for the ethanol-derived material and avoids equating its relative peak areas with conventional hydrodistilled essential-oil composition or absolute metabolite concentration.

The broader greenhouse cultivation experiment included two substrates (soil and coconut coir), four irrigation volumes (50, 100, 150, and 200 mL per irrigation event), and two mineral-nutrition conditions. The quantitative GC–MS dataset available for the present manuscript, however, comprised four substrate × nutrition groups and did not contain a quantitative breakdown across the irrigation levels. The aim of this paper was therefore to describe and compare the relative GC–MS peak-area profiles of selected volatile constituents across soil and coconut-coir substrates with and without calcium nitrate–boron supplementation, while treating irrigation observations as contextual rather than as a quantitatively tested phytochemical factor.

Method

Plant Material and Greenhouse Conditions

Pimpinella anisum L. plants were cultivated in a protected greenhouse at the Institute of Fundamental and Applied Research, TIIAME National Research University, Tashkent, Uzbekistan. Two growth substrates were used: soil and coconut coir. The source manuscript reported daytime greenhouse temperatures of 22–25 °C, nighttime temperatures above 18 °C, relative humidity of 60–70%, and a 16-h photoperiod.

The broader cultivation framework included irrigation volumes of 50, 100, 150, and 200 mL per irrigation event and two mineral-nutrition conditions: an unsupplemented control and a calcium nitrate formulation supplemented with boron (17N + 32CaO + 1B). The fertilizer is referred to throughout this manuscript as the Ca–B treatment, rather than “NPK,” because the stated formulation contains nitrogen, calcium, and boron and does not report phosphorus or potassium. The original record did not provide fertilizer concentration in the irrigation solution, application frequency, total nutrient dose, irrigation frequency, pot/substrate volume, plant density per experimental unit, cultivar/accession information, or a voucher specimen number. These details were not reconstructed or inferred.

Analytical Comparison Groups

The quantitative GC–MS table available for analysis contained four substrate × nutrition combinations: soil control, soil + Ca–B, coconut-coir control, and coconut coir + Ca–B. The source manuscript described 2–3 analytical GC–MS replicates for each combination and indicated that biological replication had been used in cultivation, but the exact number of independent biological samples

contributing to each chromatographic mean was not specified. Consequently, analytical replicate means are reported descriptively and are not treated as independent biological replication.

Sample Collection and Extraction

Aerial plant parts were collected at physiological maturity described as full flowering to early umbel formation. Plant material was chopped and macerated in 96% ethanol for 24 h at room temperature under protection from light. The extract was filtered and concentrated using a rotary evaporator under reduced pressure at a temperature not exceeding 40 °C until constant weight. Because this procedure yields an ethanolic plant extract rather than a hydrodistilled or steam-distilled essential oil, the resulting chromatographic percentages are interpreted as relative constituents of the analyzed extract fraction.

GC–MS Analysis and Compound Identification

GC–MS analysis was reported to have been performed using an Agilent 8860 gas chromatograph coupled to a 5977 mass-selective detector and an HP-5 capillary column (30 m × 0.25 mm internal diameter; 0.25 μm film thickness). Electron-impact ionization was performed at 70 eV, and helium was used as the carrier gas. The source manuscript stated that compounds were identified by comparison of mass spectra with the NIST/EPA/NIH library and by linear retention indices relative to n-alkanes.

The source record available for this revision did not contain the complete oven-temperature program, injection volume, inlet temperature, split ratio or injection mode, carrier-gas flow rate, MS scan range, source and transfer-line temperatures, solvent delay, n-alkane range, individual retention-index values, library version, or spectral-match acceptance thresholds. No values for these parameters were invented. Recovery of the original instrument method and raw chromatographic files is necessary for full analytical reproducibility and should precede journal submission.

Data Curation and Statistical Analysis

Relative peak areas were expressed as percentages of total chromatogram area and reported as means of 2–3 analytical replicates. The source table listed “estragole” and “methyl chavicol” as separate analytes. Because methyl chavicol is a synonym of estragole, the duplicate-named methyl-chavicol row was excluded from the curated table. Its values were not added to the estragole row because, without the original chromatograms and peak-identification records, it is not possible to determine whether the duplicated labels represented transcriptional duplication, two separate peaks with one misidentified, or another data-processing issue. The remaining values were retained exactly as reported.

Given the limited analytical replication and the absence of documented independent biological sample sizes for the chromatographic means, no ANOVA, post hoc testing, confidence intervals, or p values were calculated. Results are therefore descriptive and are expressed as differences in mean relative peak area (percentage points). No inference is made about absolute metabolite concentrations, essential-oil yield, or statistical significance.

Results

Reported Volatile Constituents

Seven uniquely named compounds from the supplied dataset were retained for quantitative comparison after harmonizing estragole/methyl-chavicol nomenclature (Table 1). Trans-anethole was the largest reported peak in every treatment group. The selected table is not a complete chromatographic mass balance; additional peaks were present in the original chromatograms but were not included in the summarized dataset.

ISSN: 2181-3337 | SCIENTISTS.UZ

Table 1

Selected Volatile Constituents Retained After Nomenclature Curation

Compound	Chemical class	Interpretive relevance
Trans-anethole	Phenylpropene	Characteristic major aromatic constituent of anise
Estragole	Phenylpropene	Minor aromatic phenylpropene; synonym: methyl chavicol
Limonene	Monoterpene	Citrus-like monoterpene component
Linalool	Monoterpene alcohol	Floral monoterpene alcohol
Anisaldehyde	Aromatic aldehyde	Aromatic oxygenated constituent
α-Pinene	Monoterpene	Minor monoterpene constituent
Eugenol	Phenylpropanoid	Minor phenylpropanoid constituent

Note. Compound classes are descriptive. The duplicate methyl-chavicol entry in the source dataset was not retained as a separate compound because methyl chavicol is synonymous with estragole.

Relative Peak-Area Profiles Across Substrate and Nutrition Groups

Trans-anethole ranged from 38.4% to 50.2% of total chromatogram area among the four summarized groups (Table 2). In the unsupplemented groups, soil had 42.5% trans-anethole compared with 38.4% in coconut coir, a difference of 4.1 percentage points. In the Ca–B-treated groups, soil had 50.2% compared with 46.7% in coconut coir, a difference of 3.5 percentage points.

Within each substrate, Ca–B supplementation was associated with a higher mean relative trans-anethole peak area: 42.5% to 50.2% in soil (+7.7 percentage points) and 38.4% to 46.7% in coconut coir (+8.3 percentage points). Estragole, linalool, anisaldehyde, and eugenol also showed higher reported relative areas in the supplemented groups in both substrates. Limonene showed the opposite direction, decreasing by 0.35 percentage points with supplementation in each substrate and remaining higher in coconut coir than in soil under both nutrition conditions. These are descriptive contrasts and are not statistically tested treatment effects.

Table 2

Mean Relative GC–MS Peak Area of Selected Canonical Compounds Across Substrate × Nutrition Groups

Compound	Soil control (%)	Soil + Ca–B (%)	Coconut control (%)	Coconut + Ca–B (%)
Trans-anethole	42.50	50.20	38.40	46.70
Estragole	7.80	9.60	6.50	8.90
Limonene	2.45	2.10	3.20	2.85
Linalool	1.85	2.30	1.65	2.10
Anisaldehyde	2.10	2.75	1.80	2.40
α-Pinene	0.85	0.92	1.10	1.05
Eugenol	0.62	0.88	0.50	0.70
Subtotal of listed compounds	**58.17**	**68.75**	**53.15**	**64.70**

Note. Values are mean relative peak areas (% total chromatogram area) from 2–3 analytical replicates. Ca–B = calcium nitrate + boron (17N + 32CaO + 1B). Because methyl chavicol is a synonym of estragole, the duplicate methyl-chavicol row was excluded pending raw-chromatogram verification. Selected compounds only; values do not sum to 100%.

ISSN: 2181-3337 | SCIENTISTS.UZ

Irrigation Observations

The cultivation experiment included four irrigation volumes, and the source manuscript described visually more vigorous and uniform vegetative development at 150 mL than at 50 or 200 mL per irrigation event. However, the quantitative GC–MS table did not contain treatment-specific values for the four irrigation levels. Accordingly, no result in this paper attributes differences in volatile composition to irrigation volume, and no irrigation regime is recommended on the basis of the present chromatographic dataset.

Discussion

Dominance of Trans-Anethole and Matrix-Dependent Interpretation

The largest reported peak across all four groups was trans-anethole, consistent with the established chemotaxonomic importance of this phenylpropene in *P. anisum* (Koeduka et al., 2009; Orav et al., 2008). The relative values in the present extract (38.4%–50.2%) are lower than the 76.9%–93.7% range reported by Orav et al. (2008) for hydrodistilled fruit essential oils from European samples. This discrepancy should not be interpreted as evidence of inferior plant quality because the matrices are not directly comparable: the present study analyzed ethanol-extracted aerial material collected around flowering/early umbel development, whereas conventional anise essential-oil studies often analyze distilled mature fruits. Extraction method can change both the compounds recovered and their apparent proportions (Fagbemi et al., 2021).

Substrate-Associated Descriptive Trends

Soil-grown samples had higher mean relative trans-anethole peak area than corresponding coconut-coir samples under both nutrition conditions, while limonene was higher in coconut coir. These repeated directions suggest a substrate-associated difference in the relative profile, but the mechanism cannot be determined from the current data. No measurements of substrate water potential, electrical conductivity, pH, aeration, nutrient availability, or root-zone temperature were provided. It would therefore be speculative to attribute the profile to particular moisture or aeration mechanisms. A replicated experiment that characterizes root-zone physicochemical conditions is needed before causal interpretation.

Mineral-Nutrition-Associated Descriptive Trends

The most consistent pattern in the summarized data was the higher relative trans-anethole peak area in Ca–B-treated material within both substrates. Similar-direction increases were observed for estragole, linalool, anisaldehyde, and eugenol, whereas limonene decreased slightly. Previous anise studies indicate that mineral nutrition can affect growth and essential-oil yield (Bhuvaneshwari et al., 2002; Gedik & Akgul, 2023), and plant physiology provides plausible links through nitrogen metabolism, calcium signaling, and boron-dependent structural and transport processes (Shireen et al., 2018; Thor, 2019). Nevertheless, the present formulation simultaneously supplied nitrogen, calcium, and boron. Because these components were not factorially separated and the fertilizer dose was not documented in the source record, the observed pattern cannot be attributed specifically to calcium, boron, or nitrogen, nor can it establish stimulation of the trans-anethole biosynthetic pathway.

Avoiding Overinterpretation of Relative Peak Areas

Relative peak-area percentages are compositional: an increase in the percentage of one constituent can occur because that constituent increases, because other constituents decrease, or because both processes occur. Without an internal or external standard, extraction-recovery measurements, and biomass-normalized concentration data, the present results cannot establish absolute accumulation of trans-anethole or any other metabolite. For the same reason, wording such as “increased biosynthesis,” “enhanced pharmacopoeial quality,” or “dominant driver” is not supported by the current dataset. The defensible conclusion is that the relative chromatographic profile differed descriptively across the four summarized conditions.

ISSN: 2181-3337 | SCIENTISTS.UZ

Irrigation as a Future Quantitative Factor

Water availability is biologically relevant to secondary metabolism because drought and other stress states can alter hormonal signaling and secondary-metabolite production (Isah, 2019; Jogawat et al., 2021). However, biological plausibility cannot substitute for measurement. The present study did not provide replicated GC–MS profiles at 50, 100, 150, and 200 mL irrigation levels. The irrigation observations should therefore be used to formulate a future hypothesis rather than to claim a phytochemical response.

Limitations and Priorities for Replication

This study has four major limitations. First, the chromatographic means were based on only 2–3 analytical replicates, and the number of independent biological samples contributing to those means could not be established from the source record. Second, quantitative GC–MS values were not available across irrigation levels, preventing evaluation of irrigation effects or interactions. Third, the extract was semi-quantitatively characterized by relative peak area without internal or external standards, so absolute concentrations and total volatile yield remain unknown. Fourth, the complete GC–MS method, raw chromatograms, individual retention indices, and identification-quality metrics were not available for independent verification.

Future work should use a fully specified factorial design with independent biological replication, predefined experimental units, randomized treatment assignment, and sufficient replication for inferential analysis. Irrigation should be quantified not only as volume per event but also by frequency, substrate moisture status, drainage fraction, and root-zone properties. Mineral treatments should report concentration, application frequency, and cumulative N, Ca, and B doses and, ideally, separate nutrient factors to distinguish their contributions.

Analytical validation should include a complete GC–MS method, a documented n-alkane series, retention-index reporting for each analyte, explicit library-match thresholds, representative spectra/chromatograms, and authentic standards for key compounds when available. Absolute or semiquantitative concentration should be established using appropriate internal standards and expressed per unit dry biomass or extract. Because estragole and methyl chavicol are synonymous, the duplicated source assignment must also be reconciled against the original chromatogram before any definitive compound table is submitted for publication.

Conclusion

The available GC–MS summary data indicate that the relative volatile/aromatic profile of greenhouse-grown *Pimpinella anisum* differed descriptively across substrate and mineral-nutrition conditions. Trans-anethole was the largest reported peak in all four groups, and Ca–B-treated samples showed higher mean relative trans-anethole peak area than their corresponding controls in both soil and coconut coir. Soil groups also showed higher trans-anethole than matched coconut-coir groups, whereas limonene was comparatively higher in coconut coir. These patterns are preliminary because they are based on relative peak areas from limited analytical replication, without inferential statistics or absolute quantification. The study does not quantitatively demonstrate an irrigation effect, and the ethanol-extracted matrix should not be treated as directly equivalent to distilled essential oil. The findings provide a rationale for a rigorously replicated, fully documented factorial study rather than a basis for definitive agronomic or pharmaceutical-quality recommendations.

Data and Methodological Transparency Statement

The numerical values reproduced in Table 2 are the curated values available in the supplied manuscript. Raw chromatograms, mass spectra, complete peak tables, individual retention indices, and the original GC–MS instrument method were not available for this revision. No missing analytical parameters or experimental observations were fabricated. These primary records should be recovered, archived, and

checked against the curated compound table before submission to a peer-reviewed analytical or phytochemical journal.

REFERENCES

1. Bhuvaneshwari, B., Farooqi, A. A., Sreeramu, B. S., & Srinivasappa, K. N. (2002). Influence of nitrogen, phosphorus and potassium levels on growth, seed yield and essential oil content in anise (*Pimpinella anisum* L.). *Journal of Spices and Aromatic Crops, 11*(2), 112–117.
2. Fagbemi, K. O., Aina, D. A., & Olajuyigbe, O. O. (2021). Soxhlet extraction versus hydrodistillation using the Clevenger apparatus: A comparative study on the extraction of a volatile compound from *Tamarindus indica* seeds. *The Scientific World Journal, 2021*, Article 5961586. https://doi.org/10.1155/2021/5961586
3. Gedik, O., & Akgul, F. (2023). Impact of nitrogen fertilizer on the productivity and qualitative parameters of anise (*Pimpinella anisum* L.). *Turkish Journal of Field Crops, 28*(2), 291–300. https://doi.org/10.17557/tjfc.1350494
4. Isah, T. (2019). Stress and defense responses in plant secondary metabolites production. *Biological Research, 52*, Article 39. https://doi.org/10.1186/s40659-019-0246-3
5. Jogawat, A., Yadav, B., Chhaya, Lakra, N., Singh, A. K., & Narayan, O. P. (2021). Crosstalk between phytohormones and secondary metabolites in the drought stress tolerance of crop plants: A review. *Physiologia Plantarum, 172*(2), 1106–1132. https://doi.org/10.1111/ppl.13328
6. Koeduka, T., Baiga, T. J., Noel, J. P., & Pichersky, E. (2009). Biosynthesis of t-anethole in anise: Characterization of t-anol/isoeugenol synthase and an O-methyltransferase specific for a C7–C8 propenyl side chain. *Plant Physiology, 149*(1), 384–394. https://doi.org/10.1104/pp.108.128066
7. Orav, A., Raal, A., & Arak, E. (2008). Essential oil composition of *Pimpinella anisum* L. fruits from various European countries. *Natural Product Research, 22*(3), 227–232. https://doi.org/10.1080/14786410701424667
8. Shireen, F., Nawaz, M. A., Chen, C., Zhang, Q., Zheng, Z., Sohail, H., Sun, J., Cao, H., Huang, Y., & Bie, Z. (2018). Boron: Functions and approaches to enhance its availability in plants for sustainable agriculture. *International Journal of Molecular Sciences, 19*(7), Article 1856. https://doi.org/10.3390/ijms19071856
9. Shojaii, A., & Abdollahi Fard, M. (2012). Review of pharmacological properties and chemical constituents of *Pimpinella anisum*. *ISRN Pharmaceutics, 2012*, Article 510795. https://doi.org/10.5402/2012/510795
10. Thor, K. (2019). Calcium—Nutrient and messenger. *Frontiers in Plant Science, 10*, Article 440. https://doi.org/10.3389/fpls.2019.00440

ISSN: 2181-3337 | SCIENTISTS.UZ

ISSN: 2181-3337 | SCIENTISTS.UZ VOLUME 5 ISSUE 7 JULY 2026

MATHEMATICAL MODELING OF DEMULSIFIER CONCENTRATION EFFECTS ON OIL–WATER INTERFACIAL TENSION DURING FIELD OIL TREATMENT

Sattorov Mirvohid Olimovich
Associate Professor, Department of Oil and Gas affair, Bukhara state technical university

DOI: 10.67620/sai.57a0011

ABSTRACT
Stable water-in-oil emulsions increase the hydraulic, separation, and chemical-treatment burden of field oil treatment systems. This study develops a statistically evaluated, physically bounded correlation between demulsifier concentration and oil–water interfacial tension (IFT), while explicitly separating that correlation from unvalidated claims about droplet diameter, coalescence rate, or equipment optimization. Fourteen secondary concentration–IFT data pairs (0–210 g/t) attributed to published field-oriented measurements were analyzed using a three-parameter asymptotic exponential model, $\sigma(C) = \sigma_\infty + (\sigma_0 - \sigma_\infty)\exp(-kC)$. Nonlinear least-squares estimation gave $\sigma_0 = 45.81$ mN/m, $\sigma_\infty = 13.18$ mN/m, and $k = 0.01737$ (g/t)$^{-1}$. Model performance was $R^2 = 0.973$, RMSE = 1.59 mN/m, and MAE = 1.40 mN/m. A normalized response function shows that 80%, 90%, and 95% of the modeled attainable IFT reduction are reached at approximately 92.7, 132.6, and 172.5 g/t, respectively. Thus, 100–130 g/t corresponds to about 82.4–89.5% of the modeled IFT response and can be treated as a practical screening band for diminishing returns under the analyzed conditions, not as a universal techno-economic optimum. The model is suitable as a concentration-dependent IFT submodel within broader population-balance, coalescence, settling, or electrostatic-dehydration simulations, provided those models independently represent droplet-size evolution and process hydrodynamics. The work also identifies the validation data required before the correlation can be used for field optimization.

ACCEPTED

07.08.26

Keywords: *field oil treatment; water-in-oil emulsion; demulsifier; interfacial tension; nonlinear regression; diminishing returns; population balance model; electrostatic dehydration.*

CC BY

1. Introduction

Water-in-crude-oil emulsions are generated when produced water and crude oil are dispersed under shear through chokes, valves, pumps, pipelines, and other flow restrictions. Their persistence is governed by the properties of the oil–water interface, including naturally occurring surface-active material such as asphaltenes and resins, interfacial-film rheology, dispersed-droplet size distribution, temperature, viscosity, brine chemistry, solids, and flow history (Kokal, 2005; Langevin et al., 2004; Raya et al., 2020). Stable emulsions complicate transportation and field treatment because water must ultimately be removed while meeting product-quality, corrosion, and downstream-processing constraints.

Chemical demulsifiers are widely used to accelerate phase separation. Their action is commonly associated with competitive adsorption at the interface, displacement or reorganization of natural stabilizers, modification of interfacial-film properties, and changes in interfacial tension and film-drainage

behavior (Alao et al., 2021; Alara et al., 2022; Rondón et al., 2008). However, interfacial tension alone is not a complete mechanistic description of demulsification. Interfacial viscoelasticity, adsorption kinetics, collision frequency, film drainage, temperature, continuous-phase viscosity, water fraction, and demulsifier chemistry also influence whether colliding droplets coalesce (Langevin et al., 2004; Saad et al., 2019). Recent experimental work nevertheless confirms that IFT can be a useful parameter for assessing demulsifier performance when interpreted together with separation behavior rather than as a stand-alone predictor (Freitas et al., 2025).

Mathematical descriptions of water-in-oil separation range from empirical correlations to population-balance and multiphase-flow models. Population-balance formulations explicitly track droplet birth, coalescence, breakup, settling, and size distributions and therefore provide a physically appropriate framework for predicting actual droplet-size evolution (Cunha et al., 2008; Kooti et al., 2023; Sharma & Thaokar, 2023; Su et al., 2023). Separator-scale simulations similarly demonstrate that droplet-size distribution and emulsion rheology must be coupled to hydrodynamics to predict separation efficiency (Oshinowo & Vilagines, 2020). Electrostatic coalescence introduces additional dependencies on electric-field strength, frequency, dielectric properties, and droplet interactions (Mhatre et al., 2015).

The earlier manuscript on which the present study is based correctly identified a strong concentration dependence of IFT, but it treated a qualitative diameter transformation as if it could directly predict droplet formation, coalescence, settling, and equipment optimization. It also contained calculated IFT values that were inconsistent with its own fitted equation. The revised study therefore narrows the quantitative claim to what the available data actually support: a concentration-dependent IFT submodel and a transparent diminishing-returns analysis.

Accordingly, the objectives are to (1) fit a physically bounded three-parameter exponential relation between demulsifier concentration and IFT; (2) report reproducible goodness-of-fit statistics and parameter uncertainty; (3) correct the tabulated predictions; (4) quantify saturation and diminishing returns without presenting them as a universal economic optimum; and (5) define how the correlation can be incorporated into a broader droplet-coalescence or separator model without conflating IFT with actual droplet diameter.

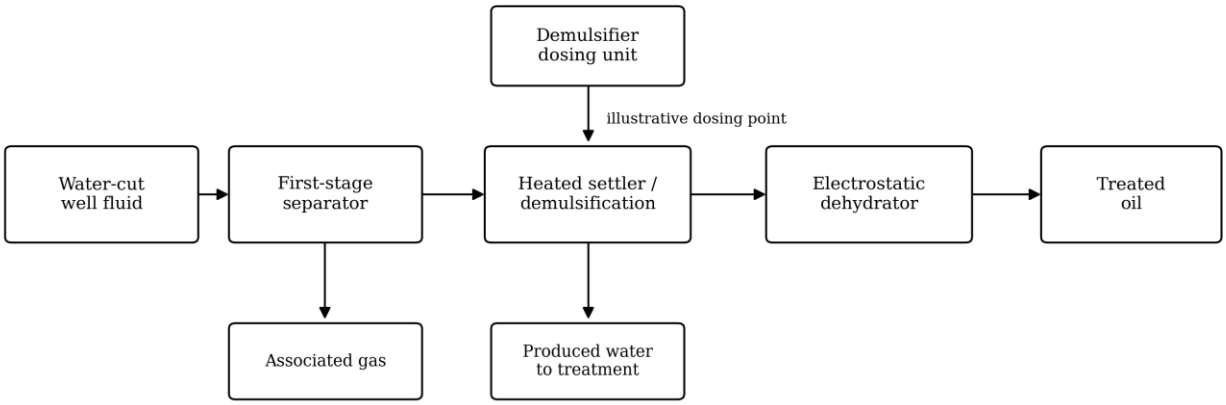


Figure 1. *Conceptual field-oil-treatment arrangement showing an illustrative demulsifier dosing point. The present concentration model informs chemical-dose screening only; the dosing location and equipment design are not optimized by the model.*

2. Materials and Methods

2.1 Data source and study scope

The analysis uses 14 demulsifier-concentration and IFT pairs reproduced in the source manuscript and attributed to Golubev and Khalikova (2004). The cited source describes stalagmometric measurements for a crude-oil emulsion from the Vvedenovskoye field and reports a concentration–IFT curve together with a fifth-order polynomial representation. Because primary instrument records, replicate measurements,

ISSN: 2181-3337 | SCIENTISTS.UZ

and pointwise measurement uncertainties are not available here, the numerical pairs are treated as secondary data rather than as newly generated experimental observations. The analyzed concentration range is 0–210 g/t, and the measured IFT values range from 45.0 to 12–13 mN/m. Equal weighting was used in regression because the source does not report heteroscedastic measurement variances for the reconstructed points. Consequently, the confidence intervals reported below describe regression-parameter uncertainty conditional on this dataset; they do not replace instrument or sampling uncertainty.

2.2 Exponential concentration–IFT model

A monotonic asymptotic exponential model was selected because it represents a rapid initial IFT response followed by saturation and remains bounded at high concentration. Unlike a high-order polynomial, the form does not diverge or oscillate when extrapolated beyond the calibration range. All three parameters were estimated from the data; therefore, the model is explicitly described as a three-parameter model.

$$\sigma(C) = \sigma_\infty + (\sigma_0 - \sigma_\infty) \exp(-kC) \quad (1)$$

where C is the demulsifier concentration (g/t, as reported by the source study), σ(C) is the oil–water interfacial tension (mN/m), σ_0 is the fitted IFT at zero demulsifier, σ_∞ is the asymptotic IFT at high concentration, and k is the empirical concentration-response coefficient, $(g/t)^{-1}$.

2.3 Parameter estimation and goodness of fit

The parameters were estimated by nonlinear least squares. Goodness of fit was evaluated using the coefficient of determination (R^2), root-mean-square error (RMSE), and mean absolute error (MAE). Approximate 95% confidence intervals were calculated from the nonlinear least-squares covariance matrix using a t multiplier with 11 residual degrees of freedom. The calculations were reproduced in Python using nonlinear least-squares routines.

2.4 Diminishing-return metrics

To avoid presenting the fitted curve as a techno-economic optimization that the available data cannot support, a normalized IFT-response fraction was defined. This metric expresses how much of the total model-predicted reduction between σ_0 and σ_∞ has been achieved at concentration C.

$$R(C) = [\sigma_0 - \sigma(C)] / [\sigma_0 - \sigma_\infty] = 1 - \exp(-kC) \quad (2)$$

For a selected response fraction f (for example, 0.80, 0.90, or 0.95), the corresponding concentration is:

$$C(f) = -\ln(1 - f) / k \quad (3)$$

The local marginal IFT reduction per unit increase in demulsifier concentration is the magnitude of the derivative of Equation (1):

$$M(C) = -d\sigma/dC = k(\sigma_0 - \sigma_\infty) \exp(-kC) \quad (4)$$

R(C) and M(C) quantify saturation and diminishing returns, but neither includes chemical price, oil value, residual-water penalties, residence time, throughput, temperature, or other process constraints. They are therefore screening metrics, not an economic objective function.

2.5 Boundary between the IFT submodel and droplet-separation models

The model does not convert IFT directly into actual droplet diameter. Actual droplet growth requires a coalescence model, droplet-size population balance, or experimental droplet-size data. Once an actual or predicted droplet diameter d is available, gravitational settling may be estimated under Stokes-regime assumptions by:

$$v = \Delta\rho \, g \, d^2 / (18 \, \mu) \quad (5)$$

where v is settling velocity, Δρ is the density difference between the phases, g is gravitational acceleration, and μ is continuous-phase viscosity. Equation (5) demonstrates why actual droplet size must be obtained independently: settling velocity scales with d^2. Population-balance and electrocoalescence studies explicitly model the droplet-size distribution and collision/coalescence mechanisms required for such predictions (Cunha et al., 2008; Kooti et al., 2023; Sharma & Thaokar, 2023; Su et al., 2023).

3. Results and Discussion

3.1 Fitted parameters and statistical performance

The fitted parameter values are summarized in Table 1. The model predicts σ_0 = 45.81 mN/m and an asymptotic high-concentration value σ_∞ = 13.18 mN/m. The response coefficient is k = 0.01737 $(g/t)^{-1}$. The fitted zero-concentration value is close to the observed 45.0 mN/m without being artificially constrained to pass through that point. The asymptote is consistent with the observed flattening of the dataset at high concentration.

Table 1. *Three-parameter exponential-model estimates and fit statistics*

Quantity	Estimate	Standard error	Approx. 95% CI	Unit
σ_0	45.81	1.55	42.39 to 49.23	mN/m
σ_∞	13.18	1.25	10.43 to 15.92	mN/m
k	0.01737	0.00238	0.01213 to 0.02260	$(g/t)^{-1}$
R^2	0.973	—	—	dimensionless
RMSE	1.59	—	—	mN/m
MAE	1.40	—	—	mN/m

The fitted equation is therefore $\sigma(C) = 13.18 + 32.63 \exp(-0.01737C)$, mN/m. It explains approximately 97.3% of the variance in the secondary dataset, with RMSE = 1.59 mN/m. Figure 2 shows that the fit captures the overall monotonic decrease and high-concentration plateau. The residual pattern includes several positive residuals between approximately 110 and 160 g/t and negative residuals near 65–80 and 190–210 g/t, so the model should be treated as a compact empirical correlation rather than a mechanistic law.

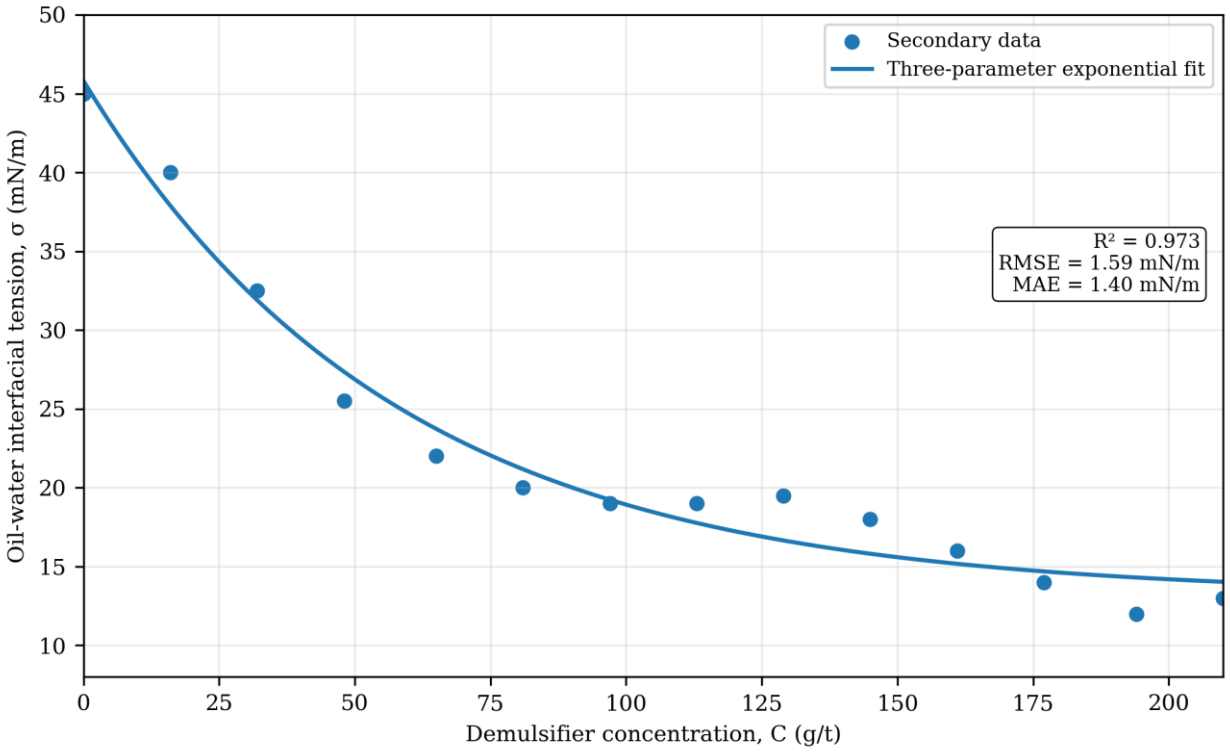


Figure 2. *Secondary interfacial-tension data and fitted three-parameter exponential model.*

3.2 Corrected calculated values

Table 2 regenerates all calculated IFT values directly from the fitted equation. This removes the internal inconsistency in the earlier manuscript, where the calculation column did not correspond to the stated fitted equation. The largest absolute residual in the present table is below 3 mN/m, and the table is numerically consistent with Equation (1).

ISSN: 2181-3337 | SCIENTISTS.UZ

Table 2. *Observed and model-calculated interfacial tension values*

C (g/t)	Observed σ (mN/m)	Calculated σ (mN/m)	Residual: observed − calculated (mN/m)
0	45.0	45.81	-0.81
16	40.0	37.89	+2.11
32	32.5	31.90	+0.60
48	25.5	27.36	-1.86
65	22.0	23.73	-1.73
81	20.0	21.17	-1.17
97	19.0	19.23	-0.23
113	19.0	17.76	+1.24
129	19.5	16.65	+2.85
145	18.0	15.81	+2.19
161	16.0	15.17	+0.83
177	14.0	14.69	-0.69
194	12.0	14.30	-2.30
210	13.0	14.03	-1.03

3.3 Saturation and diminishing returns

Equation (2) provides a transparent way to quantify where the response begins to saturate. The model reaches 80% of its attainable IFT reduction at 92.7 g/t, 90% at 132.6 g/t, and 95% at 172.5 g/t (Figure 3). At 100 g/t, R = 82.4%; at 130 g/t, R = 89.5%. Thus, the previously discussed 100–130 g/t interval can be retained only as a model-based screening band in which roughly 82–90% of the asymptotic IFT response has been realized.

The marginal-response metric leads to the same interpretation. M(0) is 0.567 mN/m per (g/t), whereas M(100), M(130), and M(200) are 0.100, 0.059, and 0.018 mN/m per (g/t), respectively. At approximately 132.6 g/t the model has achieved 90% of its total IFT reduction and the marginal effect has fallen to 10% of its initial value. This is a mathematically defined diminishing-return point, not a proof of minimum operating cost or maximum dehydration performance.

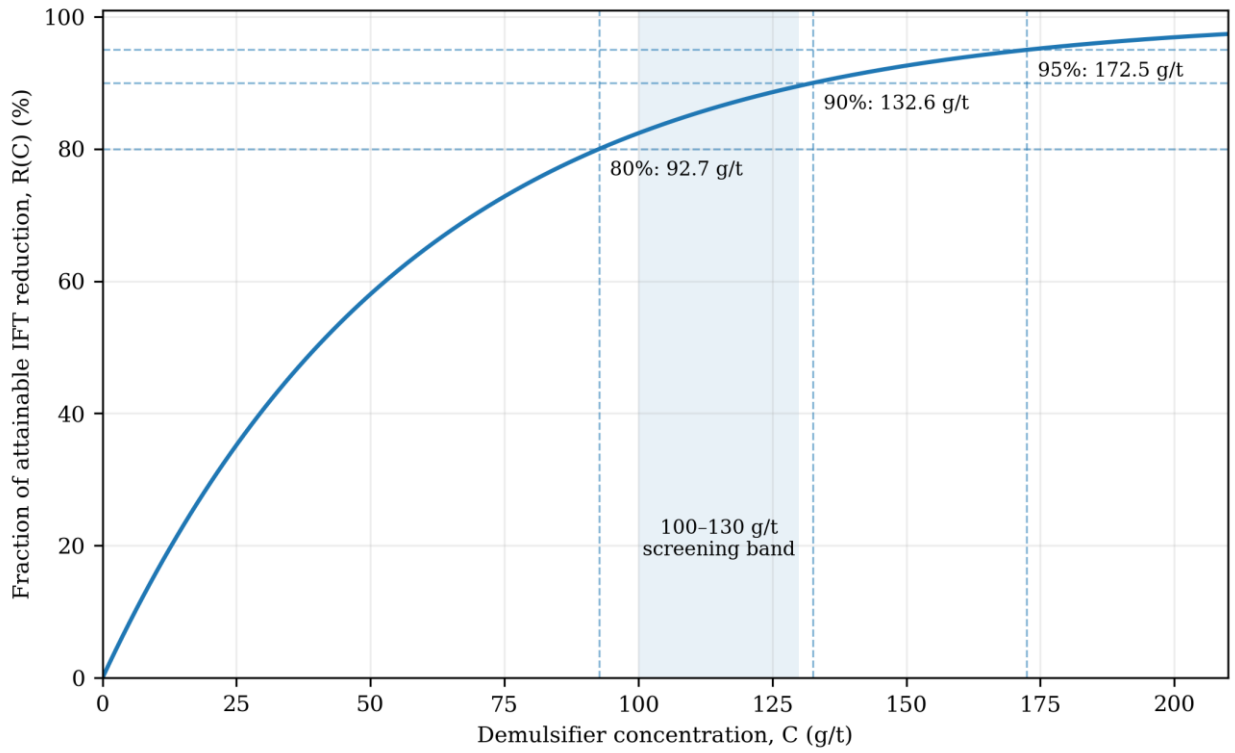


Figure 3. *Modeled fraction of attainable interfacial-tension reduction. The shaded 100–130 g/t region is a screening band for diminishing returns under the analyzed dataset, not a universal economic optimum.*

ISSN: 2181-3337 | SCIENTISTS.UZ

Table 3. *Model-based saturation indicators*

Indicator	Concentration (g/t)	Response achieved	Interpretation
80% response	92.7	80%	Onset of strong saturation
90% response	132.6	90%	Marginal effect ≈ 10% of initial
95% response	172.5	95%	Near-asymptotic response
Screening point	100.0	82.4%	Lower part of practical screening band
Screening point	130.0	89.5%	Upper part of practical screening band

3.4 Engineering interpretation and model boundaries

The correlation is most defensible as a compact computational block that converts demulsifier concentration into an expected IFT for the analyzed crude–water–demulsifier system. Such a block can be called inside a larger simulator that separately calculates droplet collision frequency, film drainage, coalescence efficiency, breakup, settling, residence time, and electrostatic effects. This modular use is consistent with population-balance approaches in which droplet-size evolution emerges from explicit aggregation and transport terms rather than from an assumed proportionality between IFT and diameter (Cunha et al., 2008; Kooti et al., 2023; Sharma & Thaokar, 2023; Su et al., 2023).

The present results do not establish a direct relation between decreasing IFT and decreasing "critical droplet diameter," and no diameter values are reported. This correction is important because the actual size of coalesced water droplets is precisely the quantity that controls settling velocity in Equation (5). Treating a decreasing proxy diameter as an actual droplet diameter would imply slower Stokes settling, contradicting the intended interpretation. A validated model must instead connect interfacial properties to coalescence kinetics and then calculate the evolving droplet-size distribution.

Similarly, Figure 1 should be interpreted as a process-integration schematic rather than an optimization result. The current dataset contains no experimental comparison of injection at the wellhead, upstream of a separator, upstream of a settler, or upstream of an electrostatic dehydrator. Injection-point selection must account for mixing energy, adsorption time, residence time, temperature, water cut, compatibility with other chemicals, and the downstream separation objective. Electrostatic equipment performance also depends on field strength, frequency, dielectric properties, viscosity, water fraction, and droplet interactions (Mhatre et al., 2015).

Finally, the 100–130 g/t range cannot be labeled economically optimal without a cost or performance objective. A genuine techno-economic optimization would require, at minimum, demulsifier cost, dehydration target, residual-water penalty, oil loss, throughput, temperature/energy demand, and residence-time constraints. The present model supplies only the concentration–IFT component of such an objective. Experimental evidence from other crude systems also shows that "optimum" demulsifier dosage depends on crude composition, asphaltene content, diluent, demulsifier formulation, and operating conditions (Rondón et al., 2008; Alara et al., 2022).

3.5 Limitations and validation requirements

First, the model is calibrated to a single secondary dataset derived from a published field-oriented study (Golubev & Khalikova, 2004). It should not be generalized to other crude oils, brines, demulsifier chemistries, temperatures, or water cuts without new calibration.

Second, the source data do not include replicate-level uncertainty. The reported confidence intervals therefore quantify regression uncertainty conditional on the listed points, not total experimental uncertainty. Future measurements should report replicate IFT values, instrument calibration, temperature, fluid composition, and demulsifier identity.

Third, the exponential relation is empirical. It provides a physically plausible monotonic saturation shape but does not resolve adsorption kinetics, interfacial rheology, film drainage, droplet collision

ISSN: 2181-3337 | SCIENTISTS.UZ

efficiency, or coalescence. Recent work indicates that IFT can be informative for demulsifier assessment, but it should be evaluated together with phase-separation performance and other interfacial properties (Freitas et al., 2025; Langevin et al., 2004).

Fourth, no independent validation dataset was available. Before field deployment, the model should be tested prospectively against new concentration–IFT measurements and against dehydration metrics such as separated-water fraction, residual basic sediment and water, droplet-size distribution, and settling time. For equipment-level prediction, those measurements should be linked to population-balance or multiphase models rather than to a direct IFT-to-diameter transformation (Oshinowo & Vilagines, 2020).

4. Conclusions

1. The concentration dependence of oil–water interfacial tension is well represented over 0–210 g/t by the three-parameter exponential relation $\sigma(C) = 13.18 + 32.63 \exp(-0.01737C)$, with $R^2 = 0.973$, RMSE = 1.59 mN/m, and MAE = 1.40 mN/m.

2. All tabulated calculated values have been regenerated directly from the fitted equation, eliminating the numerical inconsistency in the earlier manuscript.

3. Model-based diminishing-return thresholds occur at approximately 92.7 g/t for 80% response, 132.6 g/t for 90% response, and 172.5 g/t for 95% response. The 100–130 g/t interval therefore captures roughly 82–90% of the modeled IFT reduction and may be used as a screening range for the analyzed conditions, not as a universal economic optimum.

4. Interfacial tension is not converted directly into droplet diameter in the revised model. Prediction of actual droplet-size evolution, coalescence rate, and gravitational or electrostatic separation requires an independently formulated population-balance, coalescence, or multiphase model.

5. The fitted $\sigma(C)$ relation can serve as an input block within a broader field-oil-treatment simulator, but field optimization additionally requires validation across fluid compositions and operating conditions, explicit separation-performance data, and a techno-economic objective function.

Data Availability

The complete secondary numerical dataset used for regression is reproduced in Table 2. Its provenance is the concentration–IFT relation attributed to Golubev and Khalikova (2004). No new primary experimental measurements were generated in this modeling study.

REFERENCES

1. Alao, K. T., Alara, O. R., & Abdurahman, N. H. (2021). Trending approaches on demulsification of crude oil in the petroleum industry. Applied Petrochemical Research, 11, 281–293. https://doi.org/10.1007/s13203-021-00280-0
2. Alara, O. R., Abdurahman, N. H., Tade, M. O., Ali, H. A., & Alao, K. T. (2022). Demulsifier: An important agent in breaking crude oil emulsions. Chemical Engineering & Technology, 45(10), 1707–1720. https://doi.org/10.1002/ceat.202100556
3. Cunha, R. E. P., Fortuny, M., Dariva, C., & Santos, A. F. (2008). Mathematical modeling of the destabilization of crude oil emulsions using population balance equation. Industrial & Engineering Chemistry Research, 47(18), 7094–7103. https://doi.org/10.1021/ie800391v
4. Freitas, I. G., Perles, C. E., Guersoni, V. C. B., Pessanha, T. M., & Bannwart, A. C. (2025). Interfacial tension as a parameter to assess demulsifier efficiency on heavy crude oil emulsions. ACS Omega, 10(31), 34142–34150. https://doi.org/10.1021/acsomega.4c06425
5. Golubev, M. V., & Khalikova, A. I. (2004). Optimizatsiya protsessa podachi deemul'gatora [Optimization of the demulsifier injection process]. Neftegazovoe Delo, 2, 80–83. https://www.oil-info.ru/ngd/raz/Golubev_1.pdf
6. Kokal, S. L. (2005). Crude oil emulsions: A state-of-the-art review. SPE Production & Facilities, 20(1), 5–13. https://doi.org/10.2118/77497-PA

7. Kooti, G., Dabir, B., Taherdangkoo, R., & Butscher, C. (2023). Modelling droplet size distribution in inline electrostatic coalescers for improved crude oil processing. Scientific Reports, 13, 20209. https://doi.org/10.1038/s41598-023-46251-4
8. Langevin, D., Poteau, S., Hénaut, I., & Argillier, J.-F. (2004). Crude oil emulsion properties and their application to heavy oil transportation. Oil & Gas Science and Technology – Revue d'IFP, 59(5), 511–521. https://doi.org/10.2516/ogst:2004036
9. Mhatre, S., Vivacqua, V., Ghadiri, M., Abdullah, A. M., Al-Marri, M. J., Hassanpour, A., Hewakandamby, B. N., Azzopardi, B. J., & Kermani, B. (2015). Electrostatic phase separation: A review. Chemical Engineering Research and Design, 96, 177–195. https://doi.org/10.1016/j.cherd.2015.02.012
10. Oshinowo, L., & Vilagines, R. D. (2020). Modeling of oil–water separation efficiency in three-phase separators: Effect of emulsion rheology and droplet size distribution. Chemical Engineering Research and Design, 159, 278–290. https://doi.org/10.1016/j.cherd.2020.02.022
11. Raya, S. A., Mohd Saaid, I., Ahmed, A. A., & Umar, A. A. (2020). A critical review of development and demulsification mechanisms of crude oil emulsion in the petroleum industry. Journal of Petroleum Exploration and Production Technology, 10(4), 1711–1728. https://doi.org/10.1007/s13202-020-00830-7
12. Rondón, M., Pereira, J. C., Bouriat, P., Graciaa, A., Lachaise, J., & Salager, J.-L. (2008). Breaking of water-in-crude-oil emulsions. 2. Influence of asphaltene concentration and diluent nature on demulsifier action. Energy & Fuels, 22(2), 702–707. https://doi.org/10.1021/ef7003877
13. Saad, M. A., Kamil, M., Abdurahman, N. H., Yunus, R. M., & Awad, O. I. (2019). An overview of recent advances in state-of-the-art techniques in the demulsification of crude oil emulsions. Processes, 7(7), 470. https://doi.org/10.3390/pr7070470
14. Sharma, E., & Thaokar, R. M. (2023). Population balance modelling of an electrocoalescer. Chemical Engineering Science, 282, 119276. https://doi.org/10.1016/j.ces.2023.119276
15. Su, X., Yang, X., Yu, Y., Gao, F., & Wang, X. (2023). A simulation approach to predict electrostatic coalescence performance of water-in-oil emulsion using population balance model. Separation Science and Technology, 58(3), 538–550. https://doi.org/10.1080/01496395.2022.2131577

ISSN: 2181-3337 | SCIENTISTS.UZ

ISSN: 2181-3337 | SCIENTISTS.UZ VOLUME 5 ISSUE 7 JULY 2026

RECENT ADVANCES IN PROCESSING TECHNOLOGIES FOR ARONIA MELANOCARPA RAW MATERIALS: AN INTEGRATIVE REVIEW OF JUICE STABILIZATION, DRYING, EXTRACTION, ENCAPSULATION, AND BY-PRODUCT VALORIZATION

Mavlonova Madinabonu
Tashkent State Agrarian University

DOI: 10.67620/sai.57a0012

ABSTRACT

Black chokeberry (Aronia melanocarpa) is a polyphenol-rich berry whose industrial value depends strongly on processing. This integrative review evaluates peer-reviewed evidence published from 2019 through July 2026 on juice extraction and clarification, nonthermal stabilization, drying, phenolic extraction, encapsulation, and by-product valorization. The evidence does not support one universally superior technology; selection should follow the target product and the quality attribute being protected or recovered. Pulsed electric field pretreatment can increase juice yield and phenolic release, while thermosonication and high hydrostatic pressure can preserve juice color and bioactive compounds more effectively than severe thermal treatment under the studied conditions. Membrane clarification is mild but remains limited by fouling and cleaning. Freeze-drying provides strong retention of heat-sensitive compounds in premium powders, whereas spray drying is better suited to continuous production when carrier systems are optimized. Ultrasound-assisted, pressurized, enzymatic, deep-eutectic-solvent, and accelerated-solvent methods can improve recovery from pomace, although optimum conditions are compound-specific. Major research needs include microbial validation, sensory testing, scale-up, energy use, and techno-economic assessment. For Uzbekistan, the reviewed technologies should be treated as candidates for local pilot validation rather than as already proven industrial solutions.

ACCEPTED

07.08.26

Keywords: *Aronia melanocarpa, black chokeberry, anthocyanins, nonthermal processing, membrane filtration, freeze-drying, spray drying, ultrasound-assisted extraction, pomace valorization.*

CC BY

Introduction

Black chokeberry (*Aronia melanocarpa*) has become an important raw material for functional beverages, powders, natural colorants, and concentrated phenolic ingredients because its fruit contains abundant anthocyanins, proanthocyanidins, phenolic acids, and flavonols. At the same time, the fruit is naturally astringent and is therefore consumed more often in processed than in fresh form. Reviews of the species consistently identify processing as a decisive link between its phytochemical potential and the quality of products reaching consumers (Shi et al., 2024; Sidor et al., 2019; Xu et al., 2024).

The technological problem is not simply to maximize the concentration of one antioxidant marker. Industrial processing must also achieve microbiological safety, acceptable color and flavor, physical

stability, shelf life, throughput, and reasonable use of energy, water, solvents, enzymes, and packaging materials. These objectives can conflict. Thermal processes are robust and familiar but may accelerate anthocyanin degradation; mild clarification can preserve phenolics but may suffer from membrane fouling; freeze-drying can protect heat-sensitive compounds but is comparatively expensive; and intensified extraction can increase recovery while introducing solvent-recovery, scale-up, or regulatory challenges.

Recent research has therefore shifted from asking which single process is best to asking which sequence of unit operations is appropriate for a defined product. This distinction is especially important in Aronia research because juice pressing, microbial stabilization, dehydration, extraction, and encapsulation solve different engineering problems. A method that is optimal for recovery of phenolics from pomace should not be ranked directly against a drying technology used to produce whole-fruit powder. Likewise, an extraction yield cannot be treated as equivalent to retention during processing.

The purpose of the present review is to synthesize recent processing evidence by technological function rather than by a single undifferentiated ranking. The objectives are to (a) evaluate recent evidence for juice extraction, clarification, and stabilization; (b) compare drying and encapsulation routes for powders and phenolic ingredients; (c) assess emerging extraction and pomace-valorization strategies; (d) identify industrial constraints and research gaps; and (e) formulate cautious implications for future Aronia processing in Uzbekistan without claiming local validation that has not yet been performed.

Review Method

This paper was designed as an integrative review rather than a registered systematic review or meta-analysis. Its purpose is to synthesize recent technological evidence across processing stages and product objectives while clearly separating primary experimental evidence from review literature. Because the review was integrative and was not designed for quantitative effect pooling, a PRISMA flow diagram and meta-analytic estimates were not used.

The evidence base was updated through July 31, 2026. Targeted searches were conducted using PubMed and publisher platforms, including Springer Nature, ScienceDirect, Oxford Academic, the Royal Society of Chemistry, MDPI, and the American Chemical Society. Search combinations included "*Aronia melanocarpa*" or "black chokeberry" with terms such as processing, juice, pulsed electric field, high pressure, thermosonication, membrane filtration, microfiltration, ultrafiltration, freeze-drying, spray drying, encapsulation, ultrasound-assisted extraction, enzymatic extraction, pomace, polyphenols, anthocyanins, and valorization.

Core evidence was restricted to peer-reviewed original studies published from 2019 through July 2026 that directly investigated Aronia fruit, juice, pomace, or Aronia-derived extracts and reported quantitative processing or quality outcomes. Reviews were used only to establish context, terminology, and broader research directions; they were not treated as original experiments. Studies focused solely on clinical or pharmacological effects without a processing component were outside the scope. Where studies used different analytical assays, cultivars, moisture bases, or process scales, results were compared directionally rather than pooled statistically.

The synthesis was organized by processing purpose: juice release and clarification; microbial stabilization and quality preservation; drying and encapsulation; extraction and recovery from pomace; and circular utilization of by-products. Particular emphasis was placed on whether reported gains represented retention, extraction, physical stabilization, or process productivity. This distinction prevents inappropriate comparisons between technologies that act on different material streams or at different stages of manufacture.

Recent Advances in Juice Processing

Juice Release and Pulsed Electric Field Pretreatment

Mechanical pressing alone leaves a substantial fraction of soluble solids and phenolics within intact or only partly disrupted plant tissue. Pulsed electric field (PEF) pretreatment is attractive because short

ISSN: 2181-3337 | SCIENTISTS.UZ

electrical pulses increase cell membrane permeability without prolonged heating. In a 2026 study of aronia and haskap berries, Puzovic et al. (2026) applied PEF at 1.78, 5.3, and 10.7 kJ/kg before juice production. At the highest treatment intensity, aronia juice yield increased from 39.3% to 57.3%. The treatment also increased the extractability of sugars, organic acids, and phenolic compounds, although color changed progressively with treatment intensity.

The PEF results are important because they show that "preservation" is not the only mechanism by which a nonthermal technology can improve a juice. PEF may increase the amount of intracellular material transferred into the juice, so higher measured anthocyanins can reflect enhanced release rather than merely reduced degradation. This distinction should be made explicit when PEF is compared with sterilization or drying technologies. The study also identified unresolved scale-up questions concerning sensory quality, enzymatic activity, stability, and industrial implementation (Puzovic et al., 2026).

Membrane Clarification and Fouling Control

Membrane clarification is a mild alternative to clarification systems that depend heavily on thermal exposure or chemical fining. Lachowicz et al. (2019) compared ceramic microfiltration membranes with pore sizes of 0.2, 0.8, 1.4, and 5.0 micrometers for chokeberry juice. Among the tested membranes, the 0.8-micrometer membrane produced the best overall combination of low turbidity, viscosity, and precipitation while maintaining a relatively high concentration of bioactive compounds. The finding supports membrane selection as a product-quality decision rather than a simple assumption that the smallest pore size will always perform best.

More recent work has focused on the operational bottleneck of membrane fouling. Apaydin et al. (2026) applied interpretable deep-learning models to aronia juice ultrafiltration using polyethersulfone membranes under different pressures and flow rates. Their models simultaneously predicted permeate flux, fouling index, and cleaning efficiency and indicated that operation time and flow rate were more influential than membrane type within the experimental domain. Higher feed flow combined with moderate pressure produced a favorable balance among flux, fouling, and cleaning efficiency, and a 50-kDa hydrophilic membrane outperformed a 150-kDa membrane under the studied conditions. This study does not prove that artificial intelligence is necessary for juice filtration, but it demonstrates a useful shift toward multi-objective optimization rather than maximizing flux alone.

For industrial design, membrane clarification should therefore be evaluated with at least four outcomes: product clarity, retention or transmission of target phenolics, sustainable permeate flux, and cleaning requirements. A process that produces a clear juice but rapidly loses flux may be economically unattractive, while a high-flux process that removes too much color or desirable phenolic material may fail the product specification.

Nonthermal and Mild Stabilization of Juice

Microbial stabilization is necessary for commercial juice, but the severity of heat treatment can affect color and anthocyanin stability. Lv et al. (2024) compared ultra-high-temperature instantaneous treatment, thermosonication, high hydrostatic pressure (HHP), and irradiation for Aronia juice. All tested treatments provided microbial control under the study conditions, but thermosonication and HHP better preserved or enhanced total polyphenols, flavonoids, anthocyanins, and original juice color than the ultra-high-temperature and irradiation treatments. Thermosonication increased cyanidin-3-O-galactoside and cyanidin-3-O-arabinoside by 7.98% and 5.90%, respectively, whereas irradiation reduced these compounds by 15.74% and 10.46%.

These data support careful evaluation of nonthermal preservation, but they do not justify treating all high-pressure technologies as equivalent. High-pressure homogenization, high hydrostatic pressure, and ultra-high-pressure treatment operate through different mechanisms and pressure-time histories. Accordingly, results from one high-pressure technology should not be used as direct evidence for another.

When discussing commercial feasibility, pressure equipment cost, batch or semi-continuous operation, throughput, packaging compatibility, and validated microbial lethality remain central considerations.

A complementary 2025 study examined ultra-high-pressure treatment together with gallic-acid copigmentation as a strategy to improve the stability of Aronia anthocyanins in a model juice system (Zhao et al., 2025). The combined approach reduced pigment degradation and discoloration during storage under the investigated conditions. The result is promising for color stabilization, but the use of an added copigment means that it should be viewed as a formulation-plus-process intervention rather than as evidence for pressure treatment alone.

Drying and Encapsulation Technologies

Freeze-Drying for High-Retention Products

Drying extends shelf life and creates ingredients that are easier to store, transport, and formulate. However, dehydration exposes pigments and phenolics to different combinations of heat, oxygen, time, and surface area. In a direct comparison of freeze-drying, hot-air drying, oven drying, and sun drying after dipping pretreatments, Demircan et al. (2024) found that freeze-drying produced the highest process yield (29.07%-29.43%) and the strongest overall preservation of measured phenolics, flavonoids, antioxidant activity, and color. Under the most favorable freeze-drying/pretreatment condition reported in that study, total phenolics were approximately 38,176.5 mg gallic acid equivalents/kg, total flavonoids 6,537.1 mg catechin equivalents/kg, and antioxidant activity 9,602.8 mg Trolox equivalents/kg.

Freeze-drying therefore remains a strong option when the economic value of retaining heat-sensitive compounds justifies vacuum equipment, long cycle times, and high energy demand. It is particularly defensible for premium powders, research standards, nutraceutical ingredients, and high-value extracts. It is less defensible to describe freeze-drying as universally “best” without considering cost, throughput, and the intended selling price of the product.

Spray Drying and Carrier Selection

Spray drying offers a fundamentally different industrial proposition: rapid continuous powder production at high throughput, but with short exposure to elevated air temperatures and a need to manage stickiness, hygroscopicity, and pigment stability. Catalkaya et al. (2022) spray-dried an anthocyanin-rich extract from chokeberry pomace at 150 °C inlet and 90 °C outlet temperatures using several wall materials. The combination of maltodextrin DE20 and gum arabic provided the best overall performance, particularly in production yield and encapsulation efficiency, among the tested formulations.

The implication is that the performance of spray drying cannot be evaluated from inlet temperature alone. Carrier composition, feed solids, outlet temperature, residence time, atomization, and moisture targets jointly influence powder quality. For industrial functional-food ingredients, spray drying may be preferable to freeze-drying when continuous production and unit cost dominate the decision, provided that the selected formulation delivers acceptable anthocyanin retention and reconstitution behavior.

Emerging Encapsulation Carriers

Encapsulation research is also moving beyond conventional carbohydrate carriers. Aktürk Gümüşay et al. (2025) evaluated maltodextrin, gum arabic, a maltodextrin-gum-arabic blend, plasmolyzed yeast, and non-plasmolyzed yeast for freeze-dried microencapsulation of black chokeberry phenolic extract. Maltodextrin produced the highest encapsulation efficiency (98.82%), while non-plasmolyzed yeast achieved 86.58% and emerged as a viable alternative to gum arabic. Plasmolyzed yeast also showed favorable retention of phenolics during simulated gastrointestinal conditions.

These findings broaden the design space for functional ingredients, but they also highlight a critical point: encapsulation performance should be judged against the intended use. Maximum encapsulation efficiency, storage stability, gastrointestinal release, sensory impact, allergen labeling, ingredient cost, and regulatory status can favor different carrier systems. A carrier that performs well analytically may not be optimal in a beverage or bakery application if it adversely affects flavor, color, or dispersibility.

ISSN: 2181-3337 | SCIENTISTS.UZ

Extraction and Recovery of Phenolics

Ultrasound-Assisted and Pressurized Extraction

Pomace is not simply a waste stream. Because skins and residual pulp retain anthocyanins, proanthocyanidins, phenolic acids, and dietary fiber after pressing, the residue can function as a secondary raw material. One of the strongest recent demonstrations of process intensification is the ultrasound-assisted pressurized liquid extraction study by Andrade et al. (2021). Under optimized conditions using an aqueous citric-acid system, the process extracted 88.0% of anthocyanins within 45 minutes and increased total anthocyanin recovery by 19% relative to the corresponding batch process.

Aprodu et al. (2025) further demonstrated that ultrasound parameters need to be optimized rather than maximized. In their work on Aronia pomace, ultrasound amplitude was varied from 20% to 60% for 10 minutes; a 30% amplitude gave the highest total polyphenol concentration and antioxidant activity under the studied conditions. Ethanol-based extracts generally performed better than water extracts for phenolic recovery. The finding illustrates why statements such as “higher ultrasound power gives higher recovery” are unsafe without qualification: excessive intensity may not improve extraction and can increase energy demand or accelerate degradation.

Emerging solvent systems also deserve attention. Sun et al. (2026) compared ultrasound-assisted deep eutectic solvent extraction with conventional 80% methanol and 60% ethanol extraction. The deep eutectic solvent extract had the highest total polyphenol content (84.56 ± 3.85 mg/g), and 49 polyphenolic compounds were identified after purification and chromatographic analysis. The approach is attractive from a green-extraction perspective, but industrial adoption will require careful evaluation of solvent formulation, viscosity, downstream separation, recovery, food-contact acceptability, and life-cycle performance.

Enzyme-Assisted Extraction

Cell-wall-degrading enzymes offer another strategy for releasing pigments from pomace under mild conditions. Kim et al. (2024) evaluated pectinolytic and cellulolytic enzymes for anthocyanin recovery. Pectinex XXL at 0.5% gave the highest total anthocyanin extraction among the single-enzyme treatments (2,082.41 ± 85.69 mg/100 g), while a combination of 0.25% Pectinex XXL and 0.01% Celluclast increased total anthocyanin extraction to 2,323.04 ± 61.32 mg/100 g, approximately 50.7% higher than the solvent-extraction comparator used in the study.

The results make enzyme-assisted extraction especially relevant where mild temperature, food-compatible processing, and natural-color production are priorities. However, enzyme cost, activity under the actual pomace pH and solids concentration, enzyme inactivation, residence time, and downstream clarification must be incorporated into any industrial comparison. Laboratory extraction yield alone is insufficient to establish process economics.

Preservation of Pomace Before Extraction

The quality of an extraction process depends strongly on what happens to pomace before extraction begins. Sawicki et al. (2026) compared preservation techniques for Aronia pomace and then optimized accelerated solvent extraction for different polyphenol classes. Drying significantly reduced anthocyanin concentrations, while freezing and freeze-drying had smaller effects. Importantly, the optimized extraction conditions were compound-specific: conditions that favored phenolic acids were not identical to those that favored anthocyanins.

This study directly challenges the idea that one extraction condition can maximize every phenolic class. For industrial design, the first decision should be which compound group is the commercial target. The second should be how quickly the by-product can be stabilized after pressing. If pomace remains warm and oxygen-exposed before drying or freezing, subsequent extraction optimization cannot fully recover compounds that have already degraded.

ISSN: 2181-3337 | SCIENTISTS.UZ

By-Product Valorization and Circular Processing

A circular processing model treats juice and pomace as co-products rather than assigning all value to the liquid stream. Lee et al. (2024) optimized antioxidant recovery from aronia juice-processing residue using statistical multi-prediction models. Their optimized extraction conditions balanced agitation, solid loading, ethanol concentration, and solvent volume and recovered substantial polyphenol, flavonoid, and anthocyanin fractions from a material that would otherwise have limited value. The study demonstrates how process optimization can connect waste reduction with production of natural antioxidant ingredients.

The same logic is evident in the extraction and encapsulation studies discussed above. Pomace can be stabilized, extracted, purified, and converted into colorant or antioxidant powders (Andrade et al., 2021; Catalkaya et al., 2022; Kim et al., 2024). Recent reviews also describe broader applications of Aronia fractions in foods and functional ingredients (Shi et al., 2024; Wieloch & Konopacka, 2025; Xu et al., 2024). Nevertheless, "valorization" should not be assumed to be environmentally beneficial merely because a waste stream is used. Solvent consumption, energy for drying or freezing, water use, carrier materials, purification losses, and transport can offset part of the environmental benefit.

Accordingly, future by-product studies should report mass balances and, where possible, solvent recovery, energy demand, and product yield per kilogram of fresh fruit or pomace. This would make it possible to compare a high-recovery laboratory method with a lower-recovery method that may be substantially simpler and less resource intensive at scale.

Table 1

Representative Primary Studies Supporting the Comparative Synthesis

Study	Material/process	Key conditions or comparison	Main evidence relevant to processing
Lachowicz et al. (2019)	Chokeberry juice; ceramic microfiltration	0.2, 0.8, 1.4, and 5.0 μm membranes	The 0.8-μm membrane gave the best balance of low turbidity and precipitation while retaining relatively high bioactive content.
Andrade et al. (2021)	Pomace; ultrasound-assisted pressurized liquid extraction	Optimized pressure, temperature, ultrasound, solvent, and flow	Achieved 88% anthocyanin extraction in 45 min and 19% higher total anthocyanin content than the corresponding batch process.
Catalkaya et al. (2022)	Pomace extract; spray-drying encapsulation	150 °C inlet, 90 °C outlet; multiple wall materials	Maltodextrin DE20 + gum arabic performed best overall, especially for production yield and encapsulation efficiency.
Demircan et al. (2024)	Fruit; freeze-, hot-air-, oven-, and sun-drying	Drying methods after dipping pretreatments	Freeze-drying showed the strongest overall preservation and the highest process yield (29.07%-29.43%).
Kim et al. (2024)	Pomace; enzyme-assisted extraction	Pectinase/cellulase treatments and combinations	Pectinex XXL + Celluclast increased total anthocyanin extraction by about 50.7% versus the study solvent-extraction comparator.

ISSN: 2181-3337 | SCIENTISTS.UZ

Study	Material/process	Key conditions or comparison	Main evidence relevant to processing
Lee et al. (2024)	Juice-processing residue; ethanol extraction	Response-surface/multi-prediction optimization	Demonstrated recoverable polyphenol, flavonoid, and anthocyanin fractions and a process route for circular use of residue.
Lv et al. (2024)	Juice; sterilization/stabilization	UHT, thermosonication, HHP, irradiation	Thermosonication and HHP better preserved or enhanced phenolics, anthocyanins, and color than UHT and irradiation under the tested conditions.
Aktürk Gümüşay et al. (2025)	Phenolic extract; freeze-dried microencapsulation	Maltodextrin, gum arabic, blends, yeast carriers	Maltodextrin reached 98.82% encapsulation efficiency; non-plasmolyzed yeast (86.58%) was a viable alternative carrier.
Aprodu et al. (2025)	Pomace; ultrasound-assisted extraction	20%-60% amplitude for 10 min; water vs ethanol	A 30% amplitude produced the strongest total-polyphenol/antioxidant outcome within the tested range; ethanol was generally more effective.
Zhao et al. (2025)	Juice system; ultra-high pressure + gallic acid	Pressure treatment with copigmentation	Combined treatment improved anthocyanin/color stability during storage, showing value of process-formulation integration.
Apaydin et al. (2026)	Juice; ultrafiltration + interpretable deep learning	36 runs; multiple membrane/pressure/flow conditions	Models jointly predicted flux, fouling, and cleaning efficiency and supported multi-objective operating-point selection.
Puzovic et al. (2026)	Fruit/juice; PEF pretreatment	1.78, 5.3, 10.7 kJ/kg	At 10.7 kJ/kg, aronia juice yield increased from 39.3% to 57.3%, with greater release of phenolics and other soluble components.
Sawicki et al. (2026)	Pomace; preservation + accelerated solvent extraction	Drying/freezing/freeze-drying; compound-specific ASE optimization	Drying reduced anthocyanins; optimal extraction conditions differed by polyphenol class.
Sun et al. (2026)	Fruit polyphenols; ultrasound-assisted DES extraction	DES vs 80% methanol and 60% ethanol	DES extraction produced the highest total polyphenol content (84.56 ± 3.85 mg/g) and strong antioxidant activity.

Note. Values and conclusions are specific to the cited experimental conditions; they should not be interpreted as universal process guarantees. HHP = high hydrostatic pressure; PEF = pulsed electric field; DES = deep eutectic solvent; ASE = accelerated solvent extraction.

ISSN: 2181-3337 | SCIENTISTS.UZ

Comparative Technology Selection Framework

The accumulated evidence supports a decision framework based on product objective rather than a universal ranking. For clarified juice, membranes are attractive because they operate under mild thermal conditions, but fouling and cleaning govern long-term feasibility. For juice-yield enhancement, PEF is promising because it increases cell permeability before pressing. For microbial stabilization, thermosonication and HHP can provide quality advantages over severe heating under appropriate validated conditions. These functions can be combined in a processing line; they are not mutually exclusive.

For powders, the central tradeoff is typically retention versus throughput and unit cost. Freeze-drying is appropriate when maximum preservation of heat-sensitive components has high economic value. Spray drying is more appropriate when continuous production and scalable powder manufacture are priorities, provided that carriers and outlet conditions are optimized. Encapsulation adds another design layer because a wall material can improve stability but also affects ingredient labeling, cost, dispersibility, and downstream sensory quality.

For extracts, recovery should be reported by compound class and mass basis. Ultrasound, enzymes, pressure, deep eutectic solvents, and accelerated solvent extraction can all enhance recovery, but the optimum depends on the target compound, solvent system, temperature, and pretreatment history. Claims that one extraction technology has the "highest preservation" are conceptually misleading; extraction methods should instead be compared for recovery, selectivity, solvent and energy demand, and downstream purification burden.

Table 2

Evidence-Based Selection of Processing Technologies by Product Objective

Technology	**Best-fit objective**	**Evidence-supported advantage**	**Principal limitations / validation needs**
PEF pretreatment	Increase juice release before pressing	Can substantially increase juice yield and release of phenolics without prolonged heating.	Capital cost, pulse-energy optimization, color/sensory effects, enzyme activity, and scale-up validation.
Ceramic microfiltration / ultrafiltration	Clarified juice	Mild clarification with good control of turbidity; operating conditions can be optimized for quality and flux.	Fouling, flux decline, cleaning chemistry/water use, membrane replacement, and possible selective loss of compounds.
Thermosonication	Juice stabilization	In the available Aronia study, preserved functional components and color better than UHT and irradiation.	Microbial process validation, acoustic scale-up, energy use, equipment integration, sensory effects.
High hydrostatic pressure	Premium juice stabilization	Strong quality retention under studied conditions and limited thermal exposure.	High capital cost, pressure-vessel throughput, packaging constraints, validated lethality requirements.
Freeze-drying	Premium whole-fruit or extract powder	Strong retention of thermolabile compounds and color.	High energy demand, long cycle time, vacuum equipment, higher unit cost.
Spray drying + carriers	High-throughput powder / colorant ingredient	Continuous scalable powder production; carrier selection can improve encapsulation efficiency.	Thermal exposure, carrier requirement, stickiness/hygroscopicity, formulation-dependent retention.

ISSN: 2181-3337 | SCIENTISTS.UZ

Technology	Best-fit objective	Evidence-supported advantage	Principal limitations / validation needs
Ultrasound-assisted extraction	Phenolic-rich extracts from pomace	Short processing times and enhanced mass transfer; effective at optimized rather than maximal amplitude.	Solvent selection/recovery, scale-up of acoustic field, energy intensity, risk of overprocessing.
Enzyme-assisted extraction	Anthocyanin/colorant recovery from pomace	Mild processing and strong release of anthocyanins with optimized pectinase/cellulase combinations.	Enzyme cost, reaction time, pH/temperature control, downstream clarification and inactivation.
Pressurized / accelerated solvent extraction	Targeted high-value phenolic fractions	High recovery and tunable selectivity; conditions can be optimized by compound class.	Pressurized equipment, solvent recovery, temperature-sensitive compounds, scale and regulatory considerations.
Deep eutectic solvent extraction	Emerging green extraction	High polyphenol recovery and potential reduction in reliance on conventional organic solvents.	Food-grade formulation, viscosity, separation/recovery, residue limits, life-cycle and techno-economic validation.

Note. The framework summarizes best-supported uses in the reviewed literature and is not a substitute for product-specific hazard analysis, shelf-life testing, sensory validation, or techno-economic assessment.

Implications for Future Processing in Uzbekistan

The reviewed literature does not provide direct experimental evidence that the cited Aronia processing technologies have been optimized for Uzbek cultivars, utilities, supply chains, or production economics. Therefore, the technologies reviewed here should be treated as candidates for local pilot testing rather than validated recommendations for national-scale adoption.

A rational development pathway would begin with local raw-material characterization across cultivars, harvest dates, and storage periods. Key baseline measures should include fruit moisture, soluble solids, titratable acidity, anthocyanin profile, total phenolics, astringency-related compounds, pressing yield, and pomace generation. Without these data, equipment settings taken from studies in other countries may not transfer reliably.

For juice, a pilot line could compare conventional pressing with PEF-assisted pressing, followed by membrane clarification when a clear product is desired. Microbial stabilization should then be validated using the technology actually available locally, comparing conventional thermal treatment with thermosonication or HHP only where equipment access and economics are realistic. Freeze-drying should initially be reserved for high-value products because of its energy and capital intensity, while spray drying may be more realistic for larger-volume powder manufacture if carrier materials and feed formulation are locally available.

Pomace should be incorporated into the process plan from the beginning. The most important operational question is how quickly it can be cooled, frozen, or otherwise stabilized after pressing. Pilot extraction can then compare food-compatible ethanol, ultrasound-assisted extraction, and enzyme-assisted extraction before more complex pressurized or deep-eutectic-solvent systems are considered. Local techno-economic analysis should include electricity and gas prices, water demand, solvent recovery, enzyme and carrier costs, labor, maintenance, wastewater, cold-chain requirements, seasonal fruit availability, and attainable selling prices.

This staged approach is more scientifically robust than claiming that a technology is suitable for Uzbekistan merely because it performed well elsewhere. It converts the international literature into testable local engineering hypotheses and creates the data needed for subsequent scale-up decisions.

Research Gaps and Future Directions

Head-to-head processing comparisons. Many studies compare conditions within one technology but not different technologies on the same batch of Aronia. Future work should use a common raw material and standardized analytical methods to compare retention, yield, sensory quality, microbial safety, and energy use.

Industrial-scale mass and energy balances. Laboratory recovery percentages are insufficient for process selection. Studies should report product yield per kilogram of fruit, water and solvent use, specific energy demand, cleaning requirements, and waste streams.

Standardized definitions of retention and recovery. Processing papers should clearly distinguish concentration caused by water removal, true retention of a compound, extraction yield from the original matrix, and analytical values expressed on wet- or dry-weight bases.

Shelf-life and microbial validation. Nonthermal technologies require validated microbial outcomes and storage studies, not only immediate measurements of phenolics or color.

Sensory and consumer outcomes. Aronia is highly astringent. A process that maximizes phenolic extraction may intensify astringency or bitterness. Sensory evaluation should therefore be integrated with chemical optimization.

Compound-specific optimization. Recent pomace work shows that optimal conditions differ among anthocyanins, phenolic acids, and other polyphenols. Multi-response optimization should avoid assuming a single extraction point maximizes all targets.

Techno-economic and environmental assessment. High-pressure equipment, freeze-drying, solvent recovery, enzymes, and encapsulating carriers have distinct cost and environmental profiles. Life-cycle and economic studies are needed before laboratory advantages are translated into sustainability claims.

Local validation. For Uzbekistan and other emerging production regions, cultivar composition, seasonal logistics, equipment availability, utilities, food regulations, and market requirements should be measured directly rather than inferred from foreign studies.

Limitations of This Review

This integrative review is not a registered systematic review and should not be interpreted as an exhaustive evidence census. Although recent primary studies were verified against publisher or bibliographic records and the literature was updated through July 2026, the search was targeted rather than exhaustive. Therefore, absence of a study from this review should not be interpreted as evidence that the study does not exist.

Direct quantitative comparison is also limited by heterogeneity. Studies used different cultivars, harvest conditions, moisture bases, analytical standards, antioxidant assays, extraction solvents, and process scales. Values reported in one study should not be transferred to another matrix without validation. Finally, industrial applicability was assessed qualitatively from process characteristics and study design because most Aronia-specific publications do not provide complete capital-cost, operating-cost, or life-cycle data.

Conclusion

Recent processing research shows that *Aronia melanocarpa* should be treated as a family of product streams rather than as a single raw material with one “best” processing technology. PEF can improve juice release; membrane filtration can provide mild clarification; thermosonication and HHP can protect juice quality under validated conditions; freeze-drying can preserve heat-sensitive compounds in high-value powders; and spray drying can support continuous production when carrier systems are optimized. For

ISSN: 2181-3337 | SCIENTISTS.UZ

pomace, ultrasound-assisted, pressurized, enzymatic, deep-eutectic-solvent, and accelerated-solvent approaches provide complementary routes for recovering phenolic fractions.

The central conclusion is therefore product-specific. The optimal technology is the one that meets a defined safety, quality, throughput, cost, and sustainability specification for the intended product. Retention during drying should not be conflated with extraction yield, and evidence from one type of high-pressure process should not be generalized to another. Pomace preservation and valorization should be planned as part of the primary production line rather than as an afterthought.

For future Aronia processing in Uzbekistan, the reviewed international evidence provides a strong foundation for pilot-scale experimentation but not yet for claims of locally proven superiority. Local cultivar characterization, sensory studies, microbial validation, mass and energy balances, and techno-economic analysis are necessary before industrial recommendations can be considered evidence based.

REFERENCES

1. Aktürk Gümüşay, Ö., Cerit, İ., & Demirkol, O. (2025). Utilization of yeast cells as alternative carriers in the microencapsulation of black chokeberry (*Aronia melanocarpa*) phenolic extract. *Foods, 14*(4), 625. https://doi.org/10.3390/foods14040625
2. Andrade, T. A., Hamerski, F., López Fetzer, D. E., Roda-Serrat, M. C., Corazza, M. L., Norddahl, B., & Errico, M. (2021). Ultrasound-assisted pressurized liquid extraction of anthocyanins from *Aronia melanocarpa* pomace. *Separation and Purification Technology, 276*, Article 119290. https://doi.org/10.1016/j.seppur.2021.119290
3. Apaydin, A. S., Ozturk, E., & Onsekizoglu Bagci, P. (2026). Deep learning-based modeling and optimization of aronia juice ultrafiltration: A multi-output interpretable approach. *European Food Research and Technology, 252,* Article 294. https://doi.org/10.1007/s00217-026-05206-5
4. Aprodu, I., Chitescu, C. L., Grigore-Gurgu, L., & Dumitrașcu, L. (2025). Investigation of the antioxidant and antimicrobial properties of ultrasound-assisted extracted phenolics from *Aronia melanocarpa* pomace. *Applied Sciences, 15*(13), 7070. https://doi.org/10.3390/app15137070
5. Catalkaya, G., Guldiken, B., & Capanoglu, E. (2022). Encapsulation of anthocyanin-rich extract from black chokeberry (*Aronia melanocarpa*) pomace by spray drying using different coating materials. *Food & Function, 13*(22), 11579-11591. https://doi.org/10.1039/D2FO02569H
6. Demircan, B., Velioglu, Y. S., & Bozturk, M. M. (2024). Effect of dipping pre-treatments and drying methods on *Aronia melanocarpa* quality. *Food Chemistry, 457*, Article 140109. https://doi.org/10.1016/j.foodchem.2024.140109
7. Kim, J., Lee, Y., Suh, H.-J., Lee, H.-S., & Lee, C. (2024). Enzymatic extraction of anthocyanins from the pomace of aronia (*Aronia melanocarpa*). *Bioscience, Biotechnology, and Biochemistry, 88*(6), 639-647. https://doi.org/10.1093/bbb/zbae037
8. Lachowicz, S., Oszmiański, J., Kolniak-Ostek, J., & Stokłosa, D. (2019). Effect of different sizes of ceramic membranes in the process of microfiltration on physicochemical parameters of chokeberry juice. *European Food Research and Technology*, *245*(6), 1263-1275. https://doi.org/10.1007/s00217-019-03246-8
9. Lee, K. H., Kim, S., Lee, J., Son, H., Lee, J. U., Park, C., & Yoo, H. Y. (2024). Improved recovery of antioxidants from aronia juice processing residue via optimization of extraction variables based on multi-prediction models. *Sustainable Chemistry and Pharmacy, 39*, Article 101546. https://doi.org/10.1016/j.scp.2024.101546
10. Lv, X., Lan, T., Wang, S., Li, X., Bao, S., Li, T., Sun, X., & Ma, T. (2024). Comparative study on the physicochemical properties, functional components, color and anthocyanins profile of *Aronia melanocarpa* juice using different sterilization methods. *Food Innovation and Advances, 3*(2), 64-74. https://doi.org/10.48130/fia-0024-0008

11. Puzovic, A., Rinaldi, M., Assaf, N., & Mikulic-Petkovsek, M. (2026). Impact of pulsed electric field pretreatment on quality parameters of aronia and haskap berry juices. *European Food Research and Technology, 252*, Article 150. https://doi.org/10.1007/s00217-026-05081-0
12. Sawicki, J., Wójciak, W., Żuk, M., Dresler, S., Sowa, I., Skalska-Kamińska, A., & Wójciak, M. (2026). Impact of preservation techniques on polyphenols in *Aronia melanocarpa* pomace and their recovery by optimized accelerated solvent extraction. *Applied Sciences, 16*(9), 4116. https://doi.org/10.3390/app16094116
13. Shi, D., Xu, J., Sheng, L., & Song, K. (2024). Comprehensive utilization technology of *Aronia melanocarpa*. *Molecules, 29*(6), 1388. https://doi.org/10.3390/molecules29061388
14. Sidor, A., Drożdżyńska, A., & Gramza-Michałowska, A. (2019). Black chokeberry (*Aronia melanocarpa*) and its products as potential health-promoting factors - An overview. *Trends in Food Science & Technology, 89*, 45-60. https://doi.org/10.1016/j.tifs.2019.05.006
15. Sun, Y., Zhang, H., Guo, D., Wu, P., & Li, C. (2026). Separation, purification, component identification, and bioactivity analysis of polyphenols from *Aronia melanocarpa*. *ACS Omega, 11*(9), 15417-15428. https://doi.org/10.1021/acsomega.5c13084
16. Wieloch, D., & Konopacka, D. (2025). Black chokeberry extracts (*Aronia melanocarpa*) as an ingredient of functional food - Potential, challenges and directions of development. *Molecules, 30*(21), 4237. https://doi.org/10.3390/molecules30214237
17. Xu, J., Li, F., Zheng, M., Sheng, L., Shi, D., & Song, K. (2024). A comprehensive review of the functional potential and sustainable applications of *Aronia melanocarpa* in the food industry. *Plants, 13*(24), 3557. https://doi.org/10.3390/plants13243557
18. Zhao, J., Zhao, S., Wang, Y., Ma, C., Tian, J., Wang, A., & Li, B. (2025). Effect of combined ultra-high pressure gallic acid cochromism on the stability of *Aronia melanocarpa* anthocyanins in juice systems. *Food Chemistry: X, 29*, Article 102701. https://doi.org/10.1016/j.fochx.2025.102701

ISSN: 2181-3337 | SCIENTISTS.UZ

ISSN: 2181-3337 | SCIENTISTS.UZ VOLUME 5 ISSUE 7 JULY 2026

SEASONAL GROWTH PERFORMANCE OF "GAMLIN" AND "RA'NO" SWEET ORANGE CULTIVARS GRAFTED ON MEYER AND MANZUR LEMON ROOTSTOCKS

Turobova Vazira
Scientific Research Institute of Horticulture, Viticulture and Winemaking named after Academician M. Mirzaev Tashkent, Uzbekistan

DOI: 10.67620/sai.57a0013

ABSTRACT
Rootstock choice can strongly influence vegetative development of grafted citrus nursery plants, but local rootstock–scion responses must be evaluated for individual cultivar combinations. This study describes seasonal growth of the sweet orange cultivars 'Gamlin' and 'Ra'no' grafted on Meyer and Manzur lemon rootstocks under greenhouse conditions from June 1 to November 15, 2025. The stated design comprised two cultivars, two rootstocks, four biological replicates, 12 sampling dates, and measurements at the root collar and at 10, 20, and 30 cm stem positions. This structure corresponds to 16 plants, 192 plant-date records, and 768 position-level observations. Across the archived repeated observations, all four cultivar–rootstock combinations increased during the season. Descriptive final values favored Meyer rootstock: averaged across cultivars and stem positions, the final recorded growth measurement was 25.93 for Meyer compared with 17.67 for Manzur, and the mean absolute seasonal increase was 18.97 compared with 11.10, respectively. The largest absolute increase was observed for 'Ra'no' × Meyer at the root collar (26.12), whereas the largest final value occurred for 'Gamlin' × Meyer at 30 cm (34.75). These findings indicate greater vegetative development on Meyer under the conditions represented in the archived dataset. Because the original plant-level repeated-measures dataset was not available for re-analysis, previous factorial ANOVA, correlation, principal component, and cluster results are not treated as confirmatory evidence in this revision.

ACCEPTED

08.08.26

Keywords: *Citrus sinensis, rootstock, scion, Meyer lemon, Manzur lemon, nursery growth, repeated measurements.*

CC BY

Introduction

Sweet orange (Citrus sinensis) is commonly propagated by grafting, so nursery and orchard performance reflects the combined effects of the scion genotype, rootstock genotype, environment, and management. Rootstocks can influence tree vigor, size, nutrient relations, stress responses, and productivity, which makes rootstock selection a central decision in citrus production (Carvalho et al., 2024; Kunwar et al., 2023; Roberto et al., 2022). Rootstock effects are not universal: the same rootstock can produce different outcomes with different scions or under different environmental conditions. Consequently, locally relevant comparisons are needed before a rootstock is recommended for a specific cultivar or nursery system.

Several mechanisms have been proposed to explain rootstock-mediated changes in scion growth. Root system architecture, hydraulic conductance, nutrient acquisition, vascular development, and long-distance signaling can all contribute to differences in shoot vigor (Biasuz & Kalcsits, 2023; Mauro et al., 2022; Wang et al., 2025). These mechanisms should, however, be distinguished from the direct evidence provided by a growth experiment. Greater stem development alone can demonstrate a difference in vegetative performance, but it cannot by itself establish superior hydraulic conductivity, nutrient uptake, hormone transport, or graft compatibility. Direct physiological or anatomical measurements are needed to support those mechanistic conclusions.

Time-resolved measurements are useful because a single endpoint cannot describe the course of nursery development. Repeated measurements can reveal whether treatments differ mainly in early growth, mid-season acceleration, or late-season stabilization. Measurements at several stem positions can also describe how growth is distributed along the plant. Multivariate and inferential approaches can be informative when the underlying experimental unit and repeated-measures structure are modeled correctly, but repeated observations on the same plant are not statistically independent. A valid inferential analysis therefore requires plant identifiers and a repeated-measures or mixed-effects model rather than an ordinary factorial analysis that treats every observation as independent.

The archived study compared two sweet orange cultivars, ‘Gamlin’ and ‘Ra’no’, grafted on Meyer and Manzur lemon rootstocks. The practical question was whether the two rootstocks were associated with different seasonal vegetative development and whether the response depended on cultivar and stem position. The present revision has three objectives: (a) to present the archived growth results with corrected sample accounting and consistent cultivar naming, (b) to restrict conclusions to effects that are directly supported by the available measurements, and (c) to provide a statistically defensible framework for confirmatory re-analysis when the plant-level dataset becomes available.

Method

Study Design

The experiment was conducted under greenhouse conditions during the 2025 growing season. Two sweet orange cultivars (‘Gamlin’ and ‘Ra’no’) were evaluated on two lemon rootstocks (Meyer and Manzur), producing four cultivar–rootstock combinations. Four biological replicates were stated for each combination. Measurements were collected on 12 dates from June 1 through November 15, 2025, at the root collar and at 10, 20, and 30 cm stem positions. On the basis of the stated factorial structure, the experiment contained 16 biological plants, 192 plant-date records (16 plants × 12 dates), and 768 position-level measurements (192 plant-date records × 4 positions). The previously stated total of 96 plant-date records was an arithmetic inconsistency and is corrected here.

Plant Material and Nursery Conditions

The archived manuscript identifies the scions as ‘Gamlin’ and ‘Ra’no’ sweet orange and the rootstocks as Meyer and Manzur lemon materials propagated in a greenhouse nursery. It does not document the exact greenhouse location, plant age at grafting, grafting method and date, rootstock cutting age, container volume, substrate composition, irrigation schedule, fertilizer program, pest-management program, temperature, relative humidity, or light regime. These variables can influence citrus growth and should be restored from the original nursery records before submission to a journal that requires full experimental reproducibility. No values for these missing conditions have been invented in this revision.

Growth Measurements

Measurements were recorded at the root collar and at fixed positions 10, 20, and 30 cm along the stem. The archived manuscript repeatedly describes the response as stem growth or stem thickening and labels the numerical unit as centimeters. However, the measurement instrument and the exact dimensional trait (e.g., diameter, circumference, or another stem-growth metric) are not specified. Accordingly, this revision refers to the response as the stem growth measurement and retains the unit exactly as recorded in

ISSN: 2181-3337 | SCIENTISTS.UZ

the archived dataset. The underlying field sheets should be checked before publication to verify both the trait definition and unit.

Data Integrity and Statistical Analysis

Descriptive values were taken from the archived treatment table, which reports initial value, final value, absolute seasonal increase, and percentage increase for each cultivar × rootstock × position combination. Treatment-level summaries were recalculated from those reported values. The principal descriptive outcomes are the final measurement and absolute seasonal increase because percentage change can become very large when the initial value is small, as occurred for some cells.

Confirmatory factorial ANOVA, Pearson correlation, principal component analysis, Ward clustering, and simple regression are not reproduced as inferential evidence in this revision. The design contains repeated observations on the same biological plants across both dates and stem positions, so ordinary analyses that assume independent observations would underestimate within-plant dependence. A defensible confirmatory analysis should use the plant as the experimental unit, include plant identity as a random effect, treat date and position as within-plant factors, and consider an appropriate within-plant covariance structure (for example, autoregressive correlation across dates). Estimated marginal means, 95% confidence intervals, and multiplicity-adjusted contrasts should then be reported. Because the raw plant-level records were not contained in the uploaded manuscript, such a mixed-effects analysis cannot be reconstructed without inventing data.

Results

Seasonal Growth Pattern

The archived repeated-observation plot showed increasing mean growth over the June-to-November period for all four cultivar–rootstock combinations. Growth was comparatively slow during the earliest observations, increased more strongly during the middle of the season, and approached a plateau toward the final observations. The Meyer-grafted combinations ended the season at higher overall mean levels than the corresponding Manzur-grafted combinations. Because the plant-level longitudinal records were unavailable, these temporal patterns are reported descriptively rather than as statistically tested differences in slopes or date-by-treatment interactions.

Table 1

Experimental Structure and Corrected Observation Counts

Component	Level/Count	Comment
Cultivars	2	‘Gamlin’ and ‘Ra’no’
Rootstocks	2	Meyer and Manzur lemon
Cultivar × rootstock combinations	4	Four treatment combinations
Biological replicates	4 per combination	16 plants total
Sampling dates	12	June 1–November 15, 2025
Stem positions	4	Root collar; 10, 20, and 30 cm
Plant-date records	192	16 plants × 12 dates
Position-level observations	768	192 plant-date records × 4 positions

Note. The 192 plant-date count follows directly from the stated 2 × 2 × 4 × 12 design.

Final Growth Profiles

Final values and seasonal changes differed substantially among cultivar–rootstock combinations and stem positions (Table 2). The largest final recorded value was 34.75 for ‘Gamlin’ × Meyer at the 30 cm position. The same combination reached 30.05 at the root collar. ‘Ra’no’ × Meyer reached final values of 30.00 at the root collar, 26.80 at 10 cm, 27.00 at 20 cm, and 17.23 at 30 cm. In contrast, ‘Ra’no’ × Manzur produced lower final values at the root collar (12.80) and 30 cm position (13.78).

The largest absolute seasonal increase was observed for ‘Ra’no’ × Meyer at the root collar (26.12), followed by the same combination at 20 cm (24.88), ‘Gamlin’ × Meyer at the root collar (22.05), and ‘Gamlin’ × Meyer at 30 cm (21.12). The smallest absolute increase occurred for ‘Ra’no’ × Manzur at the

ISSN: 2181-3337 | SCIENTISTS.UZ

root collar (5.68). These values show that the effect associated with rootstock was not identical at every stem position and that cultivar-specific spatial patterns were present.

Descriptive Rootstock Contrasts

Averaged across the eight cultivar × position cells for each rootstock, the final measurement was 25.93 for Meyer and 17.67 for Manzur. Thus, the Meyer average was approximately 46.8% higher on this descriptive scale. The corresponding mean absolute seasonal increase was 18.97 for Meyer and 11.10 for Manzur, a descriptive difference of approximately 70.8%. Within 'Gamlin', the mean final value across positions was 26.60 on Meyer and 19.88 on Manzur; within 'Ra'no', the corresponding values were 25.26 and 15.46. These summaries consistently favor Meyer for the recorded growth outcome, but they should not be interpreted as inferential effect estimates until the repeated-measures model is fitted to the raw replicate data.

Cultivar- and Position-Specific Responses

The two cultivars displayed different spatial patterns. 'Gamlin' × Meyer showed particularly strong development at the 30 cm position, whereas 'Ra'no' × Meyer showed its largest absolute increases at the root collar and 20 cm position. The response to Manzur was also cultivar dependent: 'Gamlin' × Manzur retained a relatively high final value at 30 cm (26.15), whereas 'Ra'no' × Manzur was lowest at the root collar and 30 cm. These contrasts support a cautious interpretation of rootstock–scion interaction at the descriptive level and argue against classifying either rootstock as uniformly vigorous or weak across all positions and cultivars.

Discussion

The principal descriptive result is that plants grafted on Meyer rootstock showed greater recorded vegetative development than plants grafted on Manzur across most cultivar–position comparisons. This pattern is consistent with the broader citrus literature showing that rootstock genotype can materially alter scion vigor and tree size (Carvalho et al., 2024; Kunwar et al., 2023). Rootstock-associated differences can arise through multiple physiological pathways, including water relations, nutrient acquisition, vascular properties, and signaling, but the present dataset measured growth rather than those underlying mechanisms (Biasuz & Kalcsits, 2023; Wang et al., 2025). Consequently, the most defensible conclusion is that Meyer was associated with greater vegetative growth under the tested nursery conditions, not that Meyer was proven to have greater hydraulic conductivity, nutrient-use efficiency, cambial activity, or hormone transport.

The strong performance of 'Ra'no' × Meyer at the root collar and 20 cm position and of 'Gamlin' × Meyer at 30 cm illustrates why multiple stem positions can be informative. Growth along a young grafted plant is not necessarily uniform. Position-specific differences may reflect developmental timing, internode structure, radial expansion, or assimilate allocation, but these possibilities remain hypotheses in the absence of anatomical and physiological measurements. The observed differences can nevertheless be useful for nursery screening because they reveal where along the stem the combinations diverged most strongly.

The descriptive superiority of Meyer should also not be equated automatically with graft compatibility. Graft compatibility is a broader biological property that can involve survival, graft-union anatomy, vascular continuity, mechanical integrity, long-term growth balance, and the absence of delayed incompatibility symptoms (Mauro et al., 2022; Wang et al., 2025). Short-term vegetative vigor is relevant to nursery performance, but greater growth alone is insufficient to establish compatibility. Future evaluations should therefore combine growth with graft-union observations and, ideally, longer-term survival and orchard performance.

The present study also demonstrates the importance of aligning statistical analysis with experimental design. Twelve dates and four stem positions provide rich repeated information, but they do not create 768 independent biological replicates. The biological replication remains the number of

ISSN: 2181-3337 | SCIENTISTS.UZ

independent plants. A mixed-effects analysis of the original plant-level data would allow the contributions of cultivar, rootstock, date, and position to be estimated while correctly accounting for repeated observations within each plant. Such an analysis could also test whether the apparent Meyer advantage is stable across dates or varies during particular phases of seasonal development.

Multivariate techniques such as principal component analysis and hierarchical clustering can be useful exploratory tools, but they should be based on clearly defined observational units. If only four treatment centroids are entered, the resulting separation is descriptive and should not be presented as independent confirmation of biological effects. A stronger future approach would derive plant-level features—such as initial value, final value, absolute increase, and time-course slope for each position—and then apply exploratory multivariate analysis to the independent plants. This would preserve biological replication and make cluster or ordination patterns easier to interpret.

For nursery practice, the current results provide preliminary support for Meyer as the more vigorous of the two tested rootstocks for these orange cultivars under the represented greenhouse conditions. Whether greater vigor is desirable depends on production goals. Rapid nursery growth can shorten production cycles, but excessively vigorous rootstocks may not always be optimal for orchard density, canopy management, or long-term yield efficiency. Rootstock selection should therefore integrate nursery growth with subsequent field performance, fruit production, stress tolerance, and site adaptation (Roberto et al., 2022).

Limitations and Priorities for Confirmatory Work

Four limitations should be addressed before journal submission. First, the raw plant-level repeated-measures dataset should be recovered and analyzed with an appropriate mixed-effects model. Second, the exact measurement trait and unit must be verified from field records; the archived manuscript labels the response in centimeters but does not define whether it is diameter, circumference, or another metric. Third, the greenhouse and nursery protocol must be completed with location, plant age, grafting procedure, containers, substrate, irrigation, fertilization, pest management, and environmental conditions. Fourth, conclusions about physiological mechanisms and graft compatibility should remain explicitly tentative unless supported by direct measurements. These additions would convert the present descriptive revision into a fully reproducible confirmatory experiment.

Conclusion

Across the archived 2025 greenhouse observations, both sweet orange cultivars increased in the recorded stem growth measurement on both rootstocks, but the largest final values and seasonal increases were generally associated with Meyer. ‘Ra’no’ × Meyer produced the greatest absolute increase at the root collar (26.12), while ‘Gamlin’ × Meyer produced the largest final value at the 30 cm position (34.75). Averaged descriptively across cultivars and positions, Meyer exceeded Manzur in both final measurement and absolute seasonal increase. These findings support Meyer as a promising rootstock for vigorous nursery development of the tested cultivars under the represented conditions. They do not, by themselves, prove superior physiological efficiency or graft compatibility. Recovery of the raw repeated-measures dataset and missing nursery metadata is required for a definitive inferential assessment and fully reproducible journal submission.

REFERENCES

1. Biasuz, E. C., & Kalcsits, L. (2023). Rootstock effects on leaf function and isotope composition in apple occurred on both scion grafted and ungrafted rootstocks under hydroponic conditions. *Frontiers in Plant Science, 14*, 1274195. https://doi.org/10.3389/fpls.2023.1274195
2. Carvalho, D. U. de, Cruz, M. A. da, Vidal, T. C. M., Colombo, R. C., Yada, I. F. U., Neves, C. S. V. J., Leite Junior, R. P., & Tazima, Z. H. (2024). Rootstock selection for ‘Swatow’ mandarin trees grown

at different locations throughout the Brazilian subtropics. *Heliyon*, *10*(17), e36791. https://doi.org/10.1016/j.heliyon.2024.e36791

3. Kunwar, S., Meyering, B., Grosser, J., Gmitter, F. G., Jr., Castle, W. S., & Albrecht, U. (2023). Field performance of 'Valencia' orange trees on diploid and tetraploid rootstocks in different huanglongbing-endemic growing environments. *Scientia Horticulturae, 309*, 111635. https://doi.org/10.1016/j.scienta.2022.111635
4. Legua, P., Forner, J. B., Hernández, F., & Forner-Giner, M. Á. (2013). Physicochemical properties of orange juice from ten rootstocks using multivariate analysis. *Scientia Horticulturae, 160*, 268–273. https://doi.org/10.1016/j.scienta.2013.06.010
5. Mauro, R. P., Pérez-Alfocea, F., Cookson, S. J., Ollat, N., & Vitale, A. (2022). Editorial: Physiological and molecular aspects of plant rootstock–scion interactions. *Frontiers in Plant Science*, *13*, 852518. https://doi.org/10.3389/fpls.2022.852518
6. Oustric, J., Herbette, S., Morillon, R., Giannettini, J., Berti, L., & Santini, J. (2021). Influence of rootstock genotype and ploidy level on common clementine (Citrus clementina Hort. ex Tan) tolerance to nutrient deficiency. *Frontiers in Plant Science*, *12*, 634237. https://doi.org/10.3389/fpls.2021.634237
7. Roberto, S. R., Novello, V., & Fazio, G. (2022). Editorial: New rootstocks for fruit crops: Breeding programs, current use, future potential, challenges and alternative strategies. *Frontiers in Plant Science, 13*, 878863. https://doi.org/10.3389/fpls.2022.878863
8. Wang, P., Liu, F., Sun, Y., Liu, X., & Jin, L. (2025). Physiological and molecular insights into citrus rootstock–scion interactions: Compatibility, signaling, and impact on growth, fruit quality and stress responses. *Horticulturae*, *11*(9), 1110. https://doi.org/10.3390/horticulturae11091110

ISSN: 2181-3337 | SCIENTISTS.UZ VOLUME 5 ISSUE 7 JULY 2026

DETERMINATION OF THE BALANCING MOMENT OF A CRANK-SLOTTED MECHANISM USING THE N.E. ZHUKOVSKY LEVER METHOD

Siddikov Shuhrat[1], **Abdazimov Anvar**[1*]

[1]Tashkent State Technical University named after Islam Karimov,
2 University St., 100174 Tashkent, Uzbekistan
* Corresponding author: anvarabdazimov95996@gmail.com

DOI: 10.67620/sai.57a0014

ABSTRACT

This study presents the determination of the balancing force and balancing moment of a multiloop crank–slotted cotton-bush guiding mechanism used in the spindle drum of a cotton-harvesting machine. The analysis is performed using the N.E. Zhukovsky lever method, which enables the required balancing parameters to be obtained without directly determining reaction forces in the kinematic pairs or carrying out a complete force analysis of Assur groups. The investigated mechanism consists of a crank, sliding block, and rotating slotted link. Calculations are performed for a crank rotation angle of φ1=30∘, using previously determined kinematic parameters together with the inertia forces of the mechanism links and the experimentally established technological resistance force. The velocity diagram is rotated by 90∘ and treated as the Zhukovsky lever, after which the acting forces and inertia moment are transferred to the corresponding points. The balancing force is obtained from the moment-equilibrium equation of the transformed velocity diagram. For the considered mechanism position, the calculated balancing force is approximately 59.74 N, corresponding to a balancing moment of approximately 8.72 N·m. The proposed procedure provides a relatively simple and effective approach for evaluating the dynamic loading of the mechanism and can be applied to other crank positions to determine the variation of balancing force and moment throughout the operating cycle.

ACCEPTED

10.08.26

Keywords: *crank-slotted mechanism; cotton-bush guiding mechanism; cotton picker; N.E. Zhukovsky lever; force analysis; balancing force; balancing moment.*

CC BY

Introduction

Slotted-link mechanisms are classical mechanisms in the theory of mechanisms and machines and are widely used in mechanical engineering. They are employed when rotary or oscillatory motion must be transformed into reciprocating linear motion and can provide high linear speeds of working members. Typical applications include valve-actuation systems in internal-combustion engines, shaping and slotting machines, reciprocating pumps, presses, and packaging equipment. Table 1 summarizes several common configurations.

Table 1.

Classification of slotted-link mechanisms

Mechanism type	Motion of the slotted link	Parameter relationship	Typical applications
Crank-slotted mechanism with an oscillating slotted link	Reciprocating angular motion	l > r (l: center distance; r: crank radius)	Shaping machines; reciprocating pumps
Crank-slotted mechanism with a rotating slotted link	Continuous rotation	l < r	Slotting machines; packaging equipment
Slotted-link slider mechanism	Oscillatory	Variable	Automatic machines; presses
Double-slotted-link mechanism	Motion transmission	i = 1 (constant)	Compensating couplings

The operating principle of a slotted-link mechanism is governed by the fundamental laws of applied mechanics, kinematics, and statics [1,2]. The links are idealized as rigid bodies of finite dimensions and mass. Dynamic analysis therefore requires information about mass distribution, displacements, velocities, accelerations, external loads, inertia forces, and inertia-force moments. The balancing force and balancing moment are then determined with allowance for the working resistance force.

The trajectory of each point of a crank-slotted mechanism is determined by the link geometry and the working radii of its elements. A rotating or oscillating link acts on a translationally moving member at their kinematic connection. The guided member moves with one degree of freedom until it reaches an extreme position, after which its direction of motion reverses as the driving link continues its cycle.

A balancing force (or balancing moment) is the force (or moment) supplied by the drive that balances all forces acting on the mechanism, including inertia forces and inertia-force couples. Determination of the balancing force P′bal and/or balancing moment M′bal is therefore a necessary part of mechanism force analysis. Their point of application and direction are prescribed by the drive and transmission arrangement.

One approach for determining these quantities is the N.E. Zhukovsky lever method. The Zhukovsky lever is obtained by rotating the previously constructed velocity diagram by 90° and treating the rotated diagram as a rigid body fixed at the velocity pole Pv. External forces are transferred, parallel to themselves, to the corresponding points of this rotated diagram. The moment equilibrium of the resulting lever gives the balancing force. The method avoids the explicit solution of reaction forces in the kinematic pairs and the force analysis of Assur groups, although the required kinematic quantities, including accelerations used to obtain inertia forces, must already be known [1,2].

The objective of this work is to determine the balancing force and balancing moment of the multiloop crank-slotted cotton-bush guiding mechanism of the spindle drum of a vertical-spindle cotton picker [3] using the N.E. Zhukovsky lever method. The object of the study is the mechanism with a rotating slotted link at the crank position $\varphi_1 = 30°$.

Materials and Methods

The balancing force P′bal is first obtained from the moment-equilibrium condition of the Zhukovsky lever. It is assumed to act at point B_1 perpendicular to crank OB_1. The balancing moment is then calculated from $M'bal = P'bal \cdot OB_1$. The analysis uses the mechanism diagram at $\varphi_1 = 30°$ (Fig. 1), the previously determined velocity diagram (Fig. 2), and the previously determined acceleration quantities for this mechanism [4,5,7].

ISSN: 2181-3337 | SCIENTISTS.UZ

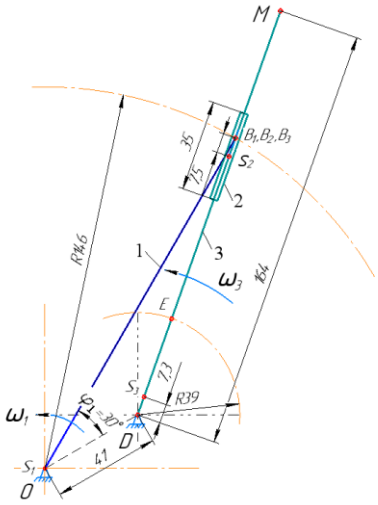


Fig. 1. Mechanism diagram at a crank rotation angle $\varphi_1 = 30°$: 1 - crank; 2 - sliding block; 3 - rotating slotted link; O and D - fixed supports; S_1, S_2, and S_3 - link centers of mass.

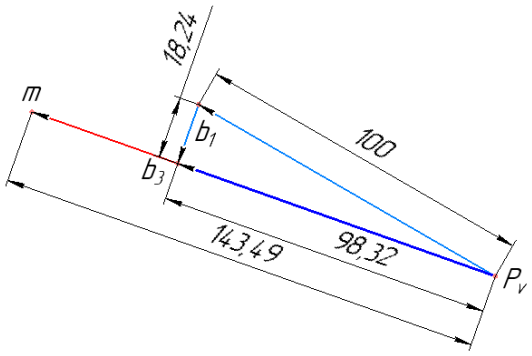


Fig. 2. Velocity diagram of the mechanism at $\varphi_1 = 30°$ ($\mu_v = 0.001$ (m/s)/mm).

Initial data and inertia quantities

The geometric and inertial data used for the considered position are as follows:

1) OD = 0.041 m - distance between the fixed supports O and D.
2) $OB_1 = 0.146$ m - crank length (link 1); crank mass $m_1 = 32$ kg. The crank center of mass S_1 coincides with the rotation axis at O, so $OS_1 = 0$. A later parameter determination for the same mechanism gives $\omega_1 = 13.2$ rad/s [7]; because $OS_1 = 0$, the centripetal acceleration of the crank mass center is zero.
3) B_2 - sliding block (link 2), length $\ell_2 = 0.035$ m and mass $m_2 = 0.036$ kg.
4) DM - rotating slotted link (link 3), length DM = 0.164 m and mass $m_3 = 1.349$ kg [7].
5) Qres = 36.61 N - working resistance (technological load) acting on the rotating slotted link at $\varphi_1 = 30°$, determined previously by electrical strain-gauge measurement [6].

$$aS_1 = \omega_1^2 \cdot OS_1 = (13.2)^2 \cdot 0 = 0 \text{ m/s}^2$$

For a link i, the inertia force and the inertia-force moment are written as [1,2]:

$$F_i = -m_i \cdot aS_i \quad (1)$$

where m_i is the link mass, kg, and aS_i is the total acceleration vector of the link center of mass, m/s². The minus sign indicates that the inertia force acts opposite to the center-of-mass acceleration.

$$M_i = -JS_i \cdot \varepsilon_i \quad (2)$$

where JS_i is the mass moment of inertia of the link about its center-of-mass axis, kg·m², and ε_i is the angular acceleration, rad/s². The minus sign indicates that the inertia moment acts opposite to the angular acceleration.

Because $aS_1 = 0$, the crank inertia force is $F_{i1} = m_1 \cdot aS_1 = 32 \cdot 0 = 0$ N.

For the sliding block at $\varphi_1 = 30°$, the previously determined center-of-mass acceleration is $aS_2 = 28.57$ m/s² [5]. Hence $F_{i2} = m_2 \cdot aS_2 = 0.036 \cdot 28.57 = 1.029$ N.

For the rotating slotted link, $aS_3 = 2.14$ m/s² [5]. Using the consistent link mass $m_3 = 1.349$ kg gives $F_{i3} = m_3 \cdot aS_3 = 1.349 \cdot 2.14 = 2.887$ N.

ISSN: 2181-3337 | SCIENTISTS.UZ

For the same mechanism and crank position, the later inertia study by the authors reports a link-3 mass moment of inertia $J_3 = 0.001566$ kg·m² and an inertia moment $M_{i3} \approx 0.099$ N·m [7]. This value is used in the equilibrium calculation below.

Construction of the Zhukovsky lever

The velocity diagram is rotated by 90° clockwise. At the corresponding points of the rotated velocity diagram, the force vectors from the loading diagram are transferred parallel to themselves: the working resistance Qres, the inertia forces F_{i2} and F_{i3}, and the balancing force P′bal. Forces tending to rotate the Zhukovsky lever clockwise are assigned a negative sign, and forces tending to rotate it counterclockwise are assigned a positive sign.

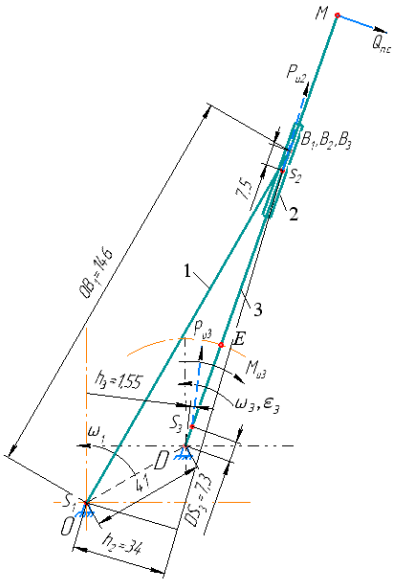


Fig. 3. Loading diagram of the mechanism at $\varphi_1 = 30°$ ($\mu_l = 0.001$ m/mm).

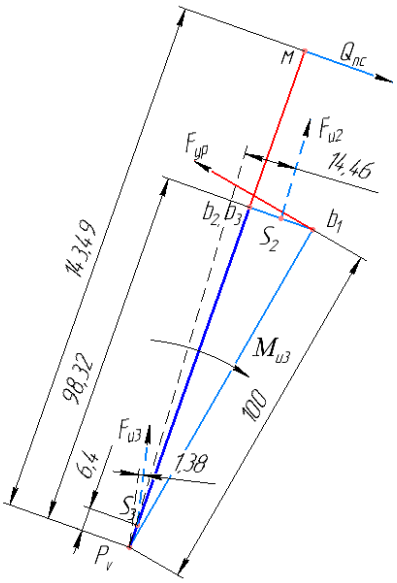


Fig. 4. Force diagram on the velocity diagram rotated by 90° for the mechanism at $\varphi_1 = 30°$.

Results and Discussion

For the considered mechanism position, the moment-equilibrium equation about the velocity pole Pv is:

$$F_{i3}\cdot hF_{i3} + F_{i2}\cdot hF_{i2} + P'bal\cdot hbal - Qres\cdot hQres - M_{i3}/\mu_l = 0 \qquad (3)$$

The scale factor is $\mu_l = 0.001$ m/mm. From the rotated diagram, the corresponding moment arms are $hF_{i3} = 1.38$ mm, $hF_{i2} = 14.46$ mm, hbal = 100 mm, and hQres = 143.49 mm.

Solving Eq. (3) for the balancing force gives:

$$P'bal = (-F_{i3}\cdot hF_{i3} - F_{i2}\cdot hF_{i2} + Qres\cdot hQres + M_{i3}/\mu_l) / hbal$$

$$= [-2.887\cdot 1.38 - 1.029\cdot 14.46 + 36.61\cdot 143.49 + 0.099/0.001] / 100 = 53.333 \text{ N}$$

The balancing moment referred to the crank is therefore:

ISSN: 2181-3337 | SCIENTISTS.UZ

$$M'bal = P'bal \cdot OB_1 = 53.333 \cdot 0.146 = 7.787\ N \cdot m \quad (4)$$

Thus, at $\varphi_1 = 30°$, the corrected balancing force is approximately 53.33 N and the corrected balancing moment is approximately 7.79 N·m. The largest positive term in Eq. (3) is the moment of the working resistance Qres, while the translational inertia-force terms are comparatively small at this particular crank position.

The Zhukovsky-lever construction is advantageous because the balancing action can be obtained from a moment equilibrium on the rotated velocity diagram without explicitly solving the reaction forces in the kinematic pairs or carrying out the full force analysis of Assur groups. Nevertheless, it is not independent of kinematic analysis: acceleration data are required to determine the inertia forces and inertia moments. The present calculation is for one representative, highly loaded crank position; a complete operating-cycle assessment would require repetition over the full crank-angle range.

Conclusions

1. The N.E. Zhukovsky lever method was applied to the multiloop crank-slotted cotton-bush guiding mechanism of a vertical-spindle cotton picker at $\varphi_1 = 30°$.

2. Using consistent link data and the supported inertia moment for the rotating slotted link, the balancing force is P′bal = 53.333 N and the balancing moment is M′bal = 7.787 N·m.

3. The method avoids explicit determination of kinematic-pair reaction forces and the force analysis of Assur groups, but it uses previously obtained kinematic quantities, including accelerations.

4. The same procedure can be applied at additional crank positions to obtain balancing-force and balancing-moment curves over the mechanism cycle; this is recommended for a full dynamic assessment.

REFERENCES

1. I. I. Artobolevsky, Theory of Mechanisms and Machines. Moscow: KnoRus, 2021, 639 p. ISBN 978-5-4365-5793-9.
2. K. V. Frolov, S. A. Popov, A. K. Musatov et al., Theory of Mechanisms and Machines, K. V. Frolov, Ed. Moscow: Vysshaya Shkola, 1987, 496 p.
3. K. Turanov, A. Abdazimov, M. Shaumarova, and S. Siddikov, “Type Analysis of a Multiloop Coulisse Mechanism of a Cotton Harvester,” in International Scientific Conference Energy Management of Municipal Facilities and Sustainable Energy Technologies (EMMFT 2019), Advances in Intelligent Systems and Computing, vol. 1258, Springer, 2021, pp. 290–305. DOI: 10.1007/978-3-030-57450-5_27
4. S. Siddikov, A. Sadriddinov, A. Abdazimov, and M. Khajiev, “Graphic and analytical study of the kinematics of the multiloop coulisse mechanism of the cotton harvester,” IOP Conference Series: Earth and Environmental Science, vol. 1231, 2023, art. 012014. DOI: 10.1088/1755-1315/1231/1/012014
5. S. Siddikov, A. Abdazimov, M. M. Atadjanova, and G. A. Abdikayimova, “Developing motion profiles for the rotating coulisse within a complex mechanism used for harvesting cotton in a vertical spindle machine,” IOP Conference Series: Earth and Environmental Science, vol. 1390, 2024, art. 012007. DOI: 10.1088/1755-1315/1390/1/012007
6. Sh. Sh. Siddikov, “Determination of the loading of a spindle drum with a cotton-bush guiding mechanism by electrical strain-gauge measurement,” Proceedings of the 2nd International Scientific Conference “Development and Production of Competitive Agricultural Machinery and Machines for Processing Agricultural Products,” Tashkent, 1997, pp. 36–37.
7. Sh. Siddikov and A. Abdazimov, “Determination of the Center of Gravity and Moment of Inertia of Moving Links of a Multi-Contour Crank-Slotted Mechanism,” Science and Innovation, 2026. DOI: 10.5281/zenodo.18149871

ISSN: 2181-3337 | SCIENTISTS.UZ VOLUME 5 ISSUE 7 JULY 2026

INVESTIGATION OF HYDROCARBON-RELATED MICROBIOLOGICAL ACTIVITY IN MARINE SYSTEMS WITHIN A BIOGEOPHYSICAL FRAMEWORK USING SLIME MOLDS

Abdullayev Vugar
PhD Baku Slavic University Baku, Azerbaijan
abvugar@yahoo.de

DOI: 10.67620/sai.57a0015

ABSTRACT

The progressive depletion of readily accessible hydrocarbon accumulations in marine petroleum systems, together with the increasing technical and economic demands of conventional exploration and production, creates an incentive to investigate complementary approaches. This study brings together three fields—microbial ecology, petroleum geophysics, and bio-inspired information processing—to develop a conceptual framework for indirect hydrocarbon sensing. The framework considers slime molds, particularly Physarum polycephalum and Dictyostelium discoideum, not as naturally established seafloor hydrocarbon indicators, but as laboratory model organisms whose chemotactic, adaptive, and network-forming behaviors may be useful for testing responses to chemical gradients associated with hydrocarbon-related microbial activity. The purpose of the study is therefore to evaluate the scientific plausibility, limitations, and potential experimental pathway of such a bio-inspired sensing concept.

The framework is based on documented relationships between petroleum systems and subsurface microbial activity. Hydrocarbon-degrading bacteria and archaea, including members of the provisional archaeal lineage "Candidatus Methanoliparia," can participate in anaerobic hydrocarbon transformation and methanogenesis in hydrocarbon-rich environments. Their metabolism can generate spatially heterogeneous chemical conditions involving methane, organic acids, redox gradients, and other metabolites. The study asks whether such microbially generated gradients could, under controlled laboratory conditions, elicit measurable responses from chemotactic model organisms such as P. polycephalum or D. discoideum. It also considers the major limitation that these slime molds are primarily terrestrial organisms and are not demonstrated to function as natural biosensors on the Caspian seafloor. Accordingly, the present work is conceptual: it proposes a biomimetic or bio-inspired sensing strategy that would require controlled laboratory validation before any field application could be considered.

ACCEPTED

10.08.26

Keywords: *Hydrocarbon exploration, biomimetic sensor technologies, slime mold behavior (Physarum polycephalum), Dictyostelium discoideum, microbial ecology and metagenomics, anaerobic hydrocarbon biodegradation, marine biogeophysics, Caspian Sea.*

Introduction

The Caspian Sea, including Azerbaijan's offshore sector, is a major hydrocarbon-bearing basin with

a long history of oil and gas exploration. Its geological setting is tectonically complex, and deformation, sedimentation, fluid migration, and reservoir architecture must be evaluated together when interpreting subsurface petroleum systems. Marine exploration is therefore technically demanding and normally relies on integrated geological, geophysical, geochemical, and drilling information rather than on a single indicator. The continuing importance of offshore hydrocarbons, even during the expansion of lower-carbon energy systems, provides a practical reason to improve the efficiency and selectivity of exploration methods. Within this context, the Caspian region provides a relevant setting in which to discuss complementary biological and geochemical approaches to subsurface sensing (Bjørlykke, 2015; Selley & Sonnenberg, 2015).

Oil and gas exploitation in the Caspian region has a long historical record, while systematic geophysical exploration and modern reservoir evaluation developed particularly during the twentieth century. The basin's tectonic framework, sedimentary sequences, structural traps, and petroleum migration pathways have made it an important subject in petroleum geoscience. Seismic methods, potential-field methods, well logging, and integrated geological interpretation are used to characterize subsurface structures and reduce uncertainty before and during drilling (Sheriff & Geldart, 1995; Telford et al., 1990). These established methods provide the physical and geological framework within which any proposed biological or geochemical indicator must ultimately be interpreted.

Over recent decades, improvements in offshore infrastructure, seismic acquisition and processing, geochemical analysis, drilling technology, and numerical modeling have broadened the range of questions that can be investigated in marine petroleum systems. This technological development also encourages investigation of unconventional complementary approaches. In particular, microbial ecology has shown that marine sediments contain spatially structured biological communities whose composition and metabolism respond to local geochemical conditions. These relationships do not by themselves establish a direct biological method for finding petroleum reservoirs, but they create a scientific basis for asking whether biologically mediated chemical gradients can provide additional information when combined with conventional geophysical and geochemical observations (Head et al., 2003; Orcutt et al., 2011).

Azerbaijan's offshore petroleum development has also been associated with large international projects, including the agreement commonly known as the "Contract of the Century." Such projects accelerated the use of modern offshore exploration, drilling, reservoir characterization, and production technologies in the Azerbaijani sector of the Caspian Sea. For the purposes of the present study, the important point is not to attribute individual discoveries to a single agreement or technology, but to recognize that modern offshore petroleum development depends on the integration of geological, geophysical, engineering, and environmental information. A proposed biological sensing method would therefore be complementary to, rather than a replacement for, established exploration technologies.

Petroleum exploration is a complex, iterative process carried out alongside broader changes in the energy sector. It commonly begins with regional geological and geophysical evaluation, followed by increasingly detailed structural, stratigraphic, geochemical, and prospect-scale analysis. Geological observations help establish the depositional, structural, and petroleum-system context, while geophysical data are used to image and constrain subsurface targets. These datasets guide decisions about whether and where exploratory drilling is justified. Field, core, well, and geophysical observations provide information on lithology, physical properties, stratigraphic relationships, structure, and bedding geometry. These data are interpreted and integrated to produce geological maps, stratigraphic correlation schemes, and structural models. The integrated models are then used to estimate whether prospective source, reservoir, seal, trap, and migration relationships are present and to identify the remaining uncertainty before drilling (Bjørlykke, 2015; Selley & Sonnenberg, 2015).

Geophysical methods are central to conventional petroleum exploration and reservoir characterization. Seismic reflection data are used to image subsurface interfaces, structural geometries, and

stratigraphic relationships by recording the propagation and reflection of elastic waves. Seismic interpretation can therefore reveal faults, folds, depositional geometries, and other features relevant to petroleum systems. Although earthquakes and tectonic deformation influence basin structure, exploration seismology should not be described as a method that primarily studies changes caused by earthquakes; its principal role in petroleum exploration is controlled-source imaging of subsurface geological structure (Sheriff & Geldart, 1995).

Gravity methods provide complementary information because variations in rock density produce measurable variations in the gravitational field. In sedimentary basins, gravity data can help constrain large-scale structural geometry, basement configuration, salt bodies, and other density contrasts. A gravity anomaly cannot normally be interpreted as a unique direct indicator of hydrocarbons, because many geological structures and lithologies can produce comparable density effects. Consequently, gravimetric observations are most useful when integrated with seismic, geological, and other geophysical information (Telford et al., 1990).

Electrical and electromagnetic methods can also contribute to subsurface characterization because formation resistivity is influenced by lithology, porosity, pore-fluid salinity, saturation, and clay content. Hydrocarbon-bearing intervals may exhibit higher resistivity than comparable water-saturated intervals, but resistivity is not uniquely diagnostic of hydrocarbons. Magnetic methods, in contrast, primarily respond to variations in magnetic susceptibility and remanent magnetization and are generally used to investigate broader geological structure rather than to identify petroleum accumulations directly. These methods therefore provide complementary constraints within an integrated exploration workflow (Telford et al., 1990).

In addition to geological and geophysical investigation, complementary geochemical exploration methods can be used to evaluate petroleum-system indicators before drilling. These methods include analyses of gases, dissolved or adsorbed hydrocarbons, petroleum-related organic compounds, pore-water chemistry, and other geochemical indicators. Such observations require geological context because near-surface anomalies can have multiple sources.

Geochemical exploration can include analysis of hydrocarbon microseepage, dissolved and adsorbed gases, petroleum-related compounds, and other chemical anomalies in near-surface sediments or fluids. Such observations may provide evidence of hydrocarbon migration, but they require careful interpretation because biological activity, sedimentary processes, and non-petroleum organic matter can generate overlapping signals. Petroleum biodegradation itself can substantially alter reservoir fluids and produce methane and other metabolites under subsurface anaerobic conditions (Head et al., 2003; Magot et al., 2000). For this reason, the present study treats microbial and geochemical anomalies as potential indirect proxies rather than as unique proof of a reservoir.

Formation resistivity is particularly important in well logging and reservoir evaluation. Electrical logs, interpreted together with porosity measurements, core information, and geological context, can assist in estimating fluid saturation and distinguishing lithological intervals. These measurements do not directly “analyze core samples”; rather, downhole logging tools measure physical properties of the formations surrounding the borehole, while core analysis provides an independent laboratory dataset for calibration and validation. Their integration helps evaluate reservoir quality, porosity, fluid saturation, and lithological heterogeneity (Telford et al., 1990).

These methods have demonstrated value in petroleum exploration and reservoir evaluation, but offshore acquisition, processing, drilling, and integrated interpretation can require substantial time and financial investment. Their cost is one reason to investigate complementary screening methods, provided that such methods are validated against established data rather than presented as substitutes.

Some hydrocarbon accumulations occur at substantial depth or in geologically complex settings, which increases exploration uncertainty and cost. This difficulty motivates investigation of additional

ISSN: 2181-3337 | SCIENTISTS.UZ

sources of information that might improve targeting before drilling. The approach developed here is therefore not presented as a substitute for seismic imaging, well logging, or geochemical analysis. Instead, it examines whether biological responses to hydrocarbon-associated microbial gradients could eventually provide a supplementary layer of evidence within an integrated exploration framework.

Digital acquisition, numerical modeling, directional drilling, improved seismic processing, and increasingly integrated geological datasets have changed petroleum exploration and development. These technologies improve the ability to characterize complex reservoirs and to manage drilling and production under difficult offshore conditions. At the same time, mature fields commonly experience declining production, while exploration of new or deeper targets can involve greater uncertainty and higher cost. Global energy systems continue to use substantial quantities of oil and gas even as investment in renewable energy expands, which reinforces the need for both efficient resource evaluation and environmental responsibility (International Energy Agency, 2024). In this context, complementary sensing concepts are scientifically relevant only if they can add information without overstating their reliability or replacing methods that are already well validated.

The discovery and development of a hydrocarbon reservoir require a sequence of geological, geophysical, engineering, economic, and environmental evaluations. Development is undertaken primarily for commercial production, while environmental protection and impact mitigation are constraints and responsibilities of the development process rather than a second purpose of exploiting the reservoir. Directional and horizontal drilling can increase reservoir contact, enable access to targets from fewer surface locations, and, in appropriate settings, improve development efficiency. These advantages are context-dependent and do not automatically guarantee higher production or lower environmental impact. After discovery, reservoir characterization, well design, completion, pressure management, production planning, and recovery strategy are integrated to determine how the field can be developed (Selley & Sonnenberg, 2015).

Rotary drilling is the dominant basis of modern petroleum well construction because it permits continuous circulation of drilling fluid, removal of cuttings, control of wellbore conditions, and use across a wide range of formations. Its effectiveness nevertheless depends on bit design, drilling fluid, well trajectory, formation properties, pressure regime, and operational objectives. Other drilling techniques are used in more specialized circumstances. Thus, it is more accurate to describe rotary drilling as a widely applicable modern method than as universally the most efficient method under every geological condition (Telford et al., 1990). Significant economic, operational, and environmental challenges remain, particularly in offshore and deepwater settings.

Offshore petroleum development continues to involve economic, environmental, and operational challenges. Geological uncertainty persists even after extensive interpretation, while mature fields may experience declining production and new targets may be smaller, deeper, or more complex. These factors encourage research into complementary methods that can reduce uncertainty or improve screening efficiency without lowering the evidentiary standard required for exploration decisions.

In producing oil and gas fields, withdrawal of reservoir fluids commonly causes reservoir pressure to decline unless pressure is supported by natural aquifer influx or engineered injection. Pressure depletion can reduce production rates and may require water injection, gas injection, artificial lift, or enhanced-recovery strategies. The recovery factor is controlled by reservoir properties, fluid behavior, drive mechanism, well configuration, and development strategy; it should not be treated as a simple direct function of pressure decline alone. As mature fields become more difficult to develop, subsurface imaging, reservoir modeling, structural interpretation, and resource assessment become increasingly important (Bjørlykke, 2015; Selley & Sonnenberg, 2015; Sheriff & Geldart, 1995). These technical and economic constraints also motivate research into complementary approaches that may reduce uncertainty at the screening stage.

ISSN: 2181-3337 | SCIENTISTS.UZ

These research efforts can also consider biological and geochemical response mechanisms as supplementary sources of information. Azerbaijan is simultaneously developing hydrocarbon resources and expanding renewable-energy initiatives, including solar and wind projects. The coexistence of conventional and lower-carbon energy development does not eliminate the continuing importance of careful petroleum-resource evaluation. From a research perspective, the relevant question is whether new methods can improve selectivity, reduce unnecessary field effort, or provide environmental information while remaining scientifically reproducible. The bio-inspired approach considered in this study is therefore framed as a research concept whose value would depend on experimental specificity, repeatability, and eventual integration with established geophysical and geochemical methods.

This need is particularly relevant in geologically complex marine basins such as the Caspian Sea. Exploration technologies must provide high-resolution information while remaining economically and environmentally defensible. Digital modeling, uncertainty analysis, integrated interpretation, and increasingly automated sensing systems can improve the efficiency of work in both mature and frontier areas. Bio-integrated and bio-inspired technologies are of interest because biological systems can adapt to heterogeneous environments and process local information without centralized control. The research question is therefore whether selected biological principles can add a useful layer to conventional subsurface characterization while remaining measurable, reproducible, and compatible with environmental constraints.

Advances in biotechnology, systems biology, biomaterials, and bio-inspired computation have created opportunities to use biological principles in engineered sensing and information-processing systems. Slime-mold research is relevant in this context because *P. polycephalum* can form adaptive transport networks and reorganize those networks in response to environmental conditions (Adamatzky, 2010, 2016; Nakagaki et al., 2000; Tero et al., 2010). In the energy and environmental sciences, microbial processes are already studied in relation to petroleum biodegradation, bioremediation, and subsurface carbon cycling (Head et al., 2003; Magot et al., 2000). These two bodies of research should not be conflated: the proposal here is to test whether a bio-inspired sensing model can respond to chemical gradients generated by petroleum-associated microbial processes, not to claim that slime molds are established petroleum-exploration organisms.

Proposal for the Application of Biological or Geochemical Methods

This study proposes the use of biological responses and microbially generated geochemical signals as complementary information in geological exploration. The term biomimetic or bio-inspired sensing is used here rather than biometric sensing, because the purpose is to imitate or exploit biological response principles rather than to identify an individual organism by biometric characteristics. Petroleum-associated microorganisms can alter hydrocarbons and produce chemical gradients in subsurface environments; such gradients may, in principle, provide indirect information about local microbial activity (Head et al., 2003; Magot et al., 2000). The proposed innovation is to investigate whether model organisms with measurable chemotactic and network-forming behavior can be used in controlled experiments to translate these gradients into observable spatial responses.

Among organisms used in bio-inspired behavior research, the acellular slime mold *Physarum polycephalum* is especially notable for its capacity to explore spatially heterogeneous environments and reorganize protoplasmic transport networks. *P. polycephalum* is an amoebozoan protist, not a fungus. Its vegetative plasmodium is a multinucleate single cell that can extend through a substrate as a branching tubular network; it should therefore not be described as a conventional multicellular organism. Experiments have shown route selection, network optimization, and adaptive reorganization in response to environmental conditions (Adamatzky, 2016; Nakagaki et al., 2000; Reid, 2023; Tero et al., 2010). *Dictyostelium discoideum* is biologically different: it is a social amoeba whose separate amoeboid cells aggregate under starvation and form a transient multicellular structure. These distinctive behaviors justify

ISSN: 2181-3337 | SCIENTISTS.UZ

their use as laboratory models, but they do not establish either organism as a natural indicator of subsurface hydrocarbons.

The plasmodium of *P. polycephalum* continuously reorganizes its tubular network through rhythmic protoplasmic flow, growth, retraction, and redistribution of material. When chemical and nutritional conditions are favorable, portions of the network can expand toward attractive regions; when conditions deteriorate, the organism can withdraw from unfavorable areas and reorganize its transport pathways. This distributed morphological reorganization has inspired studies of self-repairing and adaptive biological networks (Adamatzky, 2013, 2016; Tero et al., 2010). The life cycle should, however, be described accurately: the plasmodium is a multinucleate cell, and stress responses can include formation of resistant states such as sclerotia, while sporulation occurs through fruiting structures under appropriate developmental conditions. These processes are not a simple reversible transition between unicellular and multicellular states. The relevant feature for the present framework is the measurable reorganization of the plasmodial network in response to environmental gradients.

Adaptive movement by slime molds has opened useful research directions in bio-inspired computation, network design, and experimental studies of decentralized behavior (Adamatzky, 2016; Nakagaki et al., 2000; Reid, 2023). These findings have not demonstrated hydrocarbon detection. Accordingly, the present study treats slime-mold behavior as a possible experimental transducer of externally imposed chemical gradients rather than as evidence of an established petroleum-sensing function. Marine sediments contain diverse bacteria, archaea, fungi, and microbial eukaryotes, including amoeboid and other protistan lineages, but the presence of microbial eukaryotes in marine sediments does not establish that the terrestrial laboratory species *P. polycephalum* or *D. discoideum* naturally occur or function on deep seafloors (Orcutt et al., 2011; Orsi, 2018). *D. discoideum* remains valuable because its transition from solitary amoebae to a coordinated multicellular stage is exceptionally well studied (Bonner, 2009).

D. discoideum normally grows as individual amoeboid cells that feed on bacteria. When food becomes depleted, cells initiate a coordinated developmental program in which cyclic adenosine monophosphate (cAMP), not ordinary AMP, acts as a central chemotactic signaling molecule. Periodic cAMP signals organize cell movement toward aggregation centers, producing a multicellular aggregate and then a motile pseudoplasmodium, commonly called a “slug” (Bonner, 2009). During development, cells differentiate broadly into prestalk and prespore populations, and the migrating slug responds to environmental cues including light and temperature. The mature structure forms a fruiting body, or sorocarp, in which stalk cells support spore cells. This coordinated developmental sequence makes *D. discoideum* a powerful model for cell signaling, collective migration, differentiation, and emergent organization.

The prestalk and prespore cells occupy positions at the front and rear of the “slug,” respectively; prestalk cells are located in the anterior region, while prespore cells are situated in the posterior region (Bonner, 2009). This spatial differentiation demonstrates coordinated organization within the multicellular stage. The final stage represents the culmination of the organism’s development. At this stage, the “slug” transforms into a “sorocarp.” During this phase, the prestalk cells located at the front of the slug assume the role of a rigid supporting structure, while the prespore cells develop into spores that are resistant to environmental influences. This developmental sequence enables the population to produce resistant spores and complete its life cycle (Bonner, 2009). The spores are released into the environment, germinate, and produce new amoeboid cells, thereby completing the organism’s developmental cycle.

From a developmental and cell-biological perspective, *D. discoideum* is an established model for studying the transition from unicellular growth to coordinated multicellular development. Its aggregation, slug migration, differentiation of prestalk and prespore populations, and formation of a fruiting body provide experimentally accessible systems for investigating cell signaling, collective behavior, and

differentiation (Bonner, 2009). The organism should not, however, be used as evidence that all slime molds share the same life cycle or that these developmental processes directly imply hydrocarbon sensitivity. In the present framework, *D. discoideum* is included because its chemotactic signaling and collective migration can be measured quantitatively under laboratory conditions, allowing specific hypotheses about responses to environmentally relevant chemical gradients to be tested.

Modern microscopy, fluorescence-based imaging, genomic methods, and digital image analysis have substantially expanded the study of microbial and amoeboid systems. These tools make it possible to quantify cell movement, network morphology, spatial aggregation, and responses to controlled chemical gradients. Marine microbial chemotaxis research likewise demonstrates that microorganisms can respond to microscale chemical heterogeneity in aquatic environments (Brumley et al., 2020; Keegstra et al., 2022; Raina et al., 2022; York, 2022). In parallel, the behavior of *P. polycephalum* has been formalized in bio-inspired computational models that emphasize decentralized path selection and adaptive network reorganization (Adamatzky, 2016; Reid, 2023; Tero et al., 2010). The present study extends this conceptual direction by asking whether those experimentally measurable behaviors could be coupled to hydrocarbon-associated microbial chemistry. Such a proposal remains a hypothesis until specific metabolites, response thresholds, selectivity, repeatability, and environmental compatibility are experimentally demonstrated.

The origin and transformation of petroleum involve biological, chemical, thermal, and geological processes operating over very different time scales. Organic matter deposited in marine or lacustrine sediments undergoes early diagenetic transformation in which microorganisms can play an important role in degrading labile compounds and changing sediment geochemistry. With progressive burial, organic matter is converted into kerogen and, at greater temperature and maturity, thermally generated into oil and gas during catagenesis. Microbial activity is therefore important in early organic-matter transformation and in later biodegradation of petroleum, but microorganisms should not be described as the sole or direct cause of petroleum generation (Bjørlykke, 2015; Falkowski et al., 2008; Head et al., 2003; Selley & Sonnenberg, 2015).

The dominant geological model for conventional petroleum generation is biogenic in the broad sense that the precursor organic matter derives from biological material such as phytoplankton, zooplankton, bacteria, and other organisms deposited with sediment. During burial, this organic matter undergoes diagenesis and is incorporated into kerogen; subsequent increases in temperature and burial maturity drive catagenetic reactions that generate liquid and gaseous hydrocarbons over geological time. The relative importance of source-organism type, depositional environment, preservation, burial history, and thermal maturity varies among petroleum systems (Bjørlykke, 2015; Selley & Sonnenberg, 2015). This framework is important because microbial activity near a modern seafloor should not be equated directly with the deep thermal processes that generated a petroleum accumulation.

During early diagenesis, microorganisms consume and transform relatively labile organic compounds and influence redox conditions, dissolved inorganic carbon, sulfur species, organic acids, and other components of sediment pore water. These transformations contribute to the progressive alteration and preservation of sedimentary organic matter, but the formation of kerogen is a complex geochemical process rather than the direct product of a single microbial pathway. At later stages of burial and thermal maturation, catagenesis dominates hydrocarbon generation. In already formed petroleum reservoirs, microorganisms can again become important by biodegrading hydrocarbons, especially where temperatures and other environmental conditions permit microbial life (Head et al., 2003; Magot et al., 2000).

Organic-rich sediments and petroleum-affected environments can contain dissolved gases, reduced sulfur species, organic acids, hydrogen, methane, and many other reaction products. These compounds may form local biogeochemical gradients reflecting the combined effects of organic-matter degradation, hydrocarbon transformation, electron-acceptor availability, transport, and microbial community structure

ISSN: 2181-3337 | SCIENTISTS.UZ

(Falkowski et al., 2008; Orcutt et al., 2011). Such gradients are scientifically relevant to the proposed sensing framework, but they are not uniquely attributable to petroleum. The same or similar metabolites may arise from degradation of non-petroleum organic matter. Therefore, any biological indicator would require comparison with geochemical controls and independent petroleum-system evidence to determine specificity.

Research on the archaeal lineage "*Candidatus Methanoliparia*" has provided evidence that some members can activate and degrade non-methane alkanes under anoxic conditions while coupling the process to methanogenesis. Environmental and genomic observations from hydrocarbon seeps support a role for these archaea in anaerobic carbon cycling in petroleum-rich sediments (Laso-Pérez et al., 2019). This does not mean that *Methanoliparia* abundance is a validated exploration indicator for concealed petroleum reservoirs. Rather, hydrocarbon-associated archaeal metabolism can contribute to local methane production and other biogeochemical signatures that could be investigated as indirect proxies. Conventional exploration must still rely primarily on geological, geophysical, geochemical, and drilling evidence (Sheriff & Geldart, 1995; Telford et al., 1990).

Subsurface microbial communities can alter petroleum and generate metabolic products that modify local pore-water chemistry. In petroleum-bearing or hydrocarbon-seep environments, these effects can create microbial and geochemical "hotspots" whose spatial distribution reflects both substrate availability and local environmental conditions (Head et al., 2003; Orcutt et al., 2011). Such hotspots are conceptually relevant to indirect sensing, but they should not be described as causing the geological accumulation itself. Hydrocarbon reservoirs form through source-rock generation, migration, trapping, and preservation over geological time. Microbial activity can subsequently alter hydrocarbons, especially through biodegradation, and can thereby generate secondary chemical signals that may be detectable above or around a petroleum system (Bjørlykke, 2015; Selley & Sonnenberg, 2015).

Petroleum-system development can therefore be considered as a sequence in which organic-matter deposition and preservation are followed by diagenesis, burial and thermal maturation, hydrocarbon generation, migration, accumulation, and possible later alteration. Microorganisms are particularly important during early diagenesis and during biodegradation of existing hydrocarbons under biologically permissive conditions. Temperature, pressure, burial history, source-rock quality, and time govern the deeper thermal generation process, whereas microbial community composition and electron-acceptor availability govern many biodegradation pathways (Head et al., 2003; Magot et al., 2000; Selley & Sonnenberg, 2015). This distinction strengthens the proposed model by locating the biological signal in petroleum alteration and associated geochemistry rather than in an oversimplified account of petroleum formation.

Microbial activity can continue after a petroleum accumulation has formed, provided that temperature, water availability, nutrients, and other environmental conditions permit life. Petroleum hydrocarbons themselves can serve as substrates for diverse microorganisms in reservoirs and marine sediments, leading to biodegradation and substantial alteration of oil composition (Aitken et al., 2004; Head et al., 2003; Magot et al., 2000; Orcutt et al., 2011).

Anaerobic hydrocarbon biodegradation can proceed through several different microbial mechanisms, and it is not universally dependent on one bacterial–archaeal partnership. Some anaerobic bacteria degrade alkanes while coupling oxidation to electron acceptors such as sulfate or nitrate, whereas methanogenic degradation of complex hydrocarbons commonly involves syntrophic communities in which fermentation products such as hydrogen, formate, or acetate are consumed by methanogens. Other archaeal lineages can activate specific hydrocarbons through methyl-coenzyme M reductase-related pathways (Laso-Pérez et al., 2016, 2019; Mbadinga et al., 2011). Consequently, the microbial architecture depends on the substrate, temperature, electron acceptors, and environmental setting. For the proposed biosensing

model, the important point is that different pathways can generate different metabolite combinations and therefore different chemical gradients.

In syntrophic methanogenic systems, intermediate products such as acetate, formate, carbon dioxide, and molecular hydrogen may be exchanged rapidly between microbial partners. Consumption of these products by methanogens can keep their concentrations sufficiently low for otherwise unfavorable upstream reactions to proceed, thereby creating a thermodynamic coupling between community members (Magot et al., 2000; Mbadinga et al., 2011). Hydrogenotrophic methanogens consume hydrogen and carbon dioxide, whereas acetoclastic methanogens use acetate. These interactions can produce spatially structured zones of microbial activity in sediments or reservoirs. Whether such zones generate gradients strong and persistent enough to control the behavior of a slime-mold model organism is an empirical question and should be tested in controlled microcosms rather than assumed from the existence of the microbial process itself.

Methanogenic archaea are strictly anaerobic microorganisms that produce methane through several metabolic routes. In hydrogenotrophic methanogenesis, hydrogen is used to reduce carbon dioxide to methane; in acetoclastic methanogenesis, acetate is converted to methane and carbon dioxide. In hydrocarbon-degrading consortia, methanogens can remove fermentation products and thereby contribute to the thermodynamic feasibility of upstream hydrocarbon transformation (Magot et al., 2000; Mbadinga et al., 2011). Methanogenesis is therefore important to the present concept because methane production, together with associated organic acids and redox changes, can serve as a measurable marker of microbial activity. It should not, however, be treated as a hydrocarbon-specific signal without appropriate controls.

Interspecies syntrophy describes a metabolic dependence in which the products of one population are consumed by another in a way that makes the combined process energetically favorable. Under methanogenic conditions, fermentative or hydrocarbon-transforming organisms may generate hydrogen, formate, acetate, or other intermediates, while methanogenic archaea consume these products and form methane. This continuous product removal can maintain low intermediate concentrations and support continued substrate transformation (Mbadinga et al., 2011). The process is therefore a thermodynamic and ecological coupling, not a literal synchronization signal between cells. Its relevance to the proposed sensing system lies in the possibility that coupled metabolism can generate reproducible chemical gradients that are measurable independently of the model organism's response.

Methane may be a major terminal product of methanogenic hydrocarbon degradation, but methane formation does not itself increase the temperature of deeper sediment layers. The relevant effect is thermodynamic: consumption and production of intermediates can shift reaction energetics and maintain favorable redox conditions for continued microbial metabolism. Studies of "*Candidatus Methanoliparia*" indicate that members of this lineage possess pathways for anaerobic activation of non-methane alkanes and can couple alkane degradation to methanogenesis (Laso-Pérez et al., 2019). Such metabolism may contribute to methane-rich and chemically heterogeneous microenvironments in hydrocarbon seeps. These products could be incorporated into an experimental gradient system, but their usefulness as exploration proxies would have to be established against non-petroleum controls. Slime-mold behavior would then be measured as a response to the imposed chemistry, not assumed to be naturally coupled to the archaeal metabolism.

The microbial degradation of petroleum is therefore best understood as a collection of pathways rather than as a simple division in which archaea process only "simple" hydrocarbons and bacteria process "complex" hydrocarbons. Anaerobic bacteria can activate and degrade a range of alkanes under sulfate-, nitrate-, or other electron-accepting conditions, while specialized archaea can activate short-chain or longer-chain alkanes through methyl-coenzyme M reductase-related chemistry, sometimes in syntrophic partnerships and sometimes with more direct methanogenic coupling (Laso-Pérez et al., 2016, 2019; Mbadinga et al., 2011). This diversity is important for biosensing because the chemical products of

ISSN: 2181-3337 | SCIENTISTS.UZ

hydrocarbon degradation depend on the organisms and pathways present; no single universal microbial signal should be expected.

The discovery of archaeal hydrocarbon-activation pathways has expanded the earlier view of anaerobic petroleum biodegradation. Laso-Pérez et al. (2016) demonstrated archaeal activation of butane in a thermophilic syntrophic consortium, while later genomic and environmental work identified "*Candidatus Methanoliparia*" in Gulf of Mexico hydrocarbon-seep sediments and provided evidence for methanogenic degradation of non-methane alkanes (Laso-Pérez et al., 2019). These findings show that hydrocarbon transformation can involve archaeal enzymes directly rather than requiring bacterial activation in every case. At the same time, the organisms are difficult to cultivate, and environmental activity must be inferred from multiple lines of genomic, chemical, and physiological evidence.

Hydrocarbon-rich marine sediments can contain abundant *Methanoliparia* populations together with methane production and molecular evidence of alkane activation (Laso-Pérez et al., 2019). These observations are important for understanding anaerobic carbon cycling and petroleum biodegradation, but the manuscript does not provide an experimental basis for assigning a universal temperature range, enrichment factor, or methane-production rate to the proposed Caspian application. The scientifically defensible inference is narrower: archaeal alkane degradation can generate methane and associated geochemical heterogeneity in some hydrocarbon-rich anoxic environments. Such heterogeneity may provide candidate chemical inputs for a laboratory biosensing experiment. Demonstrating a reliable connection to a concealed reservoir would require field geochemistry, microbial community data, and independent geological validation.

Genomic evidence indicates that "*Candidatus Methanoliparia*" possesses methyl-coenzyme M reductase-related pathways associated with anaerobic alkane activation, supporting the interpretation that members of the lineage can couple hydrocarbon degradation to methanogenesis (Laso-Pérez et al., 2019). The available evidence should not be simplified into a claim of universally rapid long-chain-hydrocarbon degradation or a precisely defined substrate range. Substrate utilization, metabolic rates, ecological interactions, and regulatory mechanisms remain dependent on lineage and environmental conditions. For this study, the significance of *Methanoliparia* is therefore conceptual: it provides a documented example of petroleum-associated microbial metabolism capable of generating methane and other chemical changes that could be reproduced as experimental gradients.

Although *Methanoliparia*-associated metabolism has been investigated using environmental genomics, geochemistry, and enrichment approaches, many aspects of intracellular regulation, growth kinetics, ecological interactions, and substrate specificity remain incompletely characterized. These uncertainties do not diminish the importance of the lineage for petroleum microbiology, but they do limit claims about its direct engineering use. Future functional-genomic and cultivation studies may improve understanding of its contribution to anaerobic oil transformation and methane production. Within the present framework, the organism is therefore treated as a source of plausible hydrocarbon-associated metabolic signals rather than as a controllable component of a field-ready biosensor (Laso-Pérez et al., 2019; Magot et al., 2000).

These observations support a conceptual proposal for testing a slime-mold-based or slime-mold-inspired biosensor as an indirect indicator of hydrocarbon-associated microbial chemistry. The concept is not presently suitable for field exploration. *P. polycephalum* and *D. discoideum* are predominantly terrestrial laboratory model organisms with ecological and physiological requirements that differ markedly from those of deep marine sediments (Bonner, 2009; Reid, 2023). The Caspian Sea is brackish rather than uniformly highly saline, and conditions vary strongly with location and depth; seafloor and subsurface sediments can also become oxygen-limited or anoxic, while hydrostatic pressure increases with water depth. These conditions make direct deployment of terrestrial slime molds biologically questionable. The

ISSN: 2181-3337 | SCIENTISTS.UZ

initial research problem should therefore be addressed through contained laboratory experiments that reproduce selected chemical and physical variables rather than by assuming survival on the natural seafloor.

Signal specificity is an equally important limitation. Sulfur cycling, methane cycling, fermentation, and degradation of non-petroleum organic matter can generate metabolites similar to those associated with petroleum biodegradation (Azam & Malfatti, 2007; Boetius et al., 2000; Orcutt et al., 2011). A response by a chemotactic organism to methane-associated metabolites or organic acids would therefore indicate sensitivity to the chemical environment, not necessarily to petroleum itself. No direct mediating role of slime molds in hydrocarbon degradation has been demonstrated in the evidence reviewed here. The testable question is instead whether a slime-mold response can distinguish experimentally defined hydrocarbon-associated microbial gradients from appropriate non-hydrocarbon controls with sufficient sensitivity and specificity to justify further development.

For this reason, the proposed approach requires a staged research program. Initial work should reproduce defined gradients in microfluidic devices, sediment analogues, or other contained matrices and quantify the response of the model organism. The next stage should compare sterile chemical controls, non-petroleum organic-matter degradation, hydrocarbon-degrading microbial cultures, and mixed sediment communities. Only if reproducible specificity is demonstrated should mesocosm experiments be considered. Field-scale work would require independent geophysical and geochemical validation and careful assessment of biosafety, environmental compatibility, and monitoring requirements.

Marine and subseafloor microbial ecology should also be characterized independently before any claim is made about a natural slime-mold component of the system. Molecular surveys demonstrate extensive diversity of bacteria, archaea, and microbial eukaryotes in seafloor sediments (Orcutt et al., 2011; Orsi, 2018). However, evidence for broad microbial-eukaryote diversity is not equivalent to evidence that *P. polycephalum* or *D. discoideum* naturally inhabit hydrocarbon-rich marine sediments. A scientifically robust program would therefore use metabarcoding, microscopy, cultivation where feasible, and geochemical profiling to identify indigenous protists and other eukaryotes that may be better adapted to local conditions. The terrestrial slime molds can remain laboratory models even if future field indicators are drawn from different organisms.

The conceptual chain can therefore be stated more cautiously: hydrocarbons and other organic substrates can influence microbial community structure and metabolism; microbial metabolism can generate local chemical and redox gradients; and these gradients may be detectable by appropriately chosen biological or engineered sensors. Several limitations follow. First, terrestrial slime-mold models may be poorly compatible with marine and subsurface conditions. Second, chemical signal specificity is a major problem because microbial abundance or activity does not necessarily indicate petroleum; it may reflect degradation of general organic matter (Orcutt et al., 2011). Third, benthic gradients vary spatially and temporally. Fourth, behavioral responses measured in a model organism must be separated from background responses to salinity, oxygen, temperature, pH, and nutrient availability. These limitations define the experimental controls required to evaluate the idea.

A stepwise validation sequence is therefore essential. Controlled laboratory studies should begin with microfluidic gradient chambers, agar or hydrogel matrices, and sediment analogues in which the concentration and identity of candidate metabolites are known. The next stage should introduce natural or reconstructed microbial communities under mesocosm conditions, with parallel geochemical measurements. Only after response thresholds, selectivity, repeatability, and ecological tolerance have been established should any field-scale sensor concept be evaluated. Direct environmental release of non-native laboratory slime molds should not be assumed as part of the method; contained sensor architectures, ex situ sampling, or purely biomimetic computational implementations may ultimately be more appropriate. Algorithmic models can be developed in parallel to quantify adaptive behavior and identify which biological features are transferable to engineered sensing.

ISSN: 2181-3337 | SCIENTISTS.UZ

D. discoideum illustrates how nutrient availability can reorganize collective behavior. Under nutrient-rich conditions it exists primarily as independent, feeding amoeboid cells; under starvation, cAMP-mediated signaling coordinates aggregation and the formation of a multicellular slug, followed by differentiation into a fruiting body containing stalk and spore cells (Bonner, 2009). It should not be characterized as an "anaerobic-like" cell, because its laboratory biology is not based on adaptation to deep anoxic marine conditions. Its relevance to the present concept is instead methodological: aggregation, migration, and differentiation can be quantified as responses to defined environmental cues, providing a tractable model for studying chemically mediated collective behavior.

Biofilms provide a different form of collective organization. They are communities of microorganisms embedded in an extracellular matrix and can exhibit spatial differentiation, chemically mediated communication, cooperative and competitive interactions, and emergent community-level properties (Costerton et al., 1995; Hall-Stoodley et al., 2004; Nadell et al., 2016; Stoodley et al., 2002). Microbial mats are also spatially organized communities, but their structure reflects local energy sources and geochemical gradients. In illuminated settings, light can influence phototrophic layers; in dark seafloor or subsurface settings, redox chemistry, electron donors and acceptors, fluid flow, and substrate availability are more important than light (Orcutt et al., 2011). These systems are not phylogenetically equivalent to slime molds, but they offer useful functional comparisons in self-organization and environmental response.

Stratification in microbial mats and sediments should therefore be interpreted according to environmental context. Shallow illuminated mats may contain phototrophic surface layers, whereas deeper or dark sediments commonly show vertical zones controlled by oxygen penetration, sulfate reduction, fermentation, methanogenesis, and other redox processes. The boundaries between these zones can generate steep chemical gradients over small spatial scales (Boetius et al., 2000; Orcutt et al., 2011). Slime-mold networks and microbial mats differ greatly in persistence, metabolism, and evolutionary origin, yet both can be analyzed as spatially organized systems whose structure emerges from local interactions. This analogy may help inspire sensor design, but it does not imply that mat organization or slime-mold behavior is itself a specific indicator of hydrocarbon-rich sediment.

The use of biological sensing for subsurface hydrocarbon exploration therefore remains hypothetical and requires experimental validation. A practical research sequence would link controlled chemistry to a measurable biological response and then test whether that relationship survives increasing environmental complexity. Marine protists, including foraminifera and radiolarians, are relevant to the broader discussion because they demonstrate that diverse unicellular eukaryotes can persist in marine environments and respond to local physicochemical conditions. Their presence does not make them direct petroleum sensors, but their environmental adaptations illustrate why indigenous marine eukaryotes may ultimately be more realistic candidates than terrestrial slime molds for field-oriented biological indicators (Orsi, 2018).

Foraminifera, in particular, extend reticulose pseudopodial networks that support locomotion, feeding, and interaction with sediment particles. Many taxa occur in deep-sea environments and display substantial morphological and physiological diversity. Radiolarians are also marine protists, many of which form intricate mineral skeletons that can contribute siliceous material to marine sediments after death. These examples demonstrate the diversity of structural strategies among marine microbial eukaryotes (Fenchel, 1987; Margulis & Chapman, 2009). They are included here as ecological comparisons, not as evidence that these organisms detect hydrocarbons or that their morphology can be transferred directly to a petroleum-sensing system (Orsi, 2018).

Protist groups differ markedly in life cycle, metabolism, and ecological function, and they should not be described as collectively performing hydrogen degradation. The terrestrial slime molds considered in this study are likewise not established hydrocarbon degraders. The relevant comparison is functional rather than metabolic: many protists can move, reorganize cell shape, explore spatially heterogeneous

environments, and respond to chemical or physical gradients. These behaviors suggest possible design principles for adaptive sensing, but any link to hydrocarbon-associated chemistry must be demonstrated experimentally for a particular organism and signal rather than inferred from broad similarities among protists.

Marine sponges (Porifera) provide another example of biological reorganization at a different level of complexity. Classic dissociation experiments showed that separated sponge cells can reaggregate and, under appropriate conditions, reconstruct organized tissue (Humphreys, 1970). This property depends on cell recognition, adhesion, extracellular components, and species-specific interactions. The comparison with slime molds is therefore an analogy in self-organization rather than evidence of close cellular or evolutionary similarity. *D. discoideum* aggregates separate amoebae during development, whereas *P. polycephalum* reorganizes a multinucleate plasmodial network; sponges reorganize cells belonging to a multicellular animal. Distinguishing these mechanisms is important if they are used as inspiration for engineered sensor architectures.

Across biofilms, microbial mats, protists, slime molds, and sponges, convergent functional themes can nevertheless be identified: local interactions can produce larger-scale organization; environmental stress can alter structure and behavior; and chemical or physical cues can coordinate responses. The mechanisms, evolutionary origins, and degrees of reversibility are not the same, and it would be incorrect to claim that all of these systems undergo reversible transitions between unicellular and multicellular states. Their value to the present study lies in comparison of organizational principles rather than taxonomic equivalence. Such comparisons can inform algorithms for distributed sensing, adaptive path selection, network resilience, or signal integration while keeping the underlying biology explicit.

The preceding discussion therefore supports a biogeophysical framework in which biological populations can modify their local environment and generate or respond to spatial gradients, while petroleum systems can influence the substrates available to particular microbial communities. This interaction creates a possible indirect connection between subsurface hydrocarbon occurrence and measurable biological or geochemical signals. The connection remains non-unique and must be validated against background organic-matter cycling, fluid migration, lithological variation, and other environmental controls. Detailed marine microbiology, geochemistry, and geophysics are consequently complementary components of any future attempt to evaluate the proposed sensing concept.

Methodology: The present study uses a phased conceptual methodology that integrates petroleum geoscience, petroleum microbiology, microbial ecology, and experimental systems biology. Because the manuscript does not report a complete primary experimental dataset, the laboratory components below are presented as a proposed validation workflow rather than as completed experiments. The purpose of the methodology is to translate the conceptual relationship among hydrocarbons, microbial metabolism, chemical gradients, and biological responses into a sequence of testable steps. Each phase is designed to generate measurements that can be compared with geochemical controls and, ultimately, with conventional geophysical information.

Development of the conceptual framework: The first phase defines the causal chain to be tested. A subsurface or sedimentary hydrocarbon system may support or modify microbial activity; microbial transformation of hydrocarbons and associated organic matter can alter methane, organic acids, sulfur species, redox conditions, and other chemical variables; those changes can form local gradients; and a laboratory model organism or engineered biomimetic sensor may respond to the gradient. The model can therefore be represented schematically as follows: hydrocarbon-associated substrate or seepage → microbial transformation and community response → local biogeochemical gradient → measurable response of a model biosensor → integrated interpretation with geological and geophysical evidence. The biological response is an indirect proxy and not a direct measurement of the reservoir itself.

ISSN: 2181-3337 | SCIENTISTS.UZ

This model gives particular attention to archaeal and bacterial processes associated with anaerobic hydrocarbon degradation. "*Candidatus Methanoliparia*," for example, provides a documented case in which alkane transformation can be linked to methanogenesis in hydrocarbon-rich anoxic sediments (Laso-Pérez et al., 2019). The resulting methane and associated metabolic products may contribute to spatially heterogeneous geochemical fields. In the proposed experiment, these gradients would not be attributed to slime molds themselves; instead, selected chemical conditions would be reproduced in controlled matrices and the response of the model organism would be measured. The resulting multi-layer inference model would therefore separate four levels—geological source, microbial process, chemical signal, and sensor response—to reduce the risk of confusing correlation with causation.

Laboratory cultivation and behavioral experiments: A second phase would investigate chemotactic, migratory, and network-forming behavior under controlled laboratory conditions. P. polycephalum and D. discoideum are proposed as distinct model systems because both provide measurable responses to spatially heterogeneous chemical environments, although their biology and developmental mechanisms differ substantially (Bonner, 2009; Nakagaki et al., 2000; Reid, 2023). P. polycephalum would be evaluated primarily through plasmodial growth, network morphology, route selection, and reorganization. D. discoideum would be evaluated through amoeboid chemotaxis, aggregation dynamics, and developmental responses. Experiments should initially use defined chemical gradients before more complex microbial or sediment matrices are introduced.

Under the proposed laboratory design, matrices containing defined concentrations of candidate hydrocarbon-associated metabolites would be prepared. These could include selected low-molecular-weight organic acids, dissolved inorganic components, methane-equilibrated media where technically appropriate, or other products documented in anaerobic hydrocarbon-degrading systems. Parallel controls would contain equivalent nutrient levels without petroleum-associated metabolites, and additional treatments could include non-petroleum organic-matter degradation products. Hydrocarbon-rich natural sediment should not be treated as a chemically defined input unless its composition has been measured. The experimental matrix would therefore be characterized geochemically so that any biological response could be related to a known concentration gradient rather than to an unspecified "hotspot."

Within this framework, behavioral responses would be quantified separately for each model organism. For *P. polycephalum*, relevant variables could include directional extension, network area, branching, path length, transport-network reorganization, withdrawal from unfavorable zones, and recovery after disturbance. For *D. discoideum*, relevant variables could include single-cell migration, aggregation probability, aggregation-center formation, slug migration, and developmental timing. The term "reversion" should not be used to imply that both organisms undergo the same reversible unicellular–multicellular transition. The principal analysis would test whether response magnitude and direction change systematically with the identity and concentration of the imposed chemical gradient.

Quantitative analysis would require time-lapse imaging, microscopy, calibrated spatial measurements, and digital image-processing methods. Experimental replication should be sufficient to estimate variability within and between cultures, and treatment allocation should include appropriate negative and positive controls. Measurements could be converted into response variables such as migration velocity, orientation relative to the gradient, network density, branch persistence, aggregation time, or path efficiency. Statistical analysis would then assess whether the observed behavior differs among treatments and whether any response is reproducible across independent experiments. These data would provide the first empirical test of the proposed association between hydrocarbon-related microbial chemistry and model-organism behavior.

Simulation of marine and subsurface conditions: A third phase would test whether any laboratory response remains detectable when selected environmental constraints are introduced. Salinity, oxygen concentration, temperature, pH, and sediment structure should be manipulated independently

where possible before combinations are tested. The purpose is not to reproduce every condition of the Caspian seabed in a single experiment, but to identify which variables suppress, enhance, or confound the biological response. Because the selected slime molds are terrestrial models, direct exposure to full marine or subsurface conditions may rapidly eliminate activity; this outcome would itself be important evidence regarding feasibility. Contained or ex situ sensor formats should therefore be considered alongside direct organism exposure.

Physiological condition, chemotactic responsiveness, aggregation stability, network integrity, and recovery after stress would be monitored throughout this phase. Measurements of growth or survival alone would be insufficient, because a biosensor must retain a reproducible relationship between environmental input and measurable output. Salinity, oxygen limitation, temperature, and pH may alter motility or development independently of the target chemical signal. Factorial or sequential experiments would help distinguish these effects and determine whether a response attributed to hydrocarbon-associated chemistry persists after environmental stress is introduced.

This phase would therefore function as an intermediate feasibility test between a simplified chemical-gradient experiment and a complex sediment or mesocosm system. A model organism that responds strongly to a defined metabolite but loses all response under modest changes in salinity or oxygen would have limited field relevance even if the initial chemotaxis result were statistically significant. Conversely, a response that persists across a realistic range of confounding conditions would justify more complex testing. The outcome would determine whether the biological component should be developed further, replaced with a more marine-adapted organism, or translated only into a biomimetic computational sensor.

Interaction studies: A subsequent phase would examine interactions between the chemotaxis-sensitive model organisms and hydrocarbon-associated bacterial or archaeal communities under contained laboratory conditions. The purpose would be to determine whether a living microbial community produces spatial signals that elicit a measurable response beyond that produced by bulk nutrients or non-petroleum organic matter. Microbial community density, metabolic state, and spatial localization would be measured independently so that the strength of the biological stimulus can be separated from the response of the slime-mold model (Nadell et al., 2016; Shapiro, 1998).

Special attention would be given to microbial abundance, spatial localization, and metabolite production. Candidate measurements include methane, dissolved gases, organic acids, sulfide or sulfate where relevant, pH, and redox conditions, together with microscopy or molecular measurements of microbial biomass. The biological response could then be compared with these measured variables using correlation and regression models. A correlation would not by itself establish hydrocarbon specificity; the same analysis should be performed with control communities degrading non-petroleum organic substrates. This design would help distinguish a response to general microbial biomass from a response to a particular hydrocarbon-associated metabolic profile (Costerton et al., 1995; Nadell et al., 2016).

Data analysis and modeling: Quantitative data from the proposed experiments would be analyzed using statistical inference and computational modeling. Spatial trajectories and network structures could be reconstructed from time-lapse images and analyzed for orientation, speed, branching, path efficiency, and persistence. P. polycephalum networks can also be represented as graphs in which junctions and tubes are treated as nodes and edges, allowing comparison of network topology across treatments (Nakagaki et al., 2000; Tero et al., 2010). D. discoideum data would require different descriptors, including cell trajectories, aggregation-center dynamics, and group migration, so the two organisms should not be forced into a single biological model.

These analyses would allow environmental constraints, response variability, network stability, and self-reorganization to be compared quantitatively. For *P. polycephalum*, graph-theoretical measures could describe connectivity, redundancy, path length, and adaptation after disturbance. For microbial

ISSN: 2181-3337 | SCIENTISTS.UZ

communities, spatial statistics could describe clustering or gradients, while geochemical measurements would define the chemical field to which the organism was exposed. Combining these datasets would make it possible to test whether changes in biological organization are consistently associated with particular chemical conditions rather than with uncontrolled environmental variation (Nadell et al., 2016; Tero et al., 2010).

Empirical observations would then be incorporated into computational models only after the relevant biological relationships had been measured. The aim would not be to reproduce every mechanism of the living organism, but to formalize useful features such as decentralized response, adaptive path selection, threshold behavior, and integration of heterogeneous spatial information. Parameter values should be estimated from experimental data rather than selected to force agreement with the hypothesis. This separation between observation and model calibration is essential if the resulting algorithm is later compared with independent geophysical or geochemical datasets (Adamatzky, 2016; Shapiro, 1998).

The resulting models would therefore serve as abstractions of selected biological principles rather than literal digital copies of the organisms. Decentralized decision-making, adaptive network reinforcement, local response to gradients, and resilience after perturbation are potentially transferable design principles (Tero et al., 2010). A future ecological sensing system could use these principles to integrate spatially heterogeneous chemical measurements, even if living slime molds were not ultimately used in the field. This distinction is important because the most durable contribution of the concept may be biomimetic computation or sensor-network design rather than direct deployment of terrestrial organisms in marine sediments.

Results:

Because the present work is conceptual and the manuscript does not provide a complete primary experimental dataset, the “results” should be interpreted as testable outcomes of the proposed framework rather than as measured numerical findings. The framework predicts that hydrocarbon-associated microbial metabolism can generate spatially heterogeneous chemical conditions and that the persistence of those conditions will depend on production, consumption, diffusion, advection, and sediment properties. A validation study should therefore quantify methane and other metabolites, microbial abundance, gradient magnitude, and gradient stability rather than assume fixed values for methane yield, microbial enrichment, or diffusion coefficients. Any numerical estimate used in future work should be linked to a stated substrate, reaction, experimental system, analytical method, and uncertainty range.

A second testable outcome concerns the response of the model organism. *P. polycephalum* is known to reorganize movement and transport networks in response to environmental conditions, but this does not theoretically confirm sensitivity to hydrocarbon-associated gradients. The proposed experiments should measure movement rate, orientation, network change, and response thresholds directly under each treatment and control condition (Nakagaki et al., 2000; Reid, 2023; Tero et al., 2010). Marine-related stressors such as salinity, oxygen limitation, pH, and temperature may reduce or obscure the response. A useful biosensing signal would therefore require not merely movement, but a statistically reproducible and sufficiently specific difference between hydrocarbon-associated treatments and chemically comparable controls.

Overall, the conceptual analysis supports the feasibility of testing a biogeophysical sensing mechanism; it does not yet demonstrate that such a mechanism works in the Caspian Sea or that it can locate petroleum reservoirs. The strongest scientifically supported link is between hydrocarbons and microbial metabolism in petroleum-rich environments. The proposed second link—from the resulting geochemical gradient to a reliable slime-mold response—remains to be established experimentally. A third link—from that biological response to an exploration decision—would require independent geological and geophysical validation. Framing the result in these three stages preserves the innovative concept while

clearly distinguishing established microbial petroleum science from the hypotheses introduced by this study.

Feasibility assessment and scaling strategy: The final stage of the proposed research would critically evaluate practical applicability. The main criteria are environmental compatibility of the biological component; sensitivity, selectivity, and reproducibility of the measured response; technical requirements for imaging or signal acquisition; stability over time; ease of calibration; contamination and biosafety risks; and cost relative to established geophysical and geochemical methods. A favorable result at one stage would not automatically justify scaling. Progression from defined gradients to mixed microbial systems, mesocosms, and field-associated samples should occur only when each preceding stage demonstrates a reproducible signal and an acceptable rate of false-positive and false-negative responses.

In *D. discoideum*, intercellular coordination during aggregation is mediated by cyclic adenosine monophosphate (cAMP). Starving amoebae relay periodic cAMP signals, and neighboring cells move chemotactically toward increasing cAMP concentrations, producing wave-like patterns of coordinated migration and ultimately forming an aggregate (Bonner, 2009). Receptors, G-protein-mediated signaling, and regulation of adenylate cyclase are components of this signaling network. This well-characterized system is relevant to the present study because it provides a quantitative model of chemically mediated collective behavior. It should not be supported with the *P. polycephalum* maze-solving study, which addresses a biologically different organism and behavior.

Marine microbial systems use different molecular mechanisms for collective behavior. In many bacterial biofilms, quorum-sensing systems allow cells to respond to diffusible signal molecules whose production and accumulation depend on population and environmental context. Examples include N-acyl homoserine lactones in many Gram-negative bacteria, autoinducer-2-related signaling in diverse taxa, and peptide signals in many Gram-positive bacteria. Biofilm development is also governed by adhesion, extracellular-matrix production, nutrient gradients, competition, and many other regulatory processes (Costerton et al., 1995; Miller & Bassler, 2001; Nadell et al., 2016). Quorum sensing is therefore one component of biofilm organization rather than a universal single mechanism controlling all marine microbial communities.

A limited functional analogy can be drawn between cAMP-mediated aggregation in *D. discoideum* and chemical communication in bacterial biofilms: in both cases, local chemical information can influence coordinated behavior at the population level. The molecular pathways, evolutionary origins, cellular architectures, and developmental outcomes are nevertheless fundamentally different. cAMP signaling in a social amoeba should not be described as homologous to bacterial quorum sensing, and neither mechanism should be assumed to imply petroleum sensitivity. The value of the comparison is conceptual: it illustrates how local chemical signals can be amplified into spatially organized biological responses (Bonner, 2009; Miller & Bassler, 2001; Nadell et al., 2016).

Extracellular matrices provide another functional comparison, but the terminology must remain organism-specific. Bacterial biofilm extracellular polymeric substances (EPS) can contain polysaccharides, proteins, extracellular DNA, lipids, and other components that influence adhesion, hydration, mechanical stability, diffusion, and stress tolerance (Costerton et al., 1995; Flemming et al., 2025). Slime molds and social amoebae also produce extracellular material during particular life stages, but this should not be treated as biochemically identical to bacterial biofilm EPS. The shared engineering principle is that extracellular material can modify the local physical and chemical microenvironment surrounding cells or a biological network.

During the multicellular developmental stage of *D. discoideum*, cells and the migrating slug interact with an extracellular sheath that contributes to structural integrity and movement. In bacterial biofilms, the extracellular matrix likewise provides a physical framework within which cells are organized and protected from some environmental stresses. These systems differ in composition and developmental function, yet

ISSN: 2181-3337 | SCIENTISTS.UZ

they show how collective biological organization can be stabilized by material outside the cell membrane (Bonner, 2009; Costerton et al., 1995). For biosensor design, the analogy suggests that both signal processing and the physical matrix surrounding the sensing elements may influence response stability.

Nutrient limitation and environmental stress alter metabolism in both slime molds and biofilms, but the regulatory mechanisms are not interchangeable. *D. discoideum* responds to starvation through signaling pathways that initiate aggregation and development, while *P. polycephalum* can alter growth, network organization, and life-cycle state. Bacterial biofilms may enter slow-growing, stress-tolerant, or persister-like states through taxon-specific regulatory mechanisms. It is therefore too broad to state that glycolysis and fermentation universally become dominant or that one pathway such as (p)ppGpp explains stress adaptation across all of these systems. The defensible common principle is that environmental stress can reprogram metabolism and behavior in ways that affect sensor performance (Bonner, 2009; Flemming et al., 2025).

Stress resistance likewise takes different forms in different organisms. *P. polycephalum* can form resistant structures such as sclerotia and can produce spores through its reproductive cycle; *D. discoideum* forms spores within a fruiting body; bacterial populations can contain dormant or persister-like subpopulations; and marine protists display lineage-specific survival strategies. These states should not be grouped under a single morphological category such as “brush-like forms.” From an engineering perspective, however, the diversity of stress responses emphasizes that a living sensor must be evaluated not only for immediate sensitivity but also for recovery, stability, and repeatability after environmental perturbation.

Marine protists also illustrate specialized mechanisms of biomineralization and structural adaptation. Many foraminifera construct calcium carbonate tests, whereas radiolarians commonly form siliceous skeletons. The molecular details vary among taxa and should not be reduced to a single universal pathway without species-specific evidence. For the present argument, the important observation is simply that marine protists regulate ion transport, intracellular chemistry, organic templates, and mineral deposition to build structures under seawater conditions. These adaptations reinforce the possibility that indigenous marine eukaryotes may offer more environmentally compatible sensing models than terrestrial slime molds, although no hydrocarbon-sensing function is implied by biomineralization itself (Orsi, 2018).

Marine sponges provide an additional example of coordinated cellular organization. Dissociated sponge cells can exhibit species-specific reaggregation, demonstrating that cell recognition and adhesion can reconstruct organized multicellular structures under appropriate experimental conditions (Humphreys, 1970). This phenomenon has long served as a model for cell–cell recognition and tissue organization. Its relevance here is comparative rather than mechanistic: sponge reaggregation, social-amoeba aggregation, slime-mold network reorganization, and biofilm development all show that local cellular interactions can generate larger-scale structure, but they do so through distinct biological pathways. A biosensor design inspired by these systems should therefore extract general organizational principles without claiming biological equivalence.

Taken together, these examples support a general but carefully bounded concept: biological organization is influenced by genetic programs, signaling pathways, extracellular materials, metabolism, and environmental conditions acting together. No single mechanism is universal across bacteria, amoebozoans, protists, and animals. Nevertheless, local interactions can produce collective or network-level responses that are measurable at a larger spatial scale. This principle is relevant to bio-inspired sensing because a distributed system can integrate heterogeneous environmental information without requiring a centralized controller. The scientific task is to identify which features are transferable to a hydrocarbon-related sensing problem and which are specific to the biology of the original organism.

Discussion

This study proposes an interdisciplinary concept linking petroleum-associated microbial processes, geochemical gradients, and bio-inspired sensing. Its central objective is not to demonstrate an already established biological method for hydrocarbon exploration, but to evaluate whether a scientifically testable relationship can be constructed between known microbial transformations in hydrocarbon-rich environments and measurable responses of model organisms. The framework deliberately separates established evidence—such as anaerobic petroleum biodegradation and microbial methanogenesis—from the new hypothesis that a chemotactic slime-mold model could function as an indirect transducer of those chemical conditions.

Hydrocarbon-degrading bacteria and archaea, including "*Candidatus Methanoliparia*," can participate in petroleum-associated anaerobic metabolism and can contribute to methane production and other chemical changes in hydrocarbon-rich environments (Head et al., 2003; Laso-Pérez et al., 2019). These products may form gradients that are measurable geochemically. The hypothesis developed here is that selected gradients could also influence the movement or organization of *P. polycephalum* or *D. discoideum* under controlled laboratory conditions. Such a response would indicate sensitivity to the chemical field, not direct sensing of petroleum. The major practical limitations are therefore environmental compatibility, chemical specificity, signal stability, and the ability to distinguish petroleum-associated metabolism from general organic-matter degradation.

D. discoideum and *P. polycephalum* are primarily terrestrial model organisms, so direct survival and functional sensing on a natural seafloor cannot be assumed. Conditions in marine and subsurface sediments may include elevated ionic strength relative to terrestrial laboratory media, oxygen limitation or anoxia, variable pH, low nutrient availability, and increased pressure with depth. These factors could suppress growth, chemotaxis, aggregation, or network formation. The manuscript does not provide experimental evidence that either organism has already adapted to such conditions. Consequently, laboratory feasibility studies should determine whether the organisms can retain a reproducible response under selected stress conditions or whether an ex situ, contained, or purely biomimetic design is more appropriate.

A second major limitation is signal specificity. Methane, organic acids, sulfide, redox changes, and microbial biomass can arise from processes unrelated to petroleum, including degradation of natural organic matter. Therefore, a correlation between microbial activity and a hydrocarbon-bearing environment does not make any single microbial or chemical signal uniquely diagnostic of a reservoir. Future experiments must include non-hydrocarbon controls and should integrate the biological response with direct geochemical measurements. Any eventual field interpretation would also require geological and geophysical evidence so that a biological anomaly is treated as one layer of information rather than as a stand-alone exploration result (Orcutt et al., 2011).

Technological perspectives: If experimentally validated, the proposed framework could contribute to bio-geological engineering and biogeophysics by providing a new way to organize or interpret chemical-gradient information. Claims of reduced exploration cost cannot yet be quantified because no field-scale performance or economic dataset is presented. The most immediate technological opportunity lies in using slime-mold behavior as inspiration for adaptive algorithms, network optimization, distributed sensing, and experimental transduction of chemical gradients (Adamatzky, 2016; Tero et al., 2010). Such tools could eventually complement geophysical and geochemical data, but they should not be described as sources of seismic information unless a specific coupling to seismic measurements is demonstrated.

The conceptual framework and proposed validation strategy can be extended in future research. If terrestrial slime molds prove unsuitable under marine-related conditions, indigenous marine protists, bacteria, archaeal communities, or engineered cell-free and biomimetic systems could be evaluated as alternatives. Candidate organisms should be selected according to environmental tolerance, response

ISSN: 2181-3337 | SCIENTISTS.UZ

specificity, ease of measurement, reproducibility, containment requirements, and compatibility with sensor hardware. This broader strategy preserves the central idea—using biological organization or bio-inspired computation to interpret hydrocarbon-associated environmental signals—without making the entire concept dependent on the survival of one terrestrial model species.

Conclusion

This study presents a conceptual biogeophysical approach to hydrocarbon exploration that integrates petroleum microbiology, microbial ecology, biophysics, geophysics, and bio-inspired principles derived from slime-mold behavior. The literature supports the existence of microbial processes that transform hydrocarbons and generate methane, organic acids, redox changes, and other geochemical effects in petroleum-rich environments (Head et al., 2003; Laso-Pérez et al., 2019; Magot et al., 2000). The new contribution proposed here is to investigate whether such microbially generated chemical gradients can be translated into measurable spatial responses by a model biological system or by a biomimetic algorithm. This relationship remains a hypothesis rather than an experimentally established exploration method.

In the Caspian Sea context, the principal challenge is environmental and interpretive rather than merely computational. Terrestrial slime molds may not tolerate natural seafloor or subsurface conditions, and microbial or geochemical anomalies may be generated by non-petroleum processes. Nevertheless, *P. polycephalum* and *D. discoideum* provide experimentally tractable examples of adaptive movement, network reorganization, and collective response to chemical conditions. Their greatest value may therefore lie in laboratory proof-of-concept studies and in the development of biomimetic algorithms that can integrate heterogeneous sensor information, rather than in direct release of living slime molds into the marine environment.

Future research should focus on controlled experimental validation of the complete proposed chain: hydrocarbon-associated microbial process → measurable geochemical gradient → reproducible biological or biomimetic response → independent confirmation by conventional geological and geophysical evidence. Experiments should quantify specificity, sensitivity, response time, environmental tolerance, false-positive rates, and repeatability. If these criteria are satisfied, the approach could then be evaluated in increasingly realistic sediment and mesocosm systems. This staged strategy would allow the innovative biological concept to be tested rigorously while preserving conventional geophysical methods as the principal reference for hydrocarbon exploration.

Funding

This research received no specific grant from any funding agency in the public, commercial, or not-for-profit sectors.

REFERENCES

1. Adamatzky, A. (2010). *Physarum machines: Computers from slime mould*. World Scientific.
2. Adamatzky, A. (2013). Physarum wires: Self-growing self-repairing smart wires made from slime mould. *Biomedical Engineering Letters, 3*(4), 232–241. https://doi.org/10.1007/s13534-013-0108-9
3. Adamatzky, A. (Ed.). (2016). *Advances in Physarum machines: Sensing and computing with slime mould*. Springer. https://doi.org/10.1007/978-3-319-26662-6
4. Aitken, C. M., Jones, D. M., & Larter, S. R. (2004). Anaerobic hydrocarbon biodegradation in deep subsurface oil reservoirs. *Nature, 431*, 291–294. https://doi.org/10.1038/nature02922
5. Azam, F., & Malfatti, F. (2007). Microbial structuring of marine ecosystems. *Nature Reviews Microbiology, 5*, 782–791. https://doi.org/10.1038/nrmicro1747
6. Bjørlykke, K. (Ed.). (2015). *Petroleum geoscience: From sedimentary environments to rock physics* (2nd ed.). Springer. https://doi.org/10.1007/978-3-642-34132-8

7. Boetius, A., Ravenschlag, K., Schubert, C. J., Rickert, D., Widdel, F., Gieseke, A., Amann, R., Jørgensen, B. B., Witte, U., & Pfannkuche, O. (2000). A marine microbial consortium apparently mediating anaerobic oxidation of methane. *Nature, 407*, 623–626. https://doi.org/10.1038/35036572
8. Bonner, J. T. (2009). *The social amoebae: The biology of cellular slime molds*. Princeton University Press.
9. Brumley, D. R., Carrara, F., Hein, A. M., Hagstrom, G. I., Levin, S. A., & Stocker, R. (2020). Cutting through the noise: Bacterial chemotaxis in marine microenvironments. *Frontiers in Marine Science, 7*, Article 527. https://doi.org/10.3389/fmars.2020.00527
10. Costerton, J. W., Lewandowski, Z., Caldwell, D. E., Korber, D. R., & Lappin-Scott, H. M. (1995). Microbial biofilms. *Annual Review of Microbiology, 49*, 711–745. https://doi.org/10.1146/annurev.mi.49.100195.003431
11. Falkowski, P. G., Fenchel, T., & DeLong, E. F. (2008). The microbial engines that drive Earth's biogeochemical cycles. *Science, 320*(5879), 1034–1039. https://doi.org/10.1126/science.1153213
12. Fenchel, T. (1987). *Ecology of protozoa: The biology of free-living phagotrophic protists*. Springer. https://doi.org/10.1007/978-3-662-06817-5
13. Flemming, H.-C., van Hullebusch, E. D., Little, B. J., Neu, T. R., Nielsen, P. H., Seviour, T., Stoodley, P., Wingender, J., & Wuertz, S. (2025). Microbial extracellular polymeric substances in the environment, technology and medicine. *Nature Reviews Microbiology, 23*, 87–105. https://doi.org/10.1038/s41579-024-01098-y
14. Hall-Stoodley, L., Costerton, J. W., & Stoodley, P. (2004). Bacterial biofilms: From the natural environment to infectious diseases. *Nature Reviews Microbiology, 2*, 95–108. https://doi.org/10.1038/nrmicro821
15. Head, I. M., Jones, D. M., & Larter, S. R. (2003). Biological activity in the deep subsurface and the origin of heavy oil. *Nature, 426*, 344–352. https://doi.org/10.1038/nature02134
16. Humphreys, T. (1970). Species specific aggregation of dissociated sponge cells. *Nature, 228*, 685–686. https://doi.org/10.1038/228685a0
17. International Energy Agency. (2024). *World energy outlook 2024*. https://www.iea.org/reports/world-energy-outlook-2024
18. Keegstra, J. M., Carrara, F., & Stocker, R. (2022). The ecological roles of bacterial chemotaxis. *Nature Reviews Microbiology, 20*, 491–504. https://doi.org/10.1038/s41579-022-00709-w
19. Laso-Pérez, R., Hahn, C., van Vliet, D. M., Tegetmeyer, H. E., Schubotz, F., Smit, N. T., Pape, T., Sahling, H., Bohrmann, G., Boetius, A., Knittel, K., & Wegener, G. (2019). Anaerobic degradation of non-methane alkanes by 'Candidatus Methanoliparia' in hydrocarbon seeps of the Gulf of Mexico. *mBio, 10*(4), e01814-19. https://doi.org/10.1128/mBio.01814-19
20. Laso-Pérez, R., Wegener, G., Knittel, K., Widdel, F., Harding, K. J., Krukenberg, V., Meier, D. V., Richter, M., Tegetmeyer, H. E., Riedel, D., Richnow, H.-H., Adrian, L., Reemtsma, T., Lechtenfeld, O. J., & Musat, F. (2016). Thermophilic archaea activate butane via alkyl-coenzyme M formation. *Nature, 539*, 396–401. https://doi.org/10.1038/nature20152
21. Magot, M., Ollivier, B., & Patel, B. K. C. (2000). Microbiology of petroleum reservoirs. *Antonie van Leeuwenhoek, 77*(2), 103–116. https://doi.org/10.1023/A:1002434330514
22. Margulis, L., & Chapman, M. J. (2009). *Kingdoms and domains: An illustrated guide to the phyla of life on Earth* (4th ed.). Academic Press.
23. Mbadinga, S. M., Wang, L.-Y., Zhou, L., Liu, J.-F., Gu, J.-D., & Mu, B.-Z. (2011). Microbial communities involved in anaerobic degradation of alkanes. *International Biodeterioration & Biodegradation, 65*(1), 1–13. https://doi.org/10.1016/j.ibiod.2010.11.009
24. Miller, M. B., & Bassler, B. L. (2001). Quorum sensing in bacteria. *Annual Review of Microbiology, 55*, 165–199. https://doi.org/10.1146/annurev.micro.55.1.165

ISSN: 2181-3337 | SCIENTISTS.UZ

25. Nadell, C. D., Drescher, K., & Foster, K. R. (2016). Spatial structure, cooperation and competition in biofilms. *Nature Reviews Microbiology, 14*, 589–600. https://doi.org/10.1038/nrmicro.2016.84
26. Nakagaki, T., Yamada, H., & Tóth, Á. (2000). Maze-solving by an amoeboid organism. *Nature, 407*, 470. https://doi.org/10.1038/35035159
27. Orcutt, B. N., Sylvan, J. B., Knab, N. J., & Edwards, K. J. (2011). Microbial ecology of the dark ocean above, at, and below the seafloor. *Microbiology and Molecular Biology Reviews, 75*(2), 361–422. https://doi.org/10.1128/MMBR.00039-10
28. Orsi, W. D. (2018). Ecology and evolution of seafloor and subseafloor microbial communities. *Nature Reviews Microbiology, 16*, 671–683. https://doi.org/10.1038/s41579-018-0046-8
29. Raina, J.-B., Lambert, B. S., Parks, D. H., Rinke, C., Siboni, N., Bramucci, A., Ostrowski, M., Signal, B., Lutz, A., Mendis, H., Rubino, F., Fernandez, V. I., Stocker, R., Hugenholtz, P., Tyson, G. W., & Seymour, J. R. (2022). Chemotaxis shapes the microscale organization of the ocean's microbiome. *Nature*, *605*, 132–138. https://doi.org/10.1038/s41586-022-04614-3
30. Reid, C. R. (2023). Thoughts from the forest floor: A review of cognition in the slime mould Physarum polycephalum. *Animal Cognition, 26*, 1783–1797. https://doi.org/10.1007/s10071-023-01782-1
31. Selley, R. C., & Sonnenberg, S. A. (2015). *Elements of petroleum geology* (3rd ed.). Academic Press. https://doi.org/10.1016/C2010-0-67090-8
32. Shapiro, J. A. (1998). Thinking about bacterial populations as multicellular organisms. *Annual Review of Microbiology, 52*, 81–104. https://doi.org/10.1146/annurev.micro.52.1.81
33. Sheriff, R. E., & Geldart, L. P. (1995). *Exploration seismology* (2nd ed.). Cambridge University Press.
34. Stoodley, P., Sauer, K., Davies, D. G., & Costerton, J. W. (2002). Biofilms as complex differentiated communities. *Annual Review of Microbiology, 56*, 187–209. https://doi.org/10.1146/annurev.micro.56.012302.160705
35. Telford, W. M., Geldart, L. P., & Sheriff, R. E. (1990). *Applied geophysics* (2nd ed.). Cambridge University Press. https://doi.org/10.1017/CBO9781139167932
36. Tero, A., Takagi, S., Saigusa, T., Ito, K., Bebber, D. P., Fricker, M. D., Yumiki, K., Kobayashi, R., & Nakagaki, T. (2010). Rules for biologically inspired adaptive network design. *Science, 327*(5964), 439–442. https://doi.org/10.1126/science.1177894
37. York, A. (2022). Chemotaxis in the ocean. *Nature Reviews Microbiology, 20*, 381. https://doi.org/10.1038/s41579-022-00743-8

CONTENTS

Eshmuradov Dilshod, Abdukayumov Abdurashid, Saidova Gulchehra, Elmuradov Temurmalik
METHODS FOR IMPROVING RADIO NAVIGATION SYSTEM RELIABILITY IN THE COMPREHENSIVE ASSESSMENT OF AIR TRAFFIC MANAGEMENT SYSTEM MODERNIZATION EFFECTIVENESS 4

Indiaminov Ravshan, Urolov Sharofiddin
MAGNETOMECHANICAL DEFORMATION OF THIN FERROMAGNETIC SHELLS IN EXTERNAL MAGNETIC FIELDS: A COUPLED MAGNETOELASTIC FINITE-ELEMENT AND EXPERIMENTAL STUDY 17

Dehqonova M, Mirzayeva M
HPLC CHARACTERIZATION OF WATER-SOLUBLE VITAMINS AND FREE AMINO ACIDS IN A DRY AQUEOUS EXTRACT OF POMEGRANATE (PUNICA GRANATUM L.) PEEL 28

K.M. Quchqarov, B.A. Ergashev, M.P. Pirimmatov, A.S. Matmuratov, B.A. Gulumbaev, X.Z.To‘liboyeva
INFLUENCE OF DEFECTS ON THE ELECTRICAL CONDUCTIVITY OF SB_xSE_γ THIN FILMS PREPARED BY THE INDEPENDENT SOURCE VAPOR TRANSPORT TECHNIQUE 37

Akhrorova Barnokhon, Kholiyorova Feruza
EFFECTS OF SUBSTRATE, IRRIGATION VOLUME, AND MINERAL NUTRITION ON GROWTH, YIELD, AND VOLATILE COMPOUND ACCUMULATION IN PIMPINELLA ANISUM L. UNDER GREENHOUSE CONDITIONS 48

Gulyamov Saidakhror, Mukhitdinova Munavvarkhon
NEW UZBEKISTAN: THE EFFECTIVENESS OF ARTIFICIAL INTELLIGENCE-BASED DIGITAL TRANSFORMATION BY 2030 53

Quchqarov K, Ergashev B, Pirimmatov M, MatmuratovA, Gulumbaev B, To‘liboyeva X
INFLUENCE OF SOURCE TEMPERATURE ON THE COMPOSITION, MORPHOLOGY, AND ELECTRICAL CONDUCTIVITY OF Sb_xSe_γ THIN FILMS PREPARED BY VAPOR TRANSPORT DEPOSITION 60

Yuldoshov Boysori, Kholmuminov Asadbek
MODEL-BASED ASSESSMENT OF A 60 W MONOCRYSTALLINE PHOTOVOLTAIC MODULE AND TWO THREE-MODULE CONFIGURATIONS UNDER HOT-SUMMER CONDITIONS IN TERMEZ, UZBEKISTAN 68

Usmonova Aziza, Pulatov Khayrulla
SYNTHESIS, CHARACTERIZATION, AND POTENTIAL USE OF A SULFONATED CATION-EXCHANGE RESIN FOR HARD-WATER SOFTENING 78

Akhrorova Barnokhon
COMPARATIVE GC–MS PROFILING OF VOLATILE CONSTITUENTS IN PIMPINELLA ANISUM L. GROWN UNDER CONTRASTING SUBSTRATE AND CALCIUM–BORON NUTRITION CONDITIONS 90

Rajabov V
MATHEMATICAL MODELING OF DEMULSIFIER CONCENTRATION EFFECTS ON OIL–WATER INTERFACIAL TENSION DURING FIELD OIL TREATMENT 97

Mavlonova Madinabonu
RECENT ADVANCES IN PROCESSING TECHNOLOGIES FOR ARONIA MELANOCARPA RAW MATERIALS: AN INTEGRATIVE REVIEW OF JUICE STABILIZATION, DRYING, EXTRACTION, ENCAPSULATION, AND BY-PRODUCT VALORIZATION 105

Turobova Vazira
SEASONAL GROWTH PERFORMANCE OF “GAMLIN” AND “RA’NO” SWEET ORANGE CULTIVARS GRAFTED ON MEYER AND MANZUR LEMON ROOTSTOCKS 117

Siddikov Shuhrat, Abdazimov Anvar
DETERMINATION OF THE BALANCING MOMENT OF A CRANK-SLOTTED MECHANISM USING THE N.E. ZHUKOVSKY LEVER METHOD 123

Abdullayev Vugar
INVESTIGATION OF HYDROCARBON-RELATED MICROBIOLOGICAL ACTIVITY IN MARINE SYSTEMS WITHIN A BIOGEOPHYSICAL FRAMEWORK USING SLIME MOLDS 128

ISSN: 2181-3337 | SCIENTISTS.UZ



International Scientific Journal
Science and Innovation Series A
Volume 5 Issue 7

ISSN: 2181-3337

Published: 10.08.2026. Font: “Times New Roman”.

LLC “Science and innovation”
License Mass Media №:1597 27.04.2022
License Publisher №:455168 21.11.2024
Address: 100121, Uzbekistan, Tashkent city, Yakkasaroy district,
Shota Rustaveli Street 150, Vega Business Center, 6th floor, Room 2.
www.scientists.uz, info@scientists.uz, +998901259654